8-2007

Design and Evaluation of a Non-Intrusive Corn Population Sensor

Haizhou Li
University of Tennessee - Knoxville

To the Graduate Council:

I am submitting herewith a dissertation written by Haizhou Li entitled "Design and Evaluation of a Non-Intrusive Corn Population Sensor." I have examined the final electronic copy of this dissertation for form and content and recommend that it be accepted in partial fulfillment of the requirements for the degree of Doctor of Philosophy, with a major in Biosystems Engineering.

John B. Wilkerson, Major Professor

We have read this dissertation and recommend its acceptance:

William E. Hart, Xiaofei Ye, Paul Crilly

Accepted for the Council:

Carolyn R. Hodges

Vice Provost and Dean of the Graduate School

(Original signatures are on file with official student records.)

To the Graduate Council:

I am submitting herewith a dissertation written by Haizhou Li entitled "Design and Evaluation of a Non-Intrusive Corn Population Sensor." I have examined the final electronic copy of this dissertation for form and content and recommend that it be accepted in partial fulfillment of the requirements for the degree of Doctor of Philosophy, with a major in Biosystems Engineering.

John B. Wilkerson, Major Professor

We have read this dissertation
And Recommend its acceptance

William E. Hart

Xiaofei Ye

Paul Crilly

Accepted for the council:

Carolyn Hodges, Vice Provost and
Dean of the Graduate School

Design and Evaluation of a Non-Intrusive Corn Population Sensor

A Dissertation
Presented for the
Doctor of Philosophy
Degree
The University of Tennessee, Knoxville

Haizhou Li
August, 2007

DEDICATION

To my family.

ACKNOWLEDGEMENTS

I would like to express my deepest gratitude to my advisor, Dr. John B. Wilkerson, for his excellent guidance, caring, and patience throughout the course of this project. I also extend my thanks to my committee, Dr. William E. Hart, Dr. Phillip X. Ye, and Dr. Paul Crilly for their constant supports and ideas. Senior Research Associate, Dr. Stacy Worley, made tremendous contributions to this project, assisting with both project and proofreading. Special thanks go to his hard work and friendship.

I would like to thank David Smith and Craig Wagoner, who as good friends were always willing to give their best help on the fabrication of equipment used in this project.

Special thanks extend to Milan Experiment station and Knoxville experiment Station – Plant and Soil Science Farm for providing a welcoming and friendly environment for conducting research.

ABSTRACT

Specific objectives of this study were to develop, prototype, and test a corn population sensor. Both intrusive mechanical and non-intrusive capacitive techniques have been used to develop the stalk population sensors in previous research. However, neither could generate consistent performance. The mechanical method required high maintenance and resulted in significant underestimations of stalk counts. The performance of capacitive systems was limited by inadequate sensing distance, especially at low stalk moisture levels.

In this research, the sensitivity of the capacitive sensor was optimized for corn stalks. This system utilized a single-sided capacitive sensor, Wien bridge oscillator, phase-locked loop, and an operational amplifier to transform stalk presence to a change in electrical potential signal.

The capacitive sensor patterns were simulated using the finite element method, which provided useful conceptual information. A number of different detection element patterns were modeled and tested. The patterns examined included single-sided two-plate, interdigital, polarized interdigital, semi-interdigital, and solid ground electrode. The key parameters affecting pattern sensitivity were investigated. The most promising pattern, the solid ground electrode, was selected for further evaluation and development.

The solid ground electrode detection element was incorporated into circuitry including Wien-Bridge oscillator, a phase-locked loop used as a high-speed frequency-to-voltage converter, and an operational amplifier to provide impedance matching and

maximize data acquisition resolution. The operational configuration, optimum operating parameters, and associated component sizes were determined using both modeling and laboratory testing. With an acceptable signal-sided pattern and signal-to-noise ratio, this sensing system was investigated in a realistic production environment.

A preliminary field test was used to evaluate the sensor system (including a protective housing and mounting system) and data acquisition system to identify problems before conducting the final field test. Stalk moisture content and harvest speed were used as treatment blocks in the final test. The influences of environmental and mechanical noise and the noise-like influence of corn leaves and weeds were also investigated. The final field test accurately simulated realistic harvesting conditions and real-time data was collected for stalk identification analysis.

Post-acquisition processing, feature extraction, and principal component analysis of the extracted features were performed on the raw field data. Three sensor signal features were selected to identify stalks. A backpropagation artificial neural network technique was used to develop the pattern classification model. Numerous neural network structures were evaluated and two-layer structure with four neurons in the first layer and one neuron in the second layer was selected based on maximum prediction precision and accuracy and minimum structure complexity. This structure was then evaluated to determine the prediction accuracy at various resolution levels. Results showed that the model can predict stalk population at 99.5% accuracy when the spatial resolution is 0.025 ha. The sensor can predict stalk population with a 95% accuracy when the resolution is a 9-meter row segment (approximately 10 seconds).

Table of Contents

List of Tables

List of Figures

CHAPTER 1 – INTRODUCTION

Justification for Research

According to USDA estimates, 81.6 million acres of corn were planted and 10.8 billion bushels of corn were harvested in the United States in 2005 (USDA-UASS 2005). Producers are continuously looking for technologies to improve their production efficiency due to rising production cost and varied grain markets.

A corn population sensor can benefit producers, seed companies, researchers, and consumers. The primary advantage of this sensor is to generate a better site-specific corn stalk density maps. Improved corn stalk density maps can be beneficial in several ways. First, the improved maps can enable farmers to make better field management decisions. By using this data, farmers can obtain a geo-referenced corn plant population map that shows site-specific differences in corn population within a field. This knowledge allows farmers to respond appropriately and improve production efficiency. Point rows, which are typically found at field boundaries, result in under-estimation of yield by yield monitors. This is because yield is calculated while assuming a full header width even though a smaller area is actually being harvested. A corn stalk sensor can be used to generate a better yield map by eliminating the effect of point rows on yield map data. By mounting a population sensor on each row unit, the actual number of rows being harvested can be continuously monitored. The sensor can also be used to modify GPS-

enabled variable-rate seeding controllers through offline feedback. These modifications can aid in achieving the optimal seeding rate.

Second, seed companies can benefit from population sensors by quantifying corn plant survival rates. The availability of seed germination and stalk survival rates and yield per plant may help arbitrate disputes between farmers and seed companies.

Third, sensor determined corn stalk population information can assist researchers in other corn related areas. This data may help plant breeders evaluate new varieties in large production fields. Improved site-specific data could help researchers quantify the impact of irrigation, fertilization, and weeds on seed germination and stalk survival rates. The end result is better control of experiments with respect to management variables.

Both intrusive (mechanical) and non-intrusive (electromagnetic-based) designs have been developed during the past fifteen years. However, neither method could consistently generate the required detection precision. Under a wide range of field conditions, the mechanical design was prone to underestimate the stalk population and the capacitive design had low sensitivity and inadequate sensing distance, which limited the accuracy of detecting low moisture content corn stalks.

The potential broad applications of this sensor in corn production and the limitations of past attempts, lead us to the following objectives.

Objectives

This study will contribute to the development of a non-intrusive corn population sensor design that will provide accurate corn population measurements during harvest.

To achieve these goals, three specific objectives were indentified:

1) Identify sensing techniques that can potentially be used as indicators to quantify corn population. An optimum technique or combination of techniques will be investigated. Sensing techniques considered will include dielectrics, spectral reflectance, microwave absorption, and microwave refraction.

2) Develop and laboratory test a prototype sensor based on the selected technique or technique combinations identified from Objective 1.

3) Evaluate the prototype sensor in a production harvest environment. Data post-processing techniques will be used to investigate the difference between hand-counted population and sensor-counted population. Effects of corn leaves, weeds, and background noise will also be investigated. Sensor accuracy, stability, and repeatability will be evaluated based on these investigations.

CHAPTER 2 – REVIEW OF LITERATURE

Potential Sensor Applications

A corn population sensor has the potential to improve production agriculture efficiency. For example, it can be used to improve yield maps, field management practices, and seeding systems. Yield maps are useful for documenting and analyzing spatially-variable crop performance within a field. However, yield monitor systems sometimes provide invalid yield estimates because of complicated harvesting geometrics (Prather and Denton, 2003). One such circumstance results when point rows develop as shown in Figure 1. Point rows result in under-estimation of yield because yield is calculated assuming a full header width is being harvested, even though a smaller width is actually being harvested (Figure 2). By mounting a population sensor on each row unit, the actual number of rows being harvested can be continuously monitored. If the information is electronically communicated to the yield monitor, accuracy of yield maps will greatly improve, especially in irregularly shaped fields.

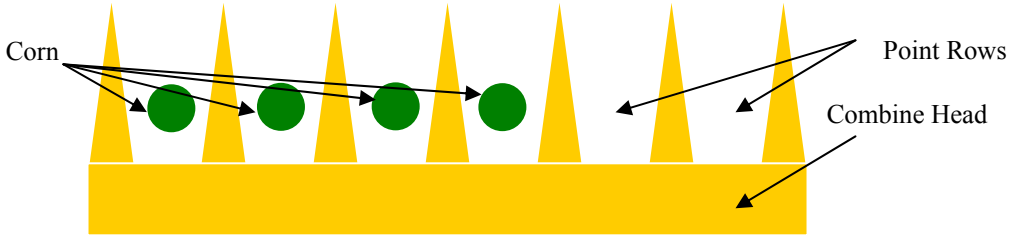

Figure 1. Point row illustration

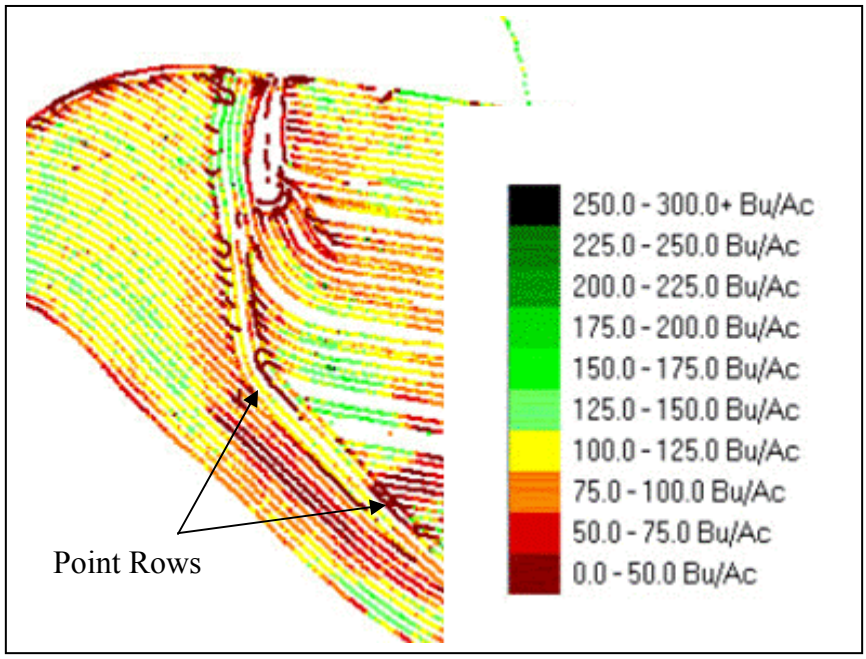

Figure 2. Corn yield map illustration. Lower yield estimates occurred on the field boundary. (Prather and Denton, 2003)

Geo-referenced corn plant population data have the potential to improve several aspects of production management. Detailed knowledge of corn plant population is important because population affects yield (Buehring and Dobbs, 2000; Yonts and Smith, 1997). Evaluation of plant population from several seasons may indicate that some fields consistently fail to produce acceptable plant stands, and are unsuitable for corn planting. Furthermore, site-specific knowledge of low population areas within fields will allow the examination of the causes of low population. Improvements may be needed in drainage, irrigation, soil fertility, and weed control in these areas. Corn plant population data can provide farmers with the knowledge needed to better manage both planting plans and field operations.

Plant spacing uniformity is another important factor that affects the crop yield. Research by Nielsen (1995) showed that increases in corn plant spacing variations due to

planter inaccuracies or reduced emergence reduced yield in some cases. GPS-enabled variable-rate seeding controllers now commercially available make it possible to adjust seeding rate to vary harvest population within a field to provide an optimal and uniform harvest population (Sudduth et al., 2000). However, seeding system failures and field specific situations can affect both optimal seeding rate and uniform plant spacing. A population sensor mounted on each harvester row can detect the row where a planter malfunction took place. Thus, this corn population sensor could be an effective aid to gather harvest population and plant location information. Detailed analysis of the problems can be used to compute an optimum seeding rate map. This map could be used to update the automated seeding system to compensate for emergence variations and provide an optimum economic yield for subsequent planting seasons.

Population information collected at harvest in conjunction with seeding rate maps can be used to compute seed germination and stalk survival rates. Because seed germination and stalk survival rates are important indicators of seed quality, this sensor will be helpful for evaluating new seed varieties. Plant population maps and yield maps can be combined to produce yield-per-plant maps. This type of data will help researchers and producers evaluate variety performance. In certain conditions, availability of seed germination and stalk survival rates and yield-per-plant values may help arbitrate disputes between producers and seed companies.

Corn Population Sensor Reviews

Because of the expected benefit from this sensor, both intrusive (mechanical) and non-intrusive (electromagnetic-based) designs have been tested during the past fifteen years, but neither could generate consistent performance. Mechanical systems have been shown to be prone to errors resulting from weak stalks and stalks growing close to one-another. The performance of capacitive systems has been limited by insufficient sensing distance, especially at low stalk moisture levels.

Intrusive methods

Early corn population sensors were mechanical. Initial design and testing of corn population sensors were described by Birrell and Sudduth (1995). The sensor consisted of a spring-loaded rod attached to a rotary potentiometer that was mounted in front of the gathering chains on the row dividers of the combine head (Figure 3). During harvest, the corn stalk caused the rod to rotate, increasing the voltage potential across the potentiometer. In 2000, Sudduth and Birrell modified their initial designs to provide better flow of plants past the sensor. The mechanism was redesigned to fit within the row divider, with only the sensor rod protruding above. A mechanical shock absorber was added to cushion the return of the sensor rod to the at-rest position.

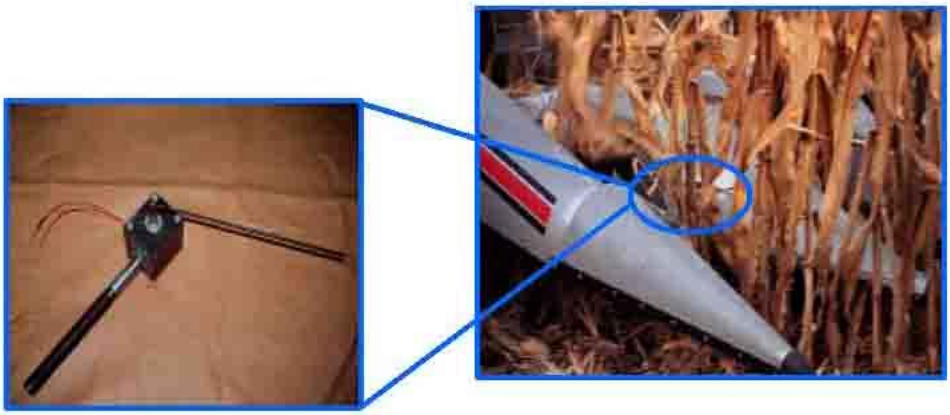

Figure 3. Redesigned mechanical population sensor (Sudduth and Birrell, 2000)

In their research, sensor-determined and hand-counted population for individual harvested rows was compared in 1997, 1998, and 1999. On average, the sensor underestimated actual population by 4.4%. The standard error of the estimate was equivalent to an error of 3 plants within 10 m of row length. However, most test blocks were analyzed using "corrected" populations, meaning that weak stalks were removed in the field and double counts (two plants immediately adjacent to one another) were removed before analysis. This research approach may show two possible intrinsic limitations of mechanical design: 1) strong weeds could be counted as corn stalks while weak stalks were disregarded, and 2) two stalks immediately adjacent to one another were counted as one. While the mechanical method only needs simple signal conditioning and it is unaffected by ambient humidity changes, it cannot overcome its intrinsic limitations in accurately quantifying corn stalk density.

Non-intrusive Methods

An electrical capacitance-based measurement technique has been studied to count corn stalks. Nichols (2000) holds a patent for a method and apparatus used to count plants as they are harvested. It includes a capacitive sensor which senses the change in dielectric surrounding a capacitive proximity sensor, which in turn is sent to a counter that tallies the plants as they are being harvested. The patent contains no documented evaluation for this invention.

Webb (2001) designed a ring-shaped coaxial capacitor proximity sensor (Figure 4a). Testing showed that this system was capable of measuring plant population with some degree of accuracy. Tractor-mounted tests indicated average absolute errors of 8.9 percent and 16.0 percent for speeds of 0.4 mph and 1.76 mph, respectively. Accuracy was moderately correlated with speed ($r=0.43$: $\alpha=0.05$). Moody (2002) improved this capacitive sensor, which consisted of a three-electrode arrangement (Figure 4b). The three electrodes were in essence two capacitors in series, and a bridge measurement technique was used to measure the capacitance between adjacent electrodes. Testing showed that the triple-plate design was much less sensitive to changes in relative humidity than a similar dual-plate design. However, in laboratory testing, neither prototype effectively generated sufficient signal-to-noise ratio (SNR) at a clearance between stalk and sensor of greater than 0.5 inch, which was determined insufficient.

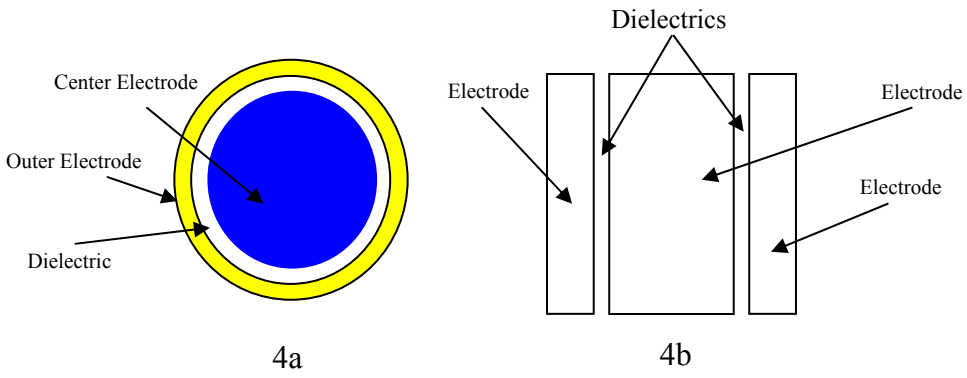

Figure 4. Capacitance-based non-intrusive corn population sensor (Webb, 2001 and Moody, 2002)

Recently, a machine-vision technique was used to develop a corn plant population sensing system for measuring early stage corn population (Shrestha and Steward, 2003). Video was acquired from a vehicle-mounted digital video camera. Algorithms were developed to sequence video frames and to segment and count corn plants. Performance of this system was evaluated by comparing its estimation of plant counts with manual stand counts in 60 experimental units of 6.0 m sections of corn rows. In low-weed conditions, the system plant count was well correlated to manual stand count ($R^2 = 0.90$). The standard error of population estimates was 1.8 plants over 33.2 mean manual plant count, or a 5.4% coefficient of variation. However, no estimation of corn stalk count was conducted under weedy conditions. Because this design was developed based on vegetation segmentation, it would be difficult for this system to separate weeds from corn plants. Therefore, high-weed conditions can be a major limitation for effectively implementing this system.

Potential Sensing Techniques

Electromagnetic and Neutron Methods for Moisture Content Measurement

Pordesimo et al. (2004) indicated that field dried corn stalks may contain at least 8% moisture content wet basis (Note: all moisture content in this dissertation is wet basis). If the water in corn stalks can be detected, the location of these corn stalks may be determined. Therefore, moisture-based techniques were investigated for a corn plant population sensor.

The most popular moisture content measurement technology used in agriculture is electric capacitance (Mizukami et al., 2006; Sacilik, et al., 2007; Schmilovitch et al., 2006). Microwave absorption and radio frequency transmission are other moisture content measurement methods that are also based on variation of electrical properties (Schajer and Orhan, 2006; Tien and Judge, 2006; Knochel et al., 2001; Trabelsi et al., 2006). Also, infrared techniques have been used to develop moisture content sensors (Ozdemir, 2006; Jezek et al., 2006). Infrared techniques involve surface determination, which must be representative of the layers of the bulk material being analyzed. Sensors using neutron activation techniques determine the hydrogen content in the material from which moisture content is inferred. Neutron activation measurements are based on the deceleration of fast neutrons in conjunction with the absorption of gamma radiation to establish density (Nagadi and Naqvi, 2007; Gehl and Rice, 2007). A nuclear magnetic resonance (NMR) moisture meter was recently produced (Sorland et al., 2004; Sanchez et

al., 2005). The measurement is based on the fact that $_1$H NMR signal intensity is proportional to the total number of proton in a sample.

All techniques noted above have been widely used in laboratory or industry applications for moisture determination. Electric capacitance is the most common design principal used by sensor manufacturers primarily based on low cost. Capacitance-based sensors can be non-contact, have the capability to detect small objects, and work with either conducting or insulating objects. However, detection of insulating objects depends on a high-loss dielectric or a dielectric constant sufficiently different from the background. The sensors' maximum sensing range can be affected by the change of the dielectric constant of air, which changes with atmospheric pressure, temperature and humidity. Atmospheric pressure and temperature have little effect on the sensitivity range (< 3% of value range in general field condition); however absolute humidity could significantly affect the sensitivity range (Baxter, 1996). These sensors also could be affected by the variation in the concentration of dissolved electrolytes within materials. Another limit to the detection sensitivity is the effect of small relative movements of sensor components which can be caused by machine vibration or thermal expansion. Such movement could change the mutual capacitance between the measuring electrodes.

Advanced electromagnetic sensing techniques have been developed to overcome some of these disadvantages. Kandala et al. (1992) found that radio frequency (RF) is very well suited for online moisture monitoring during the production of foodstuffs. In this method a resonant perturbation technique is used to determine the water content from the dielectric properties. Both real and imaginary parts of the complex permittivity of a

material are correlated to their moisture content under radio frequency resonance. In general, complex permittivity is expressed as $\varepsilon_r = \varepsilon_r' - j\,\varepsilon_r''$, where ε_r' and ε_r'' are the dielectric constant and loss factor, respectively. Thus, the system response is a measure of the total water in the RF field, which is directly related to the moisture content of the material. A relationship between moisture content and the complex permittivity was developed to measure the moisture content in individual popcorn kernels:

$$M = 36.675 - 2.1336\varepsilon'_{10} + 4.9044\ln(\varepsilon''_1) + 1.6844\times10^{-5}\left[\left(\frac{\varepsilon'-1}{\varepsilon''}\right)_1 - \left(\frac{\varepsilon'-1}{\varepsilon''}\right)_{10}\right]^2 \quad (2.1)$$

where, M is the moisture content in percent, and subscripts 1 and 10 refer to values associated with measurements at 1 and 10 MHz, respectively.

Another electromagnetic moisture content measurement technology is open microwave. Research by Knochel et al. (2001) showed the moisture content and bulk density of shelled corn can be determined by measuring microwave parameters. Such measurement does not require any contact between the material and the equipment and is fast, continuous, and non-destructive. The principal of microwave moisture measurement is that microwave beam energy changes with respect to different water content. When non-magnetic materials, such as foodstuffs, are introduced into an electric field the storage of electric energy is increased and the resonant frequency decreases. Energy dissipation in the material under examination leads to an attenuation of the resonance resulting in an exponential decay of the oscillation amplitude in the time domain and a broadening of the resonance curve in the frequency domain. Thus, two independent parameters of the material (permittivity and attenuation) can be determined by

quantifying the amplitude of the resonance around the resonant frequency by scalar and potentially low cost measurement methods. Unlike Karl Fischer titration methods or oven-drying, microwave moisture determination is an indirect method based on a dielectric measurement. Microwaves detect the mass of water in a certain volume and respond to the water concentration (Kraszewski and Nelson, 1994).

Another sensor that is commonly used in industry is Near Infrared Reflectance (NIR). NIR measurement of material's moisture content is based on the ratio of absorbed and reflected wavelengths. This technique has been developed in the past 40 years to measure the water content in fruits and vegetables. NIR technology has been improved in recent decades. McQueen et al. (1995) used two popular NIR methods (optothermal near infrared (NIR) spectroscopy and Fourier Transform Mid-Infrared-Attenuated Total Reflection (FTIR-ATR)) to measure moisture contents of cheese samples. NIR techniques are very efficient, provide quick measurements, and require minimal specimen preparation. It also offers other advantages, such as medium to high accuracy, non-contact with materials, large range of applications, and medium investment. However, it should also be noted that surface conditions can have significant impacts on NIR measurements. Also, reflective and black-body radiation from nearby surfaces can cause false readings. Dust and interference (e.g., steam and high humidity) can also have significant effects on measurement accuracy.

Moisture content measurement using NMR techniques was introduced into the agriculture area in the last decade. NMR has been regarded as a seminal tool for understanding material compounds because it directly monitors the spin state of atoms.

The nuclear spin is sensitive to the electron configuration of the parent atom and it is this fact that makes the NMR method an incisive tool for understanding physical and chemical properties of materials. Measurement is based on the fact that $_1$H NMR signal intensity is proportional to the total number of proton nuclei in a sample. Advantages of NMR techniques are that they allow a quick acquisition of results, are non-invasive, non-destructive, require little preparation of samples, easily automated, can quantify different water fractions present with different mobilities, and can simultaneous determine water and fat contents. However, high investment and effect from nearby magnetic material are strong disadvantages in many agricultural applications. One successful agriculture-related application of NMR moisture content measurement techniques was quantifying the change of moisture distribution in a rice grain during boiling (Takeuchi et al., 1997).

Optical Sensing

Computer vision is another non-contact technology that has proven effective for agricultural applications. Two general approaches have typically been used: 1) detection of geometric differences, such as leaf shape and 2) detection of the differences in spectral reflectance (Thompson et al.,1990). Spectral analysis is used to divide the crop and soil since the differences between vegetation and soil reflectance in the near-infrared region has proven successful for segmenting plants from a soil background. However, the use of ambient illumination may impact measurement accuracy. For example, measurements using image processing on sunny days may produce errors due to shadows and highlights. Both hardware-based and software-based methods have been introduced to minimize

these effects. For example, a light diffuser (cast acrylic cover) that avoided direct sun light was used to reduce the impact of ambient illumination variability (Perez et al., 2000). Also, algorithms and programs used in image processing stage have been developed to minimize the illumination effect (Zhao et al., 2003).

Laser based object detection had been successfully used for many applications. Laser technology is used to produce a high intensity and highly directional light source. Objects are detected when they block the laser light path between the source and the detection (Figure 5). However, dusty environments require frequent cleaning to maintain proper function. Also, laser detection can not discriminate between different types of objects since any opaque object can block the light path and trigger detection. The combination of high maintenance, high cost, and a lack of discrimination between corn stalks, weeds, or leaves makes laser detection unsuitable for counting corn stalks.

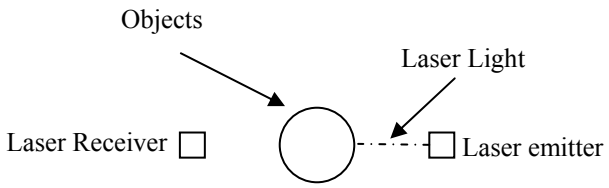

Figure 5. Laser proximity sensor illustration

Density Techniques

Density measurement techniques have been used for many years in intrusive and non-intrusive applications. Generally, the intrusive methods are only suitable for offline evaluation of density, whereas non-contact methods are suitable for both online and offline measurements.

Non-intrusive online density measurements have been widely used in industry and health care areas. The most popular non-intrusive methods are X-ray and ultrasound. X-ray measurements use a high energy density electromagnetic wave that can penetrate through solid materials. The percentage of X-ray particles which can penetrate a material depends on the density of the material. By evaluating the projected shadow of X-rays, the material density is characterized. Achmad et al (2004) developed an X-ray method of measuring the density at a point inside an object without the cumbersome processes of rotating the object, sources, or detectors, or the use of multiple sources. However, the radiation and high initial cost are the main disadvantages of X-ray techniques for discrete object detection.

Ultrasound is a mechanical wave whose frequency is above the human audible detection range. Both ultrasound reflection and transmission methods can be used to measure material density. When an ultrasound wave (beam) travels through a medium, it suffers a loss in its energy due to various mechanisms, such as beam spreading, scattering and absorption. In addition, when an ultrasound wave strikes an interface boundary between two media of different acoustic properties, part of its energy is transmitted through the boundary and the rest is reflected back. The ratio of the transmitted energy to

the incident energy is known as the transmission coefficient. Similarly, the ratio between the reflected energy to the incident energy is known as the reflection coefficient. Based on these properties, ultrasound can be used to detect change in density. Buehring and Dobbs (2000) developed a sensor that measured the reflections at the fluid–sensor interface, sound speed, and attenuation of ultrasound to determine the fluid density and solids concentration of cotton. The refraction method involves a combination of rays (due to refraction by the velocity gradient within the sample) can be used to measure the density (Lu et al., 1993). However, for ultrasound density detection, passing the sound wave through multiple layers of different media can significantly complicate density measurement and degrade the accuracy of the measurement.

Analysis of Measurement Technologies

As specified in the previous section, two classes of sensing technique are available, intrusive and non-intrusive. After comparing the advantages and disadvantages between non-intrusive and intrusive sensing methods, the following evidence supports a preference for non-intrusive corn stalk discrimination:

During harvest, a combine typically moves at speeds of 3-5 km/hour (1.8-3 mph) based on combine through put capacity, operating conditions, and operator experience. That means the population sensor needs to detect 6-10 stalks per second. The average corn stalk diameter is 2 cm by casual surveys, therefore it takes approximately 20 ms to pass the sensor. The dynamic response time of mechanical parts in the intrusive design may limit the operating speed. Thus, a non-intrusive approach can potentially increase

the dynamic response time. Furthermore, the rapid response of non-intrusive technique can be used to overcome the mechanical design limitation of separating two closely-spaced corn stalks.

The fast dynamic response of a non-intrusive approach can collect much more information that can be used to discriminate corn stalks from background noise. Using post processing procedures, weeds can potentially be recognized because of its higher frequency content

The non-intrusive approach has lower maintenance due to the lack of contact between sensors and stalks. The sensor should need less maintenance and repair and should have a longer life span.

Once the options have been limited to non-intrusive methods, the key features used to discriminate corn stalk from surrounding environment need to be specified. Two factors, moisture content and density could be potentially used as the discriminant features. As previously mentioned, air-dried corn stalks still contain moisture at a level of at least 8% (Podesimo et al, 2004). Stalks can be detected if water in corn stalks can be detected above the background environmental moisture. Therefore, moisture-based sensing techniques are feasible for corn plant population sensing at harvest. Furthermore, by investigating the relationship between stalk number and ear number, expertise proves 97% of corn stalks have only one ear. A corn ear generally has higher moisture content than a corn stalk at harvest, which is more readily detected by a moisture content sensor. Even if whole plant is completely dry, the ear still can show the property of high density which is another difference between the plant and the environment. Therefore, if a corn

ear can be detected; the existence of a corn stalk can be inferred. However, the position and variability of the position of corn ears could make ear detection quite difficult since it would be difficult to position a sensor such that ears could be reliably detected.

Therefore, only moisture and density related methods were further researched. Selection of particular methods was based on knowledge of their functional theory. The feasibility of the chosen sensing methods was evaluated. Because this sensor was intended for mounting on a combine and operated in a high dust environment, reliability, stability, sensitivity, size, speed, and cost were the key features used as evaluation criteria. Based on preliminary research, capacitance and radio frequency techniques were further investigated.

Capacitive Proximity Sensing

One of the most popular non-intrusive sensing techniques for moisture content is based on capacitive change. Capacitive sensors are non-destructive and have advantages of low cost and low maintenance.

The simplest capacitor form is two parallel plates with a dielectric material separating them (Figure 6).

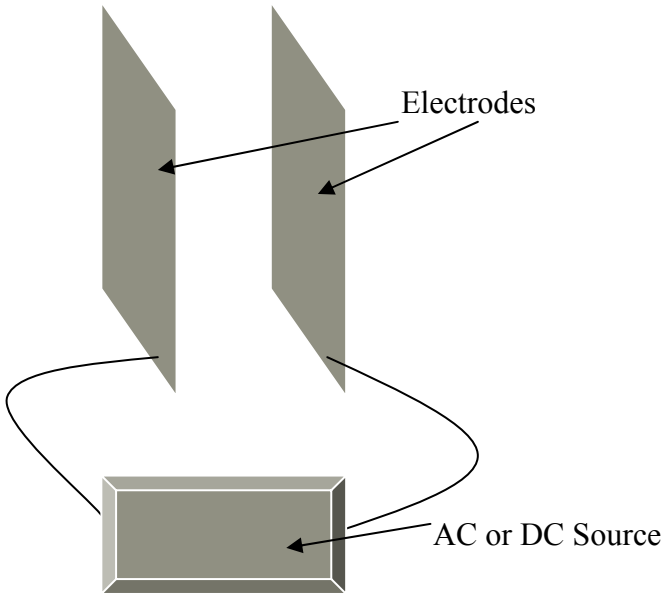

Figure 6. Parallel Two-plate capacitor schematic

A capacitor is an electrical device that stores electrical energy. Its energy storage capability is the ratio of Q/V that is constant as long as the conductors' geometry and the dielectric of the separating material are not variable. The ratio is called capacitance, which is determined by following equation.

$$C = \frac{Q}{V} \tag{2.2}$$

where C is capacitance (Farad), Q is electrical charge (Coulomb), and V is electrical potential (Volt) between two electrodes.

Theoretically, the amount energy can be held by a capacitor follows the equation:

$$W = \frac{CV^2}{2} \tag{2.3}$$

where W is energy (Joule), C is capacitance, and V is the electrical potential.

Assuming that the charge density on the two parallel conductor surfaces is uniformly distributed, and the dielectric constant between them is known, a geometric-related capacitance equation can be derived:

$$C = \frac{\varepsilon_0 \varepsilon_r A}{d} \tag{2.4}$$

where C is capacitance, ε_0 is electric permittivity of vacuum (8.854×10^{-12} F/m), ε_r is relative dielectric constant, A is the area (m^2) of one plate, and d is the distance (m) between two plates. When the geometric properties are not varied, the relative dielectric constant is the only variable that could change the capacitance.

Proximity sensing is a common application for capacitance-based sensors. Proximity sensors are used to detect the presence or motion of a nearby target without direct contact with the target. Proximity sensors also use other methods (e.g., inductance, optical, magnetic, ultrasound), however the capacitive method is the most commonly used technique for non-metallic objects. But there are some limits for the capacitive proximity sensor. First, dipole electrode pairs are preferred. A single electrode sensor has a simpler structure and a longer sensing distance because the other sensor electrode is a distant ground or a distant target. Therefore, the signal produced by the single electrode sensor can be easily disturbed by ground noise. However, when a dipole structure is selected, the sensing distance becomes the principal limitation.

Figure 7 illustrates how the change in capacitance between two electrodes and an object related to each other. The proximity sensing circuit (Figure 7) can be simplified to

an equivalent circuit (Figure 8). In this circuit, the targeted capacitances are C_2 and C_3. The targeted capacitance is impacted by C_1 and C_4. When the distance between the target and sensor increases C_2 and C_3 decreases and C_1 remains constant. The effect of C_4 will further decrease the signal strength. There are three possible situations for the proximity sensor:

- If the target is a floating metal, C2 and C3 will decrease 10% for every sense-plate-diameter (sensor largest size) increment movement.
- If the target is a grounded conductor, C4 is shorted. When the object moves to the sensor, C1 decreases due to the shielding effect. Under this situation, the capacitance combination of C1, C2, and C3 can be used as signal.
- If the object is a dielectric and the object has a higher dielectric constant than air, when the object moves to the sensor, C1 increases due to the dielectric constant change (Baxter, 1996).

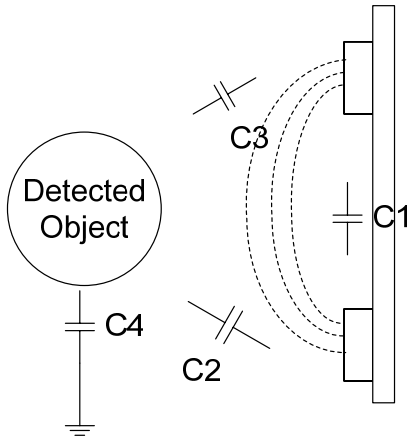

Figure 7. Capacitive proximity sensor schematic

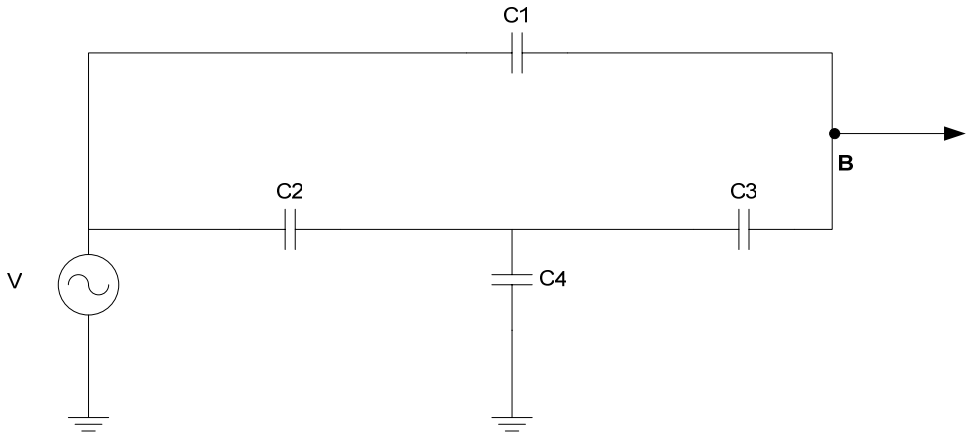

Figure 8. Capacitive proximity sensor equivalent circuit

Because the dipole design limits the sensing distance of the proximity sensor, several geometric sensor patterns have been developed to improve the sensing distance. Two of them are cylindrical pattern and interdigital pattern. The term interdigital refers to a digit-like or fingerlike periodic pattern of parallel in-plane electrodes used to build up the capacitance associated with the electric fields that penetrate into the material sample or sensitive coating (Mamishev et al., 2004). In the sensor industry, both the cylinder and interdigital patterns have been widely manufactured.

In a capacitive proximity sensor, fringe capacitance (Figure 9) plays the most important role on the sensing distance. The fringe capacitance results from the fact that the electric field lines extend past the edges of a conductor. The principal concept behind both the cylinder pattern and the interdigital pattern is to maximize the fringe capacitance. The interdigital pattern has a much more complex pattern than the cylinder pattern, but the interdigital pattern demonstrates much stronger fringe capacitance strength.

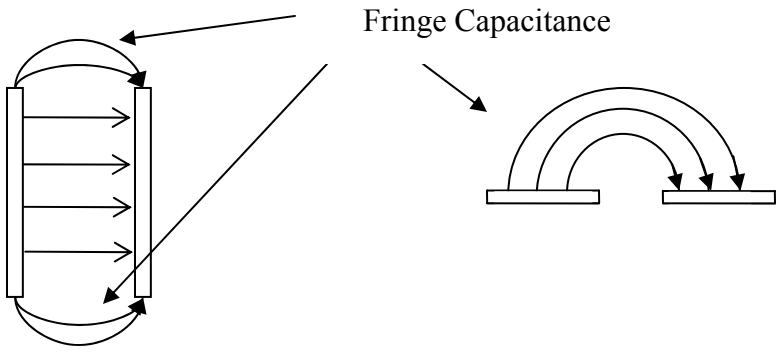

Figure 9. Fringe capacitance schematic

Due to its excellent performance, interdigital electrodes sensor have become one of the most popular capacitive sensors in recent years. This type of sensor is widely used in nondestructive testing (NDT), microelectromechanical systems (MEMS), telecommunications, chemical sensing, and biotechnology (Mamishev et al., 2004). The interdigital sensor has several desirable features: single-sided access, control of signal strength, imaging capability, and multiple physical effects in the same structure. Particularly, the single-sided sensing capability can simplify sensor fabrication, mounting, and cost, since access to both sides of the object under test and careful alignment of separated plates are not required.

Signal strength can be controlled by adjusting the finger pattern. Theoretically the penetration depth of the fringe quasi-static electric fields above the interdigital electrodes is proportional to the spacing between the centerlines of the sensing and the driven fingers and is independent of frequency. When the spacing between the driven fingers increases, the fringe capacitance decreases. Sensitivity, sensing distance, and fringe capacitance can be adjusted by changing the finger gaps. However, there are no published

theoretical equations that can be used to compute the exact signal strength based on the finger gap. Most available equations are empirical which show an approximate result. One accurate method for determining optimum finger gaps is to physically fabricate a series of sensors with different patterns and select a finger gap experimentally. This method is expensive, time consuming, and tedious.

Fortunately, there are several alternative methods available for interdigital capacitance calculation (Baxter, 1996). The first method uses Teledeltos paper. The Teledoltos paper is a black electrically paper with a thin carbon coating. The coating is evenly spread for a constant resistance. The paper can be used to model capacitors in two-dimensional field. The capacitor electrodes can be simulated by painting a pattern with silver paint. An ohmmeter is used to determine the capacitance. For example, if the paper resistance is 10 KΩ/square, and the resistance between two silver paints is 5 KΩ. This result means that two square are in parallel.

The second is a numeric method that calculates capacitance by sketching field lines. Equipotential surfaces cross the force lines at right angles and tend to parallel conductive surfaces. The electric force lines terminate at right angles to conductors. Therefore, the whole electric field is separated by electric force lines and equipotential lines into multiple areas. The capacitance of each simplified small area can be calculated. The total capacitance can be obtained by summing up the capacitance of individual areas. However, this method is a cut-and-paste approximation. The calculated result only shows a rough estimation of capacitance.

Another numeric method for capacitance calculation with a high accuracy is the finite element method (FEM). Reference data shows that FEM error compared to an analytic solution could be less than 0.18% (Baxter, 1996). This method was selected for sensor development in this research.

Chapter Summary

Both intrusive mechanical and non-intrusive capacitive techniques have been used to develop the stalk population sensors in previous research. The mechanical method has the disadvantages of requiring high maintenance and significant underestimations of stalk counts. Previous research on non-intrusive sensors focused on moisture content detection, but the sensitivity and sensing distance were limited, resulting in low stalk count accuracy. Near infrared, NMR, and microwave methods are precise methods of moisture content detection, but are prohibitively expensive and physically too large for mobile applications. Therefore, the capacitive sensing technique was chosen.

CHAPTER 3 – SENSOR DESIGN AND EVALUATION

OVERVIEW

This research consisted of five major components: detection element development, design and evaluation of the supporting circuitry, field testing of the completed sensor system, post-acquisition data processing and feature extraction, and stalk pattern classification (Figure 10).

Chapter 4 details the detection element development. A number of different detection element patterns were modeled and tested to optimize sensitivity. The patterns examined included single-sided two-plate, interdigital, polarized interdigital, semi-interdigital, and solid ground electrode. The key parameters affecting pattern sensitivity were investigated. The most promising pattern, the solid ground electrode, was selected for further evaluation and development.

Chapter 5 addresses the design and evaluation of the supporting circuitry. This circuitry included a Wien-Bridge oscillator (which incorporates the detection element pattern), a phase-locked loop used as a high-speed frequency-to-voltage converter, and an operational amplifier to provide impedance matching and maximize data acquisition resolution. Although it is not a part of the supporting circuitry, the data acquisition system that was used during field testing was also evaluated to identify and mitigate problems before going to the field. The operational configuration, optimum operating

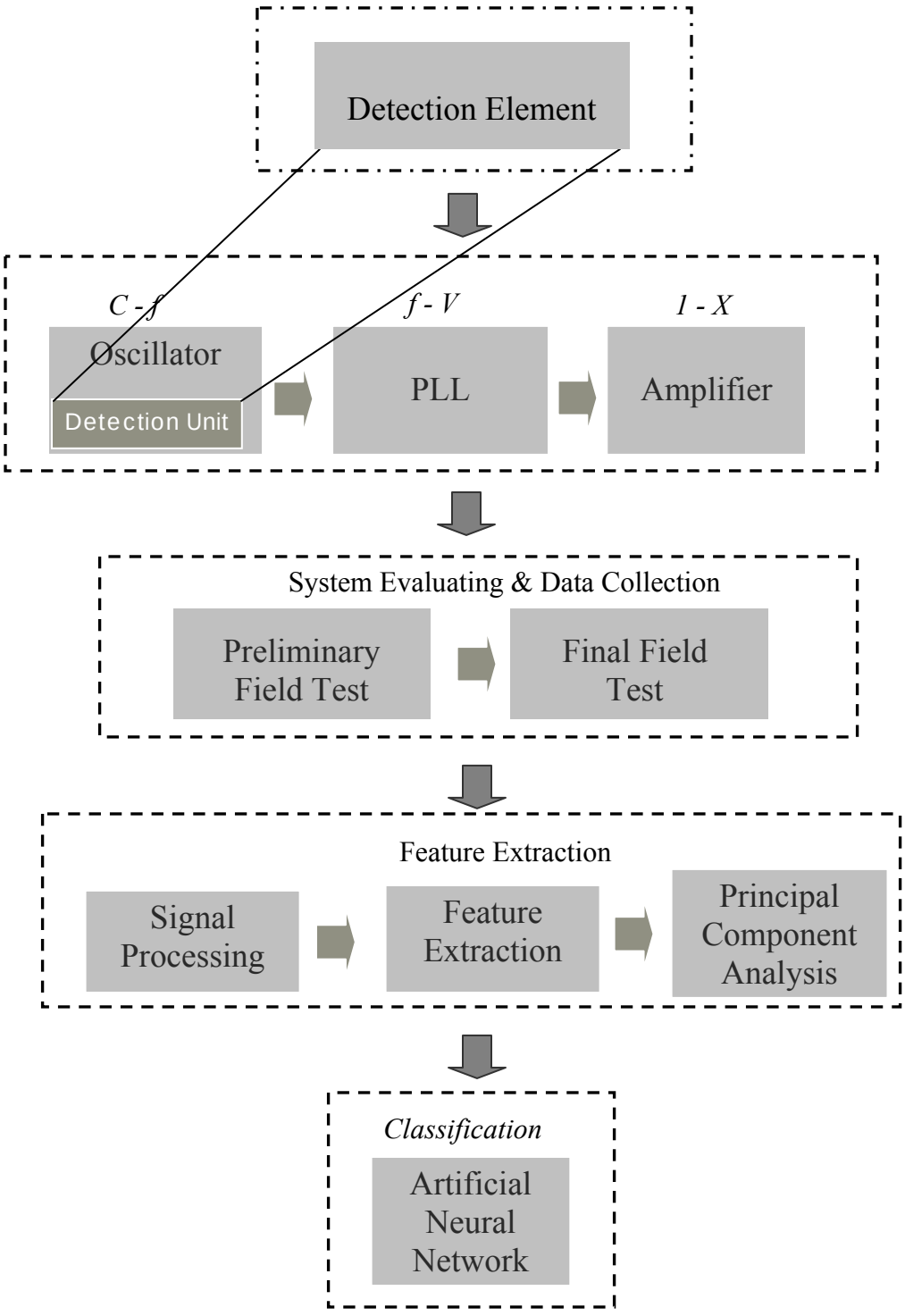

Figure 10. Research procedure flowchart

parameters, and the associated component sizes were determined using both modeling and laboratory testing.

Chapters 6 and 7 present two field test events. Once the electronic components of the sensor system were designed and fabricated, a protective housing and mounting system were designed and fabricated. The preliminary field test was used to evaluate the sensor system (including the housing and mount) and data acquisition system to identify problems before conducting the final field test. Data collected in the preliminary field test was used to develop an understanding of how the system functioned in the field. A problem was identified in the sensor design and modifications were made in the laboratory to correct this problem. Based on the results of the preliminary field test, experimental parameters and levels were identified and incorporated into the experimental design for the final field test. The experimental parameters included stalk moisture content and harvest speed. Several noise influences were also investigated (environmental and mechanical noise and the noise-like influence of corn leaves and weeds). The final field test accurately simulated realistic harvesting conditions. Real-time data was collected for use in post-acquisition processing and stalk pattern classification.

Chapter 8 discusses post-acquisition processing, feature extraction, and principal component analysis of the extracted features. Post-acquisition processing was used to minimize the impact of noise and prepare the raw data for feature extraction. Feature extraction reorganized and reduced the data set to a form conducive to later stalk pattern classification. A total of eight features were extracted. Principal component analysis was

performed to identify the most important features with respect to identifying stalk events. As a result of this analysis, five of the features were eliminated reducing the feature space dimension from eight to three. The reduction in the size and complexity of the data set was necessary to enable eventual online processing of the data by a commercialized version of the sensor system.

The final stage of this research, stalk pattern classification, is presented in Chapter 9. Artificial Neural Network techniques were used to illustrate the development of a classification algorithm. The extracted feature data set was divided into a training set and a test set. The training set was used along with a backpropagation training technique to produce matrix sets which represent the neural network model. The test set was used to evaluate the accuracy of the model developed from the training set. Numerous neural network structures were evaluated, and the optimal structure was selected based on maximum prediction accuracy and minimum structure complexity. The optimal structure was then evaluated to determine the prediction accuracy at various resolution levels from a 9 m row segment to a square kilometer field and from 5 to 50 consecutive events.

CHAPTER 4 – STALK DETECTION ELEMENT DESIGN AND EVALUATION

The general design criteria for the corn stalk sensor included:

- Detect at least 98% of the corn stalks samples at a 2.0 cm distance from the sensor.
- The difference between hand-counted and sensor-counted populations in the field environment should be less than 5% for a row length of 9 m.
- The sensor system should be small enough for easy mounting on a combine header.
- Circuit complexity should be minimized to reduce prediction cost.
- Precision alignment of sensor components should not be necessary.
- The final design should be sufficient for technology transfer to industry.

Preliminary Static Test for Changes in Dielectric Constant

A preliminary test was necessary to assure that a capacitive proximity sensor could detect trace capacitance changes between the dielectric constant of a corn stalk and ambient air. Furthermore, this test also was used to better understand the general relationships among the most critical factors (sensor-to-stalk distance, dielectric constant, and capacitance change).

A static test station was built for this evaluation. The static station consisted of an adjustable plate type capacitance test fixture and a frame to support specimens (Figure 11). This fixture was fabricated using polyethylene with a low dielectric constant (ε=2). The initial detection element was a simple two-plate capacitor. The plate electrodes were mounted on the test fixture. The distance between the plate electrodes was adjustable from 8.5 cm to 21 cm. The electrodes were connected via Kelvin clip leads to a programmable LCR meter (7600 precision LCR Meter Model B, QuadTech, MA) that measured the electrical parameters for computing change. The complex dielectric was calculated in accordance with ASTM D 150-98 (ASTM 2003).

Corn stalks with moisture contents ranging from approximately 8% to 80% moisture content were tested to investigate the relationship between moisture content and capacitance of the sensor. The moisture content of each stalk was determined after testing by weighing the stalk, drying the stalk in an oven for 72 hours at 103°C, and re-weighing the dried stalk. Moisture content was calculated on a wet basis:

$$MC_{w.b.} = \frac{W_{wet} - W_{dry}}{W_{wet}} \times 100\% \tag{4.1}$$

where W_{wet} is the wet stalk weight and W_{dry} is the oven-dry stalk weight. The stalks were tested at a stalk-electrode distance of 4.5 cm.

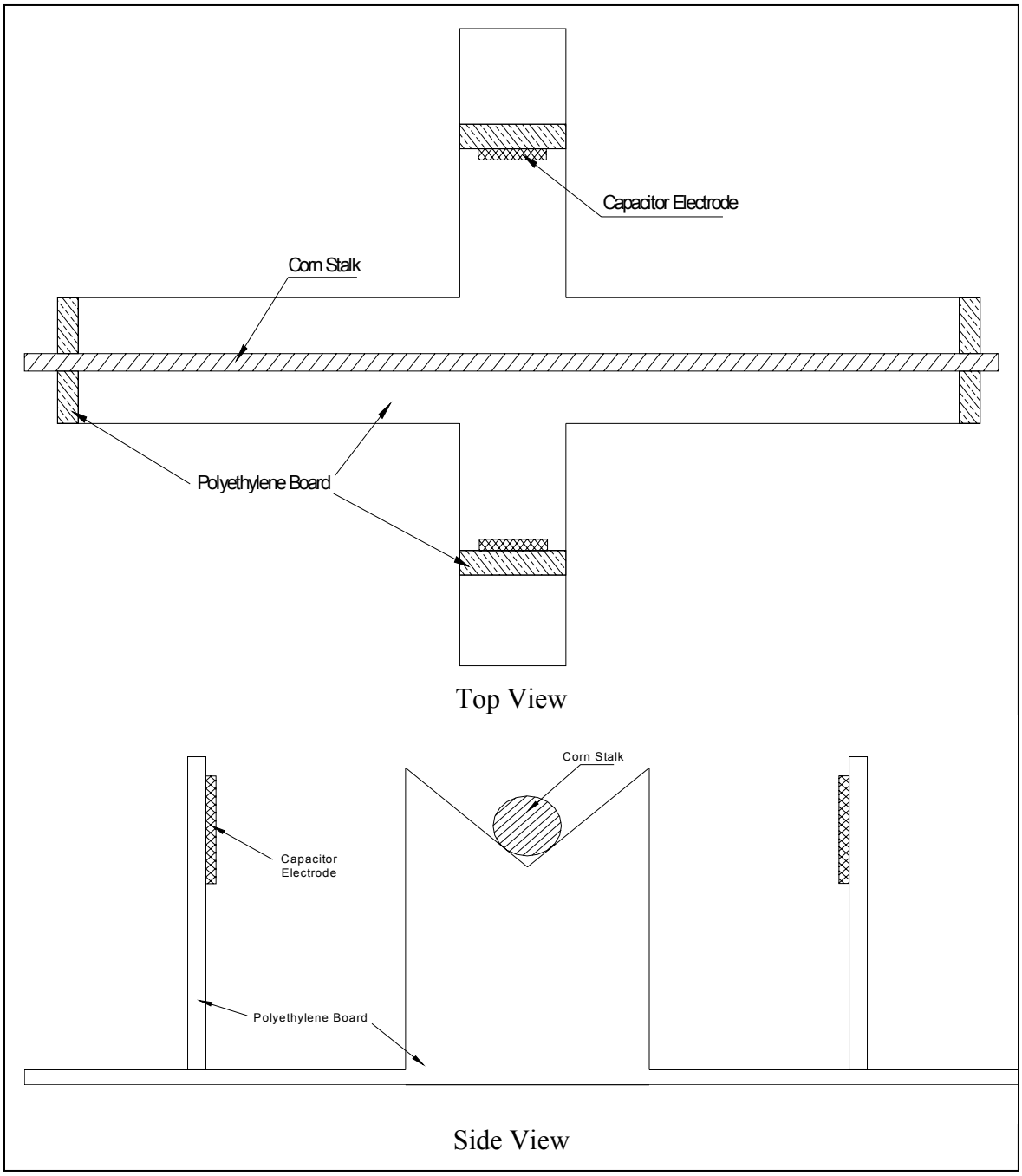

Figure 11. Static test fixture schematic

Two rubber rods (2.54 cm) with different dielectric constants (2.9 and 8.0 at 300 KHz at 25 C) were used in place of corn stalks to better isolate the effect of stalk-sensor distance by maintaining a constant specimen dielectric constant. The rubber rods were tested at 300 KHz (more details on this frequency selection later) and inter-electrode distances of 8.5, 13, 17, and 21 cm were tested.

For both corn stalks and rubber rods, baseline capacitance was measured with no specimen in the test fixture. The specimen was then placed in the test fixture and the capacitance measurement was repeated. The capacitance change was calculated by subtracting the measured baseline value from the measured capacitance with a specimen in place.

The results from the static tests are shown in Figure 12, Figure 13, and Figure 14. It was found that the capacitive detection element can detect a stalk with moisture content of 45% over the frequency range from 200 Hz to 2M Hz (Figure 12). The average capacitance is 550 *pF*, ranged from 505 to 585 *pF*, and the capacitance variation is approximately 8%. These results showed that the capacitance change was reasonably constant across the entire frequency band. This data indicated that within the test range frequency has relatively little effect on the capacitance change caused by a corn stalk. A target frequency of 300 kHz was chosen for further testing due to the operating parameters of the oscillator selected in the supporting circuit design. A detailed discussion of the supporting circuit design is presented in Chapter 5.

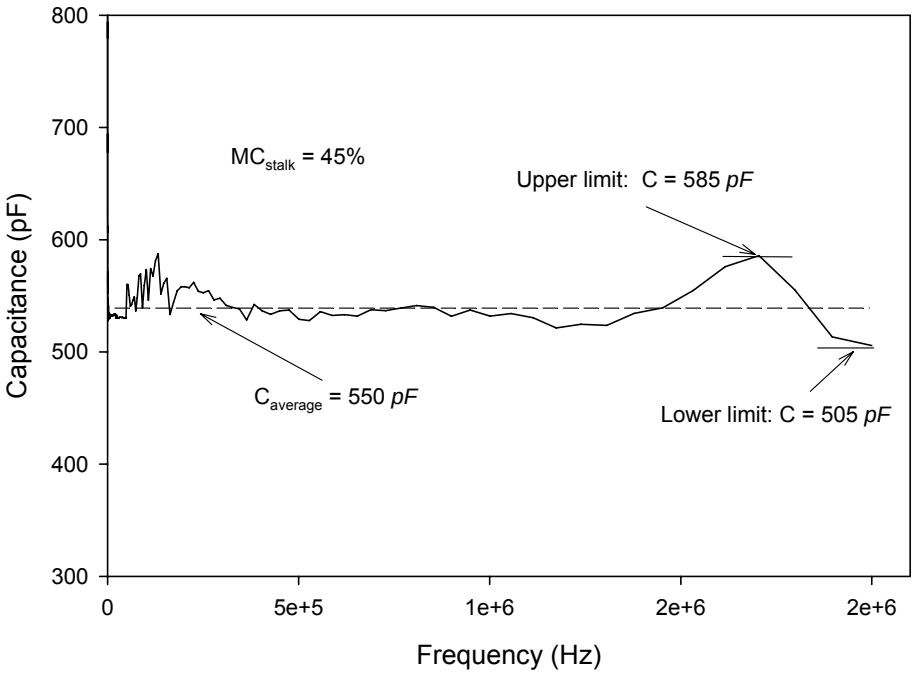

Figure 12. High moisture content corn stalk capacitance at different frequencies

Corn stalks with different moisture contents were used to determine detection element response to moisture content (Figure 13). Moisture content of the corn stalks range from 8% to 80% and capacitance changes were measured at 300 KHz. Results showed that the capacitance change to moisture content relationship was non-linear, but was reasonable well fit by an exponential curve (Figure 13). The capacitance change varied most rapidly at low stalk moisture contents. This showed that a small amount of water can change stalk dielectric constant significantly when stalks were relatively dry. When the moisture content was larger than 60%, the capacitance change was maintained close to a constant value. This indicates that once a threshold moisture content was reached, further increase in the moisture content would not result in a proportional increase in detection element output.

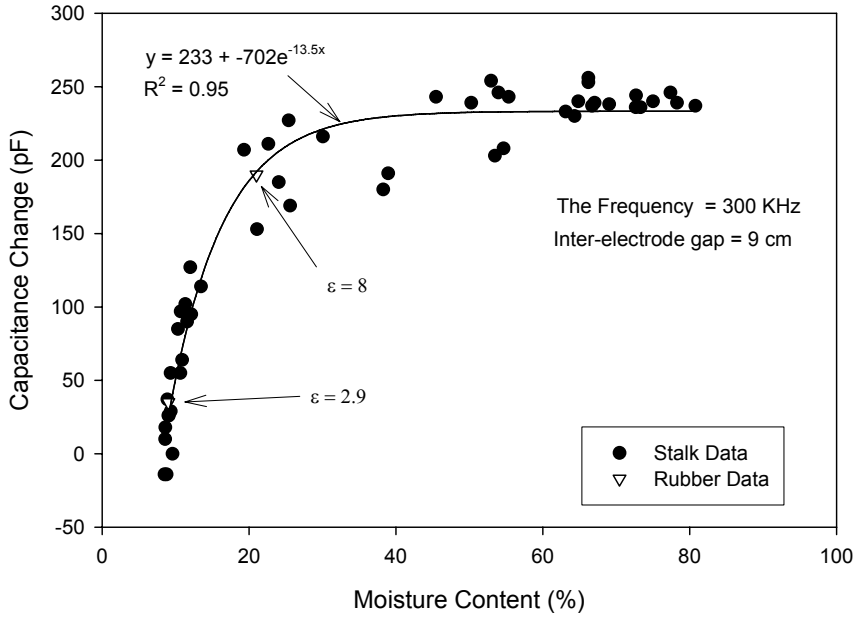

Figure 13. Capacitance change at different stalk moisture contents

Two rubber rods with different dielectric constant were used to simulate corn stalks at two moisture contents. The dielectric constant of the rubber rods provide a consistent and stable test standard that is not impacted by ambient conditions. The rods were tested using the same procedure as the corn stalks. The results of these tests allowed the approximation of equivalent stalk moisture content of the rubber rods. The capacitance change due to the presence of rubber rods at 300 KHz was 35 *pF* and 190 *pF* for dielectrics of 2.9 and 8, respectively. Therefore, the equivalent stalk moisture contents of the rubber rods were 9% and 21% for dielectric constants of 2.9 and 8.0, respectively. The rubber rods were used to represent corn stalks in further laboratory test.

The rubber rods were used to evaluate the effect of sensor-to-specimen distance (Figure 14). When the sensor-to-specimen distance was increased from 8 to 21 cm, the percentage capacitance change in the detection element decreased from 6 to 1% and 3.5

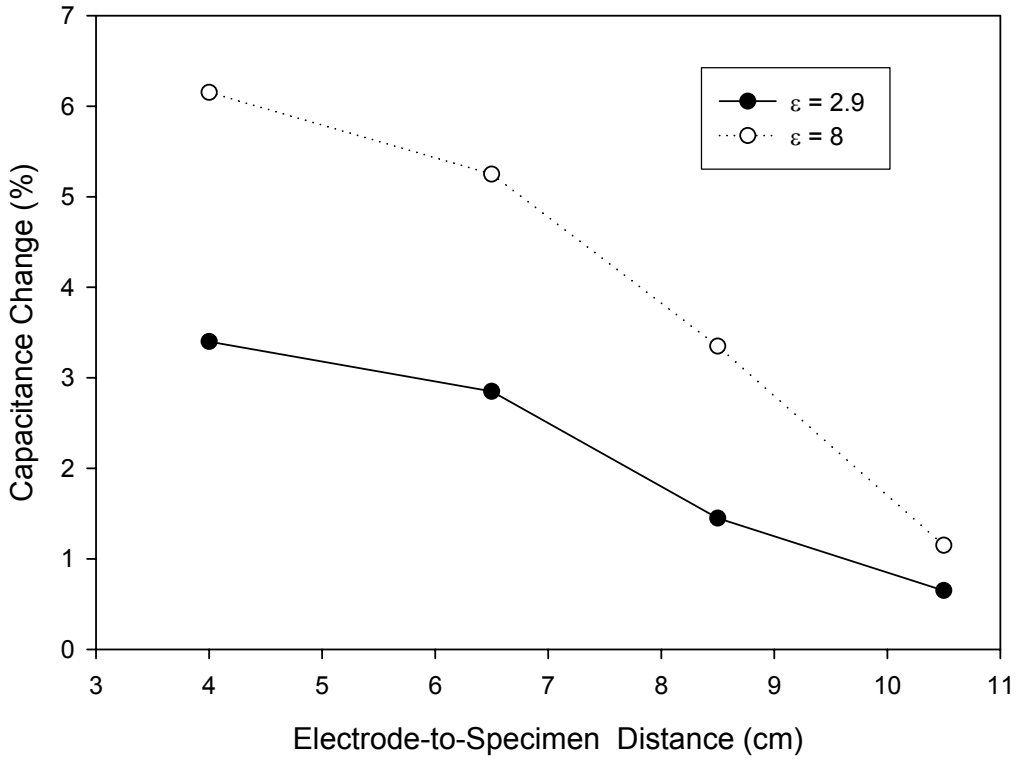

Figure 14. Capacitance change with respect to electrode-to-specimen distance for rubber rods

to 0.5% for rubber rods with dielectric constants of 8 and 2.9, respectively. This shows that the sensor-to-specimen distance is a critical parameter for capacitive sensor design in addition to stalk moisture content.

Electrode Geometry Optimization through FEM

FEM analysis was used to develop and evaluate capacitive detection element patterns after the preliminary test proved the validity of the capacitive sensor concept. There were two design requirements for the model development. One was to expel the sensor's capacitance as far as possible from the sensor surface in order to increase the

maximum effective sensing distance. The other was to maximize the capacitance change resulting from the presence of a corn stalk and therefore maximize sensitivity.

FEM Analysis Background

FEM is a numerical procedure that is widely used to solve engineering problems where mathematical models of physical phenomena are known. Mathematical and physical concepts are generalized to governing equations (generally partial differential equations). These governing equations represent balances of mass, force, or energy. The basic mathematical concept consists of approximating real scalar fields (e.g., temperature fields) by subdividing the domain of definition (e.g., the volume of the body) into geometrical elements (e.g., parallelepipeds). Simple arithmetic functions (interpolating functions) are defined over the geometrical elements. A finite element is a geometrical element and associated interpolating functions.

Maxwell's equations, a set of equations written in differential or integral form, are the basic governing equations for analyzing electromagnetism. These equations describe the relationships among the fundamental electromagnetic quantities. For general time-varying fields, Maxwell's equations can be written as:

$$\begin{aligned} \nabla \times H &= J + \frac{\delta D}{\delta t} \\ \nabla \times E &= -\frac{\delta B}{\delta t} \\ \nabla \cdot D &= \rho \\ \nabla \cdot B &= 0 \end{aligned} \tag{4.2}$$

where H is the magnetic field intensity, J is the current density, D is the electric displacement or electric flux density, E is electric field intensity, B is the magnetic flux density, and ρ is the electric charge density.

A set of constitutive relations can be used to state the macroscopic properties of a closed system:

$$\begin{aligned} D &= \varepsilon_0 E + P \\ B &= \mu_0 (H + M) \\ J &= \sigma E \end{aligned} \tag{4.3}$$

where ε_0 is the permittivity of vacuum, P is the electric polarization vector, μ_0 is the permeability of vacuum, M is the magnetization vector, and σ the conductivity. The electric polarization vector describes how the material is polarized when an electric field E is present. Similarly, the magnetization vector describes how the material is magnetized when a magnetic field H is present.

In the SI system, the permeability of vacuum is $4\pi \cdot \times 10^{-7}$ H/m. The velocity of an electromagnetic wave in vacuum is given as c_0 and the permittivity of vacuum is derived by the relationship:

$$\varepsilon_0 = \frac{1}{c_0^2 \mu_0} = 8.854 \times 10^{-12} \tag{4.4}$$

P is generally a function of E. P can be used to interpret the electric dipole moments. Some materials can have a nonzero P even when there is no electric field present. For linear materials, the polarization is directly proportional to the electric field:

$$P = \varepsilon_0 \chi_e E \tag{4.5}$$

where χ_e is the electric susceptibility. By combining equation 3.7 and 3.9, we can derive the following equation:

$$D = \varepsilon_0(1+\chi_e)E = \varepsilon_0\varepsilon_r E \tag{4.6}$$

where ε_r is the relative permittivity.

In FEM, a static electric model is realized by using the electric potential V. The classical Poisson's equation can be derived by combining the definition of the electric potential with Gauss' law and the continuity equation:

$$-\nabla\cdot(\varepsilon_0\nabla V - P) = \rho \tag{4.7}$$

This equation is used for the electrostatics application mode.

In FEM, boundary conditions are also critical. The governing equations determine the physical behaviors of materials. The boundary conditions determine the behavior at interfaces. In electrostatics application, boundary conditions of current flow, electric insulation, electric potential, ground, continuity need to be considered (Comsol, 2006).

The electric potential boundary condition:

$$V = V_0 \tag{4.8}$$

specifies the voltage at the boundary. In an electrostatic model, the electrical potential is a dependent variable. But its value needs to be defined at some point or over some area.

The ground boundary condition:

$$V = 0 \tag{4.9}$$

specifies a zero potential at the boundary.

The electric insulation boundary condition:

$$n \cdot J = 0 \tag{4.10}$$

specifies that no current across the boundary.

The current flow boundary condition:

$$n \cdot J = n \cdot J_0 \tag{4.11}$$

specifies the normal component of the current density flowing across the boundary.

The continuity boundary condition:

$$n \cdot (J_1 - J_2) = 0 \tag{4.12}$$

specifies that the normal component of the electric current is continuous across the interior boundary.

The capacitance of a capacitor, C, is calculated from the stored electric energy, W_e, in the capacitor and the applied electrical potential, V_0. The stored electric energy is obtained from domain integration of the field energy density:

$$C = \frac{2W_e}{V_0^2}$$
$$W_e = \frac{1}{2}\int_{\Omega} D \cdot E dV \tag{4.13}$$

Since capacitance and the integration of electric field energy density are linearly related, both parameters may be used interchangeably for comparing detection element pattern output.

A commercial finite elements software package, Femlab (COMSOL, 2005), was used for corn stalk population sensor model development.

Detection Element Development Procedure

Optimization of the detection elements was accomplished by repeating the following sequence of steps:

- Capacitance and electromagnetic field distribution of different detection element patterns were compared by computer simulation.
- The most promising patterns were fabricated and evaluated.
- By investigating and analyzing the fabricated pattern in the laboratory, more promising patterns were further examined and modified.
- The FEM was used again to simulate the modified pattern effects mathematically.
- The best pattern from this stage were fabricated again and evaluated in laboratory. This process was repeated until an acceptable pattern was developed.

Electrode Geometry Optimization through FEM

In the FEM simulation, several assumptions and boundary conditions were considered. The dielectric constant of the ambient environment was assumed to be 1 ($\varepsilon_{dry\ air}$ = 1.0005) for all models. Ambient air in production environments contains water vapor that increases the dielectric constant, but a constant reference level was chosen for comparative purposes. Three-dimensional detection element models were placed into a 20 cm × 20 cm × 10 cm space and two-dimensional models were placed into a 1 m × 1 m space due to computer limitations. This limited space suppressed the electric field which

may affect the simulation accuracy. The space boundaries were set as insulation boundaries, which made the space an isolated system. Detection elements were made of copper and the electrode surfaces were set at either 10 V or ground.

Parallel-Plate Capacitor Modeling

The first step in modeling the detection element was to develop a model of a basic parallel-plate capacitor model. The base capacitance of this configuration is high because of its geometric structure (large area of overlaid electrodes). A 20 mm × 20 mm parallel-plate capacitor model with an electrode gap of 10 mm was developed (Figure 15). Figure 16 is a 2-dimensional representation of the 3-dimensional field produced by the simple parallel-plate capacitor. Figure 16 shows some electric field beyond the parallel-plate capacitor frame, which is a result of fringe capacitance. Based on equation 3.3 which ignores the effect of fringe capacitance, the theoretical capacitance of this model was 0.354 *pF*. The integration of power density of this model by FEM was 3.342×10^{-11} *J*. Based on the equation 4.12, the capacitance by FEM was 0.668 *pF*. The 0.314 *pF* difference between the modeled and theoretical values was due to fringe capacitance.

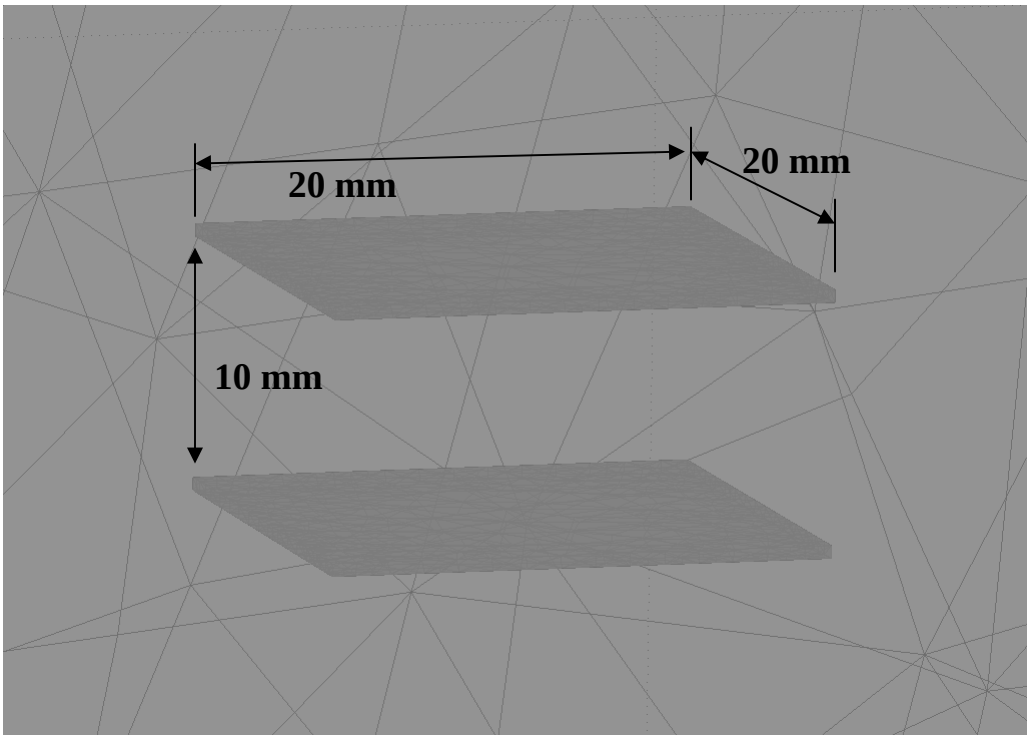

Figure 15. Parallel-plate capacitor 3-dimension electric field schematic

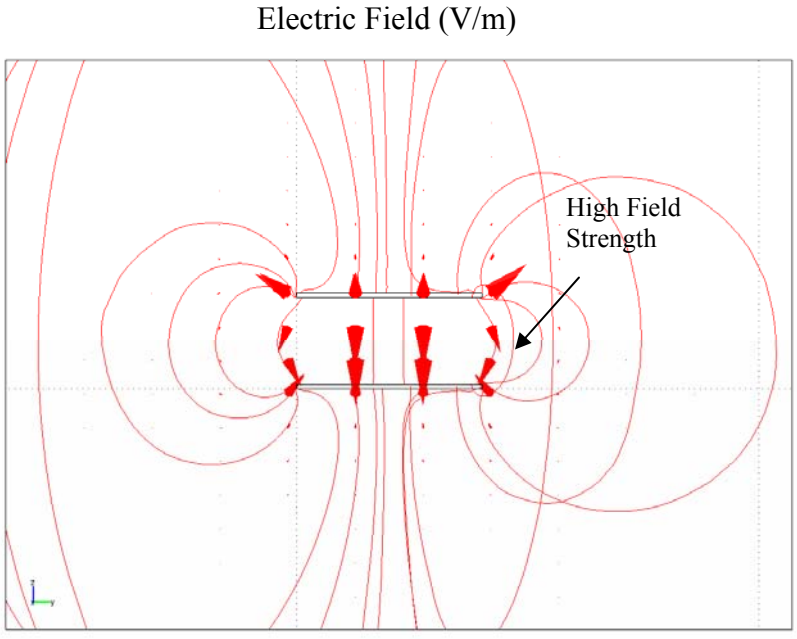

Figure 16. Parallel-plate capacitor 2-dimension electric field schematic

Single-sided Two-plate Pattern Modeling

The two-plate parallel design illustrated the most fundamental concept of a capacitance-based sensor. However, this configuration does not meet the design requirements because it was not single-sided and required careful alignment of the two electrode plates. Therefore, the next step was to convert a simple two-plate parallel capacitor to a single side pattern.

Figure 17 demonstrates a gradual process of converting a parallel-plate detection element to a single-sided detection element. Figure 17 shows how the fringe capacitance changes during the conversion. During this procedure, the normal capacitance between the electrodes is transferred to the fringe capacitance. In the final configuration, the majority of capacitance is fringe capacitance.

Figure 18 shows the energy density for a simple single-sided two-plate proximity sensor configuration. Each electrode had dimensions of 2 cm × 2 cm and the gap between the electrodes was 1 cm. The energy density distribution is shown in Figure 18. The integration of energy density for this design was $1.67 \times 10^{-11} J$ as compared to 3.34 ×

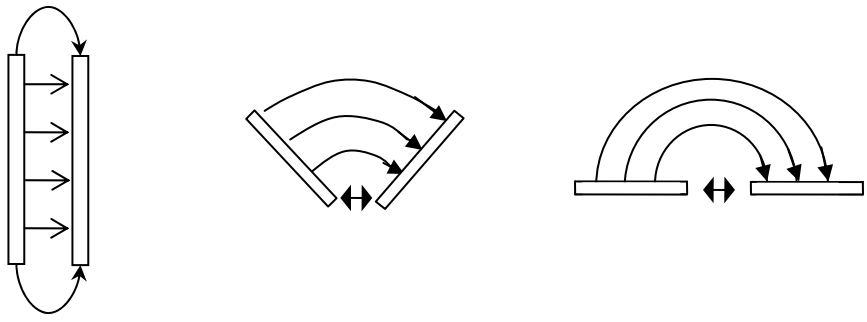

Figure 17. Transition from parallel-plate to fringe field capacitor.

10^{-11} *J* for the parallel two-plate design. The transformation reduced the total capacitance by 50% and the normal capacitance is almost entirely eliminated leaving only fringe capacitance. The energy density distribution was examined to identify possible improvements in fringe capacitance. Most of the capacitive energy was on the edges of the inter-electrode gap, therefore, increasing the length of the inter-electrode gap was a promising way to increase the fringe capacitance.

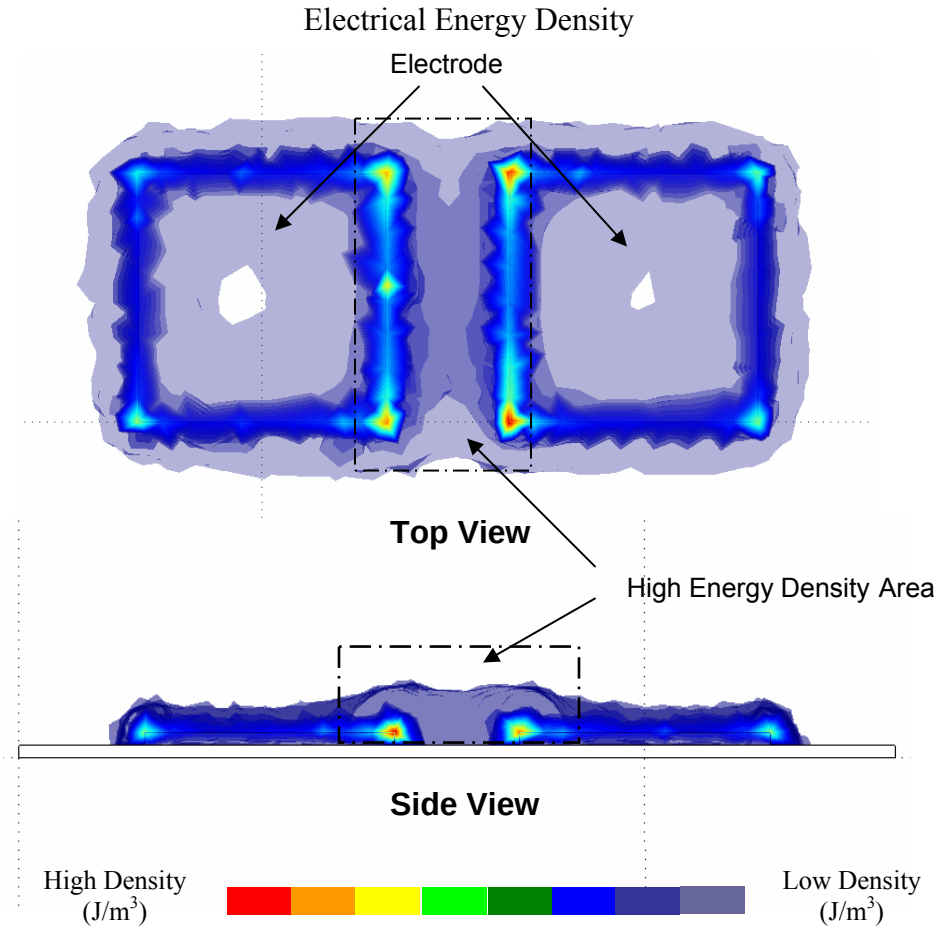

Figure 18. Single-sided two-plate detection element energy density map

One of the most popular commercial capacitive proximity sensor patterns is a cylindrical pattern (Figure 19). The cylindrical pattern can be derived from the single-side two-plate sensor by curving the inner edges. The cylinder pattern has two advantages: relatively stronger fringe capacitance as compared to the single-sided two-plate pattern for a given electrode area (since the ratio of inter-electrode gap length to total electrode area is increased) and ease of manufacturing.

A cylinder pattern model was built using Femlab (Figure 19). The inner electrode has an area of 4 cm^2 and an outer electrode has area of 4 cm^2. The inter-electrode gap was 1 cm. The average inter-electrode gap length (10.23 cm) is approximately five times that of the single-sided two-plate pattern. The integration of energy density was 3.45×10^{-11} *J* which was more than double that of the single side two plate pattern (1.67×10^{-11} *J*). However, the energy density in the central area of this sensor is low (Figure 19). While the cylindrical pattern increased the fringe capacitance significantly, there was still room for further improvement of the fringe capacitance.

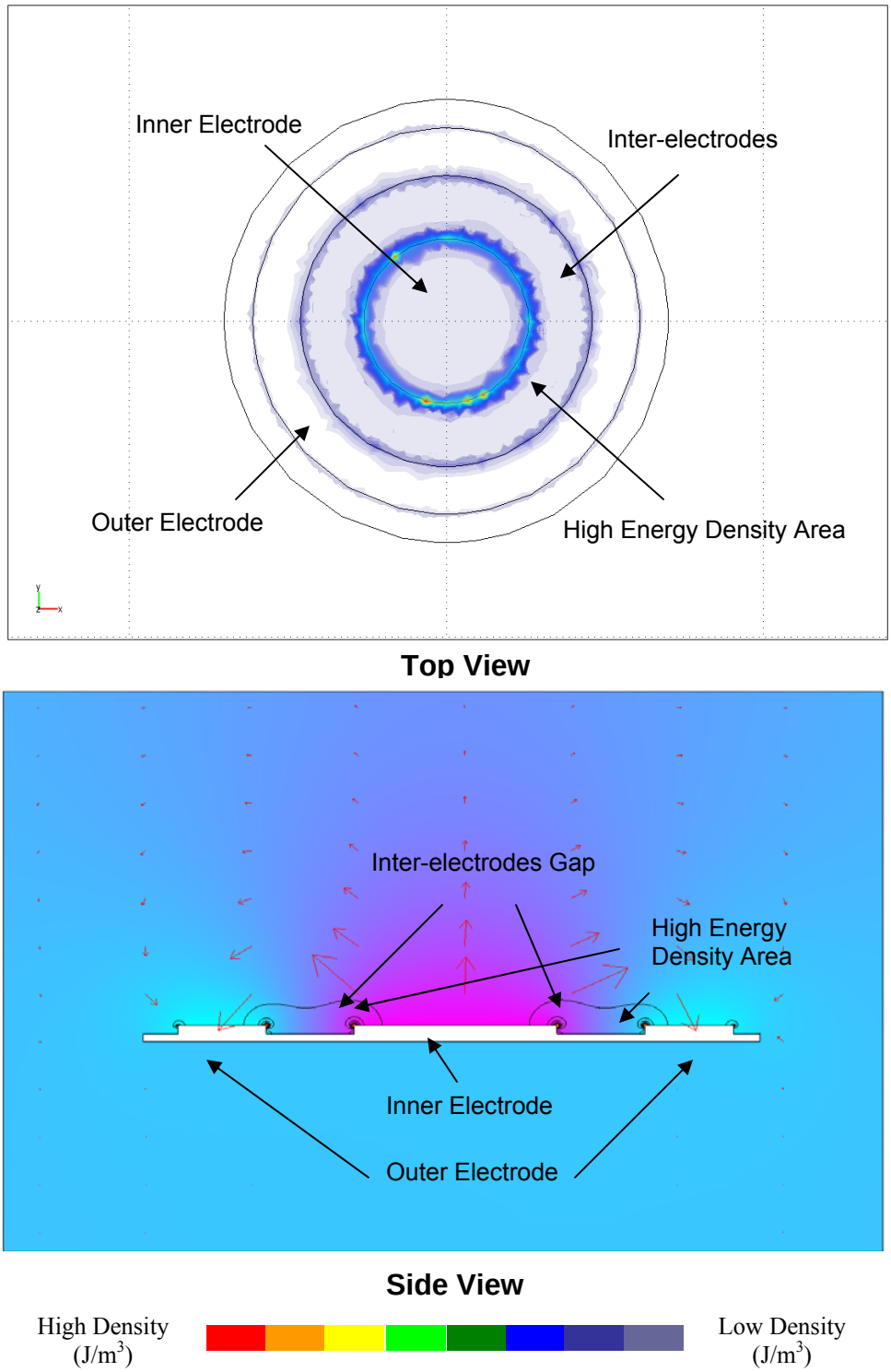

Figure 19. Cylindrical detection element energy density map

Interdigital Pattern Modeling

As previously mentioned, the interdigital pattern is another commercially-used detection element pattern. Two-dimensional models were used for future model development since the complexity of the interdigital pattern produced 3-dimensional models that could not be executed on the available computer resources. an interdigital two-dimension rectangular proximity sensor model (Figure 20) was built by minimizing the areas of low field density in Figure 19. Every positive electrode (except the electrodes at two ends) had two adjacent ground electrodes, and vice versa. The integration of energy density of this pattern was 9.05×10^{-9} *J/m* (energy density per unit length of the 2-dimensional representation). The 2-dimensional model was linearly extended into three dimensions to produce the same electrode area as the 3-dimensional cylindrical pattern. The integration of energy density for the modified interdigital pattern was 1.1×10^{-10} *J*. The interdigital pattern showed significantly improved fringe capacitance (more than 3 times the cylindrical pattern). The integrations of energy density of different patterns are listed in Table 1. The relative capacitive strength of each pattern can be readily compared by setting the smallest value (single-side two plate pattern) to unity.

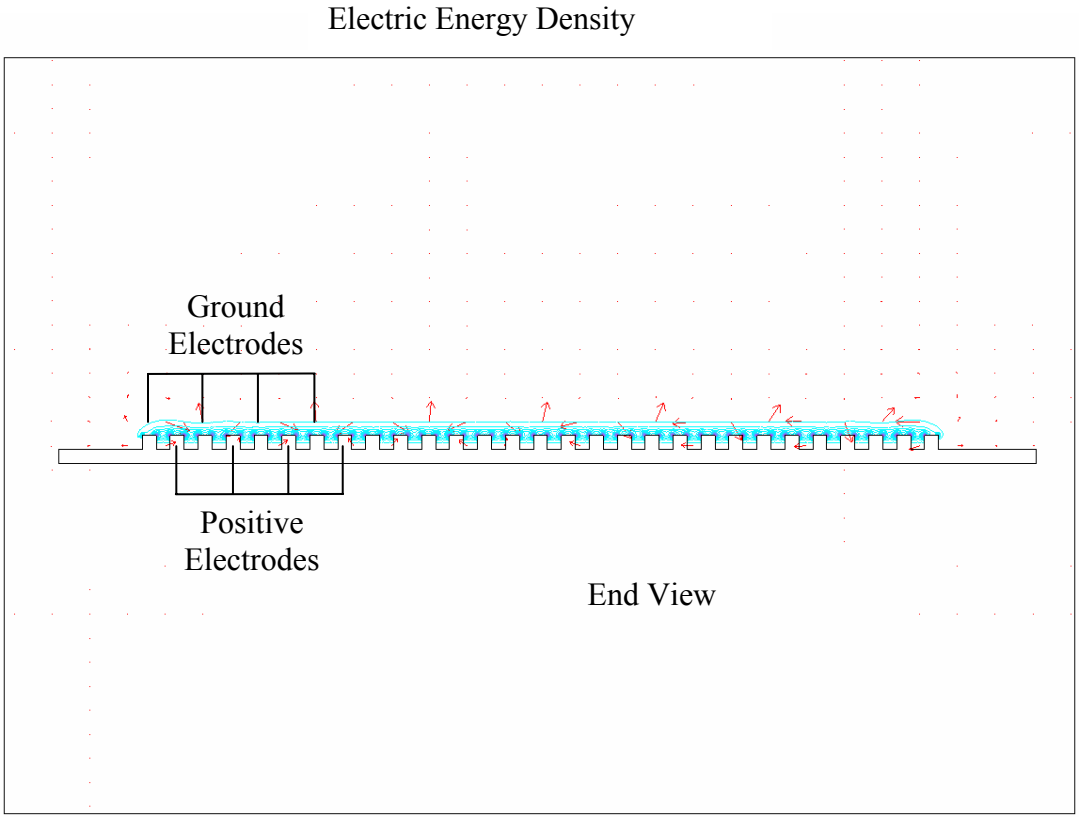

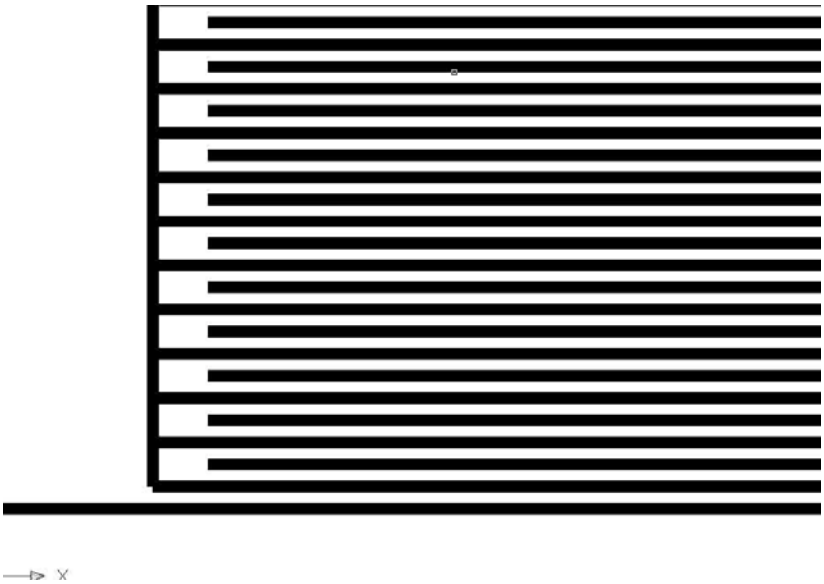

Figure 20. Interdigital sensor profile

Table 1. Integration of modeled energy density for four different patterns

Patterns	Two-plate parallel	Single-side two-plate	Cylinder	Interdigital
3 Dimensions (10^{-11} J)	3.34	1.67	3.45	11 *
Normalization	2	1	2.07	6.59

* Data from modified 2-dimensional model

Interdigital Pattern Evaluation

The interdigital detection element pattern was physically fabricated by a printed circuit board (PCB) plotter (LPKF ProtoMat 92s/II) in the laboratory. The pattern was approximately 5 x 10 cm in size with a 0.2 mm electrode width and a 0.2 mm inter-electrode gap. This prototype was used to evaluate the interdigital pattern and compare modeled and experimental results.

Two methods were used to evaluate the capacitor: a high sensitivity LCR meter (7600 precision LCR Meter Model B, QuadTech, MA) used to measure capacitance changes and a universal counter (Agilent 53131A) used to measure frequency changes in response to capacitance changes in a Wien Bridge oscillator (the selection and design of this oscillator will be addressed in the following chapter.) Only one detection element pattern was used with the LCR meter but two detection element patterns were required in the Wein Bridge. Two detection elements were used with the Wein Bridge for all laboratory test and the preliminary field test. The results obtained using the LCR meter

were also used in the design and evaluation of the oscillator. For the oscillator, the theoretical frequency to capacitance relationship is given by:

$$f = \frac{1}{2\pi RC} \tag{3.18}$$

where f is the oscillation frequency (Hz) and R and C are resistance and sensor capacitance in the oscillation circuit with units of ohms and Farads, respectively.

Theoretically, we expect the results from the two methods to be similar. For example, if the capacitance change is small (less than 10%) it should induce a similar frequency change (inverse direction). The data from both test methods are presented in Table 2. The results from the LCR meter showed that both absolute change (F) and relative change (%) relative to base capacitance were detectable for the interdigital pattern. The relative change is more important because it more closely represents sensitivity (8.6% at 0.5 cm and 0.45% at 2.5 cm).

Table 2. Evaluation data on rubber rod (dielectric constant = 8) by two different methods (method 1: LCR meter method; method 2: oscillator method)

Method	No Sample (air)	Measured data		Absolute change (percentage change)	
		Stalk-sensor distance			
		0.5 cm	2.5 cm	0.5 cm	2.5 cm
LCR meter	110.7 pF	120.2 pF	111.2 pF	9.5 pF (8.6%)	0.5 pF (0.45%)
Oscillator	290 KHz	273 KHz	N/A *	-17 KHz (-5.9%)	N/A *

* SNR was too low to obtain reliable mesurements

Results from the oscillator showed that sensitivity decreased dramatically when the detected object was moved away from the sensor surface. The SNR decreased tremendously when the stalk-sensor distance increased. The frequency change for the interdigital sensor was 17 KHz at 0.5 cm. The frequency change at 2.5 cm was obscured by noise and not measurable.

The detection instruments significantly impacted the experimental results. First, the high sensitivity LCR meter internally averaged repeated measurements (200 per test) which minimized the impact of random influences on the measured value and enabled the device to detect extremely small changes in capacitance. While measurements using the

laboratory LCR are more precise, this method was not feasible for integration into a field application due to cost, size of the instrument, and the number of computations required to obtain the end result.

The results indicated that the fringe capacitance created by the interdigital design was near the sensor surface. Both the absolute and percentage change in the capacitance is relatively large in the space near the detection element. Conversely, the absolute change and relative change decreased when the test object was moved away from the detection element. While the sensitivity of the interdigital pattern is high when the sensor-stalk distance is small, the rapid drop in sensitivity as sensor-stalk distance increases indicated that the field is not expelled far enough from the pattern surface to provide adequate sensing distance.

Polarized Interdigital Pattern Modeling

The basic interdigital pattern was modified in an attempt to enhance the sensitivity. Additional qualitative analysis models considering the effect of the presence of a corn stalk on sensor behavior were used to suggest modifications to the basic interdigital pattern. Specifically, the impact of corn stalks on the electric field produced by the sensor patterns was studied. For each detection element pattern model, a stalk element was located 1.5 cm from the pattern surface, and integration of the field energy density (per unit length of the model) was performed with (ε_{stalk}= 5) and without (ε_{stalk} =ε_{air} = 1) the stalk element present in the model. The difference in integrated field energy density was then converted to a percentage change of capacitance. The integrated field

energy density and percentage change in capacitance due to the presence of a stalk was used as the basis for comparing the different detection pattern models.

Figure 21 illustrates the impact of a corn stalk on the capacitance produced by the basic interdigital pattern. The high intensity electric field exists between adjacent positive and ground electrodes but is not projected away from the pattern surface. A stalk located a relative far distance away from the pattern surface has little impact on the high density field located near the pattern surface. This behavior suggested the first modification of the basic interdigital pattern which involved moving all the positive electrodes to one end of the pattern and all the ground electrodes to the other end of the pattern to produce a polarized interdigital pattern (Figure 22). The results from the basic and polarized interdigital patterns are compared in Table 3. For the basic interdigital pattern there was no significant change in capacitance (0.009%). Such a small change would make accurate stalk detection nearly impossible. While the polarized interdigital pattern produced only 7% of the base capacitance of the basic interdigital pattern, the percentage change in capacitance (0.99%) was more than 100 times that of the basic interdigital pattern. A capacitance change of approximately 1% was far more likely to provide an accurate basis for stalk detection.

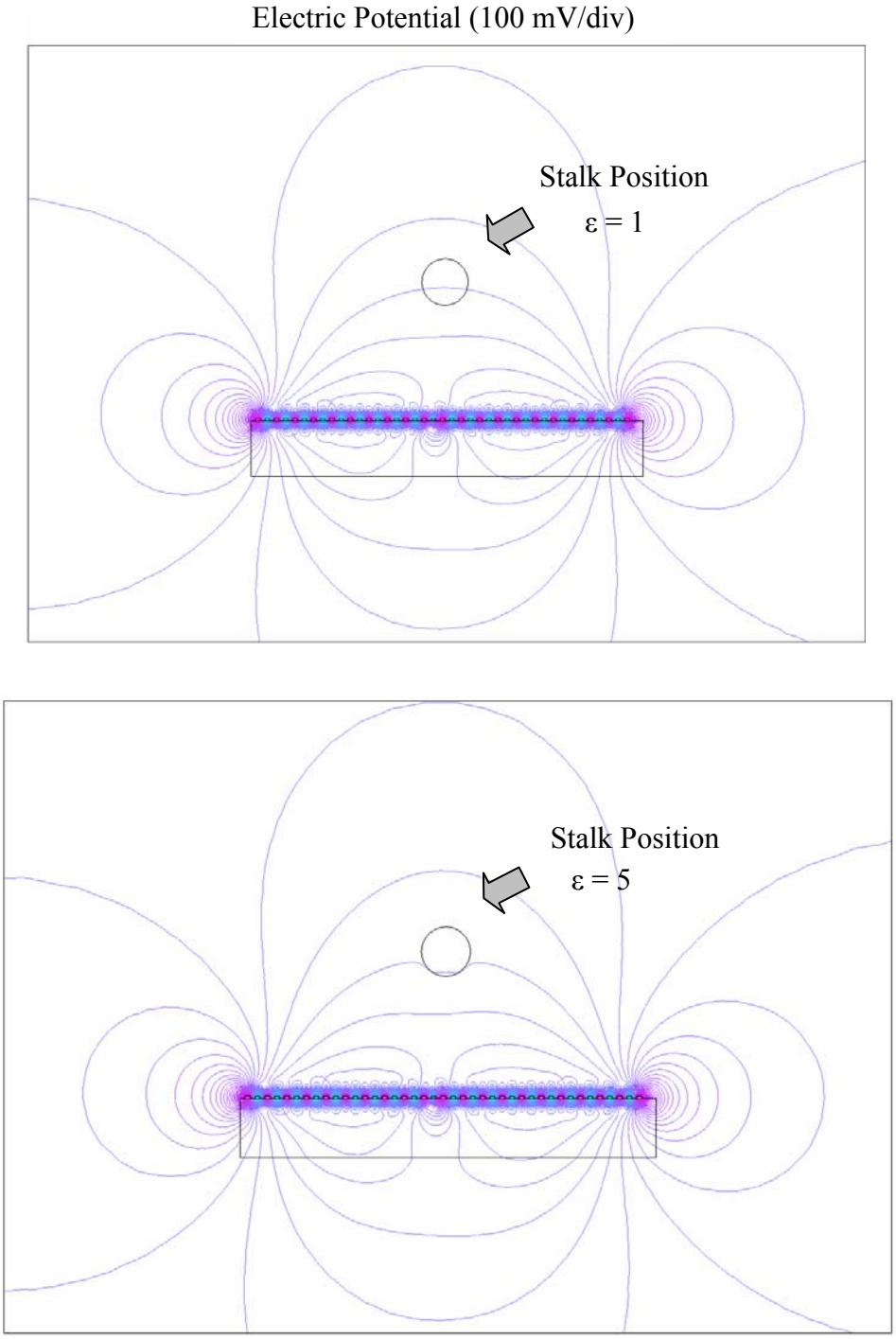

Figure 21. Basic interdigital pattern model electrical potential lines

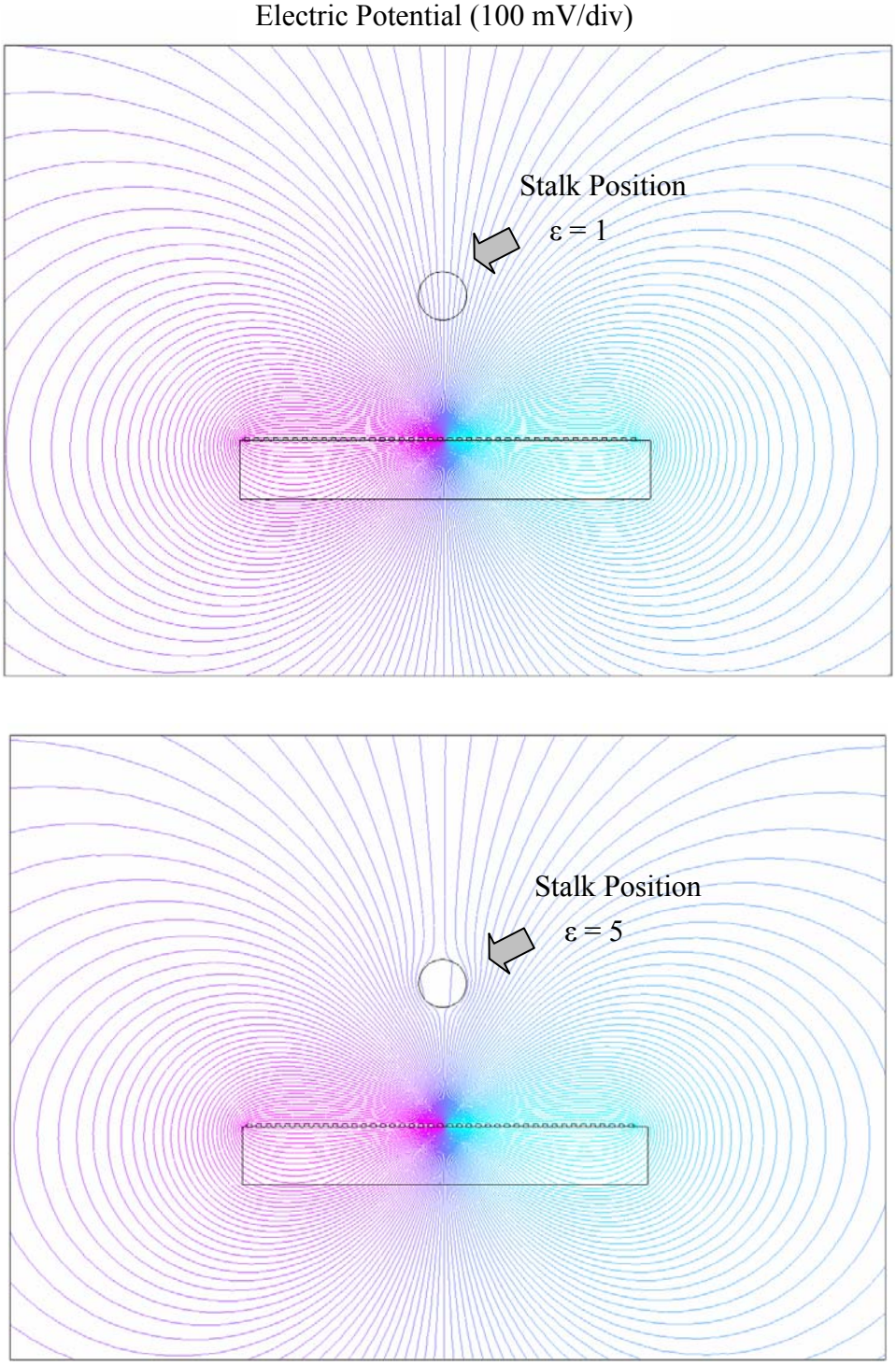

Figure 22. Polarized interdigital model electrical potential lines

Table 3 The change of two interdigital patterns with/without stalk by FEM

	Basic Interdigital Pattern		Polarized Interdigital Pattern	
	With Stalk	Without Stalk	With Stalk	Without Stalk
Integration of Energy Density (J/m)	1.80928×10^{-8}	1.80926×10^{-8}	1.26947×10^{-9}	1.25708×10^{-9}
Capacitance Change	0.00886%		0.99%	

For the polarized interdigital model, different sensor-stalk distances (0.5, 1.0, 1.5, 2.0, and 2.5 cm) were modeled with and without stalk elements present. The difference between integrated electric field energy density with and without the stalk element present and the corresponding capacitance change were calculated and the results are presented in Figure 23. The results showed that when the stalk element was moved away from the pattern surface, the capacitance change decreased. These results correlated well with the preliminary tests of the two-plate parallel capacitor (Figure 14).

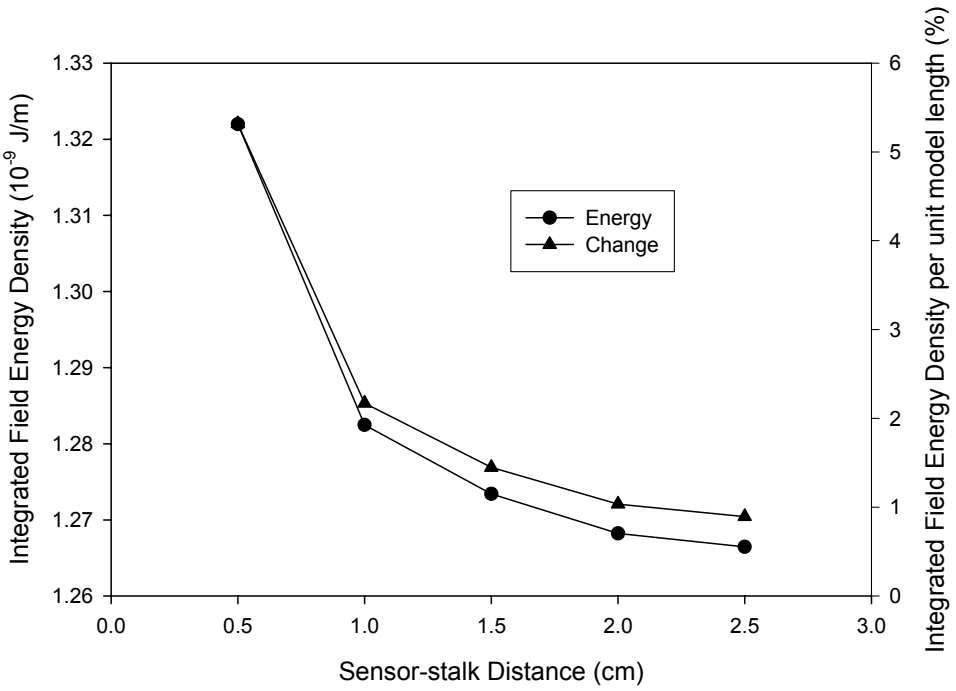

Figure 23. Modeled relationship between integrated field energy density and sensor-stalk distance for polarized interdigital pattern.

Additional prototypes were fabricated and tested in the laboratory by cutting electrode digits from 0.05 mm thick adhesive-basked copper tape and attaching them to 1.25 cm thick ultra-high molecular weight (UHMW) polyethylene blocks (ε=2.3). While this construction technique was not as precise as using the PCB plotter, it allowed rapid prototyping of numerous patterns. These prototypes were evaluated to identify the most promising patterns for later PCB plotter fabrication.

The polarized interdigital pattern was the first pattern fabricated in this manner. Laboratory tests showed that the polarized interdigital pattern did produce a measurable frequency change (~3 kHz change from the 300 kHz base frequency) in the oscillator output with a 2 cm stalk-sensor distance. As previously noted, the basic interdigital pattern did not produce a measurable change under these conditions. However, as the test

specimen was passed across the polarized interdigital pattern, two frequency peaks were observed. One occurred at the midpoint of positive electrodes and the other at the midpoint of ground electrodes. These dual peaks could pose a serious problem for later stalk detection since the detection element responds relatively slowly to the presence of a stalk. Successive higher frequency signals would overlap with each other making discrimination between the two signals very difficult.

Semi-Interdigital Pattern Modeling

A modification was made to the polarized interdigital pattern to eliminate the dual signal peaks. All but one of the positive electrodes were changed to ground electrodes to produce the semi-interdigital pattern. This pattern was simulated using FEM and two prototypes of this pattern were physically fabricated in the laboratory using the copper tape method. The ground electrode width, inter-electrode gap, and sensor-stalk distance were varied. The two prototypes were connected with the oscillator and a universal counter was used to measure the frequency change both with and without a test specimen. The sensor effective area was evenly divided into 4 parts. The boundaries of these four parts (position 1 to position 5) were chosen to test the impact of specimen location (Figure 24). Simulated stalk elements were placed in front of the modeled sensor at these 5 positions and the capacitance change was calculated. Rubber rods were placed in front of the prototype patterns at these five locations and the capacitance change was measured using the LCR meter.

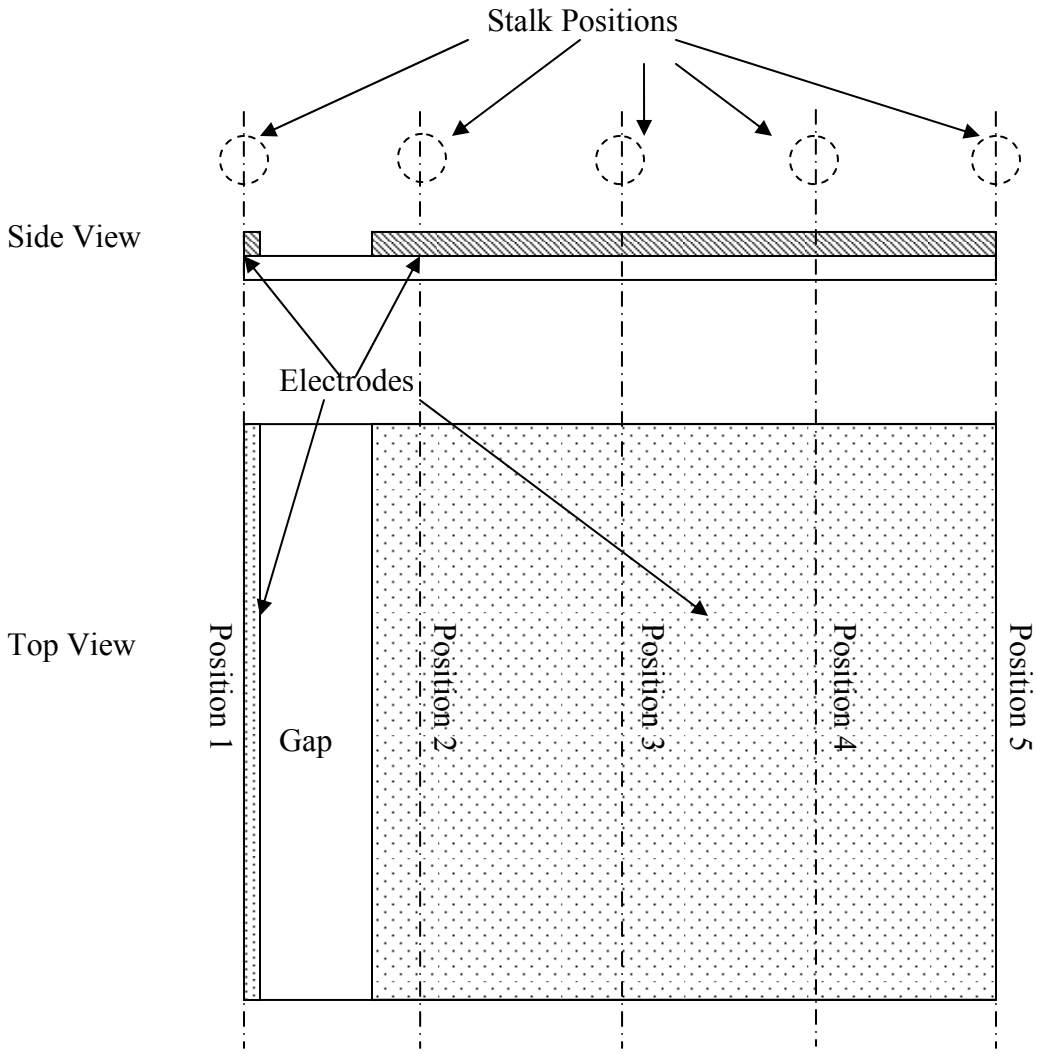

Figure 24. Five specimen positions for the static test

The simulated detection pattern response showed only one peak corresponding to Position 1 (Figure 25). The capacitance change at Position 1 and a 0.5 cm sensor-stalk distance was 4.76%. When the stalk element was moved to Position 5 and a 0.5 cm sensor-stalk distance, the capacitance change dropped to 0.17%. The modeling also showed that the sensor-stalk distance had a significant effect on the capacitance change. The capacitance change at Position 1 decreased from 4.76% to 0.45% when the sensor-

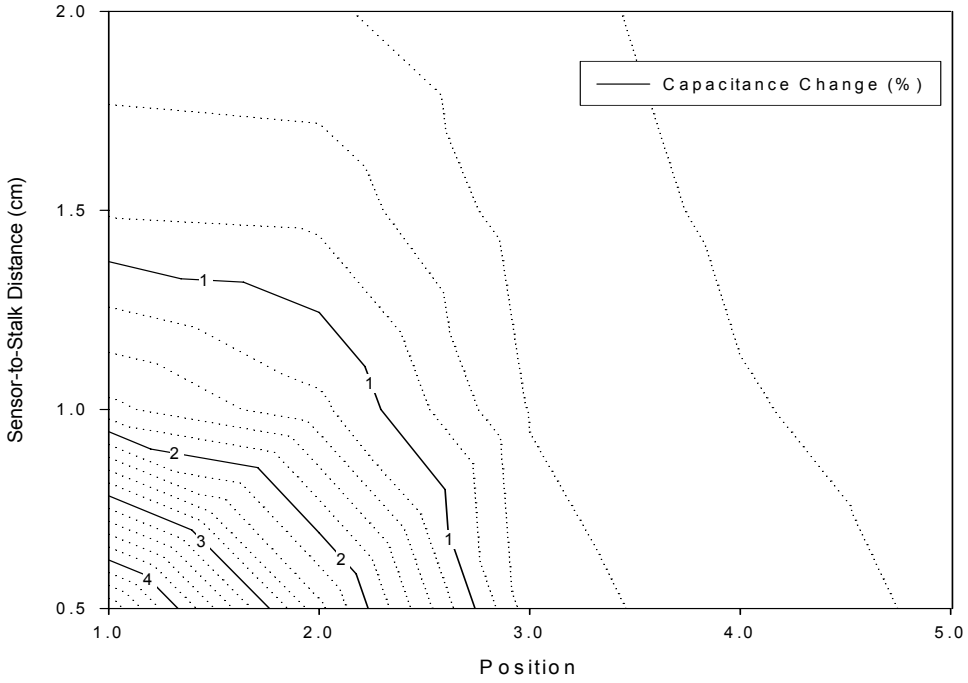

Figure 25. Modeled capacitance change at different positions and sensor-to-stalk distances

stalk distance increased from 0.5 cm to 2.0 cm. Since the strongest signal was obtained at Position 1, future modeling used only Position 1 to compare detection pattern response. Qualitative laboratory tests confirmed that the dual signal peak problem was eliminated by the electrode pattern modification.

Solid Electrode Pattern Modeling

To simplify detection pattern fabrication, a final pattern modification was evaluated. The semi-interdigital pattern was simplified by integrating the ground electrodes into a single, wide electrode producing the solid electrode pattern. FEM simulation of the solid electrode pattern was compared to the semi-interdigital pattern model with a stalk element located at Position 1 and a 1.5 cm senor-stalk distance. The

capacitance change was 1.32% and 1.26% for the semi-interdigital and the solid patterns, respectively. The difference between these two patterns was less than 5%. The electrical fields for these two patterns were also very similar (Figure 26 and Figure 27). Laboratory tests using the oscillator were not able to detect a difference between the semi-interdigital and solid electrode patterns. It is likely that the very small difference in the modeled performance of these two patterns was less than the resolution of the laboratory measurements. Based on these results, the simple solid electrode pattern was selected for further investigation.

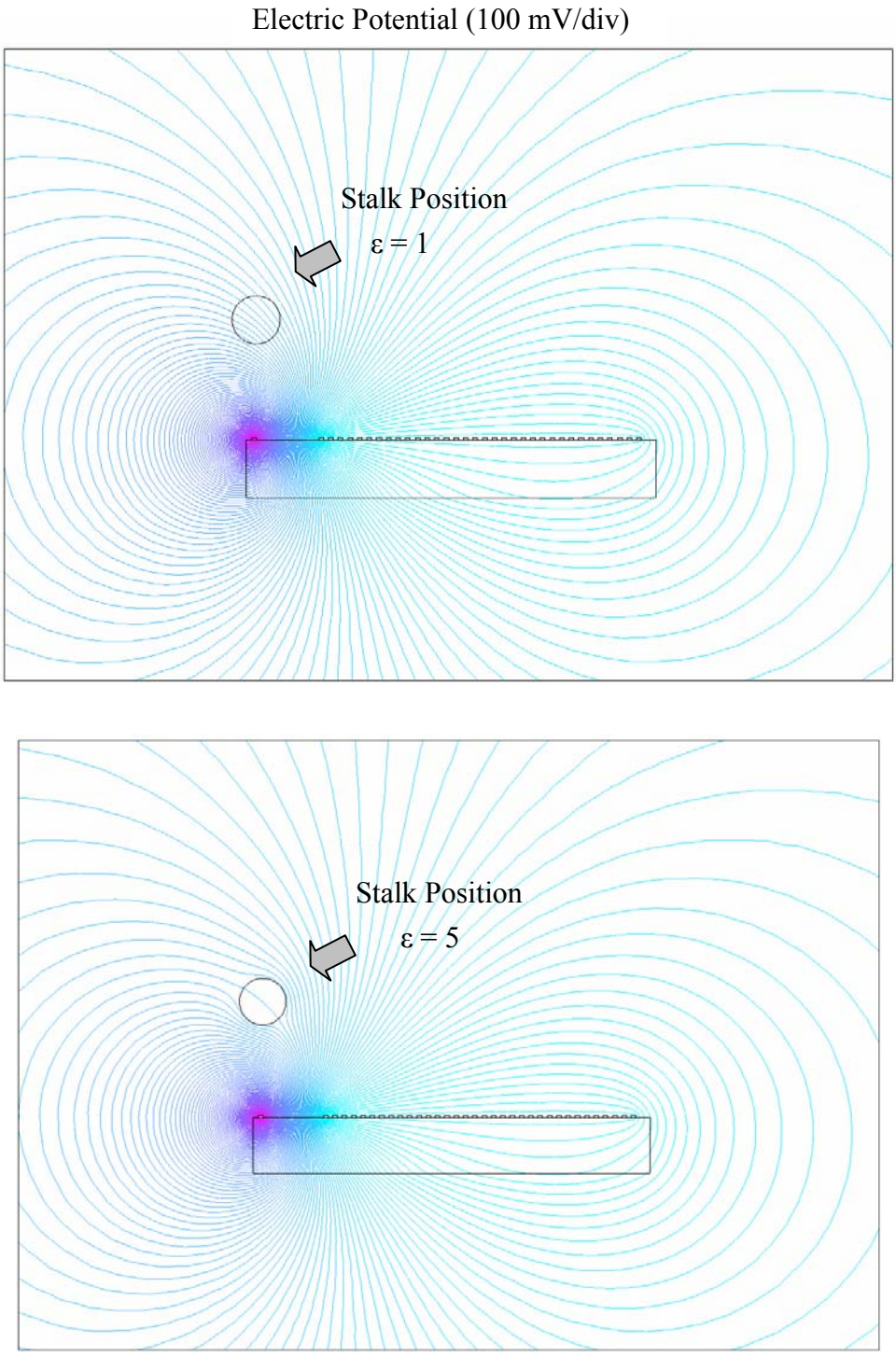

Figure 26. Semi-interdigital sensor pattern electrical potential lines with and without a stalk

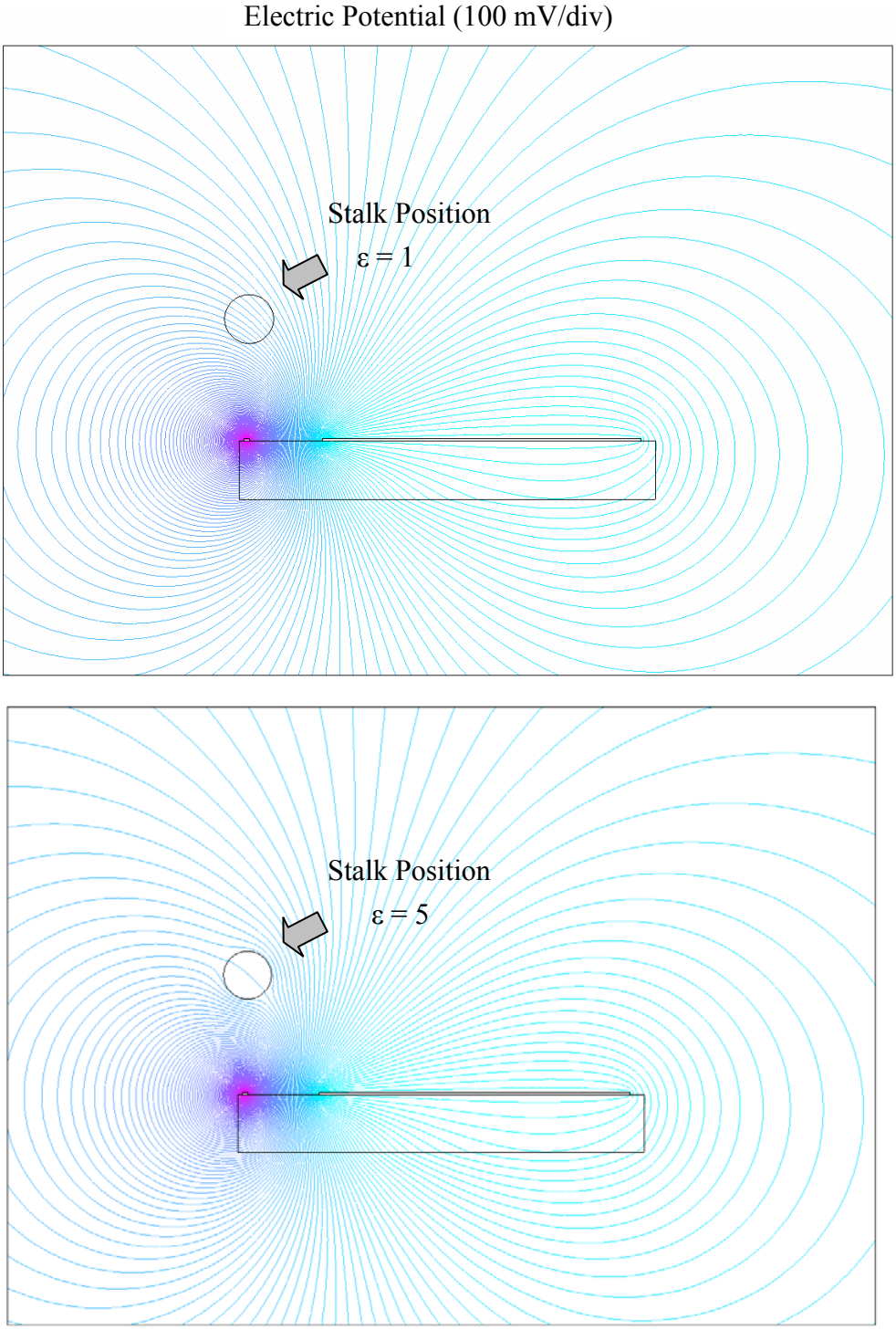

Figure 27. Solid pattern electrical potential lines with and without a stalk

Solid Electrode Pattern Evaluation

The solid electrode pattern performance was evaluated using the following procedure:

1. Several patterns with different parameters were modeled to identify the most critical parameters and properties for the pattern.
2. Modeled patterns were fabricated to investigate the critical parameters and to determine the sensor geometric specifications.
3. The final pattern was fabricated to investigate the effect of corn stalks with different moisture contents.

There are several parameters that could potentially affect the performance of the solid electrode pattern: electrode width, inter-electrode gap, electrode thickness, and electrode length (Figure 28). Based on modeled results, sensitivity was primarily determined by the electrode width and the inter-electrode gap. Increasing electrode length linearly increased the base capacitance of the pattern but does not increase the percentage capacitance change, which was directly related to sensitivity. Varying electrode thickness did not significantly affect sensitivity (less than 1% difference between 0.1and 0.5 mm) and probably would not justify the increased material costs.

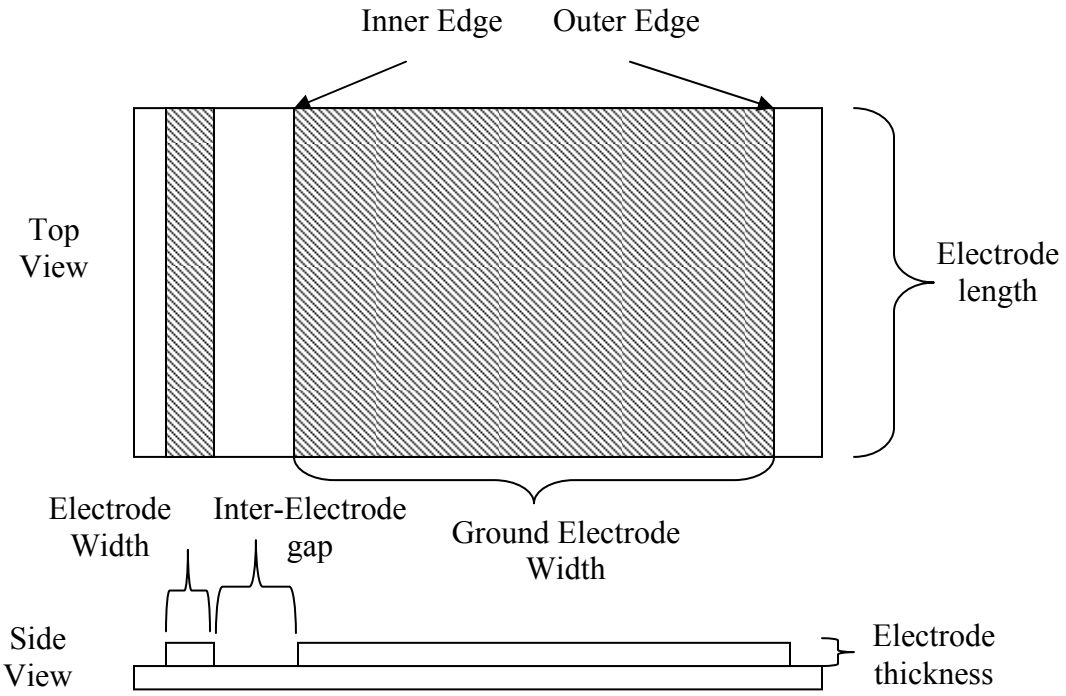

Figure 28. Critical parameter for solid electrode pattern

Modeling was used to evaluate the effect of the ground electrode width and inter-electrode gap. Different ground electrode widths (5, 10, 20, 30, 40, 50, 60, and 85 mm) and inter-electrodes gaps (5, 10, 20, 30, and 40 mm) were modeled and the results are presented in Figure 29. The sensitivity increased as the inter-electrode gap was increased, but the rate of increase drops sharply once the inter-electrode gap reaches 20 mm. Successive 10 mm increases in inter-electrode gap from 10 to 20, 20 to 30, and 30 to 40 mm resulted in sensitivity increases of 73%, 17%, and 5%, respectively. Due to the need to minimize sensor size, the 20 mm inter-electrode gap was preliminarily selected as the best balance of performance and size.

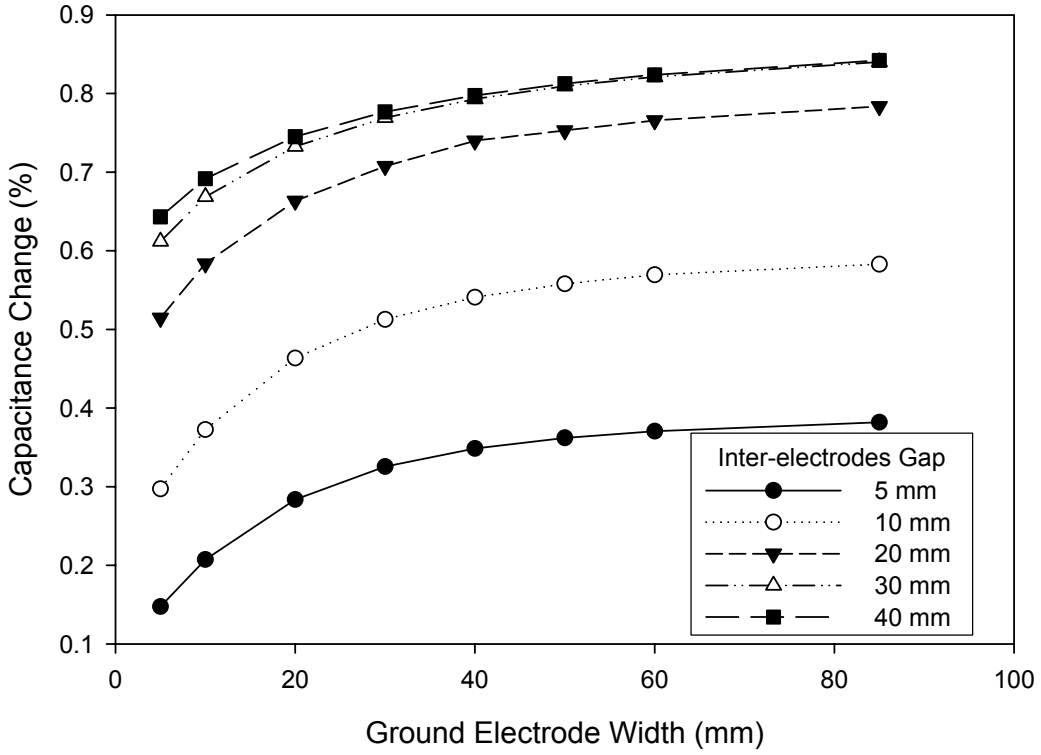

Figure 29 Modeled capacitance change for solid electrode pattern at different ground electrode widths and inter-electrode gaps

Similarly, increasing the ground electrode width improved sensitivity and successive increases in ground electrode width resulted in diminishing increases in sensitivity. Successive 10 mm increases in ground electrode width from 30 to 40, 40 to 50, and 50 to 60 mm resulted in sensitivity increases of 4.6%, 1.8%, and 1.7%, respectively. There is little return for increasing ground electrode width beyond 50 mm. Later experimental testing showed that a wider ground electrode can extend the signal width. This means more data points can be collected from each stalk for a given sampling rate, which could benefit post-processing. However, a wider signal could cause the signals from successive stalks to overlap and make discrimination of individual stalks more difficult. A ground electrode width of 50 mm was preliminarily selected as the best

compromise between sensitivity, physical size, data points per stalk event, and stalk discrimination.

Solid Electrode Pattern Parameter Determination

Detection element patterns were fabricated using the copper tape technique and tested to evaluate pattern performance and compare analytical and experimental results. First, the impact of ground electrode width was evaluated. The positive electrode width and inter-electrode gap were fixed at 2 mm and 20 mm, respectively. Patterns with ground electrode widths of 20, 30, 40, 50, 60, and 70 mm were fabricated and tested. The test results are presented in Figure 30. Second, the impact of inter-electrode gap was evaluated. The positive electrode width and ground electrode width were fixed at 2 mm and 50 mm, respectively. Patterns with inter-electrode gaps of 20, 25, 30, 35, 40, and 50 mm were fabricated and tested. The test results are presented in Figure 31. In these laboratory tests, the corn stalks were located at Position 3, which was different from Position 1 used in the model. The sensor-stalk distance was 2.5 cm. While the results can not be used to directly validate the FEM model, the results are useful in identifying trends and making relative comparisons.

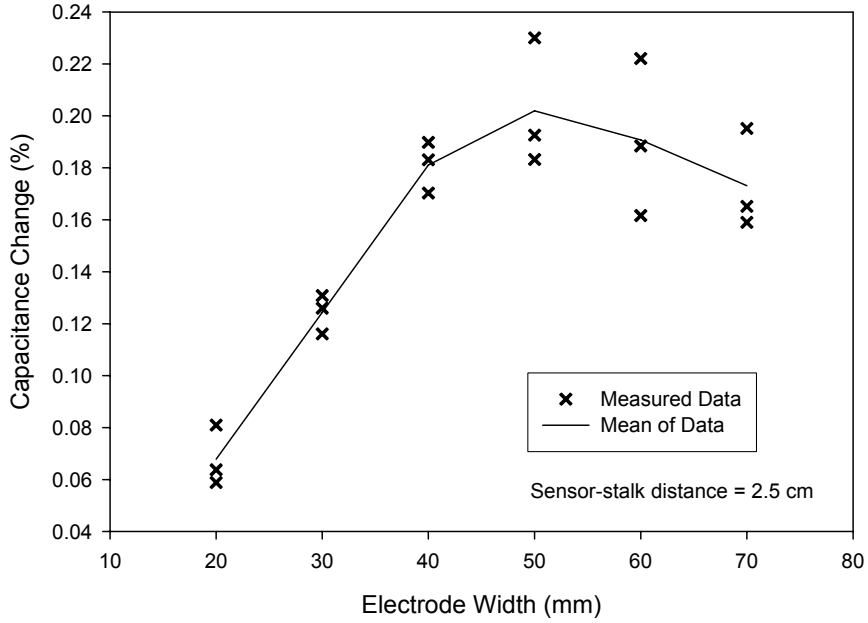

Figure 30. Modeled and measured change for different ground electrode widths

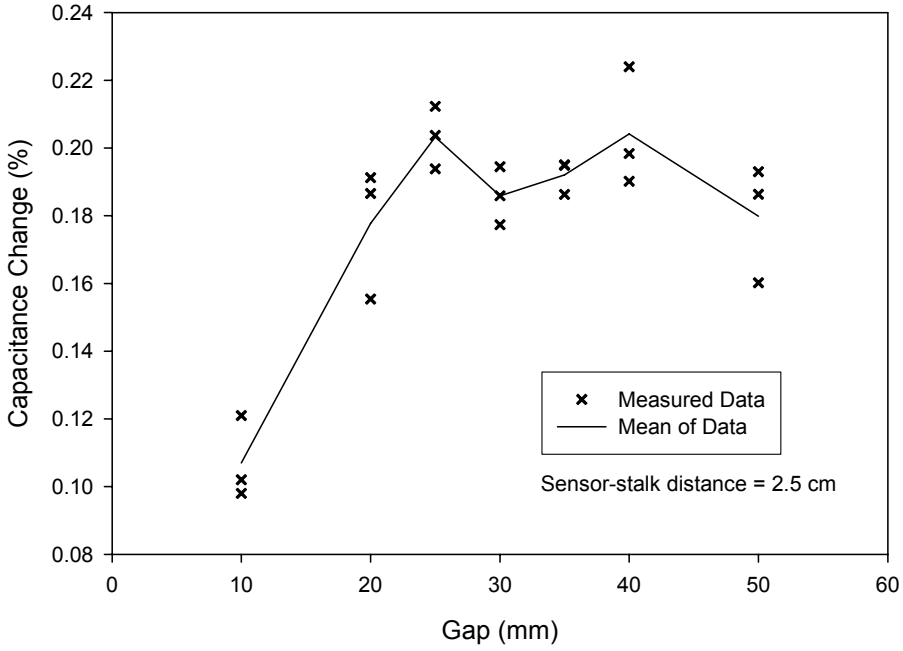

Figure 31. Modeled and measured capacitance change for different inter-electrode gaps

The experimental relationship between ground electrode width and pattern sensitivity was generally similar to the modeled relationship. Both the simulation and testing showed a stronger sensitivity response to ground electrode width when ground electrode width was less than 40 mm and a weaker response when ground electrode width exceeded 40 mm. However, the specific shape and magnitude of the response was different for modeled and measured performance. The measured response indicated a rate of sensitivity increase greater than that indicated by the modeled response at ground electrode widths less than 40 mm. The average experimental rate of sensitivity response to ground electrode width was more similar to the modeled response for ground electrode widths exceeding 40 mm. The average experimental rate of sensitivity response indicated a decrease in sensitivity at ground electrode widths greater than 50 mm. However, the variability in the experimental measurements at ground widths exceeding 40 mm was considerable and greater than the variability for ground electrode widths less than 40 mm. Therefore, while the experimental results may indicate a decrease in sensitivity, the confidence in the magnitude of these measurements is not high enough to conclusively support a difference between modeled and measured behavior.

The modeled and measured responses of sensitivity to inter-electrode gap were also similar in terms of general trends. The incremental increase in sensitivity was greatest at gaps less than 20 mm and attenuated at gaps greater than 20 mm. However, the experimental response did not follow the consistent and smooth curve suggested by the modeled results and differs in shape and magnitude. The measured rate of sensitivity increase was greater than the modeled rate at gaps less than 20 mm and less that the

modeled rate at gaps greater than 20 mm. As with sensitivity response to ground electrode width, the variability in the measured data was relatively high, therefore, confidence in the exact magnitude of the measured values was not high. Also, the average measured rate of sensitivity response to inter-electrode gap did not consistently continue to increase at gaps greater than 20 mm, as indicated in the modeled response.

The variability in the measured data may be a result of several factors. First, the copper tape technique of prototype fabrication was not as precise as the PCB plotter method. Human error in fabrication could have contributed to the variability in the data. This might help explain deviations from the expected response between different pattern prototypes (i.e., different ground electrode widths or different inter-electrode gaps). However, this does not explain the variability in the measurements from a single prototype. Variability in the results from a single prototype was likely due to the sensitivity of the test equipment connections. The magnitude of the prototype pattern base capacitance was on the order 1 pF. Even the short leads that were used to connect the LCR meter to the prototype patterns had a significant capacitance with respect to that of the patterns. Therefore, even relatively small changes in the positional relationship between the connecting leads could have a significant impact on the measurements. While careful laboratory procedures minimized the impact of the connection lead capacitance, some variability was unavoidable.

The combination of the experimental and simulated data supported the selection of the following pattern parameters as the best comprise between sensitivity, stalk

discrimination, and pattern size: 2 mm positive electrode width, 20 mm inter-electrode gap, 50 mm ground electrode width, and 100 mm electrode length.

The third step in evaluating the pattern performance was to evaluate the response to corn stalks with different moisture contents. The test fixture in Figure 11 was used and the stalks were located at Positions 1 through 5 (Figure 24). Stalk moisture contents of 10%, 15%, and 21% and sensor-stalk distances of 1.2 cm, 2.5 cm, and 3.7 cm were tested. The LCR meter was used to measure capacitance with and without stalk specimens. The relative percentage change in capacitance was calculated from these values.

The static test results for the final detection element pattern are shown in Table 4 and Figure 32. Regardless of specimen position, stalks with higher moisture content produced a larger change in capacitance than drier stalks. As expected, the relatively higher dielectric constant associated with wetter stalks had a greater impact on the electric field and therefore resulted in a larger capacitance change. For example, at Position 4 and a sensor-stalk distance of 2.5 cm, the capacitance change was -0.52%, 0.24%, and 0.97% for stalk moisture contents of 10%, 15%, and 21%, respectively. For a given stalk moisture content and position, the capacitance change decreased as the sensor-stalk distance was increased,. For example, at Position 4 and a stalk moisture content of 21%, the capacitance change was 3.28%, 0.97%, and 0.73% for sensor-stalk distances of 1.2, 2.5, and 3.7 cm, respectively. This result also agrees well with previous modeling and experimental results.

In addition to these general trends, three phenomena were observed. First, if moisture content is sufficiently low, the sensor-stalk distance at which the stalk can be

Table 4. Static test results for the final detection element pattern.

Moisture content	10%		15%			21%		
Sensor-stalk Distance	1.2 cm	2.5 cm	1.2 cm	2.5 cm	3.7 cm	1.2 cm	2.5 cm	3.7 cm
Positions	Δ C							
1	-0.44%	-0.34%	0.27%	0.04%	0.04%	0.63%	0.10%	0.11%
2	-0.60%	-0.49%	0.56%	0.12%	0.06%	1.87%	0.57%	0.12%
3	-0.67%	-0.56%	0.60%	0.19%	0.09%	2.73%	0.82%	0.58%
4	-0.57%	-0.52%	0.46%	0.24%	0.09%	3.28%	0.97%	0.73%
5	-0.66%	-0.68%	0.36%	0.07%	0.08%	3.04%	1.07%	0.50%

*** Capacitance change at 10% M.C. and 3.7 cm was not measurable**

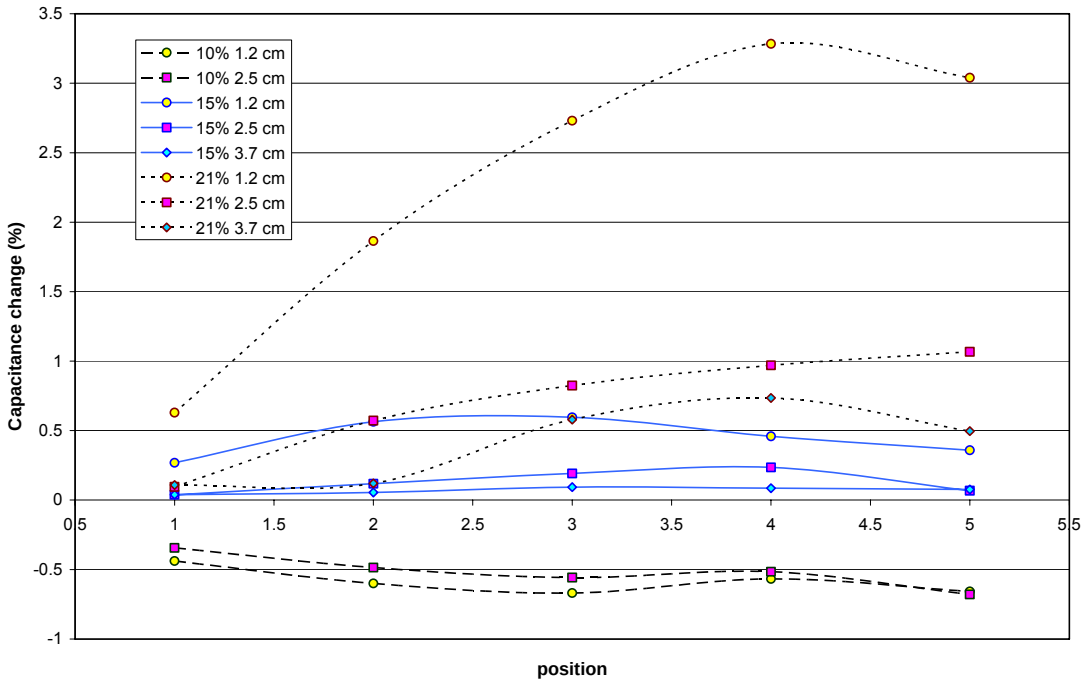

Figure 32. Static test results for the final detection element pattern.

effectively detected decreased with moisture content. Therefore, there is a lower limit to the moisture content that can be detected over a given sensor-stalk distance. Second, it is possible that the dielectric constant of the stalk may be low enough to produce a negative change in the relative capacitance, even at very small sensor-stalk distances. In this case, the dielectric constant of the stalk is actually lower than that of the ambient air. Finally, it is possible that the dielectric constant of the stalk is so similar to that of the ambient air that it will produce no measurable change in the relative capacitance. In this situation, the stalk would be effectively invisible to the detection element. However, later testing indicated that this phenomenon was observed under laboratory conditions that would be rather unlikely to occur in the harvesting environment. The corn is typically harvested in September and October when the ambient temperatures begin to decrease. At these lower temperatures, the absolute humidity of the air at saturation decreases and limits the maximum dielectric constant of the air. Also, heavier dew during the night tends to increase the moisture content of the stalks, resulting in a higher stalk dielectric constant. Extremely moist conditions that could produce this phenomena, such as those associated with rainfall events, typically delay harvesting due to the monetary penalty of harvesting higher moisture content grain and the potential damage to the fields from harvesting equipment in wet conditions.

Chapter Summary

In this chapter, a corn stalk population sensor detection element was developed and evaluated through FEM analysis and laboratory testing. In the preliminary tests, the

capacitive sensing technique showed potential as a technique to detect the presence corn stalks. The sensing ability was affected by the detection element geometry, stalk moisture content, and sensor-to-stalk distance. However, the effect of moisture content is not linear. The largest capacitance change increase occurred in the low moisture content range. Therefore, the detection element is most sensitive to moisture content changes for dry stalks, which is desirable.

FEM was a useful tool for modeling various electrode geometries and optimizing the detection element pattern. While the FEM could not be fully validated by experimental results, the model provided useful conceptual information. The change in integrated of energy density (which is linearly related to capacitance) proved to be the key parameter in evaluating the efficacy of a detection element pattern in simulation. Investigations through both simulations and fabricated prototypes provided a final sensing element pattern design. The final configuration was 72 x 100 mm with a 100mm electrode length, a 2 mm positive electrode width, a 20 mm inter-electrode gap, and a 50 mm ground electrode width.

CHAPTER 5 – CIRCUIT DESIGN AND EVALUATION

Once a detection element design was developed, the next logical step was to develop the circuitry required to detect and process the capacitance change of the detection element. The basic idea for signal acquisition in this project was to transform capacitance variation to voltage variation. For this circuit the design requirements were:

1. Effectively transform capacitance variation to a voltage signal,
2. Maintain an acceptable SNR,
3. Provide a circuit dynamic response greater than the dynamic response of the detection element,
4. Optimize circuit component values to maximize circuit output sensitivity to detection element capacitance change, and
5. Minimize circuit complexity and physical size to facilitate mounting, improve reliability, and minimize manufacturing costs.

Circuit Design

There are several ways to transform changes in capacitance to a change in frequency. The first method is a current-to-voltage transformation. When the capacitance in a circuit changes, it can change the circuit current. This current change

can be transformed into a voltage by passing this current through a resistor and measure the resulting voltage. Another way is a current-to-voltage integrated circuit (IC). The IC both amplifies the current and transforms the current into a voltage signal. The IC is the simplest way to carry out capacitance-to-voltage transformation. However, current-to-voltage transformations also transform and amplify noise as well as the signal. Furthermore, the thermal noise of a resistor may be significantly larger than capacitance-induced change in this application, resulting in a very low SNR.

The second method is a capacitance-to-voltage IC (e.g., Analog Device AD7745). This method can yield very high resolution (up to 24 bits), but the complex IC design and high resolution measurement results in a response rate less than the stalk passage rate during harvest. This type of IC is most commonly used for static sensor design (e.g., moisture measurement, impurity detection, etc.).

The third method is to use an oscillator and a frequency-voltage-converter. Capacitance variation is transformed to frequency variation in the oscillator, then transformed to a voltage variation by the frequency-voltage-converter. The oscillator and frequency-to-voltage converter method was selected for further development since it had the highest potential to meet the design requirements. A functional diagram of the circuit design and data acquisition system is presented in Figure 33.

Figure 33. Functional diagram of sensor circuitry and data acquisition system

Oscillator Circuitry Background

An oscillator is a device or mechanism for producing or controlling oscillations. A stable electrical oscillator has at least one active device and satisfies two conditions: the phase condition and amplitude condition. The amplitude condition requires that the cascaded gain and loss through the amplifier feedback network must be greater than 1. When the gain is too low oscillation ceases. When the gain is too high the active device saturates and clips the output wave. The phase condition requires that the frequency of oscillation be at the point where loop phase shift totals an integer multiple of 2π (Gottlieb, 2006).

The frequency or phase stability can be affected by ambient conditions (e.g., temperature or humidity) since the oscillation frequency is determined by circuit components. The operation frequency also can be intentionally changed by adjusting the component values. There are two different types of oscillators: fixed frequency oscillators and variable frequency oscillator (VFO) (with variable capacitors or inductors). A fixed frequency oscillator can be used to measure capacitance change by measuring the phase shift for a fixed frequency oscillation. However, the phase shift is relatively insensitive to small capacitance changes, it is difficult to compensate for phase shift noise,

and phase shift is more difficult to measure than frequency change. Only VFOs can be used to convert capacitance or inductance variations to frequency variations, therefore, a variable frequency oscillator (VFO) with capacitive elements was selected for this design. A VFO can be tuned to select a desired frequency by adjusting the value of one of the components. The variable component is usually a capacitor, but could be an inductor.

Oscillation is typically generated by amplifying random noise (Figure 34). Noise at a selected frequency is fed back positively and amplified repeatedly. The amplification slows and eventually halts as the output voltage approaches the power rail. Oscillation is the state where the power loss and power supply reach equilibrium.

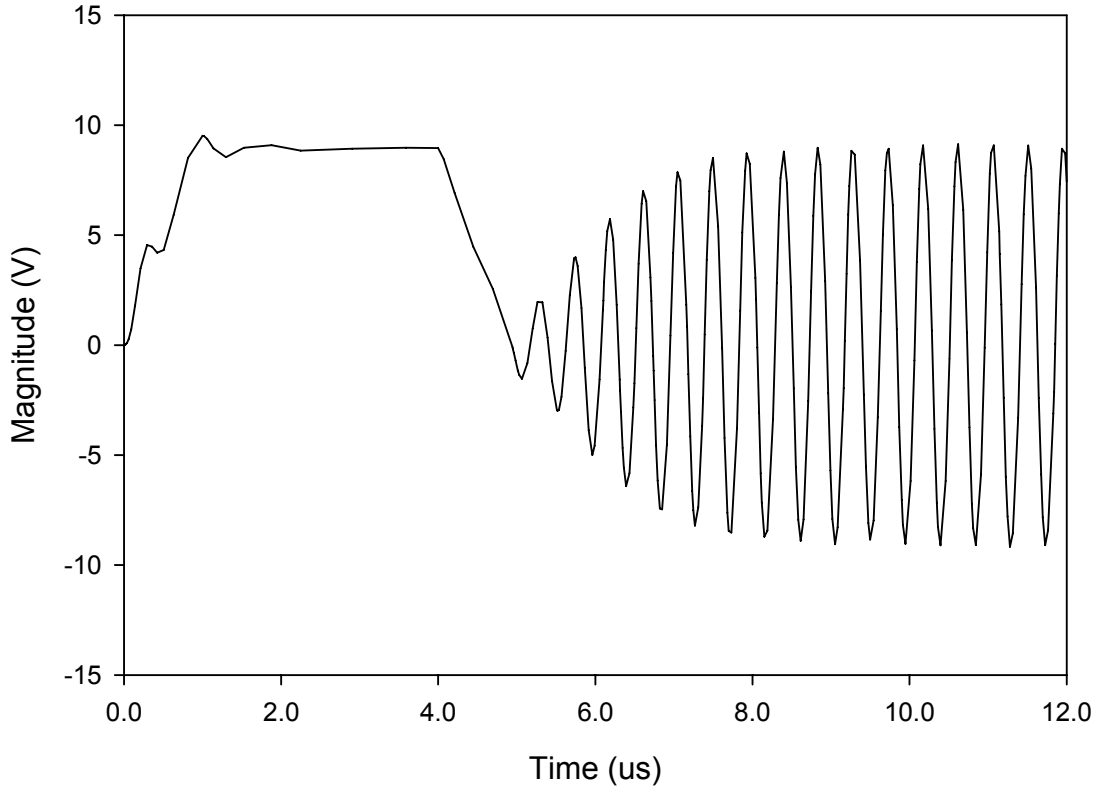

Figure 34. The oscillation initiation from thermal noise.

The Wien Bridge oscillator (Figure 35) is a popular low frequency oscillator because it produces a sine-wave output with minimum circuit complexity. This circuit can generate an oscillation using internal thermal noise amplified by an operational amplifier. The Wien Bridge actually is a half bridge in the positive feedback loop of the amplifier and produces a maximum response at the resonant frequency. Negative feedback is used to set loop gain to unity at the oscillation frequency, which stabilizes the frequency of oscillation and reduces harmonic distortion. The dependence of the oscillation frequency on system components, especially C_1 and C_2, is useful in converting the variance of a capacitor into a change in frequency.

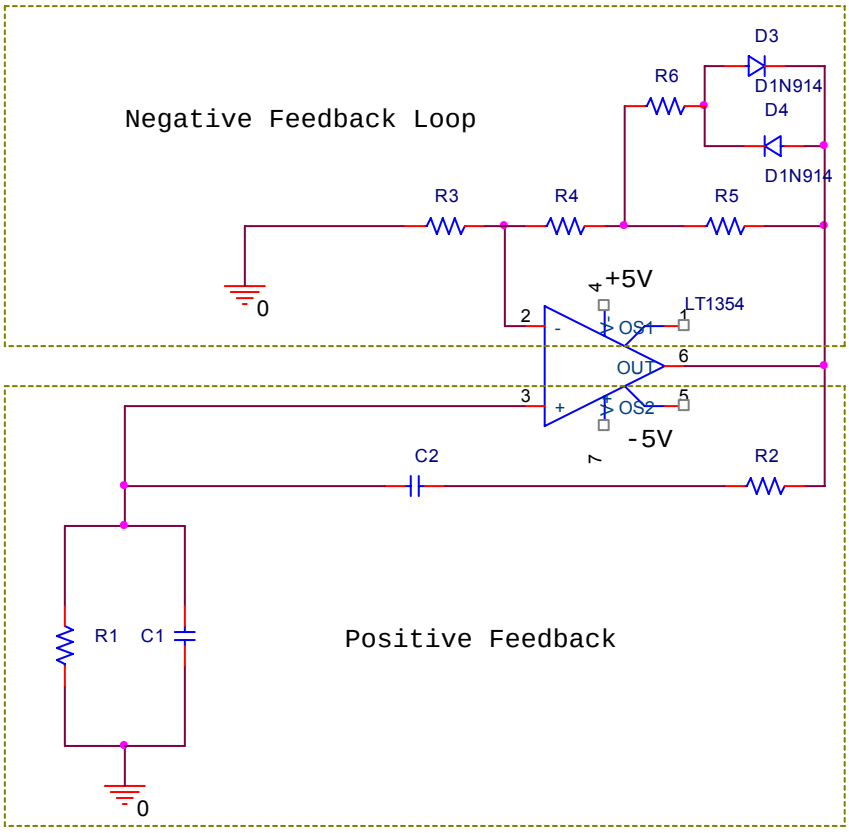

Figure 35. Circuit schematic of a Wien-Bridge oscillator.

In the circuit, R_1 and C_1 form a low-pass filter and R_2 and C_2 form a high-pass filter. The low-pass and high-pass filters together form a frequency selection circuit. The resonant frequency of the oscillator is defined where phase angles of C_1R_1 and C_2R_2 are equal in magnitude and opposite in direction. This phenomenon induces oscillation.

Wien Bridge oscillator behavior is better described by a mathematical gain analysis (Williams 1991). From gain analysis, the gain of the entire circuit must be 3 for the oscillation to be stable. If the gain is greater than 3, the oscillation is amplified and continues to increase until saturation is reached. If the gain is less than 3, the oscillation is attenuated and eventually ceases. Therefore, the stable oscillation frequency is:

$$f = \frac{1}{2\pi RC} \tag{5.1}$$

where $C = C_1 = C_2$ and $R = R_1 = R_2$.

Wien Bridge Oscillator Design

The physical interaction between the detection element, a corn stalk, and the earth is illustrated in Figure 36. The corn stalk creates a capacitance between the stalk at the sensing location and the earth (C_7). Capacitance is also developed between the corn stalk and each of the electrodes in the detection element (C_3, C_4, C_5 and C_6). An equivalent circuit for the physical interaction between the cornstalk, detection elements, and the earth is presented in Figure 37. In the sensor system design, the detection elements are capacitors C_1 and C_2 in the Wien Bridge oscillator circuit (Figure 38). The targeted capacitances are C_3, C_4, C_5 and C_6 and is contaminated by C_7. Grounding the stalks

reduces C_7 and prevents charge build-up on the stalk. Later laboratory tests showed that the lack of an earth ground for the stalks decreased the signal strength. Fortunately, the stalks have a direct connection to earth ground in the harvest environment.

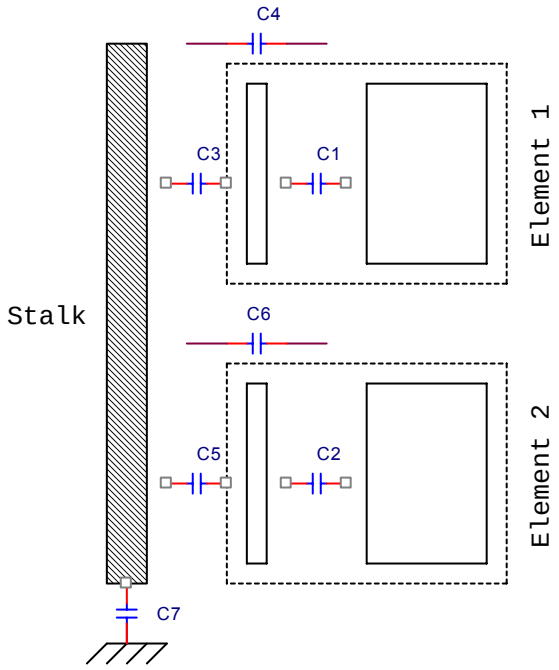

Figure 36. Physical representation of detection element interaction with corn stalk

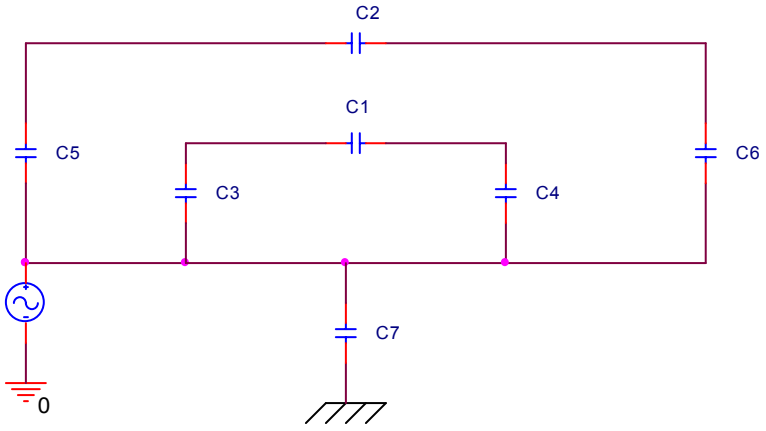

Figure 37. Equivalent circuit representation of detection element interaction with corn stalk

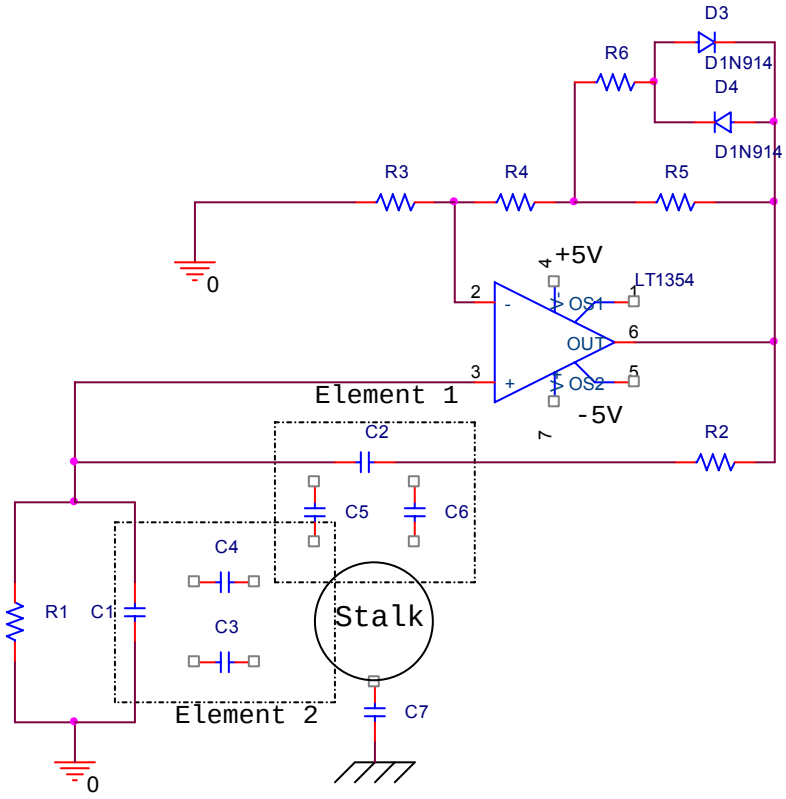

Figure 38. Circuit schematic of a Wien-Bridge oscillator including the detection elements and corn stalk.

A corn stalk is a dielectric material with a dielectric constant typically higher than the ambient air. When the stalk approaches the detection elements, C_1, C_2, C_3, C_4, C_5 and C_6 increase. The combined capacitance change affects the oscillator circuit and creates a corresponding frequency change. The change ratio ($\Delta C_{combined}/ C_{combined}$) is more critical than the base capacitance values because it represents the sensor sensitivity.

Initially, a general purpose amplifier (741) was used for the oscillator development. However, both the Pspice model and laboratory testing showed that the oscillation output frequency cannot exceed 150 KHz. Therefore a higher-speed amplifier

(Linear AT 1354) was chosen. This amplifier had a 12MHz Gain-Bandwidth and a slew rate of 400V/μs. The slew rate is the maximum rate of change in the amplifier output. The AT-1354 will theoretically allow the oscillator to operate at a frequency up to 4 MHz without excessively distorting the signal.

The oscillator was modeled using Pspice, a commercial circuit modeling package. A milliamp level thermal noise current was used to initiate the oscillation and the capacitances were kept constant (1.3 pF) during the simulation to isolate the influence of the two resistors R_1 and R_2. The modeled oscillator response indicated that the Wien Bridge oscillator can generate a steady frequency output when the capacitances and resistances are stable. The output frequency changed when either the capacitances or resistances changed, but the two capacitors (C_1 and C_2) and the two resistors (R_1 and R_2) do not equally impact frequency change in the circuit. The capacitances (C_1 or C_2) are determined by the geometry of the detection element and dielectric constant in the sensing field. The resistances (R_1 and R_2) can be used to select the base operating frequency. The modeled effects of R_1 and R_2 (Table 5) indicated that when either resistance is increased, the base operating frequency of oscillator decreased. The model also showed that the oscillator behavior was not stable for all values of R_1 and R_2.

Table 5. Modeled frequency output of oscillator for different bridge resistances

C1 = C2 = 1.3 pF	Frequency (KHz)	
Resistance (KΩ)	R1 (R2 = 50 KΩ)	R2 (R1 = 50KΩ)
1	*	1211.4
25	*	1042.2
50	963.9	963.9
75	789.5	876.1
100	667.5	826.0
125	581.5	736.1
150	520.1	655.5
175	465.5	589.4
200	422.0	541.7
225	384.5	499.5
250	353.3	460.6
275	327.7	441.1
300	306.3	*
325	287.8	*
350	270.8	*

* No stable oscillation.

The circuit was evaluated in the laboratory once modeling was completed. Since the capacitive elements in the Wien Bridge oscillator are the detection elements, the values of R_1 and R_2 that would maximize the sensitivity of the oscillator output to detection element capacitance change needed to be determined. The oscillator was fabricated on a printed circuit board with potentiometers for R_1 and R_2. Each resistor was varied by adjusting the potentiometers from approximately 10 to 250 kΩ while fixing the other resistor at approximately 50 kΩ. Both capacitors (C_1 and C_2) were fixed at 1.3 pF and a universal counter was used to measure the oscillation frequency. The experimental results are presented in Table 6.

Table 6. Measured frequency output of oscillator with different resistances

C1 = C2 = 1.3 pF	Frequency (KHz)	
Resistance (KΩ)	R1 (R2 = 50 KΩ)	R2 (R1 = 50KΩ)
10	499	170
25	246	161
50	152	152
100	89.5	149
150	66.8	158
200	49.8	170
250	52.3	180

The experimental results indicated that when R_1 is increased, the base operating frequency of oscillator decreases. However, changing the value of R_2 has little effect on the base operating frequency.

The data were plotted to graphically compare trends (Figure 39 and Figure 40). In both figures, the difference between the simulated output from Pspice and measured output from printed circuit board was considerable. For example, when R_1 and R_2 were

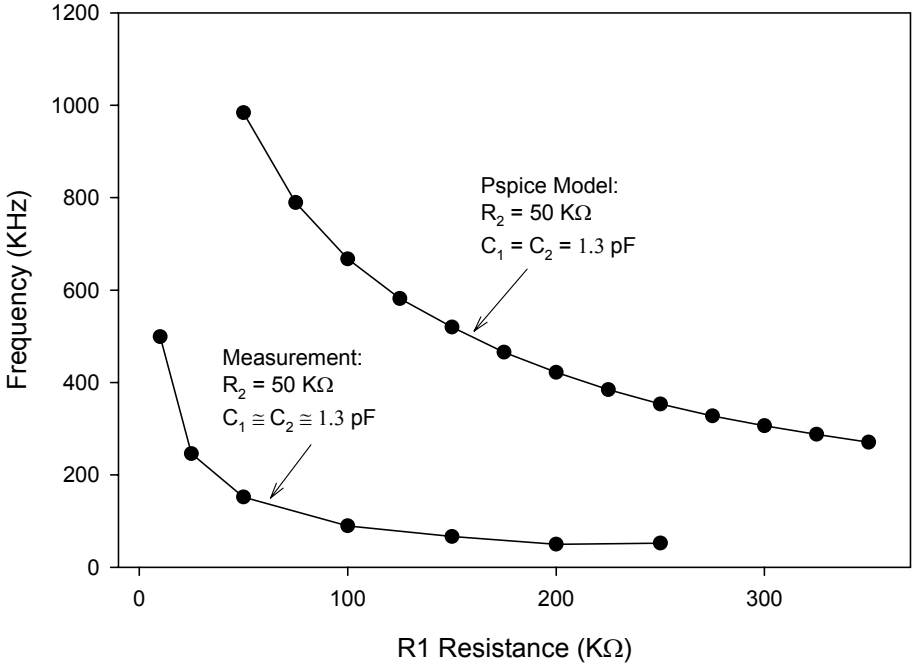

Figure 39. Modeled and measured effect of R_1 on the oscillation frequency

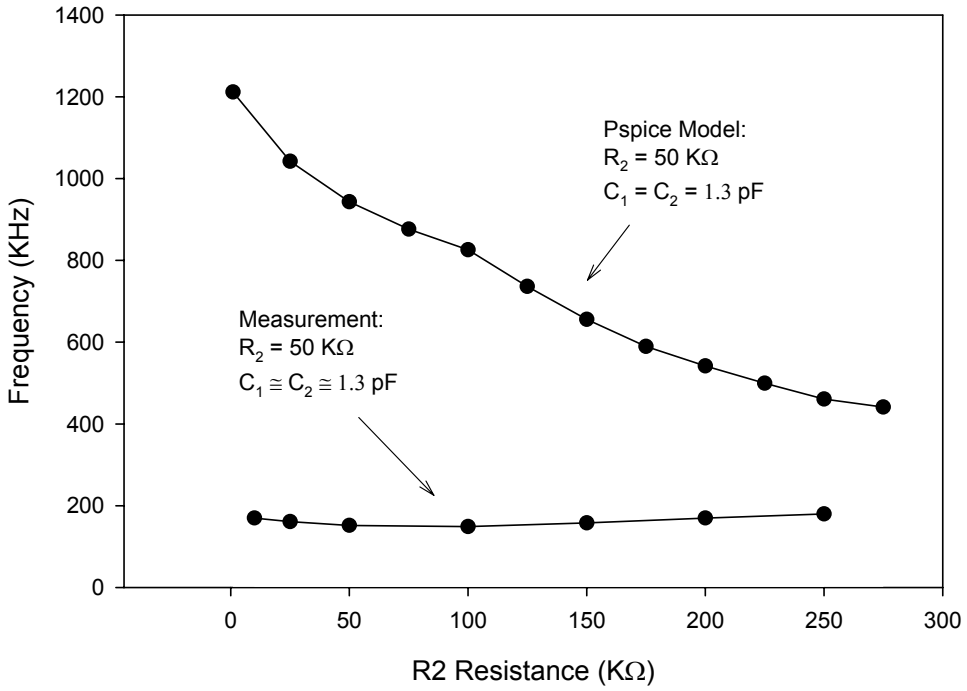

Figure 40. Modeled and measured effect of R_2 on oscillation frequency

50 KΩ, the measured and modeled responses were 152 and 950 KHz, respectively. The difference was probably due to the low sensor capacitance coupled with parasitic capacitance on the PCB. The sensor capacitance was less than 1.5 pF and the complex circuit board layout introduced parasitic capacitors into the circuit which could have been of the same order of magnitude as the sensor capacitance. Parasitic capacitances are both unmeasurable and unstable. The addition of parasitic capacitances results in a very complex capacitance space with complex interactions. The Pspice model does not accurately represent the actual circuit if the parasitic capacitances are significant. Figure 41 illustrates the impact of parasitic capacitance on circuit and modeling complexity. Parasitic components result in a much more complex circuit, especially, when the parasitic components are of the same order of magnitude as the operational components.

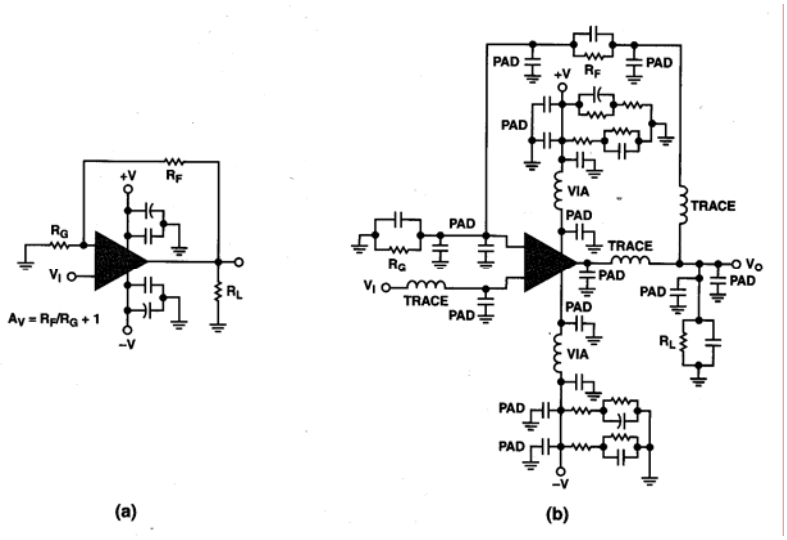

Figure 41. Typical OPAMP circuit, as designed (a) and with parasitic (b) (Analog Devices, 2005)

By comparing Figure 39 and Figure 40, the experimental and modeled results of the effect of R_1 share a similar trend, but differ considerably in magnitude. However, there is little similarity to be found between the modeled and measured results with respect to R_2. While the modeled data indicated a significant response to R_2, measured results indicated that the response is almost constant with respect to R_2.

It is logical to focus on using the measured results to complete the oscillator design considering the large discrepancies between the modeled and measured results along with the fact that the model likely does not accurately represent the actual circuit behavior. Therefore, the optimal values of R_1 and R_2 were determined experimentally. A two-dimensional test matrix was developed for R_1 and R_2 with resistance values of 10, 25, 50, 100, 150, 200, and 250 KΩ. The oscillator and detection elements were attached to the static test fixture described in Chapter 4 and a rubber rod with a dielectric constant of 8 was used as the test specimen. The base frequency was measured for each test

condition (R_1 and R_2) with and without a specimen and the relative change in oscillator frequency was calculated.

The oscillator output frequency change with respect to R_1 and R_2 is shown in Figure 42. The darker areas indicate regions of higher sensitivity. Three relatively sensitive areas (Areas 1, 2, and 3) were identified. Area 1 represents only a local, not global, maximum. Area 2 is located in a region where stable oscillator behavior is questionable. Experimental measurement of frequency in this area showed a large drift. Therefore, Area 3 was chosen to represent the optimum combination of R_1 and R_2. The selected values of R_1 and R_2 were further refined in the laboratory to determine the optimum operational parameters resulting in final values of 43 KΩ and169 KΩ for R_1 and R_2, respectively. The base output frequency of the Wien Bridge oscillator was 245 KHz.

Two corn stalk specimens (10 and 85% moisture content) were used to confirm adequate function of the oscillator. The measured frequency changes were 9 and 0.4 kHz for stalk moisture contents of 10 and 85%, respectively. These frequency changes relative to the 245 kHz base frequency were 3.7 and 0.16%, respectively.

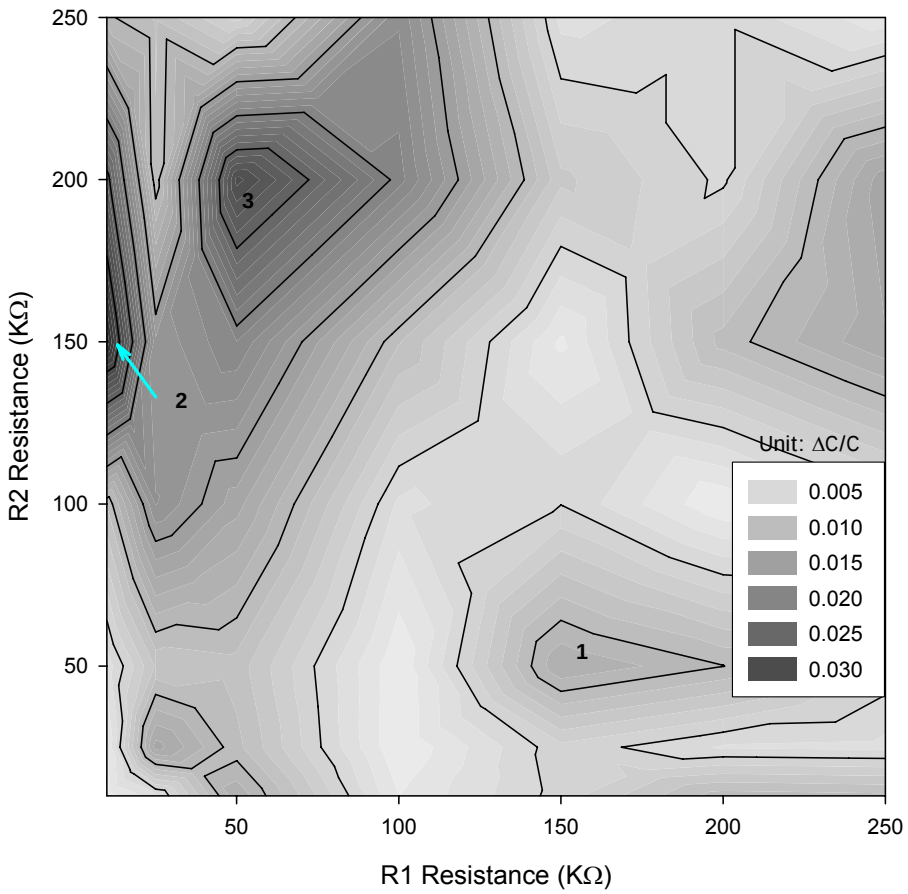

Figure 42. Sensor sensitivity with R_1 and R_2.

Frequency to Voltage Converter Background

A commercially available PLL IC was used as an Frequency-to-voltage converter. A popular general purpose PLL IC, 74HCT4046, was selected for this PLL design.

A PLL is a circuit that synchronizes an output signal with a reference signal with respect to frequency and phase. When the PLL is locked, the phase error between the oscillator output and the reference will either be zero or remain constant. There are three

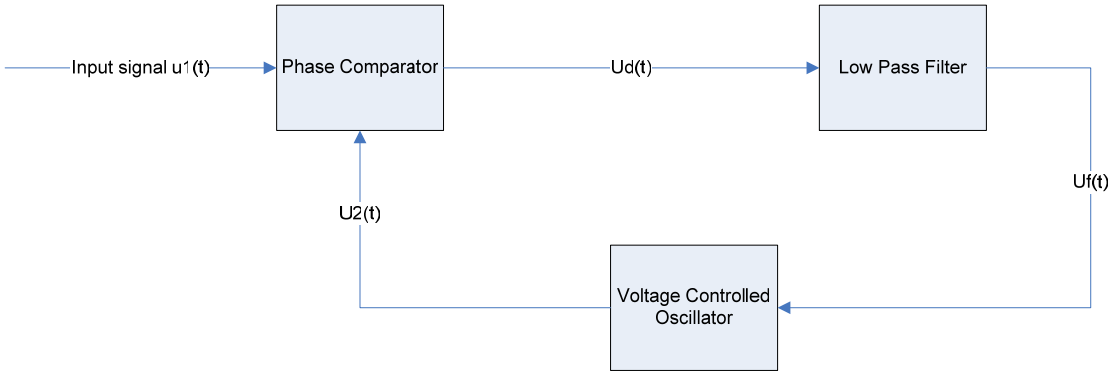

Figure 43. Phase-locked loop functional schematic

basic functional blocks in a PLL (Figure 43): a voltage-controlled oscillator (VCO), a phase comparator (PC), and a low pass filter (LF).

There are three different types of phase comparators (PC) available in the selected PLL: an exclusive or (XOR), J-K flip-flop, and a phase-frequency comparator (PFC). Although a linear multiplier is not included in the selected PLL, it is useful to examine this type of phase comparator to better understand the function of a PLL.

For a linear multiplier phase comparator, two inputs are required: an input signal and the output from a VCO. A sinusoidal input signal, $u_1(t)$, is generally assumed:

$$u_1(t) = U_{10}\sin(\omega_1 t + \theta_1) \tag{5.2}$$

where U_{10} is the amplitude of the input signal, ω_1 is the radian frequency, and θ_1 is the phase. Generally, the VCO output, $u_2(t)$, is a square wave:

$$u_2(t) = U_{20}\,rect(\omega_2 t + \theta_2) \tag{5.3}$$

where "rect" is square waveform, U_{20} is the amplitude of the input signal, ω_2 is the radian frequency, and θ_2 is the phase. For simplification, the phases are assumed to be constant over time. So, the product of the inputs, u_d , is:

$$u_d(t) = u_1(t) \cdot u_2(t)$$

$$u_d(t) = U_{10}U_{20}\sin(\omega_1 t + \theta_1)[\frac{4}{\pi}\cos(\omega_2 t + \theta_2) + \frac{4}{3\pi}\cos(3\omega_2 t + \theta_2) + \cdots] \quad (5.4)$$

If the PLL is locked, the frequencies ω_1 and ω_2 are identical, therefore:

$$u_d(t) = U_{10}U_{20}\left(\frac{2}{\pi}\sin\theta_e\right) + \text{high frequency component} \quad (5.5)$$

where θ_e is the phase error. The first term is the DC component and the high frequency component is attenuated by a low pass filter.

The EXOR type phase comparator is level-sensitive, while the JK-flip-flop and PFC types are edge-sensitive. Therefore, the EXOR is less noise-sensitive and is typically used in high noise environments. The PFC behaves differently dynamically than the other PCs in that its output signal depends on not only on phase error but also on frequency error. The PFC generally will lock under conditions where the other PCs will not and therefore is preferred when operated in low noise environments (Best, 1999).

There are three types of first-order low pass filters that are used with PLLs: a passive lead-lag filter, active lead-lag filter, and active proportional-integral (PI) filter. The passive lead-lag filter has one pole and one zero. It is transfer function F(s) is given by:

$$F(s) = \frac{1 + s\tau_2}{1 + s(\tau_1 + \tau_2)} \quad (5.6)$$

where $\tau_1 = R_1C$ and $\tau_2 = R_2C$.

The zero of this filter is crucial because it has a strong influence on the damping factor of the PLL system. The active lead-lag filter is similar to the passive but has an

additional gain term Ka, which can be chosen to be greater than 1. The transfer function, F(s), is given by:

$$F(s) = K_a \frac{1 + s\tau_2}{1 + s\tau_1} \tag{5.7}$$

where $\tau_1 = R_1C$ and $\tau_2 = R_2C$, and $Ka = C_1/C_2$.

The active PI filter's transfer function is given by:

$$F(s) = \frac{1 + s\tau_2}{s\tau_1} \tag{5.8}$$

where $\tau_1 = R_1C$ and $\tau_2 = R_2C$. This filter has a pole at s = 0 and therefore behaves like an integrator.

There are four key parameters specifying the frequency range in which the PLL can be operated (Best, 1999):

1. **Hold range**: The frequency range over which a PLL can statically maintain phase tracking. A PLL is conditionally stable only within this range.
2. **Pull-out range:** The dynamic limit for stable operation of a PLL. If tracking is lost within this range, a PLL normally will lock again, but this process can be relatively slow if it is a pull-in process.
3. **Pull-in range:** The range over which a PLL will always become locked, but the process can be relatively slow.
4. **Lock range:** The frequency range within which a PLL locks within one cycle between reference frequency and output frequency. Normally the operating-frequency range of a PLL is restricted to the lock range.

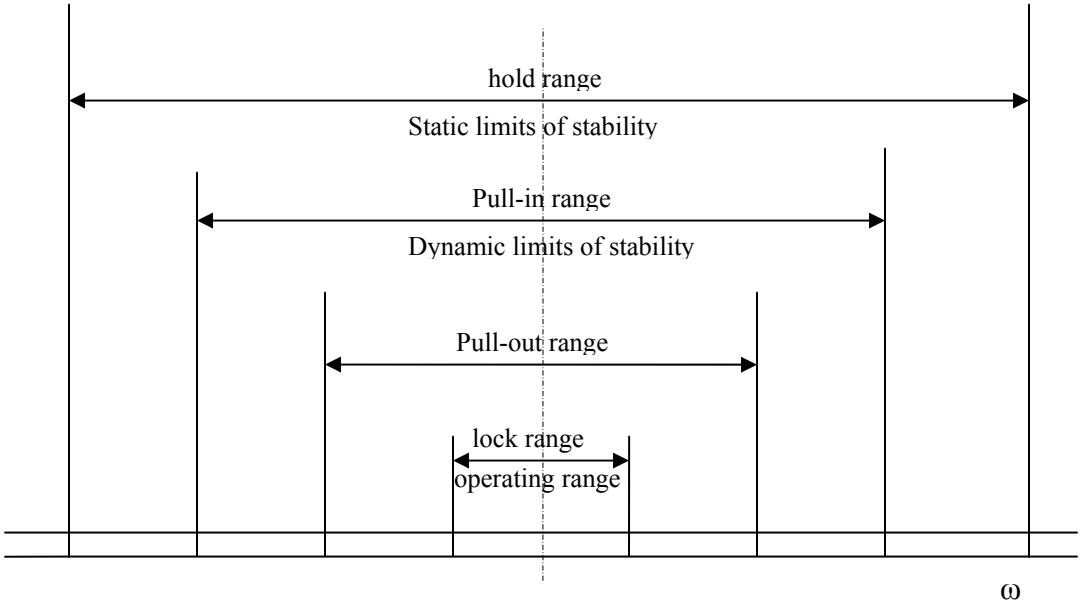

Figure 44. Scope of the static and dynamic stability limits of a linear second order PLL

The relationship between these parameters is graphically represented in Figure 44.

Frequency-to-Voltage Conversion Design

The basic requirement for a PLL design is to relock the PLL in a short time when frequency changes. This means the PLL can track input frequency change. As previously discussed, the capacitance change of the detection elements is a relatively slow process. This continuous slow capacitance change induces a continuous slow frequency change. Therefore, once the frequency is locked, the frequency change will generally be in the lock range where very little time is required to relock the PLL.

The operation frequency band and dynamic properties (e.g. lock-up time, bandwidth, and stability) of the PLL needed to be determined. The operation band is

determined by its central frequency and offset frequency (Figure 45). The central frequency is the VCO output frequency when the VCO input voltage is half the PLL supply voltage (½ V_{cc}) (Austin, 2002). The PLL central frequency was matched to the oscillator output frequency (245 kHz) by selecting external components (resistor R_{11} and capacitor C_{11}) (Figure 45).

The offset frequency is half the linear operating band width. The PLL output resolution (V/Hz) is the allowable linear output voltage range (V_{max}-V_{min}) divided by the operating band width. A smaller offset frequency will therefore increase PLL output sensitivity. However, the output voltage can be saturated if the offset frequency is too small. The operating band width should be large enough to contain the entire output range of the oscillator. Previous tests showed that a high moisture content stalk (MC = 85%) produced a 9 KHz change in oscillator output frequency. A safety factor of 2 was used to ensure the operating band width would contain all reasonable oscillator output frequencies and baseline drift. An offset frequency of 20 kHz was selected, which corresponds to an operating band width of 40 kHz. The offset frequency was set by selecting an appropriate value for the external resistor R_{12}.

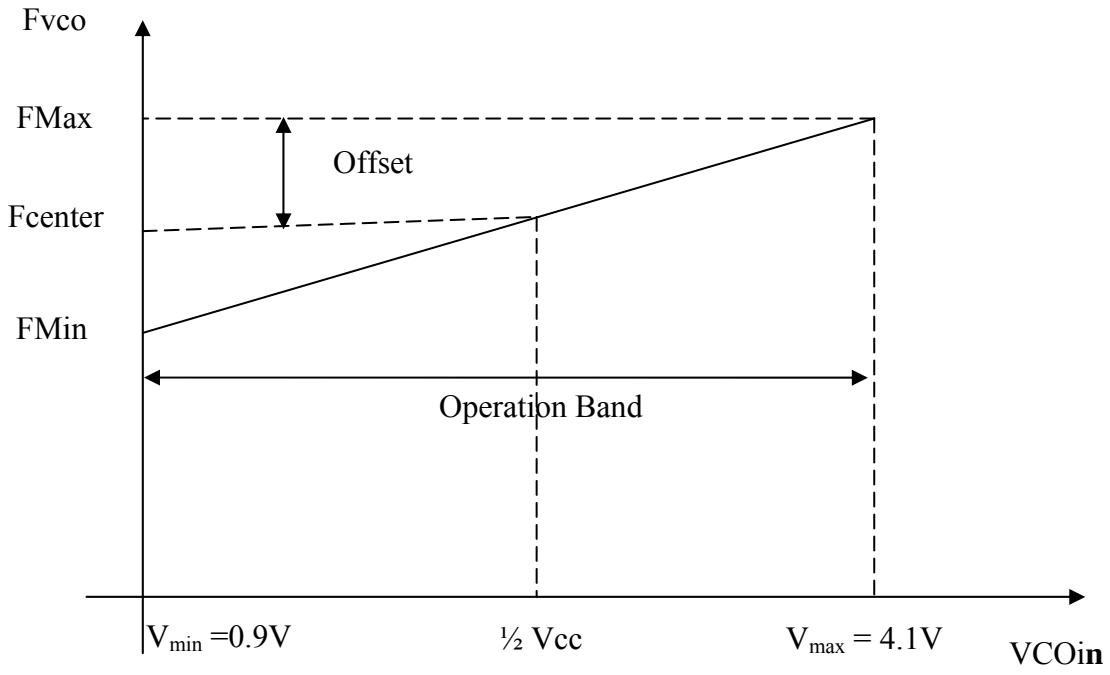

Figure 45. PLL center and offset frequencies (linear operation)

Approximate values for the external components (R_{11}, R_{12}, and C_{11}) were determined by referring VCO performance curves in the PLL datasheet (Appendix B). A value of 10 nF was selected for C_{11} and the power supply voltage for PLL was 5 V. The desired center and offset frequencies were obtained at resistances of approximately 100 and 50 KΩ for R_{11} and R_{12}, respectively.

Final values of the external components were determined experimentally by using a programmable power supply (HP E3631A) and a universal counter. The programmable power supply was used as the VCO input and 10 *nF* was selected for C_{11} The programmable power supply was set to one-half V_{cc} (2.5 V) to produce the center frequency on the VCO output pin. The VCO output was measured using the universal counter and R_{11} was adjusted to obtain the target output frequency. The power supply

voltage was changed to V_{min} (0.9V)and V_{max} (4.1V) and R_{12} was adjusted to obtain the desired offset frequency (20 kHz). The final values for C_{11}, R_{11}, and R_{12} were 10 nF, 100 KΩ, and 33 KΩ, respectively.

The dynamic properties (lock-up time, PLL bandwidth, and the desired stability) of the PLL are determined by its low pass filter, therefore the low-pass filter is a critical component in the design. Assuming a corn stalk diameter is 1 centimeter (an extremely small stalk diameter), a combine harvesting speed of 6.5 km/h (an extremely high harvest speed), and an average stalk gap of 10 cm (15 cm typically), the stalk appearance frequency is 18 Hz with a 5.5 ms passing time for each stalk. These two values represent a reasonable upper limit for corn harvest. The actual sensor response was considerably slower than 5.5 ms (more details provided later). For this design, the lock-up time was set at 2 ms with a damping factor (ξ) near 0.7 ($0.4 < \xi < 1$). The design lock-up time was approximately one-third the expected minimum passing time. A damping factor near 0.7 provided a good balance between stability and speed. Phillips PLL design software was used to determine initial component values for the low pass filter.

The final component values for the low pass filter were determined experimentally after connecting the oscillator and PLL circuit. A dynamic test simulated dynamic field conditions and was used to test the sensor's dynamic response properties. The low pass filter component values were adjusted to increase the SNR while reasonably sacrificing dynamic performance, since the designed 2ms lock-in time is far faster than the sensor response. The peak-to-peak noise magnitude was approximately 80 mV and the signal level was typically greater than 1 V. Therefore, the final SNR was

greater than 10 in laboratory testing. The final values of the low-pass filter were 1200 pF and 200 KΩ for C_{13} and R_{13}, respectively.

Amplification for DAQ Interface

An operational amplifier (OPAMP) was used to provide impedance matching of the PLL output and DAQ input, bias offset adjustment of the PLL output, improved digital acquisition resolution, and improved SNR in the acquired signal.

An AD627 amplifier was used (Figure 46) because of its simple circuit configuration. This device offers flexibility by allowing the user to set the gain of the device with a single external resistor (R_G). With no external resistor, the AD627 is configured for a gain of 5. The amplifier output voltage (V_{out}) for a given input (V_{in+}), reference voltage (V_{ref}) and offset voltage (V_{in-}) is given by:

$$V_{out} = [V_{in}(+) - V_{in}(-)] \times (5 + 200\Omega / R_G) + V_{ref} \tag{5.9}$$

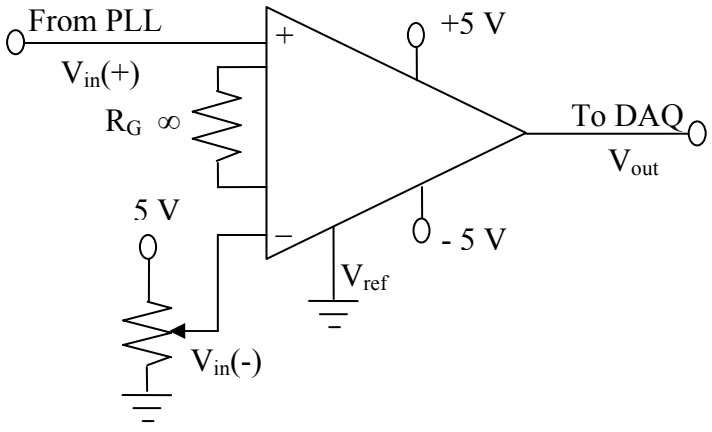

Figure 46. Active amplifier AD 627 schematic graph

The input signal to theAD 627 was the PLL output to the low-pass filter and the OPAMP output was connected to the DAQ. The amplifier gain was set to 5 by leaving the R_G terminals open. An adjustable offset voltage was connected to the inverting input of the AD627 to remove the PLL output base voltage (0.9 V). This allowed maximum amplification (5X) without exceeding the dynamic range (± 5 V) of both the AD627 and DAQ. The offset voltage also allowed for baseline drift compensation in the field by resetting the zero output point.

There are two possible PLL output pins. One pin is the demodulator output, which has high output impedance. The other output pin which serves as the input to the low-pass filter. The output impedance of this pin is dependent in part on the external low-pass filter components. Experimental testing showed that the low-pass filter pin had a much better SNR than the demodulator output pin. Therefore, this pin was used as the PLL output signal. However, the input impedance of the DAQ was somewhat low (144 kΩ). Connecting the DAQ input to the low-pass filter pin significantly changed the properties of the PLL low-pass filter and adversely impacted PLL function. The addition of the AD627 (20 GΩ input impedance) between the PLL and DAQ eliminated the impact on the PLL low-pass filter and restored proper PLL function.

Laboratory Evaluation of Detection Element and Circuit

Methodology

The detection elements and supporting circuitry were fabricated using the PCB plotter to evaluate the sensor system circuitry (two detection elements, oscillator, PLL, and OPAMP) including any parasitic capacitance effects. Two dynamic test fixtures were used to evaluate the sensor system circuitry. One fixture (Figure 47) allowed the specimen passing speed to be adjusted from 0 to 5 m/s and was used for dynamic response testing. The other (Figure 48) was used to better simulate field harvest conditions and the interaction of multiple stalks. Corn stalks in this fixture were grounded by a conductive wire to simulate earth grounding.

In the first fixture (Figure 47), a 90-V DC variable speed motor was used to control the speed of the flywheel. Holes at various intervals on the flywheel were used to simulate the variable gaps between stalks in the field. The sensor was mounted on the top of the fixture and the specimens were passed by the sensor. Corn stalks with different moisture contents (ranging from 18% to 35%) were placed on the flywheel and tested at different speeds (1, 2, 3, 4, and 5 m/s). Sensor-stalk distances of 0.5, 1.0, 1.5, 2.0, and 2.5 cm were evaluated.

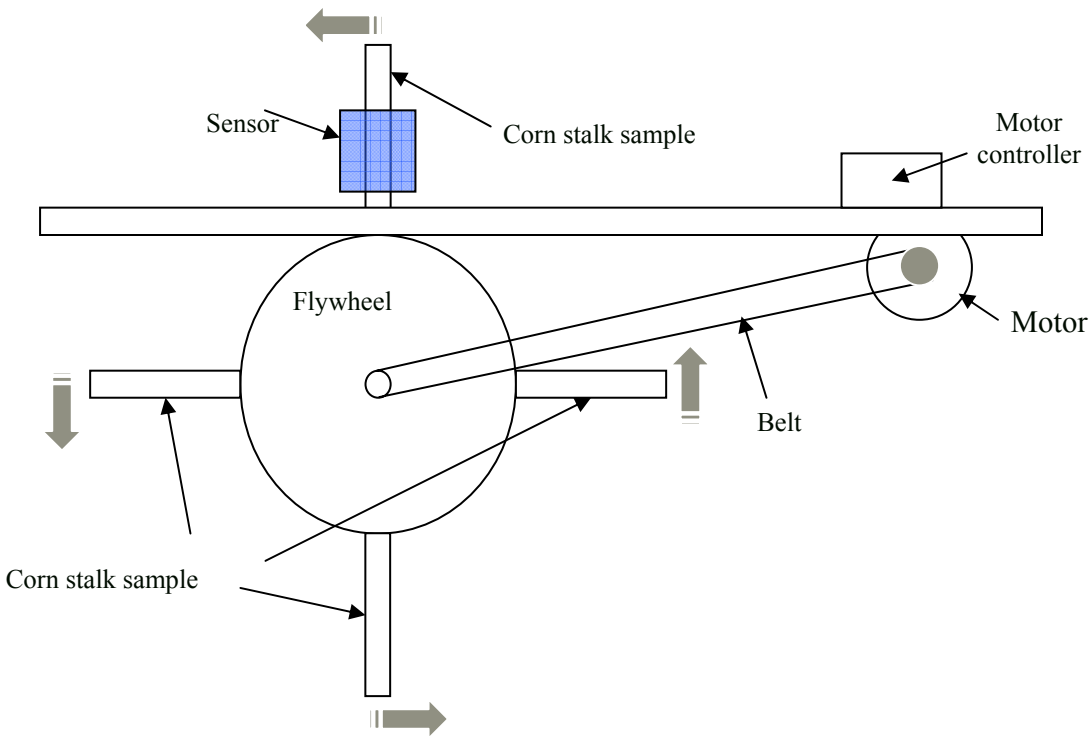

Figure 47. Schematic of the first dynamic test fixture

The pitfall of the first test fixture is that the corn stalk could not pass the sensor parallel with the sensor electrode. The stalk reaches the low right corner first and leaves the low left corner last. This required the fabrication of another fixture that better simulated the passage of stalks in a field environment. In the second fixture, a rectangular wood frame was built (Figure 48). Two rows of one-inch diameter holes were drilled at center-to-center distances of 5, 7.5, and 15 cm. An informal survey conducted in the field (August 2006) indicated that more than 95% of corn stalks were spaced greater than 10 cm apart and less than 2% of the stalks were spaced less than 5 cm apart. Corn stalks chosen randomly in the field were placed in the fixture and a wire connected to an earth ground was tied to the corn stalks. Two steel rails attached to the

floor were used to guide the wood frame along a straight path. The OPAMP portion of the supporting circuit was not used during these tests and the PLL output was measured using a digital oscilloscope (Tektronix TDS-3014). An infrared transmission optical sensor was also used to more

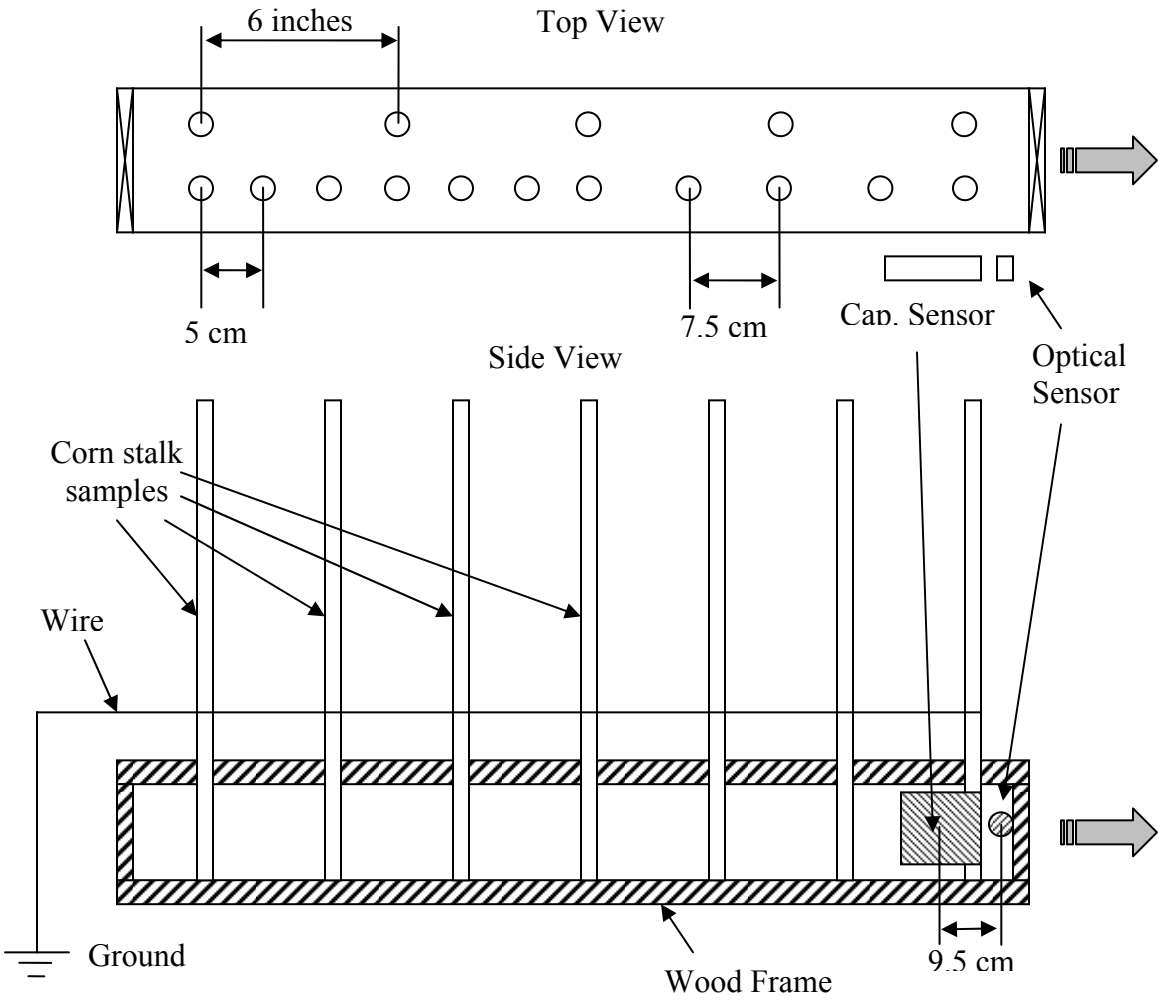

Figure 48. Schematic of the second dynamic test fixture.

Figure 49. The second dynamic test fixture

precisely locate the stalks and correlate the sensor output with actual stalk location. The two sensors were mounted beside the frame with 9.5 cm between the centerlines of the two sensors.

In the second fixture test, stalks harvested from field were placed in the frame. Data were collected over a one month period as the stalks were allowed to air dry. The stalk samples were harvested on Aug 11th, 2006, and had an average stalk moisture content of 85% at harvest. The leaves and ears were carefully removed to minimize the effect from leaves and improve the optical sensor reference. The samples were mounted into the holes with different gap combinations. Two oscilloscope channels were used to simultaneously record both sensor outputs. The fixture was pushed to move it along the

rail channel at speeds ranging from 0.8 to 1.48 m/s (1.8 – 3.31 mph), which is representative of the harvesting speed range (2 – 3 mph). The test was repeated every three days to represent a range of moisture contents. Parameters such as stalk spacing, sensor-to-stalk distance, and sensor position were kept constant. At the end of one month of testing, the average moisture content decreased from approximately 85% to 25%. The individual stalk moisture content ranged from 15% to 35% in the last test, which was conducted on September 6th, 2006, one week before the preliminary field test.

Results

The first dynamic test fixture was used to investigate the relationships between the signal width, signal magnitude, harvest speed, the sensor-stalk distance, and stalk moisture content. The definitions of signal width and signal magnitude are shown in Figure 50; positive signal peaks correspond to stalks, signal width is the time gap between two stalk peaks, and signal magnitude is the voltage difference between a stalk peak and the baseline voltage.

Figure 51 shows the signal width at different harvest speeds when the corn stalk moisture was 35% and the sensor-stalk distance was 2 cm. The signal width decreased when the operation speed increased. The relationship between signal width and operation speeds was nearly linear, which was expected.

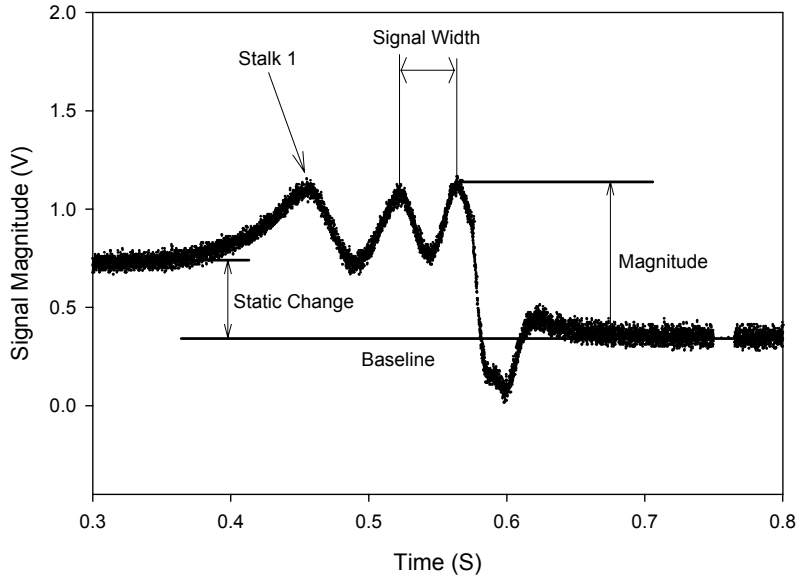

Figure 50. Definition of signal width and signal magnitude

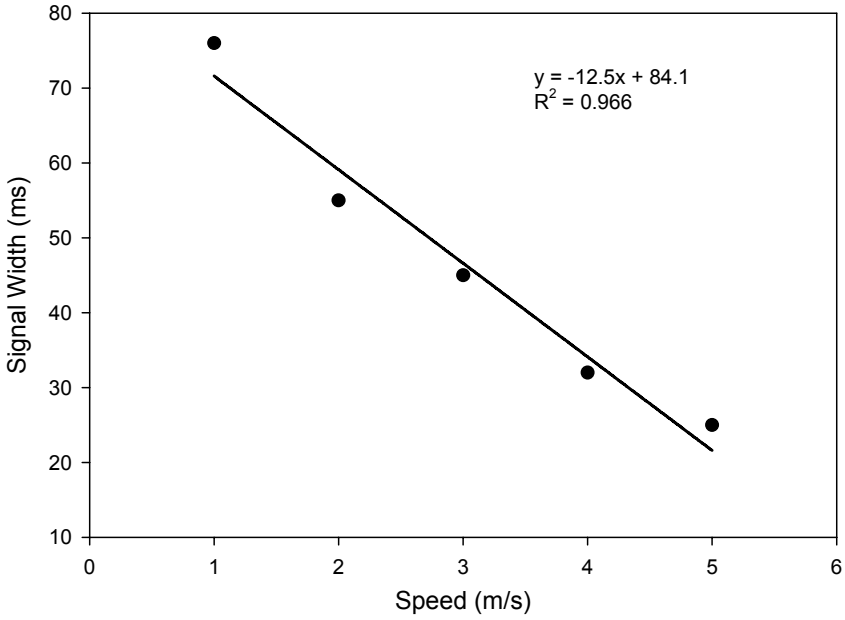

Figure 51. Signal width at different operating speeds (first dynamic fixture test)

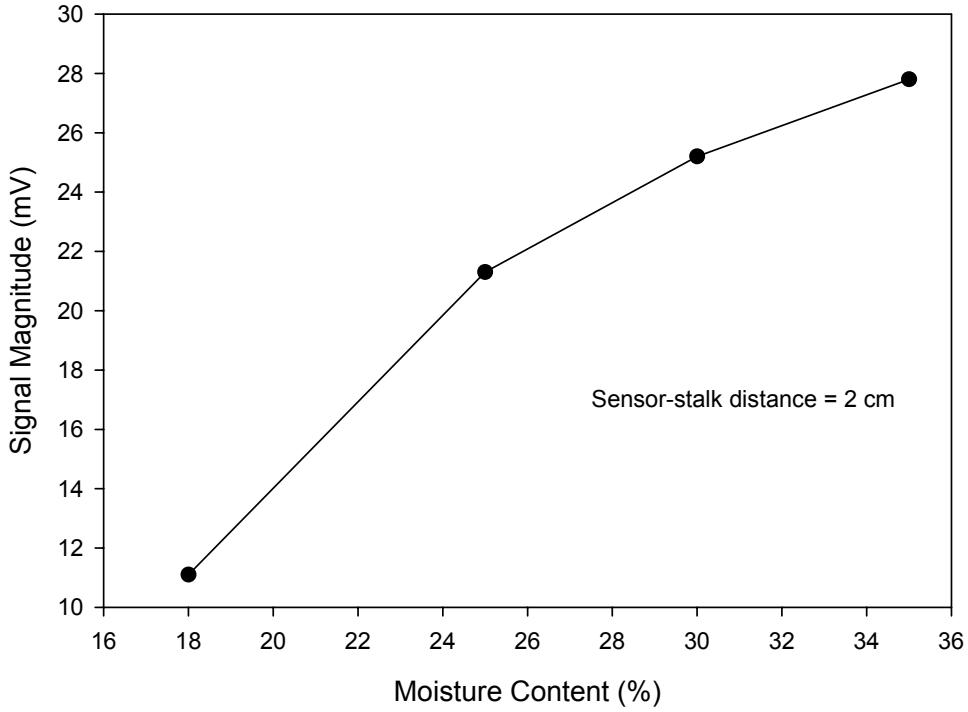

Figure 52. Signal magnitude at different corn stalk moisture contents (first dynamic fixture test)

Figure 52 illustrates the signal magnitude at different corn stalk moisture contents when the operation speed was 4 m/s and the sensor-stalk distance was 2 cm. The signal magnitude increased when the moisture content increased. The rate of signal magnitude increase was 1.46 mV/%MC and 0.52 mV/%MC for moisture content range of 18% to 25% and 30% to 35%, respectively. The signal sensitivity was greater at low moisture content. Similar behavior was observed in the static preliminary test (Figure 13), .

Figure 53 shows the signal magnitude with respect to the sensor-stalk distance when the operation speed was 4 m/s and moisture content was 35%. The signal magnitude was dramatically affected by the sensor-stalk distance. The rate of signal strength decrease was much larger when the stalk less than 2 cm from sensor

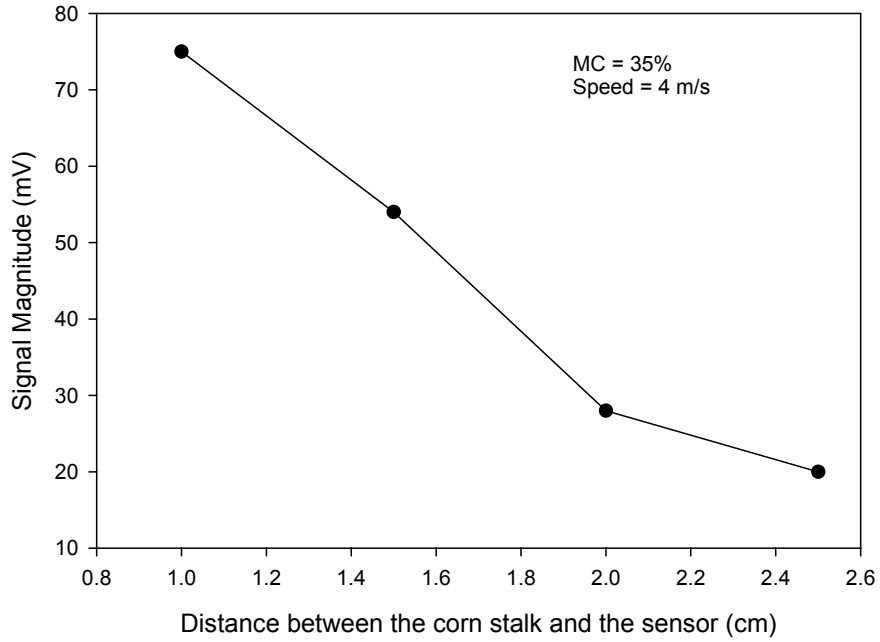

Figure 53. Signal magnitude at different sensor-stalk distance (first dynamic fixture test)

(approximately 5.7 mV/mm) as compared to when the stalk was more than 2cm from the sensor (approximately 1.2 mV/mm).

The second fixture was used to better simulate some aspects of the field environment and to investigate the relationship among multiple corn stalks. The results of the first test are shown in Figure 54. The upper plot was the signal from the capacitive sensor and the lower plot was from the optical sensor. The gap between two corn stalks was 15 cm. The positive peak corresponded to a stalk for the capacitive sensor and the negative peak corresponded to a stalk for the optical sensor.

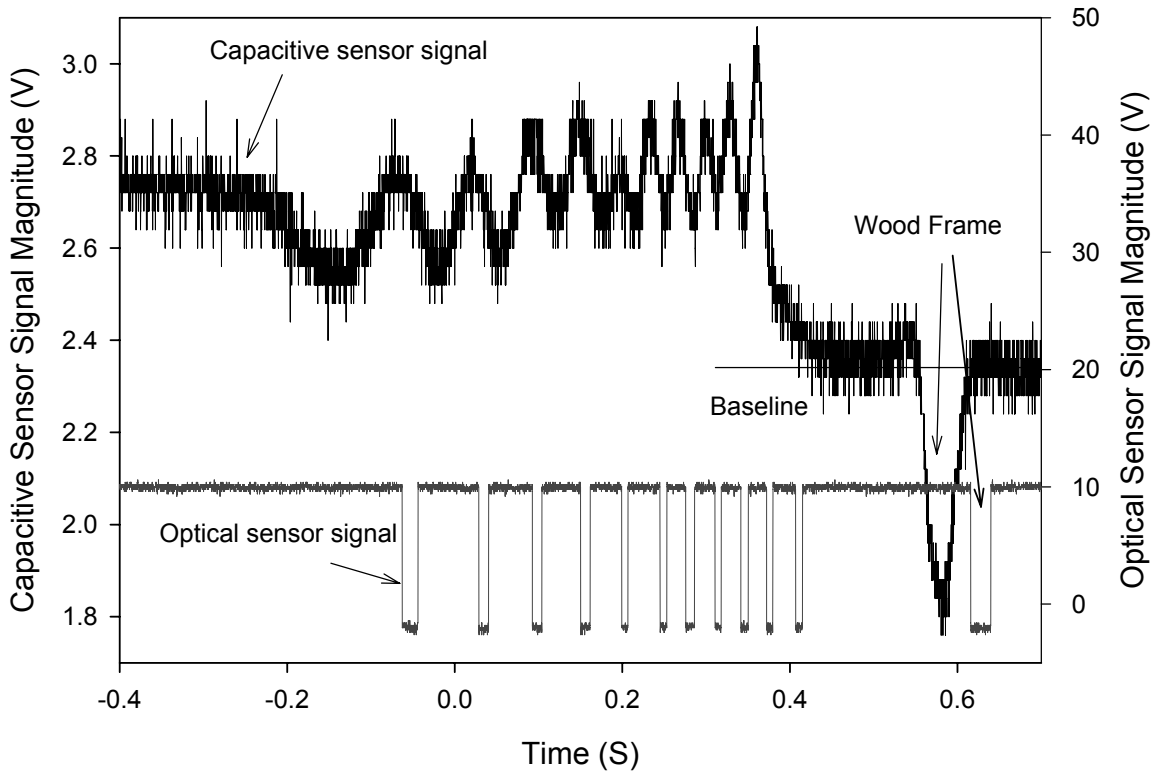

Figure 54. Sensor output from first test using the second dynamic test fixture

The gap between stalks did affect the output signal shape. The sensor output did not completely return to baseline levels after the passage of each stalk. Instead, the corn stalks signals overlap with each other. By inspecting the last corn stalk signal, the capacitive sensor required approximately 70 ms to discharge from peak to baseline levels. This recovery time was far longer than the average signal width (30 ms) at a speed of 1 m/s. The slow response explains why successive stalk signals were overlaid. The overlaid signal pattern could affect stalk discrimination. However, even at high stalk moisture contents (~85%) and a 15 cm gap (average gap), the individual stalks can still be discriminated. When moisture content was lower, the successive stalk signals were

easier to separate for a given stalk spacing because dry stalks produced lower peak signal magnitude and required less time to return to baseline output levels.

The absolute air humidity can also affect the signal shape. There was a signal output magnitude below the baseline after the corn stalks that represented the wood frame, which is wider and drier than any corn stalk. The signal magnitude was below the baseline when the wood frame passed the sensor. The dielectric of the wood would have to be lower than the dielectric constant of the ambient air for this to occur. The dry air dielectric constant is 1.0005 ($\varepsilon_{vacuum} = 1$). However, the ambient air is a mixture of dry air and water vapor. The baseline represents the ambient air dielectric constant, which changes with psychrometric properties. Any material with a lower dielectric constant than ambient air will generate a signal below the baseline. If stalks have a dielectric constant close to that of ambient air, it will be difficult for the sensor to discriminate between a corn stalk and air. However, as previously discussed, a stalk with a dielectric constant lower than that of ambient air is unlikely to exist under field conditions.

Tests performed at two different speeds on the same day are presented in Figure 55. The two signal patterns were similar; but the signal strength was somewhat different. For example, the peak-to-peak magnitude of the ninth stalk was 0.88 V and 1.36 V at the fast and slow speeds, respectively. However, the signal pattern from a test conducted at higher stalk moisture content (Figure 54) differs considerably from the signal pattern from a test conducted at lower stalk moisture content (Figure 55). The higher stalk moisture content was conducted in August and the lower stalk moisture content was conducted after the stalks were allowed to air dry for one month. In the earlier,

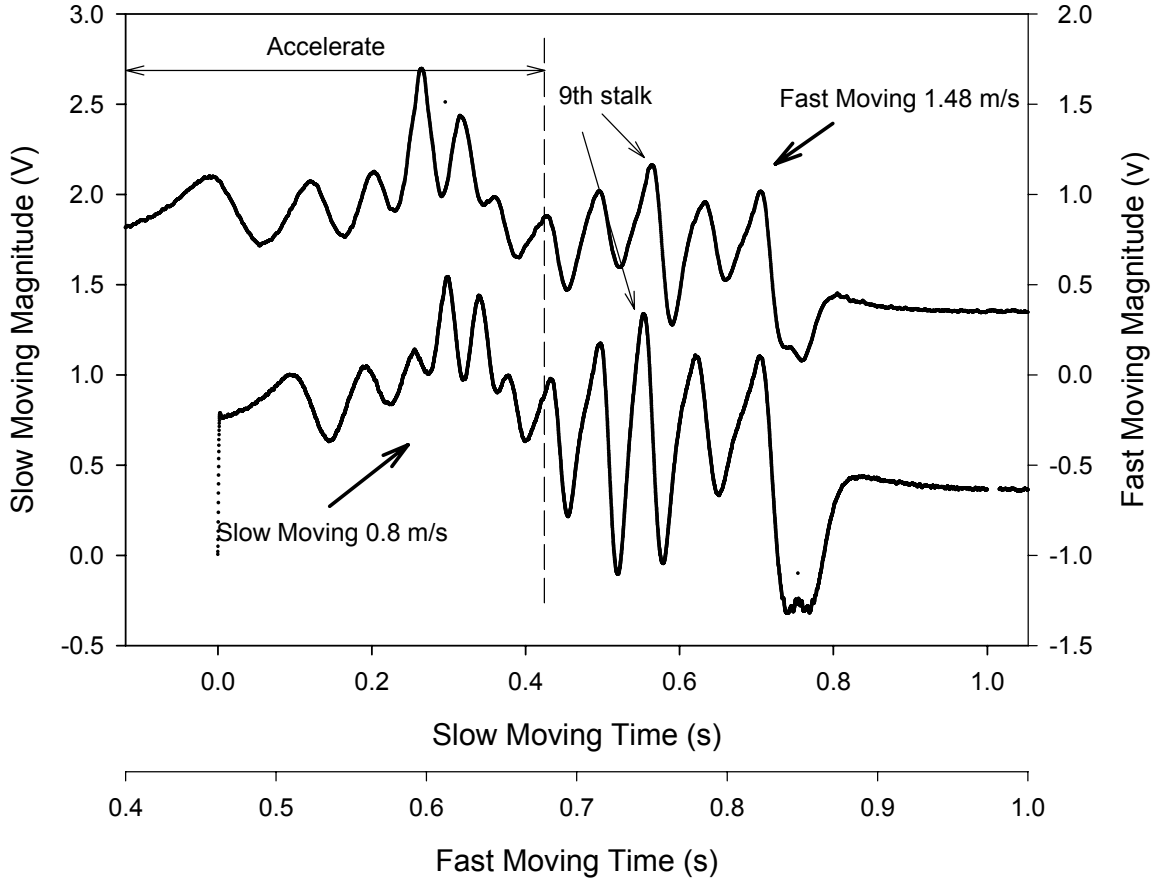

Figure 55. Signal pattern comparison between 0.8 m/s and 1.48 m/s test speeds (last test, second dynamic fixture)

wetter test, the sensor output did not fall back to the baseline level until all the specimens had passed the sensor. However, in the later, drier test, the sensor output crossed below the baseline level after the passage of some specimens. This phenomenon was likely due to the electronic dynamics of the sensor system. At higher moisture contents, the high signal strength prevented the sensor output from returning to baseline levels. For drier stalks the sensor output had sufficient time between stalks to return to baseline levels and

the electronic dynamics of the sensor was capable of driving the sensor output below the baseline levels before the next stalk forced the output to recover.

Chapter Summary

The final sensor circuitry design used a Wien Bridge oscillator, a PLL, and an OPAMP to transform a very small change in detection element capacitance to an output voltage change. While the Pspice model was useful in concept, the modeled results did not agree well with the experimental results. The Pspice model did not accurately represent the physical circuit due to the significant impact of parasitic capacitance. However, experimental development of the sensor circuitry was successful.

Based on the laboratory evaluations, the sensor and data acquisition systems met the design requirements:

1. The sensor system effectively transformed the capacitance variation to a voltage signal.
2. The base capacitance of the sensor was 1.3 pF and the change due to the presence of a stalk was less than 1% of the base capacitance. The circuit sensitivity proved sufficient to detect the presence of corn stalks with a wide range of moisture contents (approximately 10%-85%).
3. SNR was acceptable and typically exceeded 10.
4. The dynamic response of the sensor circuits was sufficient to detect capacitance changes in the detection elements and the dynamic response of the sensor system

was sufficient to discriminate between adjacent stalks spaced 7.5 cm apart over a wide range of stalk moisture contents (approximately 10%-85%).

CHAPTER 6 – PRELIMINARY FIELD TEST

Both the static and dynamic tests showed that the sensor was able to detect the corn stalks in a laboratory environment. A field evaluation was necessary to ensure the sensor has a similar performance in a production environment. Before a final field test was conducted, a preliminary field test was used to investigate some critical factors that could potentially affect the success of the final field test: stalk moisture content, physical sensor mounting, efficacy of the data acquisition system, signal pattern, and sensor efficacy. Without a full understanding of these factors, the final field test could be a partial or complete failure. The pitfalls found in the preliminary test were used to improve the sensor in the laboratory before the final test.

The purpose of the preliminary field test was to:

1. Design, assemble, and test the sensor mount and sensor housing
2. Investigate the moisture content distributions across adjacent stalks
3. Test the sensor and data acquisition system under realistic harvesting conditions
4. Perform simple analysis of the collected signals and improve the sensor as necessary

Sensor Enclosure and Mounting Design

Sensor enclosure is important for mounting and protecting the sensor in a realistic production field test. An effective sensor housing system assures the sensor will survive in the mechanically violent harvesting environment without interfering with the function of the sensor and prevent damage from environmental exposure (i.e. wind, rain, dirt, UV, etc.). An effective sensor mount will maintain a fixed position and protect the housing from physical damage from the effects of normal mechanic impacts during harvest (corn stalks, weeds). The sensor could be struck more than 10 times per second by both corn stalks and weeds. A sensor without protection will collect a tremendous amount of dust in a short time, which could affect circuitry performance and change sensor capacitance properties.

The correct selection of sensor housing material was critical to maintain optimum performance while still protecting the sensor. An electromagnetically transparent material was required. Any metal material would shield the sensor from the corn stalk's influence. Therefore, only non-metalic materials were considered. However, most non-metallic candidates with good electromagnetic permeability were rejected because of their low structural rigidity. Glass-reinforced polystyrene (fiberglass) was selected since it exhibits both acceptable mechanical and electrical properties. Other research showed that fiberglass has been widely used for radar enclosures (Moorehouse and Bradish 2006). This fact reinforced the decision to choose fiberglass for the sensor housing.

Several factors (e.g. fiberglass effect, air gap effect, and sensor mount material effect) needed to be tested in the laboratory to minimize the impact of the housing on

sensor function. An air gap was left between the sensor surface and the fiberglass housing to prevent direct contact between the sensor and the housing and minimize the transmission of mechanical impacts from the housing to the sensor. However, this gap increased the sensor-to-stalk distance and needed to be minimized. A minimum gap of 2 mm was selected as the best balance between sensor function and protection, resulting in a 5.3 mm increase in the sensor-stalk distance (including 3.3 mm fiberglass thickness).

The static test fixture was used to evaluate potential impacts of the fiberglass housing and air gap on sensor behavior. The sensor was attached to the fixture with and without the housing and a rubber rod with a dielectric constant of 8 was used to test the impact of the enclosure. The sensor-stalk distance was set at 2 cm from the detection element surface without the housing and the sensor-stalk distance was set at 2 cm from the surface of the fiberglass housing with the housing in place. The absolute signal magnitude was approximately 1.3 V without the housing and 1.5V with the housing in place. The 200 mV reduction was significant but did not excessively degrade the ability of the sensor to detect stalks. Therefore, glass-fiber reinforced polystyrene was used to fabricate the sensor housing and the detection element was positioned 2 mm from the inside surface of the housing.

The sensor mount was designed to attach the sensor housing to the irregular surface of the corn header, guide the stalks close to the sensor housing, and help protect the sensor system from mechanical impacts. The mounting fixture consisted of two parts with one part mounted on each side of the row. One side of the fixture provided sensor mounting and the other side helped guide the corn stalks and push them closer to the

sensor surface to reduce sensor-stalk distance and increase the signal strength. The main challenges of the mount design were to avoid knocking down stalks and causing the corn header to clog during harvest. A streamlined shape was used to minimize stalk knock-down and clogging. A triangular metal wedge on the sensor mount was used to protect the housing from direct stalk impact. The initial design concept is shown in Figure 56.

The materials for sensor mount needed to be selected carefully. From a purely mechanical point of view, steel was the ideal material since it is strong, rigid, low cost, and simple to fabricate. However, metallic materials could impact the sensor performance. The need to investigate the potential influence of steel on sensor performance was compounded by the fact that the sensor would be mounted in close proximity to steel components of the corn header. The second dynamic test fixture was used to test the influence of steel on the sensor. A steel plate with area of 50 cm × 50 cm was attached to the back of the sensor housing. When the test stalks were placed in front of the sensor, no measurable difference was observed in the sensor output with and without the steel plate attached to the back of the sensor housing. Therefore, the sensor mount was fabricated from steel.

The sensor housing and mounting hardware installed on the corn header and field-tested over a three-hour harvesting period. After harvesting, the sensor produced stable signals and the sensor housing showed no noticeable wear. From direct observation and video replay, it was found that corn stalks could pass the sensor mount smoothly without any sensor-mount induced knock-down or clogging. The stalks also were gently pushed close to the sensor surface by the stalk guide. Therefore both the sensor housing and

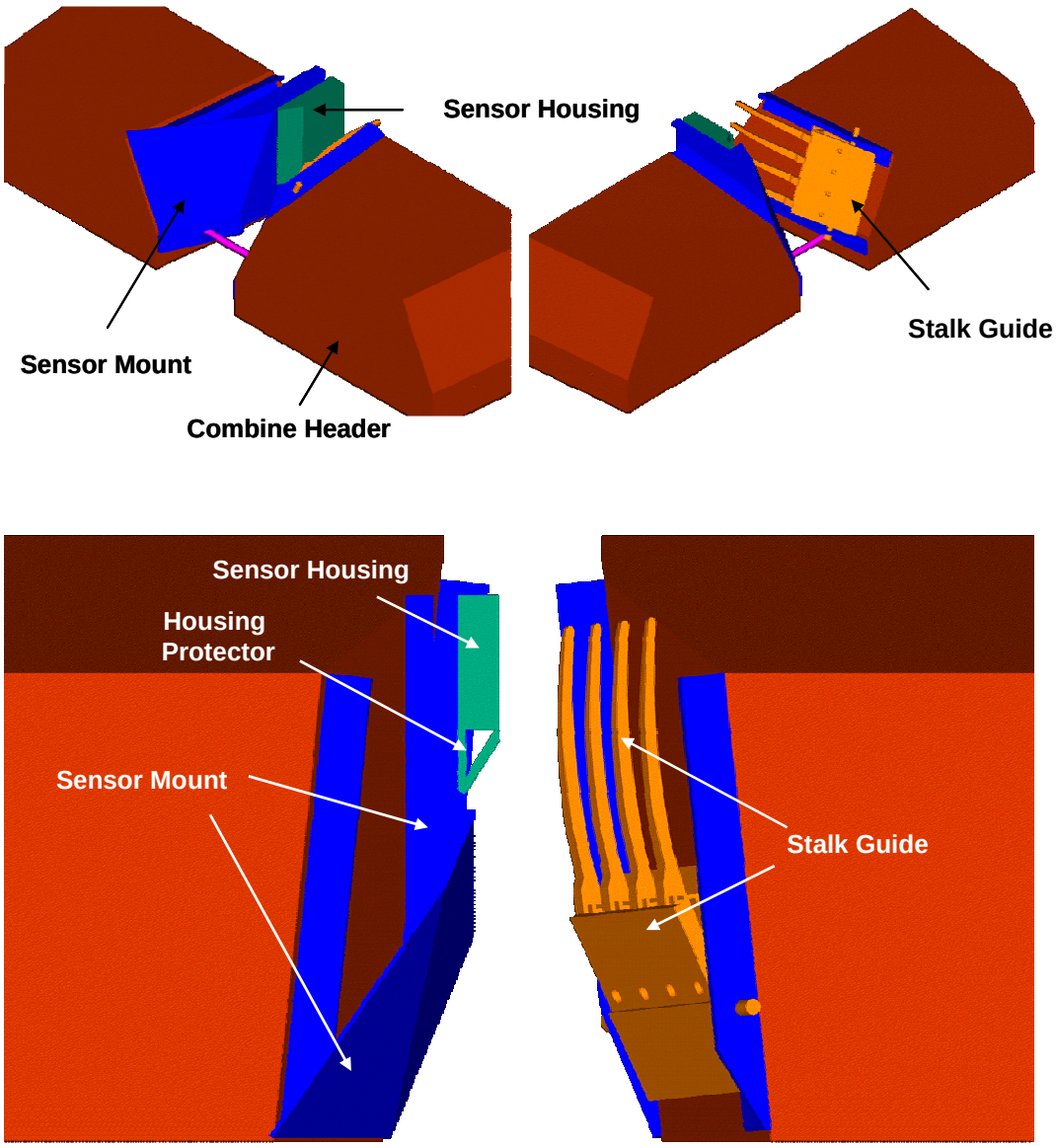

Figure 56. Sensor mounting fixture.

mount were found to be effective and no modifications were required before final field test.

Stalk Moisture Content Distribution

Knowledge of the actual stalk moisture content distribution pattern was important for the experimental design of the final field evaluation. , Stalk sample collection and the experiment design for the final field test could be simplified if moisture contents between two adjacent stalks were highly correlated. However, if the correlation was low, statistical considerations would be necessary for the experiment design of the final field test.

Three stalk rows were chosen to determine localized and field-wide stalk moisture content distributions. Observation of the visible condition of corn stalks in the field was used in an attempt to select three stalk rows representative of low, medium, and high stalk moisture content. Ten successive stalks were cut from each stalk row and samples approximately 20 cm in length were cut from the stalks approximately 75 cm above the stalk root. The stalk samples were marked and transported to the laboratory in sealed plastic bags where the wet-basis stalk moisture content was determined.

The moisture content of the three sample rows is shown in Figure 57. Row 2 was very dry (average moisture content was 9.3%) with a coefficient of variability of 9.5%. Row 3 was fairly wet (average moisture content was 65%) and had a coefficient of variability of 13%. Row 1 had a large variation in moisture content, with an average moisture content of 42% and a coefficient of variability of 57%. The variability in stalk

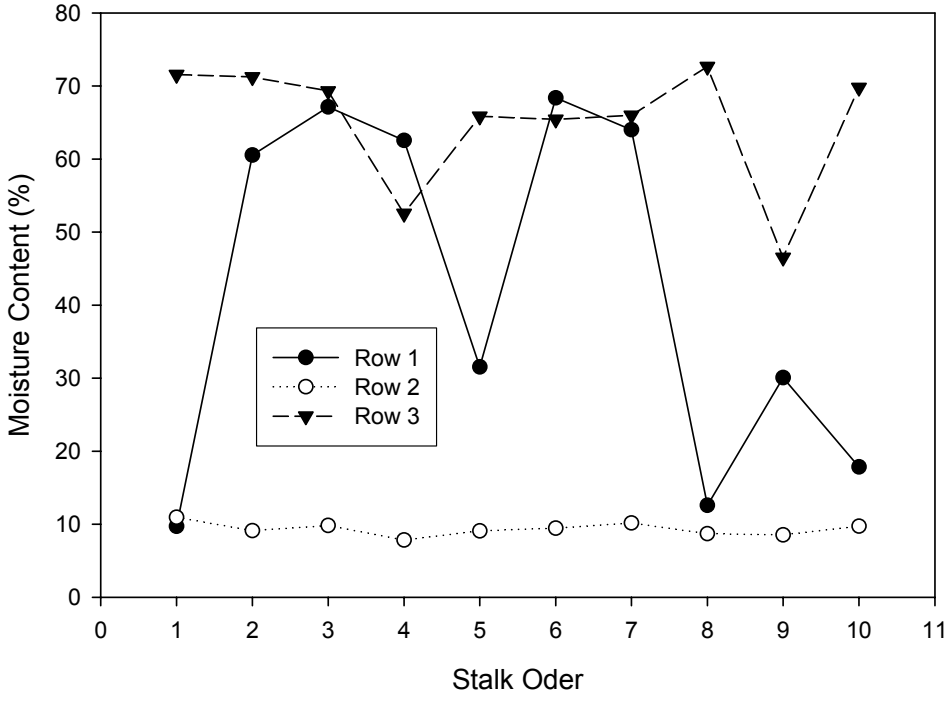

Figure 57. Stalk moisture content relationship among continuous stalks

moisture content indicated that the moisture content of an individual stalk could not be predicted based on the moisture content of adjacent stalks. The results also suggested a larger sample would be needed for the final field test and more sentinel stalk samples would be needed for correct moisture content representation.

Preliminary Field Test Procedures

The preliminary field test was performed at the Milan Experimental Station, Milan, Tennessee on September 14, 2006. A Case-IH 2344 combine with an attached Case-IH 1063 6-row corn header was used. The sensor was mounted in the far right harvest row (as viewed from the operator's station). A 12-bit DAQ (National Instrument, USB-6008) was connected to the sensor output and was controlled by a laptop PC in the

combine cab. One multi-conductor shielded cable (~ 4 m) was used to supply power to the sensor system and connect the sensor system output to the DAQ and a three-meter USB cable was used to connect the DAQ to the laptop PC. The DAQ sampling rate was set at 10KS/s and the input range was ± 5 V. A LabVIEW program was developed to record and store sensor output waveforms (voltage magnitude vs. time).

The sensor system was tested by harvesting corn from production fields. During the test, 6 rows of corn stalks were selected. The number of corn stalks in each row was determined by hand counting before harvest. There were approximately 45 stalks in each row. Stalks that were very close to each other (inter-stalk gap < 8 cm) were marked with bright-colored paint that could be detected in video recordings of the harvesting process. The marked stalks were used to investigate the discrimination capability of the sensor and were also used as flags to correlate the hand count information to sensor output data.

Sensor System Evaluation and Results

By design, no anti-aliasing filter was used in the DAQ. During laboratory testing a digital oscilloscope with a 1.25 Gs/S sampling rate and a 100 MHz bandwidth was frequently used measure the sensor system output and the frequency content was routinely examined. None of these laboratory test indicated high frequency components that could be aliased when the sensor system was digitally sampled at a lower sampling rate. The DAQ output was also directly compared to oscilloscope measurements in the laboratory. Since no significant high frequency content was observed, the maximum sampling rate for the DAQ system (10 kHz) was selected for use in the field tests. In

addition, the stalk passage frequency was typically 10 Hz and not likely greater than 18 Hz. Therefore, the frequency range of interest is 0 to 20 Hz. Based on Nyquist theory, a 10 KHz sampling frequency can accurately represent frequencies from 0 to 5 KHz. The probability of an aliased frequency falling into the 0 to 20 Hz range is 1:250. By comparing the stalk and noise pattern in the low frequency range, it was found that the stalk-related signal was much stronger than noise at low frequencies (Figure 58). This means that even if the aliasing components from background noise fall into the frequency band of interested, the effect on stalk signals would likely be limited. Furthermore, the design is unlikely to produce high frequency signal components. First, the capacitive sensor was a slow response device; therefore the frequency output of the oscillator and the PLL output voltage changed slowly. Second, the PLL itself is a second order low pass filter that filters most high frequency components. The only probable source of high frequency signal content was environmental noise. The digital oscilloscope was also used during the preliminary field test and no high frequency signal content was observed. Therefore, the exclusion of an anti-aliasing filter was deemed an acceptable risk at this stage of the sensor system development, but should be included prior to commercialization. Signal shapes, signal magnitude, SNR, and signal overlay were investigated to evaluate the sensor system performance. Signals were visually inspected and signal peaks were counted to estimate the stalk count. The analyzed data and hand counted data were compared (Table 7). The data showed that the sensor system had potential for counting stalks. The estimated count and hand count were equal for two rows and the count error was no more than 2 stalks per sample row with the exception of

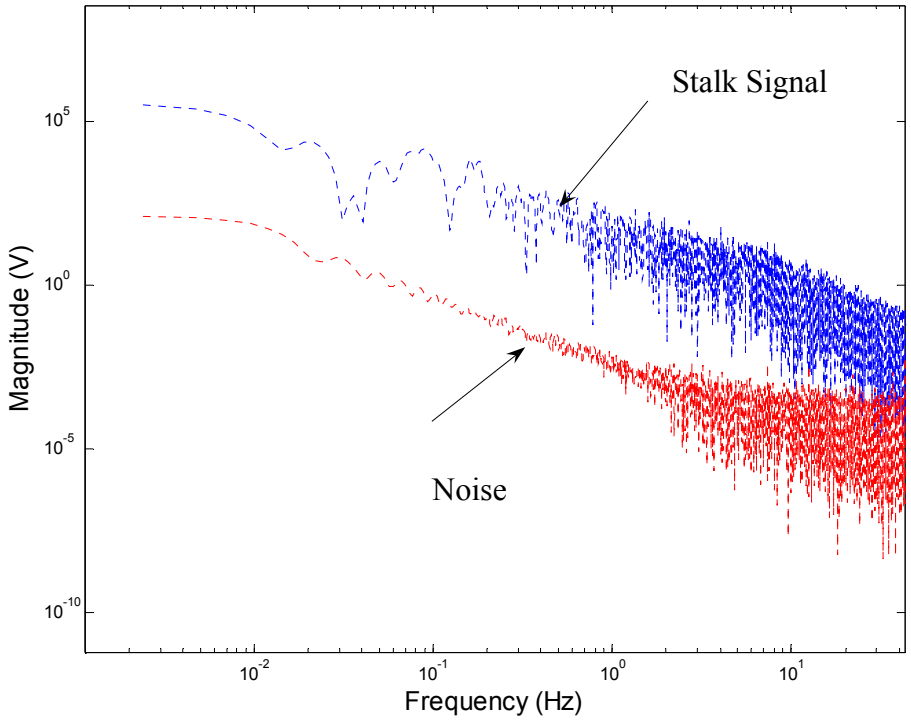

Figure 58. Stalk and noise pattern in frequency domain.

Table 7. Stalk hand count and sensor estimated count from the preliminary field test

	Row					
	1	2	3	4	5	6
Hand count	47	45	41	44	42	46
Count estimated from measured data	42	44	43	44	43	46
Error	-5	-1	+2	0	+1	0

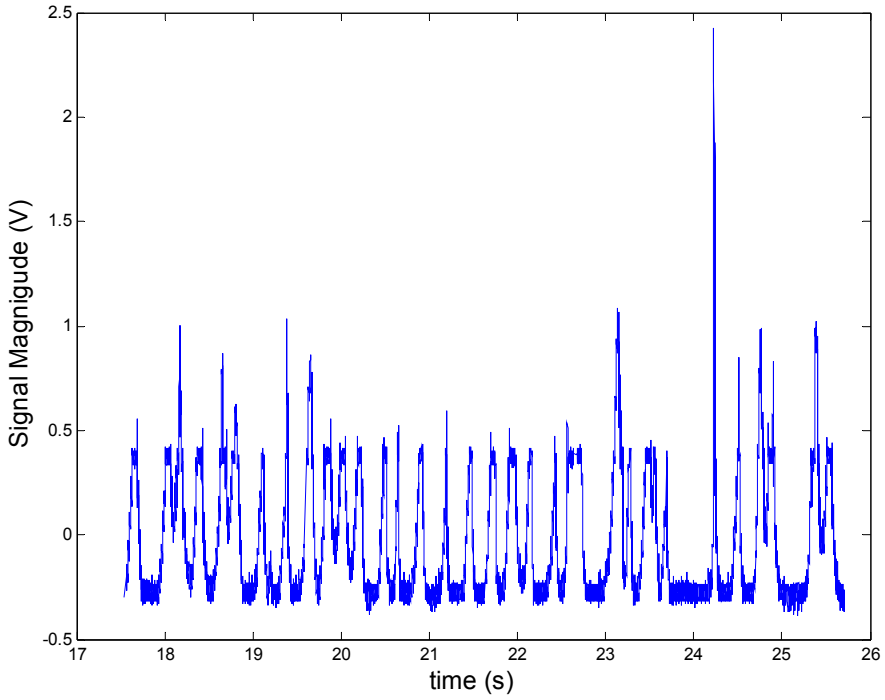

Figure 59. Typical sensor output signal from the preliminary field test

the first row, which had an error of 5 stalks. The number of stalks in each row was recorded, but not detailed information (e.g. individual location, stalk diameter, location of weeds, etc.) for each stalk. The most important result of this test was that it indicated the need to collect more detailed information about the test rows in the final field test.

A typical sensor output signal is presented in Figure 59. The peak-to-peak noise magnitude was approximately 70 mV. The average signal magnitude level was 650 mV. Therefore, the SNR in preliminary test was close to 10, which was very similar to that observed in the laboratory. Therefore, environmental noise in the field environment was not significantly different than observed in the laboratory.

Discrimination capability was investigated by examining the signal from closely-spaced stalks that were marked before harvest. The gap between these stalks was measured in the field at 6 cm, which was 25% less than minimum spacing tested in the laboratory. From the figure, the signal peaks corresponding to the two closely-spaced stalks can be easily identified through visual inspection.

A consistent signal shape would be helpful for signal processing and data classification. However, the signal shapes varied significantly (Figure 60). The second half of this graph (> 3.5 s) is much simpler than the first half. The stalk signal in the second half only had one peak for each stalk. However, each stalk in the first half had two peaks, one positive and one negative. The fact that two very different patterns can be produced by the sensor presents a much more difficult situation for pattern recognition. Laboratory analysis later found that the two different patterns was a result of a more complex capacitance pattern between the stalk and the two detection elements (Figure 61) than was originally considered during detection element development. This more complex interaction affected the function of the capacitive sensors (Figure 62). In theory, the two-detection element design theoretically should improve signal strength, but this was not always true in the field test.

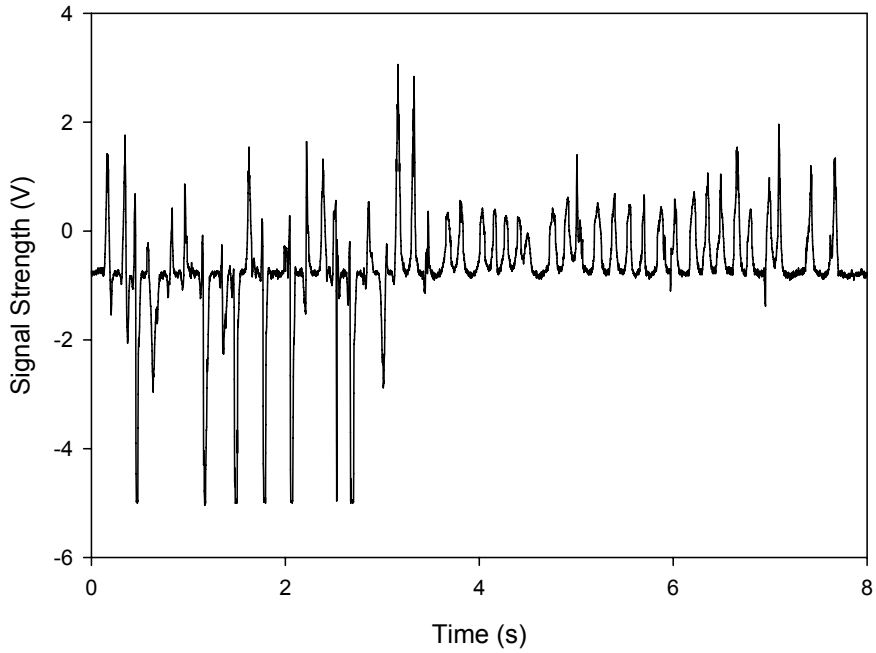

Figure 60. Example sensor output pattern from the preliminary test.

The capacitive interaction between a stalk and the detection element was simplified and the interaction between the two detection elements was eliminated by removing one of the detection elements and replacing it with a fixed value capacitor. By experimentally comparing the impacts of the two capacitors in the oscillator, C_1 and C_2, C_1 was found to be more sensitive to the presence of a stalk. Therefore, the C_2 was replaced by a fixed value capacitor of approximately 2 pF. The new single sensor pattern was tested in laboratory and the elimination of the "push-pull" phenomena that occurred in the preliminary field test was confirmed. However, the sensitivity did not show a significant change. This single-capacitor design was used for the final field evaluation (Figure 63 and Figure 64).

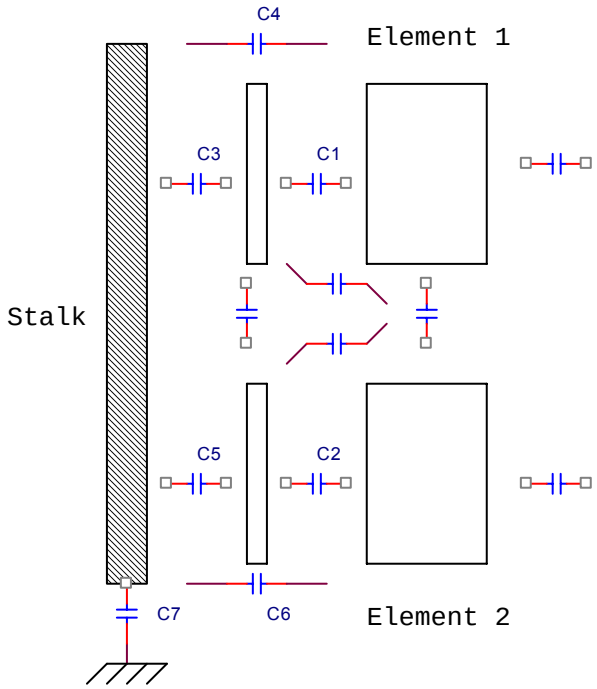

Figure 61. Physical representation of the more complex detection element interaction with corn stalk

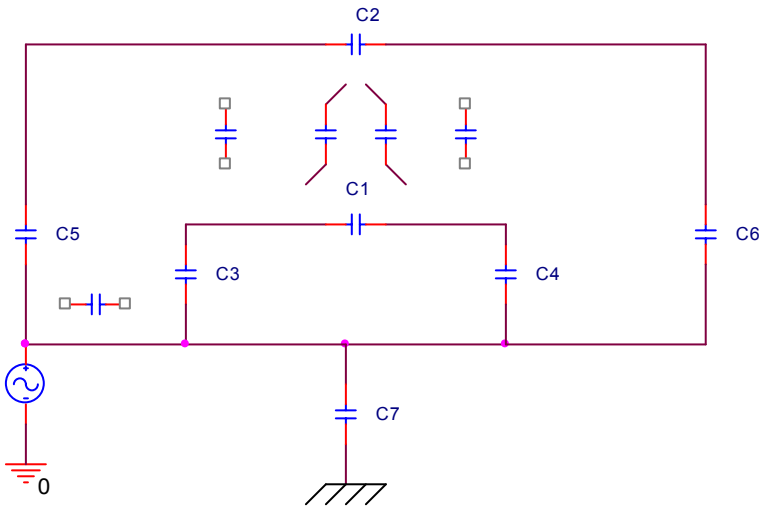

Figure 62. Equivalent circuit representation of the more complex detection element interaction with corn stalk

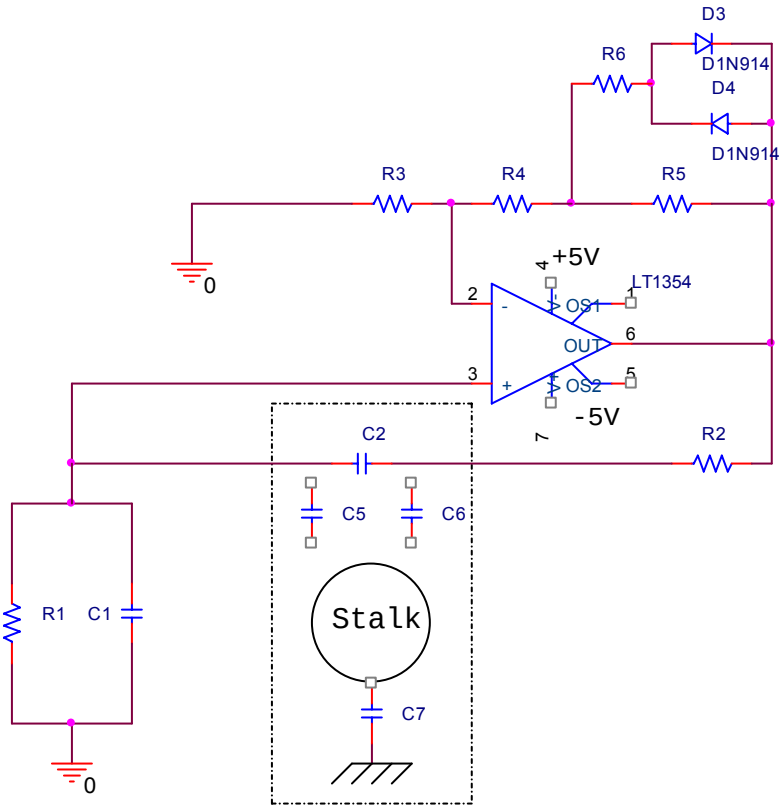

Figure 63. Circuit schematic of a Wien-Bridge oscillator with the final detection element configuration and corn stalk.

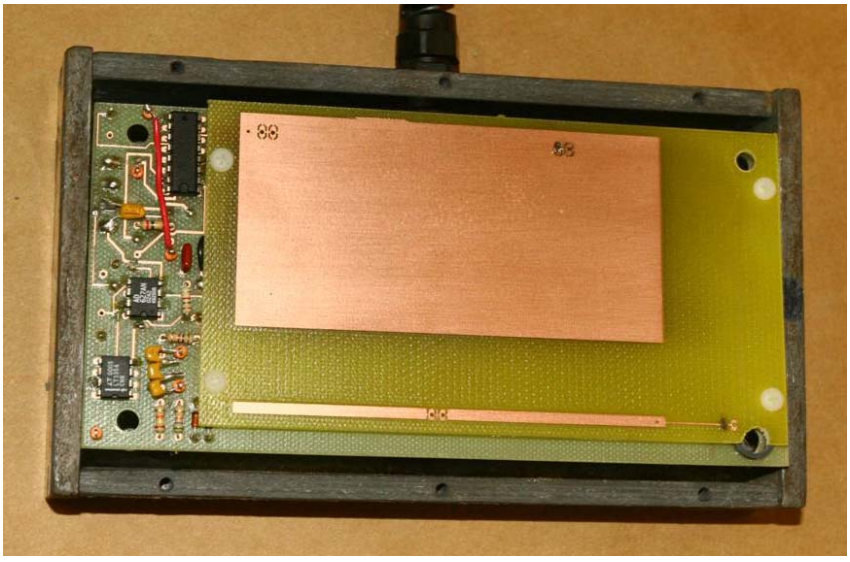

Figure 64. Photograph of the sensor used for the final field test.

Chapter Summary

The fiberglass sensor housing had little effect on the sensor output but protected the sensor components against damage from both mechanical impacts and environmental factors with no noticeable impact on performance. The sensor mount effectively attached the sensor housing to the combine header and protected the sensor housing from mechanical impacts. No stalk knock-down or clogging was observed during harvest operations.

The measured stalk moisture content distribution in the field indicated that stalk moisture content, between adjacent stalks and across the entire field, varied significantly. The moisture content of one stalk could not be used to predict the moisture content of adjacent stalks. Therefore, a larger sample size was needed to represent the wide range in moisture content during the final field test.

The data acquisition system effectively collected and stored the sensor output with a SNR of approximately 10. This SNR proved that both the sensor system and data acquisition system were effective in the production environment. No high frequency signal components that could be aliased into the frequency range of interest (0-20 Hz) were observed.

The sensor efficacy was tested by comparing the stalk count estimated from the collected data to hand counts. The small errors between these counts indicated that the sensor could effectively be used to count stalks. However, the more significant finding was that more detailed information needed to be collected in the final field test to enable a better correlation analysis between sensor output and stalks in the field.

One significant problem was identified. The recorded sensor output showed two different sensor output patterns could be produced (Figure 60). The potentially negative impact on later stalk pattern classification was identified and sensor system modifications were implemented to correct this problem. The modification was tested in the laboratory and the elimination of the problematic behavior was confirmed. As a result, one of the detection elements in the oscillator circuit was replaced by a fixed-value capacitor to produce the final sensor system design which was used during the final field test.

CHAPTER 7 – FINAL FIELD EVALUATION

The final field evaluation was conducted at the Milan Experiment Station, Milan, Tennessee on October 11 and 12, 2006. The combine, corn header, sensor mount, sensor housing, and DAQ system were the same as those used in the preliminary test. The sensor was modified as noted in chapter 6.

Noise Investigations

Three potential noise sources were investigated: environmental noise, presence of weeds, and corn leaves. Background noise could be caused by mechanical effects, electromagnetic interference, or environmental conditions. Three control tests (background noise test, weeds test, and leaves test) were developed to investigate these effects. The speed for these control tests was at 0.9 m/s (2 mph). The environmental effects were investigated by monitoring the sensor behavior during the entire test process to identify longer-term variations in sensor behavior that could be associated with changing weather conditions.

Background Noise and Signal Drift

The first control test was the background noise investigation. This test was performed with the combine running over previously harvested field areas. The sensor

was exposed to potential mechanical and electromagnetic noise sources in the absence of corn stalks or weeds to isolate the impact of background noise. Although background noise could likely include cyclic components, as a whole it can be treated as a random event. Therefore, a Gaussian distribution for the background noise could logically be assumed.

Representative raw and filtered background noise waveforms are presented in Figure 65. The peak-to-peak noise magnitude in the raw data was approximately 100 mV (SNR > 2). The application of a first order low pass Butterworth filter with a cutoff frequency at 80 Hz reduced the peak-to-peak noise magnitude to approximately 25 mV. In the preliminary field test, the signal strength of a dry stalk was typically greater than 200 mV, resulting in a SNR greater than 8 for the filtered acquired data. The similarity between the SNR of laboratory tests (SNR > 10) and field tests indicated that the noise environments of laboratory and field conditions are similar.

The same raw noise data was transformed to the frequency domain using a Fast Fourier Transform (FFT) (Figure 66). There was a weak peak around 200 Hz. The magnitude across the rest of the frequency spectrum was relatively constant. With the exception of the single peak, the assumed Gaussian distribution for the background noise is reasonable.

The sensor output was relatively stable over long periods of time when the psychrometric properties of the ambient air were relatively stable. However, when psychrometric parameters changed, the sensor signal base drifted. For example, a signal drift of approximately 90 mV occurred over a 60 second period during testing on October

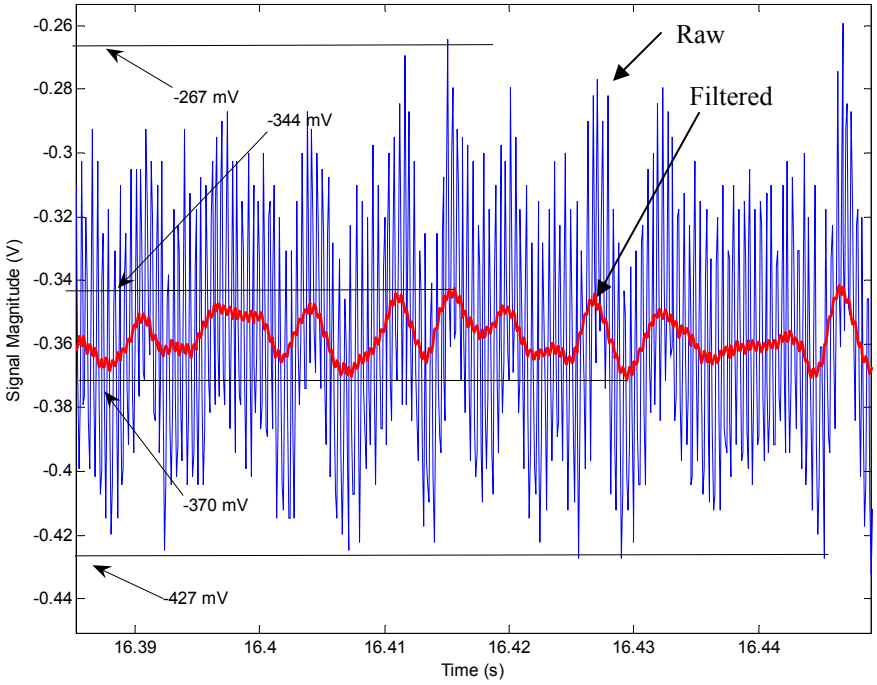

Figure 65. Typical raw and filtered background noise (time domain)

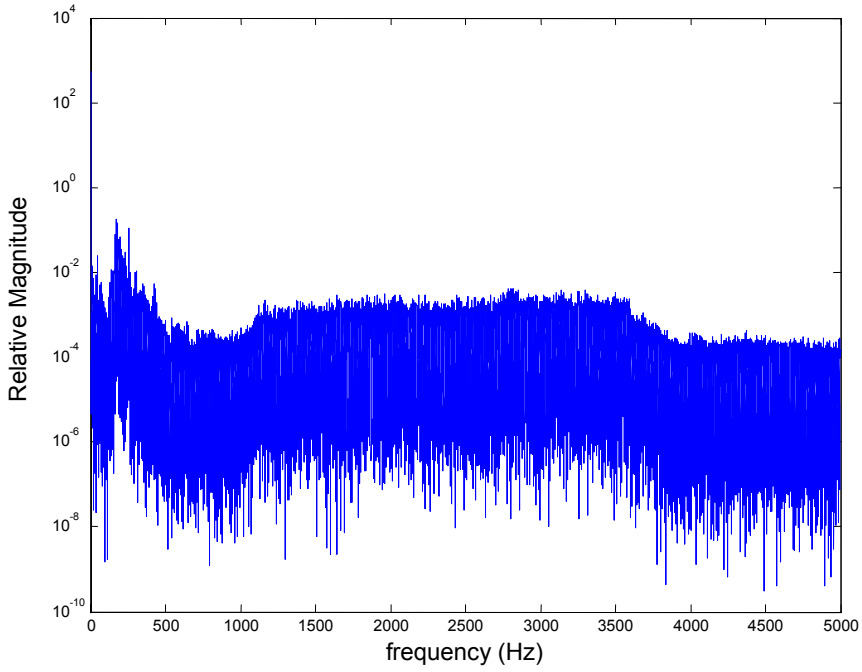

Figure 66. Typical raw background noise (frequency domain).

12. Humidity measurements during that same time period showed that relative humidity changed from 75% to 73% and the winds were gusty.

Comparison of the data collected on October 11 (dry and sunny, RH ≈ 50%) to that collected on October 12 (after a light shower, RH ≈ 75%) showed that a baseline shift of more than 1 V (10% change of full scale). The average temperatures for the two harvest days were similar (< 5 ºC difference) but there was a significant change in humidity. There was a similar change in sensor baseline from the evening of October 10 (when the sensor was installed and a function test performed) and the late-morning harvest on October 11. The relative humidity was not measured on October 10, but the presence of heavy dew when the sensor was installed indicated that the relative humidity was near saturation levels. It is logical to attribute the baseline drift to weather changes. This data confirms that the sensor is sensitive to psychrometric changes in the ambient air. However, with the exception of the weed effects testing, no evidence of sensor system saturation was observed during harvesting, which indicated the designed bandwidth of the oscillator and PLL were sufficient to maintain sensor system functionality over a broad range of ambient conditions.

Weed Effect Investigation

The second control test was a weed interference investigation. During this test, a field (identified as N26) with high-density sickle pod was chosen for the weed effect investigation. The mature sickle pod had a high moisture content relative to the dry corn stalks. The sickle pod was taller than 1.5 meters and 90% of the weed stalk diameters

were thicker than 0.5 cm. The weeds were dense enough to prevent a human from passing and are not representative of a modern production operation.

Corn stalks were carefully removed from two rows without changing the weed pattern and these rows were used to collect pure weed signal patterns. Both stalks and weeds were kept in their original states in four additional rows and these rows were used to determine if the sensor could discriminate stalks from weeds. Figure 67 and Figure 68 are representative of the filtered (80 Hz, first-order, Butterworth low-pass) time-domain sensor output collected from rows in which the corn stalks were removed before harvest and rows with both corn stalks and weeds, respectively. The moisture content of the weeds was high enough to saturate the sensor system from time to time, resulting in clipped signals as noted in both figures. No clear difference could be found between rows with and without stalks by comparing these two figures. Therefore, it is unlikely that the sensor system can discriminate corn stalks against a background of high-density, high-moisture weeds.

The time-domain signals were transformed into the frequency domain using an FFT (Figure 69) in an effort to identify differences between the signals produced by weeds with and without corn stalks. The two signals differ even less in the frequency domain. The stalk information was hidden inside weed noise and the SNR was too low to allow stalk detection.

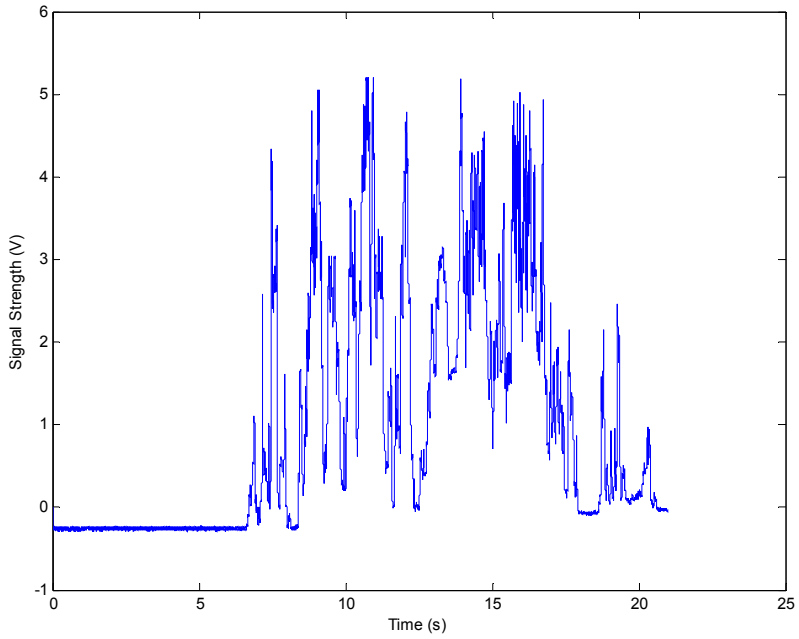

Figure 67. Typical filtered weeds-only sensor output

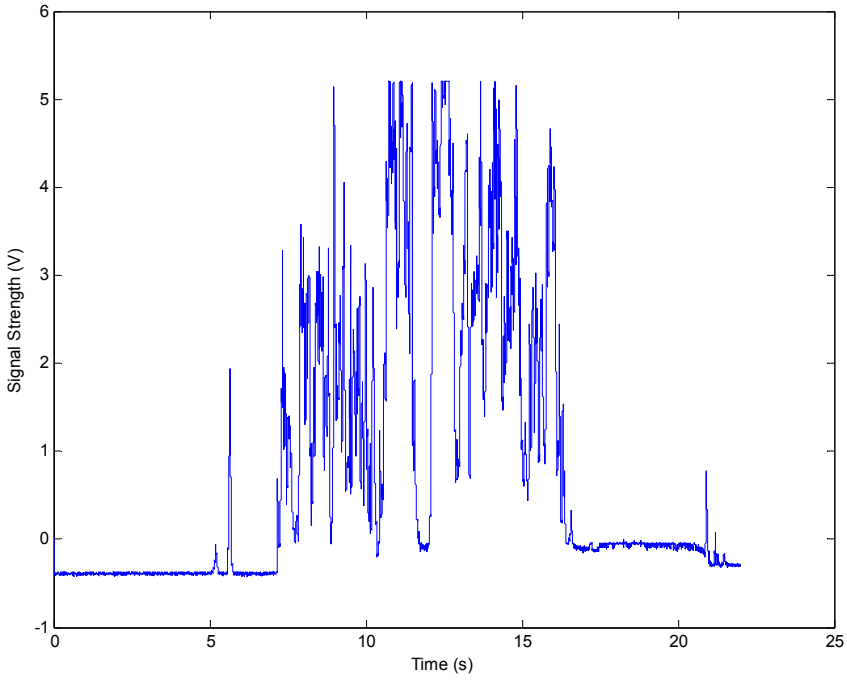

Figure 68. Typical filtered weeds-and-stalks sensor output

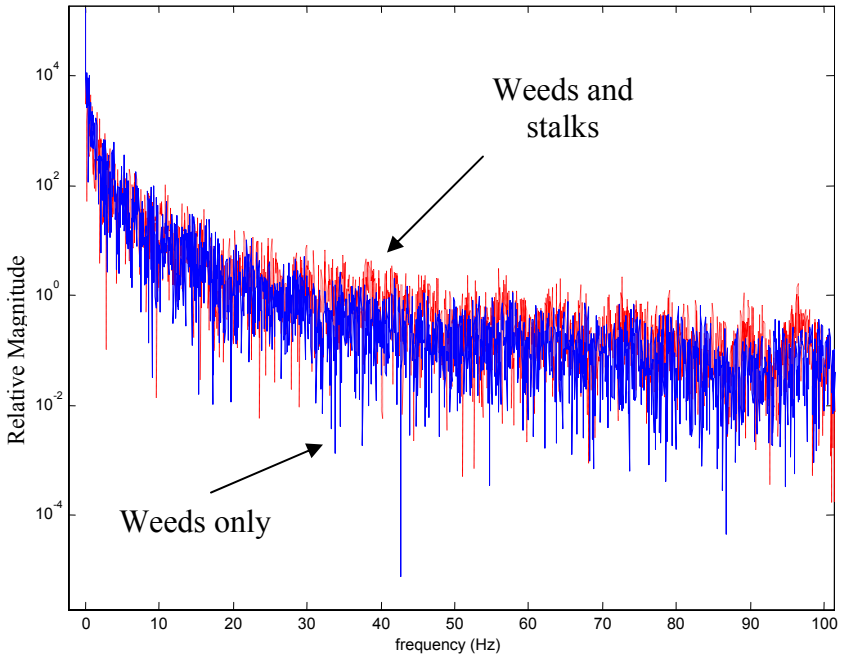

Figure 69. Comparison of weeds-only and weeds-and-stalks filtered sensor output (frequency domain)

The weed-only data was also compared with test data (dry stalk and low weeds) obtained in field A11 to identify differences in frequency content (Figure 70). The principal difference is in signal magnitude, particularly at lower frequencies. The sensor output from the weeds is significantly higher than that from corn stalks. The magnitude difference may be attributed to the high moisture content of the weeds, but the low frequency of the sensor output in response to weeds was not expected. The weed branches were small in diameter and very closely spaced, therefore, the passing frequency of the weeds should be much higher than that of the corn stalks and should result in a higher-frequency sensor output. However, the slow response of the detection element caused overlap in the sensor output when high moisture content stalks spaced 15 cm apart were tested in the laboratory. The closely-spaced high moisture weed branches

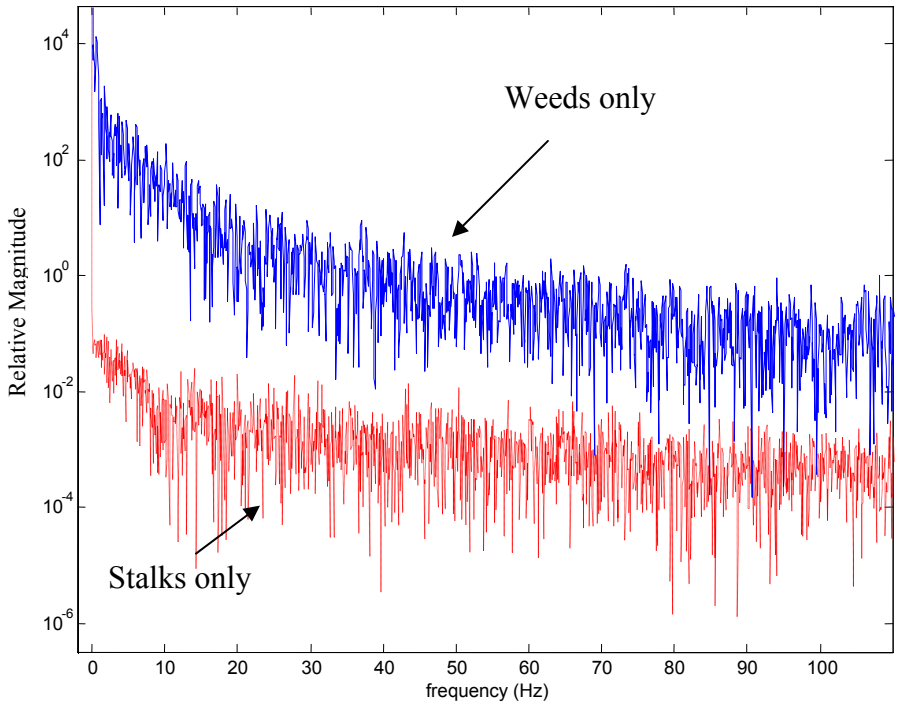

Figure 70. Comparison of weeds-only and stalks-only filtered sensor output (frequency domain)

could produce similar overlapping output signals, effectively masking the true frequency of weed passage. While stalks can not be detected against a heavy weed background, the very high-magnitude, low-frequency sensor output from the presence of heavy weeds may provide a means of identifying areas of high weed density. This information could be used to prevent inaccurate prediction of stalk counts in low weed density areas by segregating data from high-weed areas and could be used to flag these areas as an aid in improving weed management.

Impact of Corn Leaves on Sensor Accuracy

The third control group was used to investigate the effect of corn leaves on stalk discrimination. A long row was chosen for this test where ten adjacent stalks were removed and ten left in place to obtain a series of ten-stalk sample rows. The gap between two rows was the length of 10 stalks that were removed. A total of eight 10-stalk sample rows were prepared for a total length of approximately 25 meters. The leaves, ears, and weeds were removed in every other sample row, leaving half the sample rows in the original field condition. The signal from the modified stalk rows was generated purely by corn stalks and the signals from the unmodified rows were used as a basis for comparison to investigate the effect of leaves on the senor output.

The filtered (80 Hz, first-order, Butterworth low-pass) sensor outputs for stalks with and without leaves are presented in Figure 71 and Figure 72, respectively. Figure 72 (without leaves) shows a very clean signal pattern from the stalks, as expected. In Figure 71 there are some ripples in the signal (indicated by arrows), which could be from leaves. Data from two other adjacent sample rows, one with leaves and one without, are presented in Figure 73. In this figure, the sample row without leaves showed a more complex signal pattern than sample row with leaves. The same dataset was analyzed in the frequency domain (Figure 74) and no significant pattern difference was found. The unexpected pattern may be due to variability in stalk moisture content and sensor-stalk distance, since these two factors may dominate the effect of leaves. While the leaves may have some effect on the signal, in most conditions the impact of leaves are not likely to dominate the influence of stalk moisture and sensor-stalk distance.

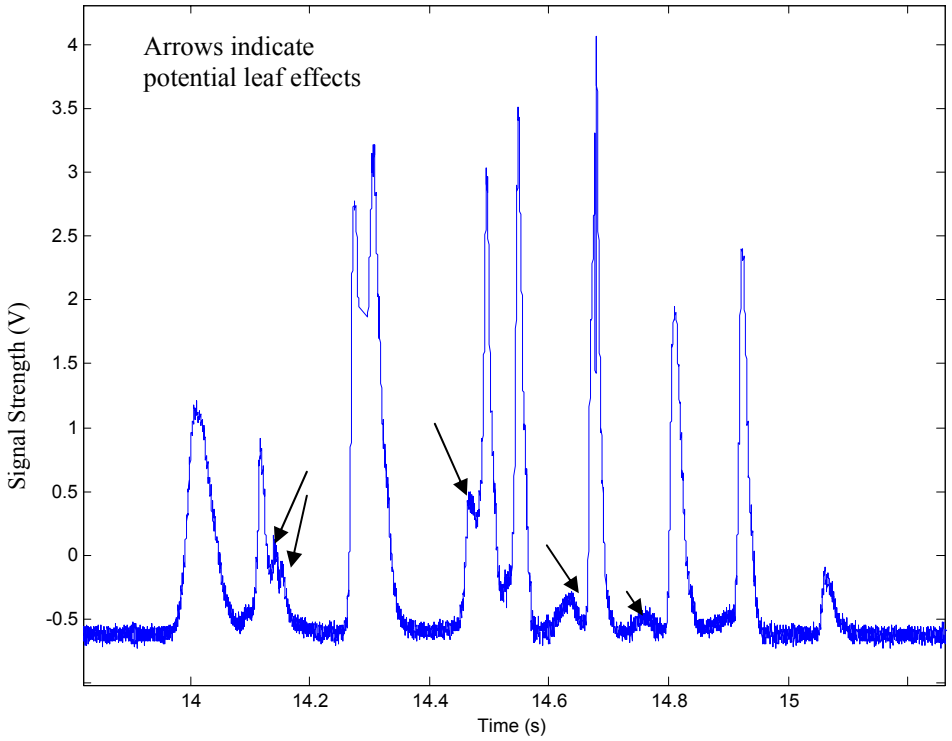

Figure 71. Filtered sensor output from stalks with leaves (time domain)

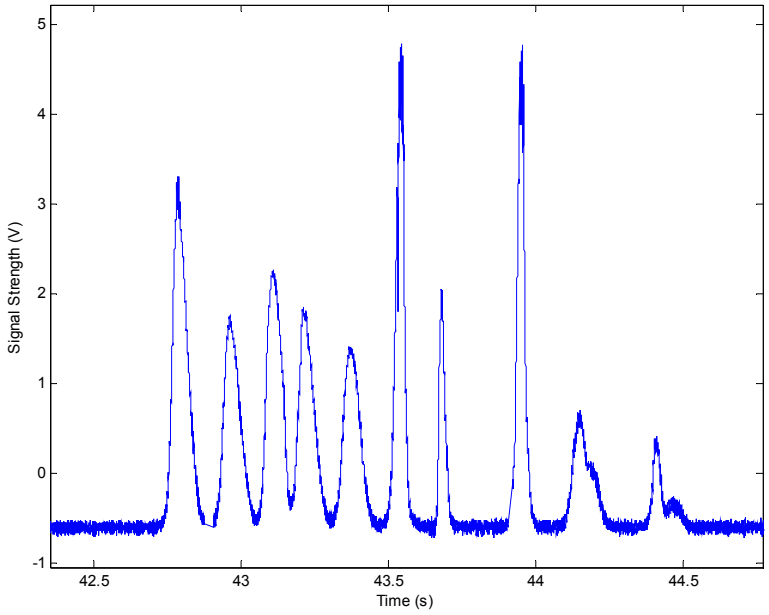

Figure 72. Filtered sensor output from stalks without leaves (time domain)

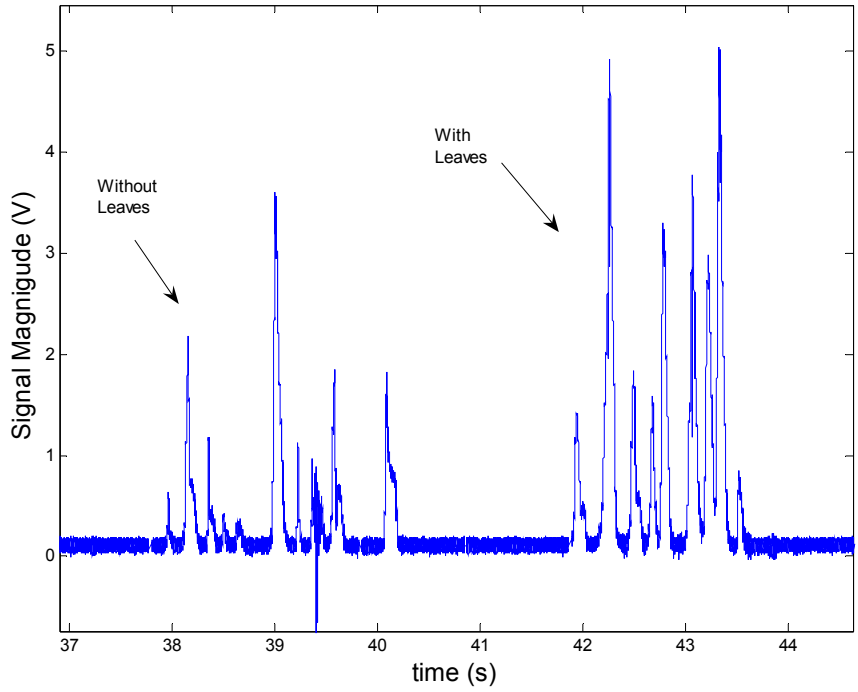

Figure 73. Filtered sensor output from stalks with and without leaves (time domain)

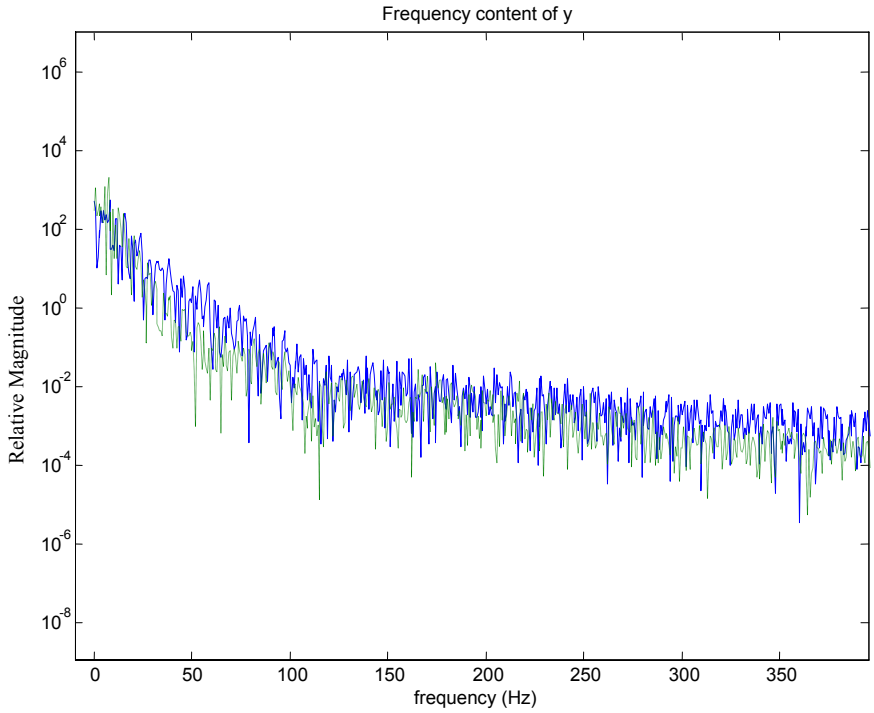

Figure 74. Filtered sensor output from stalks with and without leaves (frequency domain)

Ear Effects

One impact on sensor output not considered prior to the final field test was observed during the final testing: the effect of corn ears. An ear of corn typically has a higher mass and moisture content than stalks. The sensor output may be affected significantly if an ear passes by the sensor. The wide, relatively high magnitude signal block in Figure 75 resulted from the presence of an ear. This phenomenon was only observed once during three hours of harvesting. An ear was observed on video being rolled around in front of the sensor by the gathering chains on the header while the combine was in the gap between two subsamples (i.e., no stalks passing through the headers). Once harvesting of the next subsample began, the ear was pushed away from

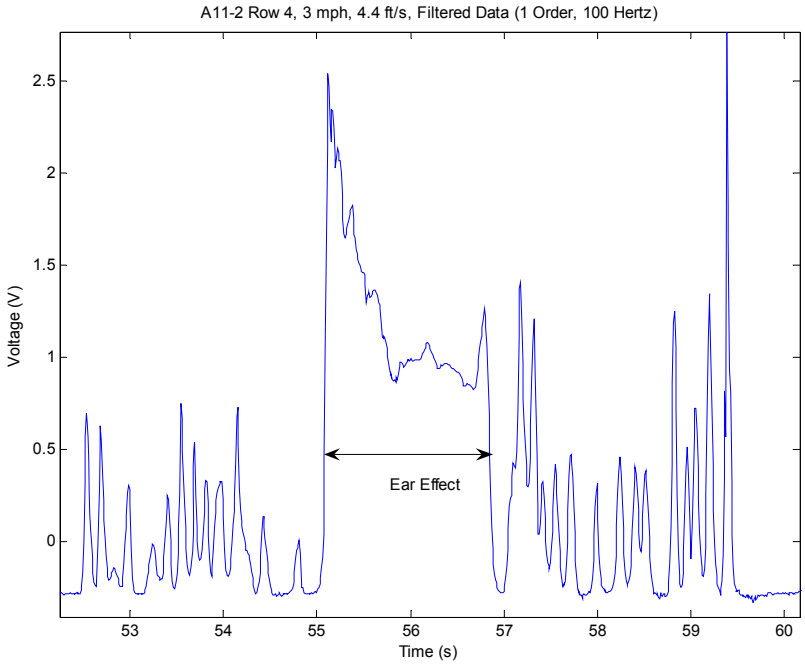

Figure 75. Possible ear effect on signal pattern

the sensor and the sensor output returned to a more typical pattern. While the impact of an ear is considerable, the rarity of this event should have a minimal impact on stalk count.

Sensor System Performance

Stalk moisture content and sensor-stalk distance were the two most important factors that could potentially affect sensor performance. The sensor-stalk distance was stochastic during harvesting and could not be controlled or measured. However, the moisture content was roughly related to psychrometric history of the ambient air and corn maturity. Psychrometric parameters, specifically temperature and absolute humidity, can increase or decrease stalk moisture content. Associated weather events such as rainfall and dew can also significantly affect stalk moisture content. Early-maturing stalks were prone to be drier than the later-maturing stalks. Because both psychrometric parameters and crop maturity are difficult to control, a combination of time (psychrometric parameters) and fields (maturity) were used to obtain different moisture contents.

The goal was to obtain three groups of stalks with different moisture contents representative relatively dry (< 20%), medium (~ 35%), and relatively wet (> 60%) stalk moisture contents. Two corn fields with different planting times and three harvest times were used. The early-planting field (identified as A11) was very dry and the late-planting field (identified as A22) still had relatively high moisture stalks. The early-planting field was harvested at two different times. The first harvest occurred in the afternoon

following a period of several days of relatively dry weather conditions and the second harvest was conducted in the morning following a light rainfall event the previous night.

The randomized split plots with replication method was used for this experiment design. The combination of three harvest times and two different fields were used as three treatment blocks in the experimental design. In each time-field block, corn was harvested at three speeds (0.9 m/s, 1.1 m/s, and 1.34 m/s). Each sample unit was repeated twice at each harvest speed in each time-field block. Each unit had 6 subsamples of 31 stalks.

Each subsample (Figure 76) was a row-segment of approximately 9.1 m (30 feet) and had more than 32 stalks. The subsample row was counted 15 stalks from each end towards mid point (approximately 3 meters). The two stalks nearest the center of the space between the two sets of 15 stalks were not cut. All other stalks in this area were cut to create gaps between the "sentinel" stalks and the two sets 15-stalk adjacent rows. One of these two stalks was randomly selected, cut just prior to harvest, and sampled for moisture content using the same procedure as the preliminary test. The remaining stalk was painted with bright-colored marking paint to facilitate recovery immediately following harvesting. A similar MC specimen was taken from the painted stalk post-harvest. The sentinel stalks cut before and after harvesting were used to evaluate the moisture content relationship between two adjacent stalks and the field-wide moisture content distribution. The sentinel stalks cut after harvests were used to correlate moisture content to signal strength. The gaps between the sentinel stalks and the 15-stalk sets helped to identify the signal peak associated with the sentinel stalk.

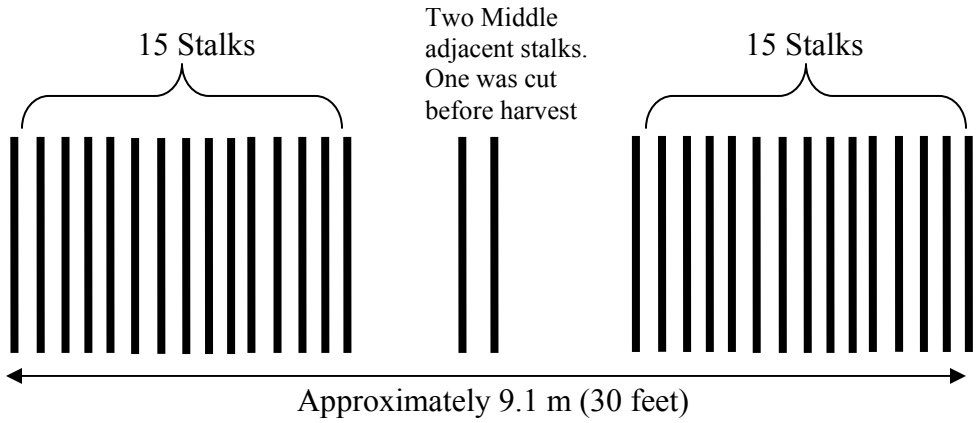

Figure 76. Final field test subsample schematic

The presence of weeds and location of each individual stalk in each subsample were recorded prior to harvesting. The location was measured by placing a measuring tape along the stalk row. Each stalk position was recorded to the nearest 0.1 foot (~ 3 cm). The diameter of stalks greater than 2.6 cm and less than 1.5 cm were measured using dial calipers and recorded.

Moisture Content and Signal Strength Relationship

The sentinel stalk moisture content was determined just prior to and after harvesting. The results were segregated by time-field block and compared to characterize the differences in the time-field blocks using a t-test. The moisture content difference between A11 (October 11 and October 12 harvests) and A22 were significant ($p << 0.0001$). The difference between the morning and afternoon tests in A11 was also significant ($p = 0.035$). The average moisture contents of the three groups were 22.3%, 34.1%, and 70.4% for A11 (October 11), A11 (October 12), and A22, respectively. In A22, 85% of stalks had moisture content greater than 60%. In A11 (October 11), 45% of

stalks had moisture content lower than 20% and 24% of stalks has moisture content lower than 15%. These results indicated that sensor data was collected over a representative stalk moisture content range.

The stalk moisture content data were also used to evaluate the difference in moisture content between adjacent stalks by calculating the difference between the pre- and post-harvest sentinel stalks. The distribution of this difference is shown in Figure 77. The results showed that the moisture content difference between two adjacent stalks could be greater than 60%. The correlation coefficient between the pre-harvest sentinel stalks and post-harvest sentinel stalks is 0.27. The stalk moisture content difference distribution and the correlation coefficient confirmed the finding from the preliminary field test that the moisture content of a stalk cannot be used to predict the moisture content of an adjacent stalk.

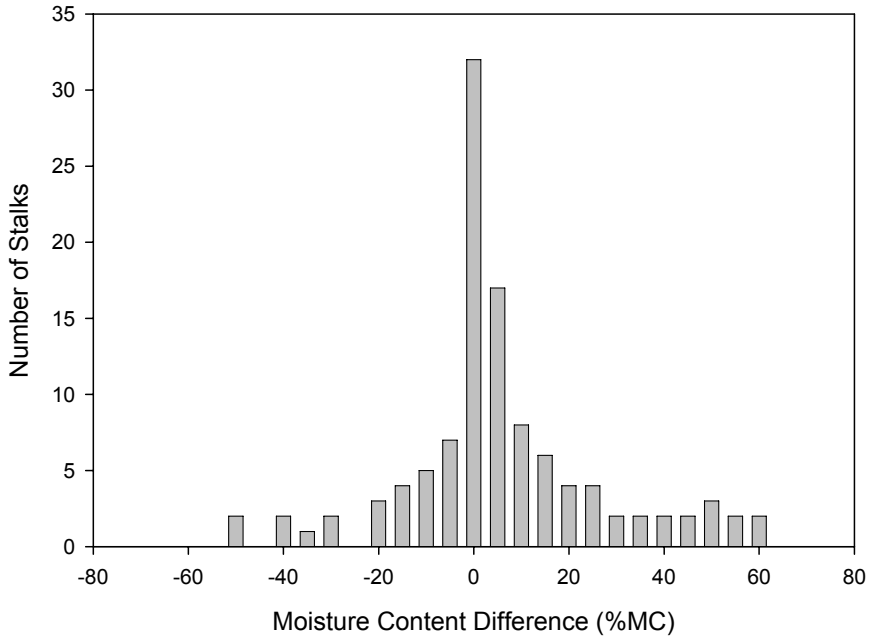

Figure 77. Distribution of stalk moisture content difference between sentinel stalk pairs

The post harvest sentinel stalks were also used to find the relationship between moisture content and signal strength. The signal peak generated by an example sentinel stalk is shown in Figure 78. The sentinel stalk signal was conspicuous because adjacent stalks were removed before harvesting. Therefore, the signal from the sentinel stalk can be easily identified and its strength could be compared to the measured moisture content. The signal strength was calculated as the absolute difference between peak and baseline sensor output. The moisture content and signal strength of each individual painted stalk were correlated using linear regression (Figure 79). R-squared for this model was 0.17, which is quite low. This means only 17% of the variation in the signal strength can be explained by the moisture content. Much of the remaining 83% of the variability is likely due to the strong relationship between signal strength and sensor-stalk distance (as determined in the laboratory) and the variability in the sensor-stalk distance during

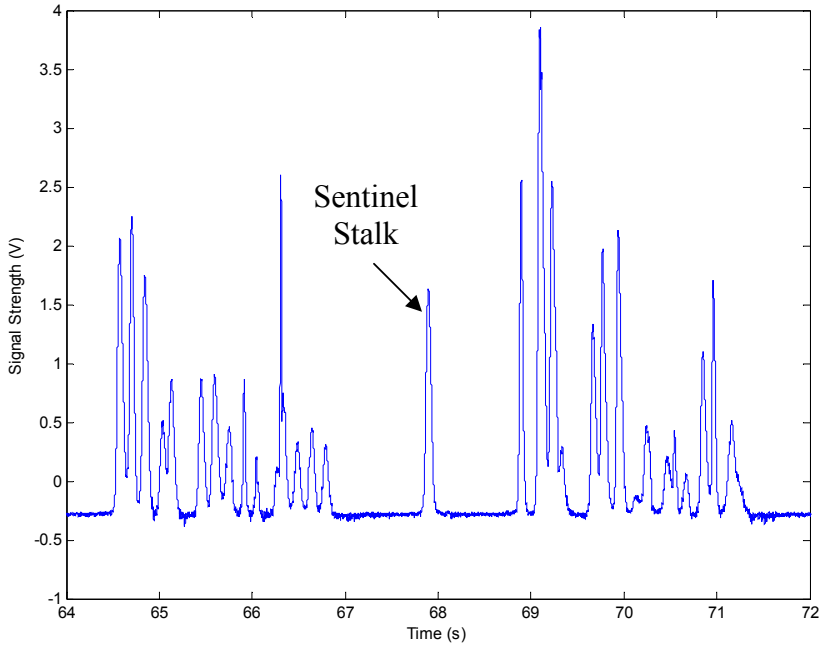

Figure 78. Processed data by first order Butterworth low pass filter with cut off frequency at 500 rad/sp

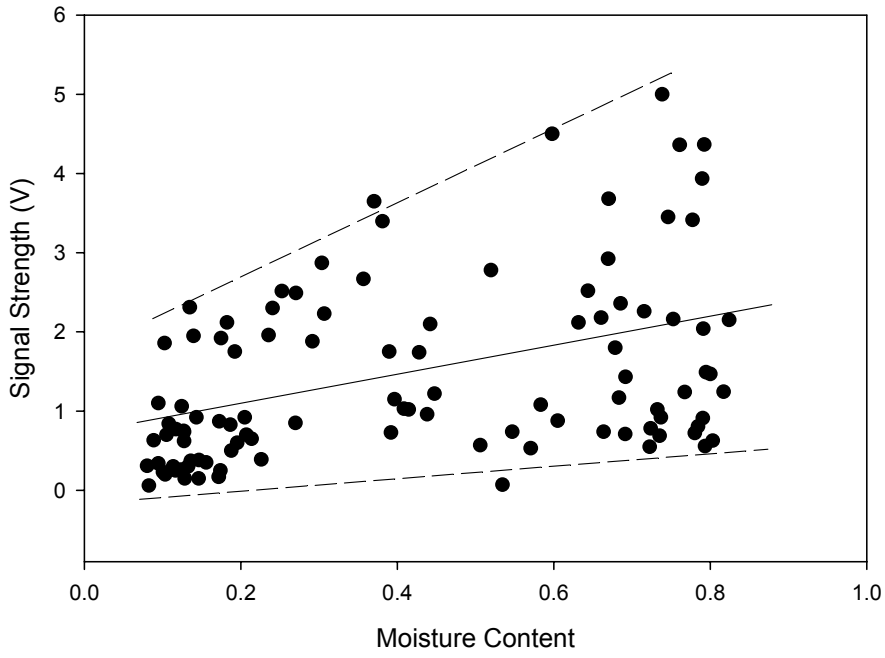

Figure 79. Moisture content and signal strength of sentinel stalks.

harvesting. If the sensor-stalk distance were controlled, the correlation model fit might improve dramatically. However, no valid model of the signal strength to stalk moisture content relationship can be built from the data collected during the final field test.

Chapter Summary

Background noise produced by electromagnetic, environmental and mechanical influences were investigated. The total peak-to-peak noise magnitude was approximately 100 mV. A digital low-pass filter was used to effectively attenuate the noise magnitude to approximately 25 mV and achieved a minimum SNR of 8 without losing useful signal information. Sensor output baseline drift with respect to environmental conditions was also observed. The designed operational frequency band of the sensor system was sufficient to maintain sensor functionality over a wide range of environmental conditions.

The impact of corn leaves, ears, and weeds on sensor performance were investigated. While leaves may have some affect on sensor output, the impact was minimal and did not dominate the primary influences of stalk moisture content and sensor-stalk distance. An ear of corn can have a significant impact on sensor output, but such interference by ears is an extremely rare event and the impact on stalk count should be negligible. The presence of high-density weeds totally obscured the stalk signals and prevented the detection of discrete stalks. However, the signal pattern associated with high-density weeds may be used to exclude high weed areas to avoid biasing field stalk counts. This pattern could also be used to flag high-density weed areas.

Moisture content data collected from the sentinel stalk pairs was useful in characterizing the field-wide moisture content distribution, but the variability in moisture content between the two stalks of a sentinel pair confirmed the earlier finding that the moisture content of a stalk can not be used to predict the moisture content of nearby stalks. Finally, the influence of sensor-stalk distance prevented the development of a model of the relationship between signal strength and stalk moisture content from the field collected data.

CHAPTER 8 – FEATURE EXTRATION

The final field test data in raw form was not directly useful for counting stalks. This chapter focuses on the extraction of useful information from the raw data. A number of post-acquisition data processing techniques were applied to help define event-specific features: digital filtering, downsampling, moving average, and thresholding. These features were the input for the neural network pattern classification discussed in Chapter 9.

Digital Filtering and Downsampling

The raw data contained a significant amount of high frequency noise. Low-pass digital filtering and downsampling with averaging was used to remove unwanted high frequency noise. Three types of digital low-pass filter (Butterworth, Chebyshev, and Elliptic) with four orders (0, 1, 2, and 3) and three cutoff frequencies (40, 80, and 160 Hz) and five downsampling rates (10, 20, 50, 100, and 200) were evaluated to find the optimum signal processing parameters. Downsampling was performed by averaging a number of data points into a single point. The optimal parameters for these two techniques were determined by visual comparison of the raw and processed data.

The filter parameters were varied and the filtered and raw signals were visually compared. Preference was also given to simplicity and minimal computational

requirements. A first order Butterworth low-pass filter with cutoff frequency at 500 rads/sec (approximately 80 Hz) was chosen. The raw and filtered signals are presented in Figure 80 and Figure 81, respectively. The peak-to-peak noise magnitude in the raw signal was approximately 100 mV. The low-pass filter attenuated the noise magnitude to approximately 25 mV. The SNR was increased from approximately 2 to 8 (assuming minimum signal strength of 200 mV).

Downsampling with averaging in blocks of 100 points was selected. The resulting effective sampling rate was 100 Hz (Figure 82). After downsampling, the peak-to-peak noise magnitude was further attenuated to approximately 20 mV and the SNR was increased further increased to approximately 10. Visual comparison of the signal patterns before and after processing confirmed that the fine detail for each stalk event was retained while most of the unwanted high frequency noise was suppressed (Figure 80, Figure 81, and Figure 82).

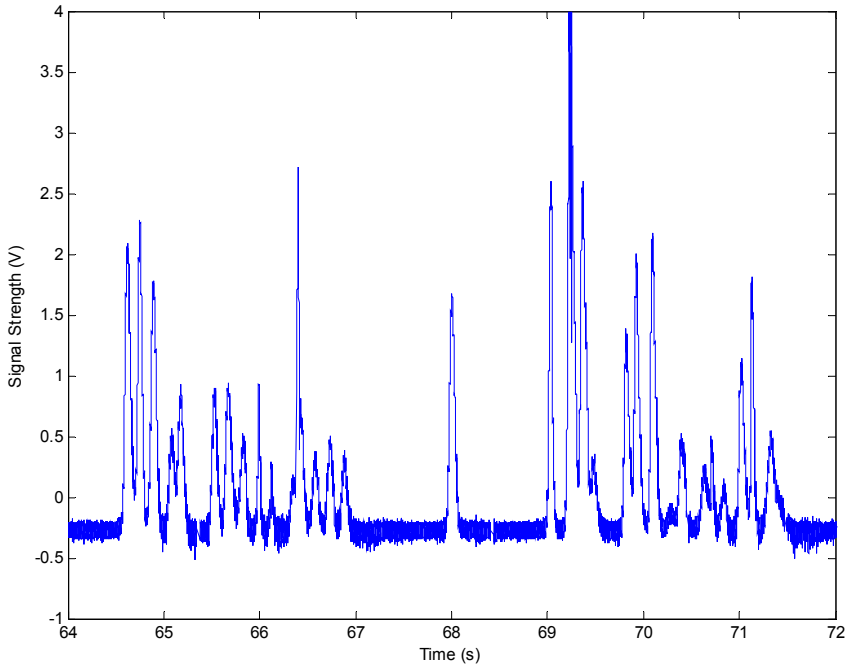

Figure 80. Typical raw sensor signal

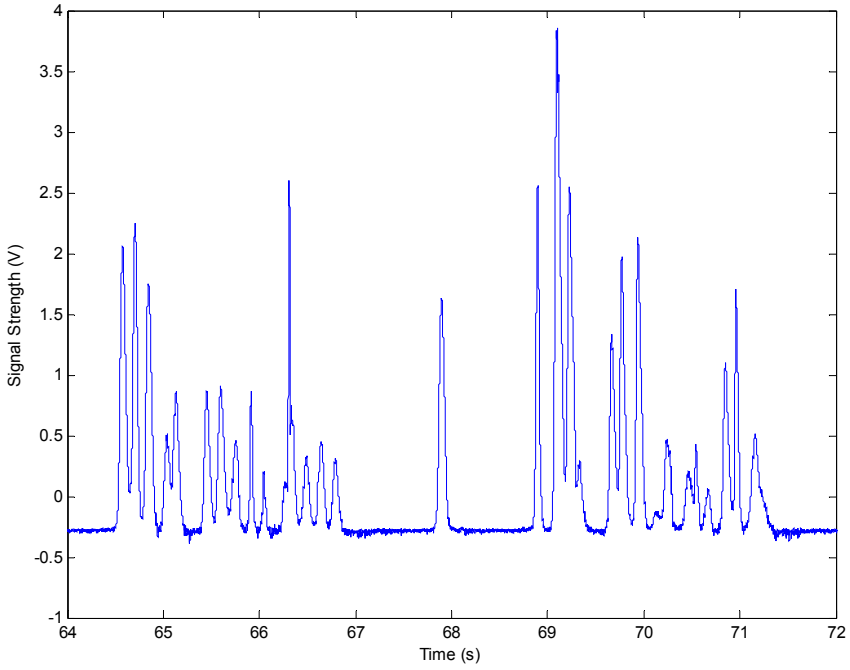

Figure 81. Typical sensor signal filtered by a first order Butterworth low-pass filter with an 80 Hz cut off frequency

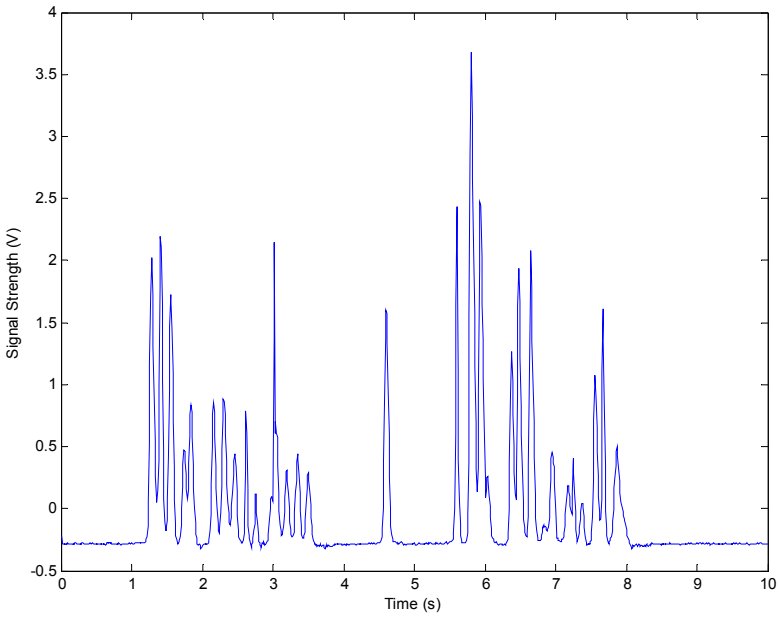

Figure 82. Typical filtered sensor signal after downsampling with averaging to 100 Hz

Moving Average and Threshold

A moving average and a threshold were used to remove slow signal drift and signal overlay. The moving average was subtracted from the filtered data to remove slow signal drift. Different moving average windows were tested to find the optimum size. When the window size was too small, the values of the filtered data and the values of the moving average were very close. The difference between them was close to zero. Therefore, stalk discrimination was lost. When the window size was too large, the moving average was close to a DC signal and little slow signal drift was removed. The optimal window size was determined by trial and error by visually comparing the raw and processed data to obtain a balance between event discrimination and drift removal.

The relationship between the downsampled data and the moving average is shown in Figure 83. A good balance between stalk discrimination and drift removal was achieved when the window size was between 11 and 13 (110 – 130 ms), and a window size of 13 was selected. The signal pattern after subtracting the moving average from the filtered and downsampled signal is presented in Figure 84.

The signal pattern oscillated above and below the time axis after the application of the moving average. A minimum threshold was applied to help separate the events and simplify the signal pattern by eliminating the portion of the signal below the threshold. While the application of the threshold eliminated almost half the signal magnitude information, the loss of information was offset by an increase in the ease of discrimination between adjacent events. Visual inspection of the processed data was

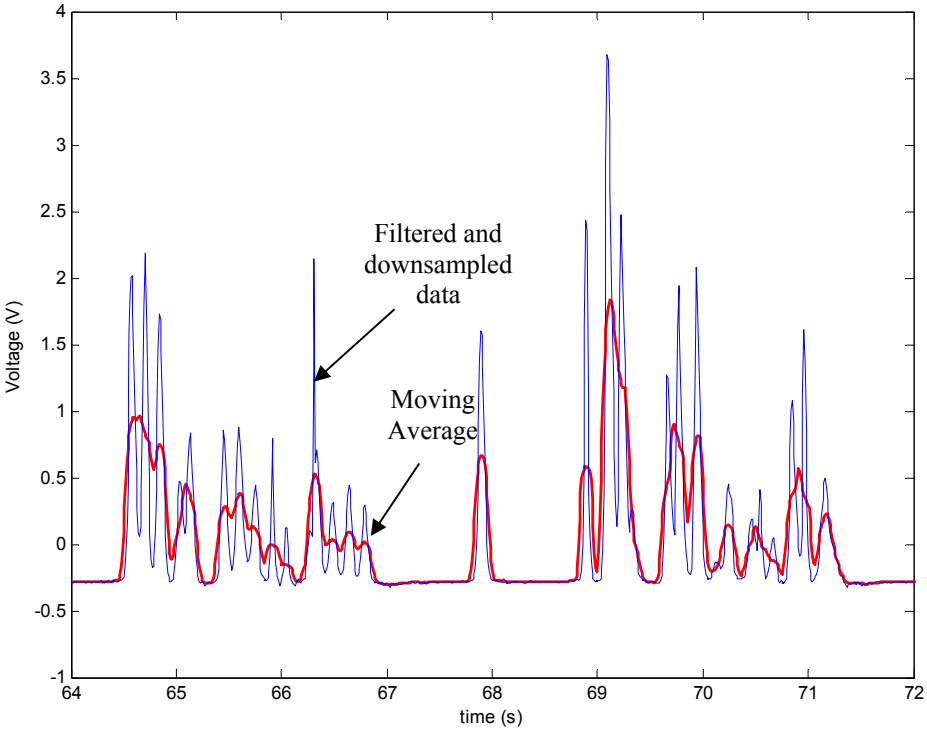

Figure 83. Typical filtered and downsampled sensor signal and moving average

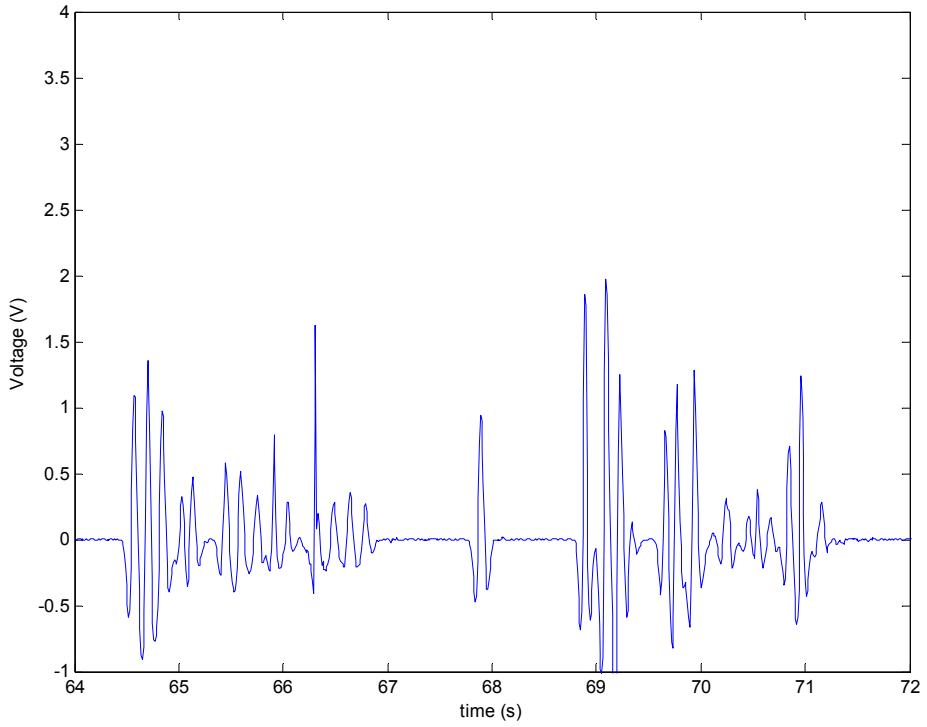

Figure 84. Signal pattern acquired by subtracting moving average from filtered and downsampled sensor signal

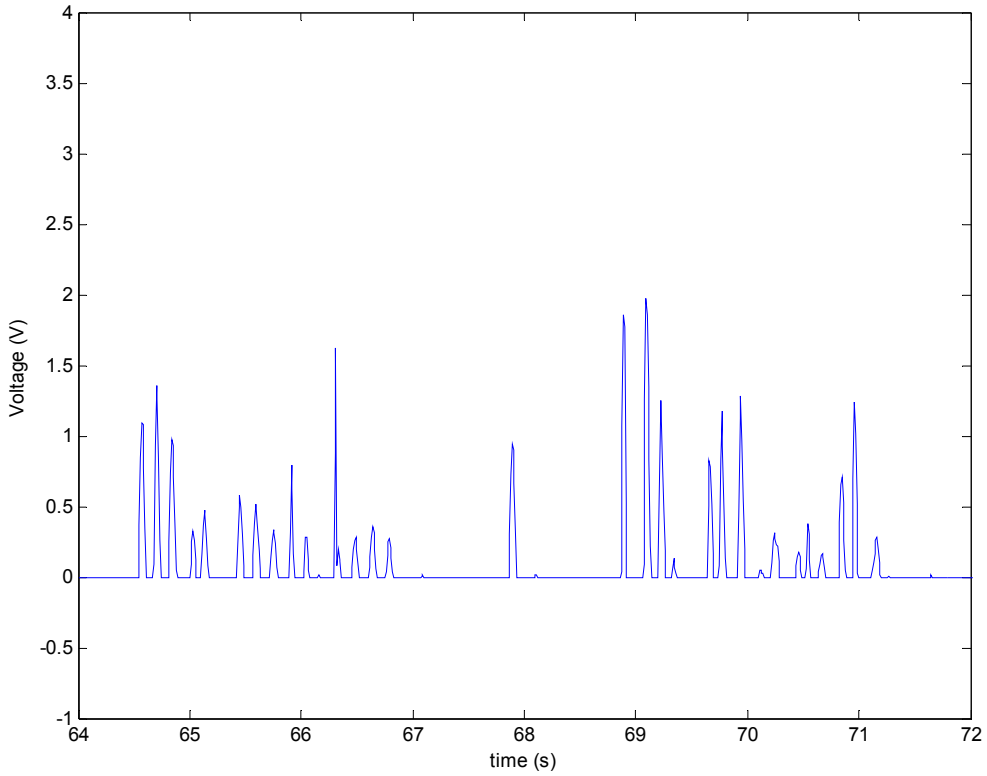

Figure 85. Typical signal pattern after all data processing techniques were applied

used to identify a threshold (10 mV) that balanced the need to simplify the signal data and the need to preserve enough data to effectively characterize the sensor output (Figure 85). Each peak above the threshold defined an event, which may or may not correlate to a stalk.

Each stalk position was recorded before harvesting, therefore, each stalk could be correlated to the events in a dataset. Every event was identified as either Stalk (1) or Non-stalk (0) by comparing the events with corn stalk positions (Figure 86). However, a stalk may exist where there is no corresponding event. This situation was very rare, (0.7 % of total number of stalks) and only happened in very dry conditions. In this situation, a signal point with magnitude of 0.01 was inserted represent the stalk missing from the

signal and marked as 1. The events were aligned with stalk locations for most stalk events, but some misalignment occurred. This could be a result of the measurement resolution (0.25 cm) or repositioning of the stalk during harvesting. The event dataset after correlation with stalk position information was named the "true dataset".

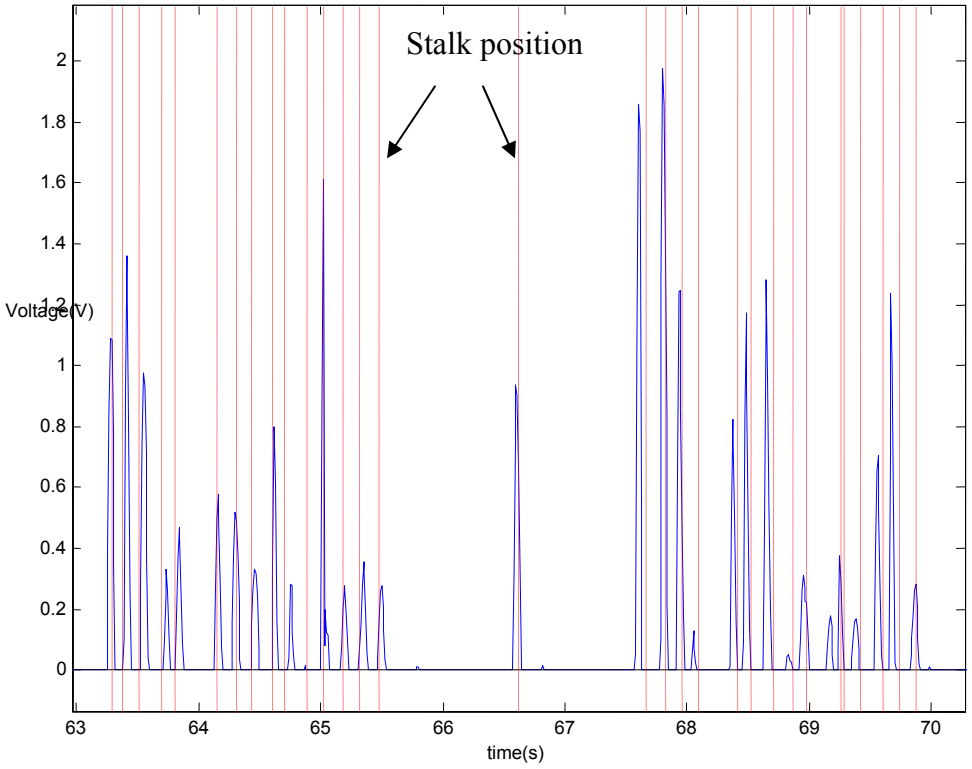

Figure 86. Typical processed sensor signal correlated with measured stalk positions

Feature Extraction

While signal processing significantly simplified the signal data, additional processing was required to further reduce the size of the data set and reorganize the data into a form conducive to later stalk pattern classification. Feature extraction is a method of characterizing each signal event (a discernible signal peak) with a finite set of attributes, which minimizes the data set size while retaining enough information to accurately characterize the events. An ideal feature extractor would yield a representation that makes the job of the pattern classifier trivial, therefore, the feature extraction is critical to the success of pattern classification. Features were carefully defined to preserve aspects of the signal that would be most useful in identifying stalks.

The extracted features were defined based on previous experimental results and understanding of the sensor system interaction with corn stalks. In this project, a total of eight features were extracted from each event: 1) peak magnitude, 2) peak width, 3) peak top gap, 4) peak bottom gap, 5) number of local maxima in one peak, 6) peak magnitude average, 7) preceding peak magnitude, and 8) following peak magnitude (Figure 87). These signal features are correlated to stalk physical properties and stalk spacing and therefore contain unique information that represented stalk events.

The peak magnitude (1) and the event width (2) represent the maximum signal magnitude and signal width of each event. These features represented signal strength for individual stalks. The event width was a time variable represented by the downsampling index. The original DAQ field sampling rate was 10KS/s and downsampling block size was 100, which produced 100 data points for each second. Therefore, each index

increment was equal to 10 ms. The event width was represented by the difference in index numbers of the start and end points of an event. The peak width contained individual stalk moisture content and harvest speed information. The signal width of a high moisture content stalk was typically greater than a drier stalk. The signal slope was represented by the combination of Features 1 and 2.

The peak top gap (3) was the index number difference between the current event peak magnitude and the preceding event peak magnitude. The peak bottom gap (4) is the index number difference between the starting point of the current event and the final point of the preceding event. Feature 3 represented the stalk spacing. This feature also contained harvest speed information and characterized the stalk passage frequency. The combination of Features 3 and 4 contained stalk diameter information.

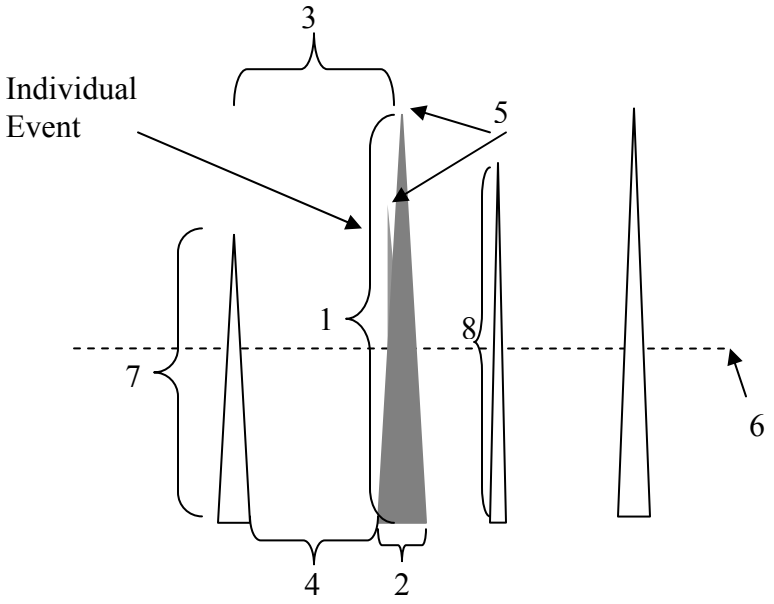

Figure 87. Eight features of an individual event

The local maxima number (5) was determined by the number of peaks in one event. There may be more than one peak in an event if two stalks were closely spaced or if weeds or leaves significantly impacted the sensor signal.

The peak magnitude average (6) was determined by a group of events (Figure 88). Eleven events were chosen, the current event, five events before the current event and five events after the current event. The two events with the smallest peak magnitudes were discarded because they have higher probability to be non-stalk information. The average of the remaining nine events was the peak magnitude average. This feature represented the moisture content of stalks around the current stalk. This allowed a localized dynamic threshold to be considered.

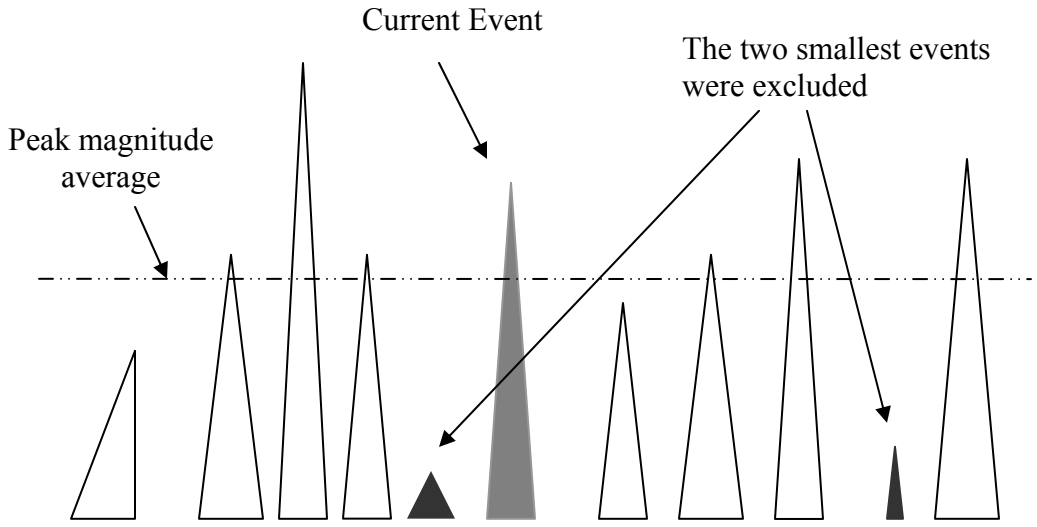

Figure 88. Definition of the peak magnitude average

The preceding peak magnitude (7) was the peak magnitude of the event immediately preceding the current event. The following peak magnitude (8) was the peak magnitude of the event immediately following the current event. The combination of these two features represented localized signal strength content.

Principal Component Analysis

The set of extract features was deliberately made as comprehensive as practical to preserve as much signal information as possible. However, not all extracted features have equal weight in identifying stalks in the processed signal. Some features may also be linear multiples or combinations of other features, and therefore provide little additional useful information. These "excess" features do not improve the final effectiveness of classification, but do increase the classification model size and require much more computation power for classification and prediction. Therefore, feature dimension reduction is very important to decrease model size and increase model prediction speed. Principal component analysis was used to reduce the feature set dimensions.

Principal component analysis provides the proportion of total variability associated with a component. Components correlated with a larger proportion of the total variability more effectively describe the total variability, and therefore contribute more to accurate pattern classification. Components correlated with little variability contribute little to accurate pattern classification and may unnecessarily complicate the pattern classification process. When the threshold was set to eliminate components responsible

for less than 2% of the total variability, the feature space dimension was reduced from 8 to 6. When the threshold was increased to 10%, the feature space dimension was further reduced to 3. Artificial neural network tests (more details in next chapter) showed no significant difference between 6 and 3 dimensions. However, when the feature space was dimension decreased to 2, the model efficiency decreased dramatically (from 99.5 % to 63%). Therefore, three features were selected for pattern classification. The three critical features were identified by analyzing the feature eigenvalues: peak magnitude, average peak magnitude, and peak top gap. These features are account for 25%, 22%, and 21% of the total variability, respectively.

This feature reduction means each event had three input vectors and one output vector. The three input vectors were the three features and the output vector was the event type (1 or 0, for stalk and non-stalk events, respectively). More than 3500 events were extracted from the final field test data. Both the input data set (3×3500) and output dat set (1×3000) were stored in the final dataset, which is a four-dimensional data set (4×3500).

Chapter Summary

The raw data from the final field test was processed in preparation for stalk pattern classification (Chapter 10). A first-order Butterworth low-pass filter with a cutoff frequency of 80 Hz and a 100 point downsampling with average were used to filter high-frequency components from the raw data and reduce the raw data set size. A moving average with a window size of 13 (130 ms) was used to remove slow signal drift and

signal overlap. A minimum threshold level was used to eliminate negative signal components and help separate signal peaks. Each remaining signal peak was defined as an "event".

Eight features were extracted for each individual event. The eight features included information pertaining to individual stalk moisture content, average stalk moisture content, harvesting speed, stalk spacing, stalk diameters, closely spaced stalks, the effects of weeds and leaves, and stalk moisture content variation over a small area. Principal component analysis was used to eliminate features that were less effective for stalk pattern classification to simplify the feature dataset. Three features, peak magnitude average peak magnitude, and peak top gap, balanced processing efficiency and classification effectiveness. These three features and the event type (stalk or non-stalk) were recorded to form the final feature dataset.

CHAPTER 9 – PATTERN CLASSIFICATION FOR STALK NUMERATION

A primary goal of this research was to develop a method to accurately classify stalks based on real-time sensor output. Therefore, an effective classifier is very important to the successful development of this sensing system. Artificial neural network techniques were chosen to develop the classifier based on key features identified in chapter 8.

Methodology

Artificial Neural Network Background

An artificial neural network (ANN) is a computing paradigm that is loosely modeled after cortical structures of the brain. ANNs are composed of simple elements operating in parallel. As in a natural neural network, an ANN is defined largely by the connections between elements. An ANN can be trained to perform a particular function by adjusting the values of the connections between elements so that a particular input leads to a target output (Figure 89) (MathWorks, 2002).

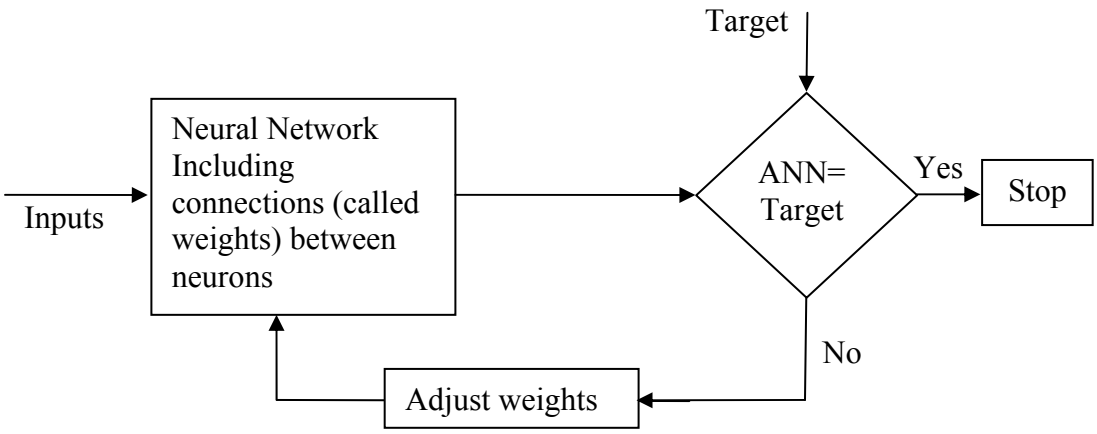

Figure 89. Schematic of Artificial Neural Network learning process

An ANN architecture consists of the number of layers, the number of neurons in each layer, layer bias, the transfer function of each layer, and the inter-layer connections. No single structure is ideal for all applications. All ANNs have an input and output layer, most also have one or more hidden layers between the input and output layers, and each hidden layer contains one or more neurons. These additional layers are known as hidden layers since they are internal to the ANN. ANNs with no hidden layers are a special case used for linear classification and are known as linear networks or perceptrons. Layers with a single neuron are linear and layers with multiple neurons are non-linear.

If the inputs and target output can be linearly mapped, then a perceptron is reliable and very fast. Most ANN applications are more complex and require multiple layers composed of multiple neurons to provide reliable classification. Model complexity and computational requirements increase with the number of layers and neurons. Also, overly complex models tend to "overfit" the data. Overfitting occurs when the learning process produces a classification model so complex that all variability in the data is

described by the model. While this will provide a perfect classification of the data used to teach the ANN, subsequent data may be poorly classified. There are several techniques that can be used to avoid overfitting including: careful selection of model complexity, the use of a very large training set, and a combination of training and validation.

Generally, a two layer sigmoid-linear network can represent any functional relationship between inputs and outputs if the sigmoid layer has enough neurons. A non-linear ANN is most frequently used for multiple feed-forward layers, which is more flexible. A multilayer feed-forward network with differentiable transfer functions can be trained by a backpropagation method to perform function approximation, pattern association, and pattern classification.

Neural Network Development Procedure

An ANN was used as a function approximation tool. That is, the neural network was used to develop a non-linear model to predict stalk count given collected features. Once a trained neural network was verified (tested against data not used in the training process) to be an effective classifier, this neural network can function as the prediction model. Neural network training was an offline process in this application, meaning the raw data was collected in the field and the training process was performed in the laboratory. Training can be a time-consuming and computationally intensive process that normally cannot be easily performed in the field.

Verified neural network parameters consist of one or more matrixes. The number and dimensions of the matrixes is dependent on the neural network structure. More layers require more matrixes to describe the model and more neurons in a layer require a larger matrix to describe the layer. After the network was trained and the matrixes were defined, the matrixes serve as the model for real-time prediction. Only these matrixes and the layer activation functions are necessary to process the collected features online. Online extracted features from the sensor signal are multiplied by the first matrix and the first layer activation function is applied. The results are multiplied with the second matrix (if any) and the activation function of the second layer is applied to the product. This process is repeated until all layers have been applied and the final result is produced.

Implementation of the ANN using Matlab produced a numeric final result (0 or 1). Values of 1 resulted in classification of the event as a stalk and values of 0 resulted in classification as a non-stalk event (or noise).

Before the structure could be determined, the training and test set needed to be defined. Overfitting was carefully considered when partitioning the final feature set into the training and test sets. A large training set is more likely to represent all possible behaviors of the system being modeled and therefore is more likely to prevent overfitting. A large test set is more effective in evaluating the network prediction accuracy and identifying potential overfitting. The rule of thumb for avoiding overfitting is that the training set size is at least 30 times the number of input neurons in the network.

The final feature set (as described in Chapter 8) consisted of the three-dimensional input feature vector extracted from sensor output and the one-dimensional

target output vector based on hand-count and stalk position data. Because the dataset was large (more than 3000 events), 20% of the dataset was used as the training set and the remaining 80% was used as the test set, which would allow up to 20 neurons without overfitting. The data were partitioned sequentially to ensure both the training and test sets were as representative of the entire body of data as possible. Every fifth extracted feature and associated event type was moved to the training set (i.e., features 5, 10, 15, …, N/5; where N is the total number of features in the final feature set). The remaining features defined the test data set.

The training set was used together with a supervised learning method to train the neural network. The neural network converted the three features into a stalk or non-stalk (1 or 0) output. Training involved running the neural network with the features as the arguments of the model, calculating the output vector, and comparing it with the target output vector. If the stopping criterion was met, the training process stopped. If the stopping criterion was not met, the values in the model matrixes were modified to increase the likelihood of matching the target vector on the next iteration and the process was repeated. Mean square error (MSE) between successive iteration outputs was used as the stop function. The training was stopped when the MSE was less than the threshold value (0.01).

The trained network model was tested to evaluate model accuracy once the training process was complete. The features in the test set were input into the model and a stalk or non-stalk output (1 or 0) was generated. The sum of the model output for all

features in the test set was the predicted stalk count. The predicted count was compared with hand-count to determine prediction error:

$$\text{Prediction error} = [(\text{Prediction mean} - \text{Hand count})/\text{Hand count}] \times 100\% \quad (9.1)$$

The initial states of the model matrixes during training were randomly generated; therefore, repetition of the training process could produce different results. Random generation of the initial matrix states provided a means of evaluating the stability of an ANN structure by examining the variability of the training results. The training process was repeated 30 times to produce 30 sets of matrixes describing 30 different models for a given ANN structure. The test data set was applied to each of the 30 models and the predicted counts were examined to determine prediction error and the variability in the prediction. The most desirable model was chosen based on accuracy, stability, and simplicity. Accuracy was indicated by prediction error, stability was represented by the standard deviation of the predicted counts, and simplicity was a function of the number of layers and neurons in the structure.

Pattern Classification

Pattern classification is used to partition data into groups by defining discrimination boundaries between the groups. The discrimination boundary may be as simple as a straight line or may be a very complex, multi-dimensional surface. The complexity and dimensionality of the discrimination boundaries depend on the size and variability of the feature space which is the input to the classification process. The neural

network structure and parameter values defined the discrimination boundaries in this application.

The simplest strategy for pattern classification was to use a single ANN to partition data into two groups: stalk or non-stalk. This strategy is very effective if the data is well segregated (i.e, few data points lie near the discrimination boundary). However, the confidence in classification of data near the boundary may be low. The definition of the discrimination boundaries through the development of the neural network structure and parameter definition divided these data between the two groups to preserve overall accuracy of the classification process.

The classification of the data near the discrimination boundary may result in individual classification errors. If there are two possible classification groups (positive and negative), there are four possible classification outcomes: true positive, true negative, false positive and false negative. Classifying a stalk event as a stalk event was defined as a true positive and classifying a non-stalk event as a non-stalk event was defined as a true negative. Incorrect classification of a stalk event as a non-stalk event or a non-stalk event as a stalk event were defined as false negative and false positive, respectively (Table 8). The division of the classification errors into the two classification groups is illustrated in Figure 90.

Table 8. Possible outcomes from classification with two categories

		Hand-Count True Data	
		Non-stalk	Stalk
Prediction Category	Non-Stalk	True Negative	False Negative
	Stalk	False Positive	True Positive

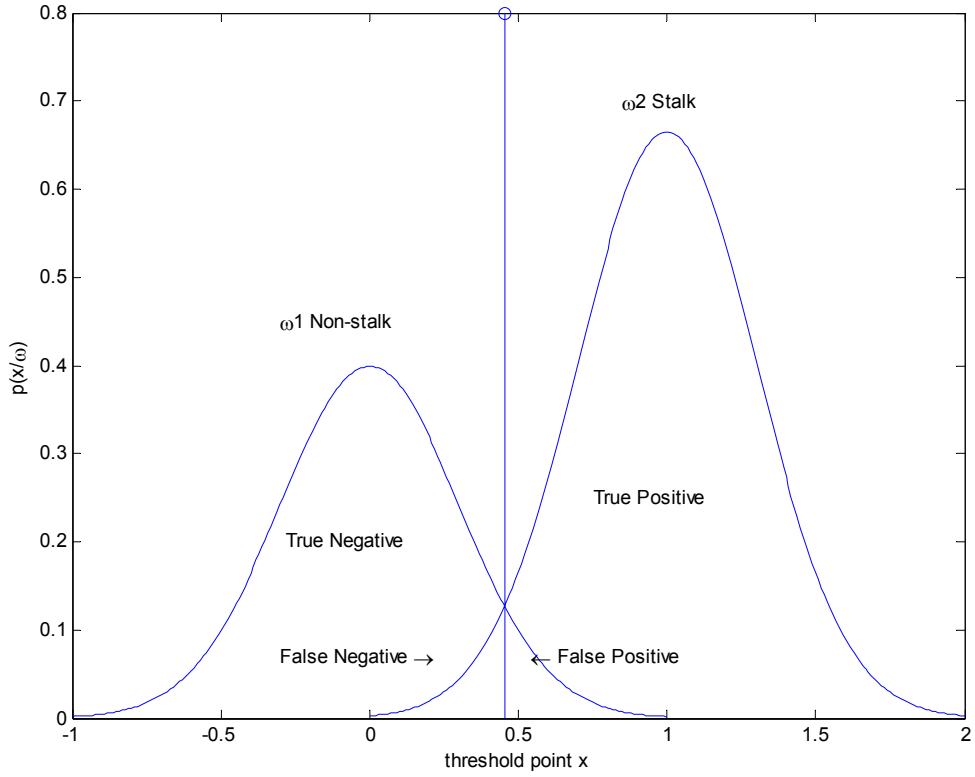

Figure 90. Illustration of classification into two categories

Another classification strategy added a separate category for the data near the discrimination boundary. Since the correct classification of these data was not certain, this third category was named "I Don't Know" (Table 9 and Figure 91). Correct predictions (true positive and true negative) were the same as defined in the first strategy. This strategy combined both false positive and false negative errors into a single category, "I Don't Know". The third category provides a mechanism to quantify potential errors or warn of conditions where prediction uncertainty may be large rather than simply dividing errors into the other two categories.

Multiple neural network models were necessary to implement the three-category classification strategy. The additional models provide the extra dimension required to define the third category. The data near the discrimination boundary were prone to simultaneously have both stalk and non-stalk properties. As a result, different neural network models may classify these events differently since each model defines a different discrimination boundary. The output of all models were be compared to determine the final classification of an event into one of three categories.

Table 9. Possible outcomes from classification into three categories.

		Hand-Count True Data	
		Non-Stalk	Stalk
Modeled Data	Non-Stalk	True Positive	I Don't Know
	Stalk	I Don't Know	True Negative

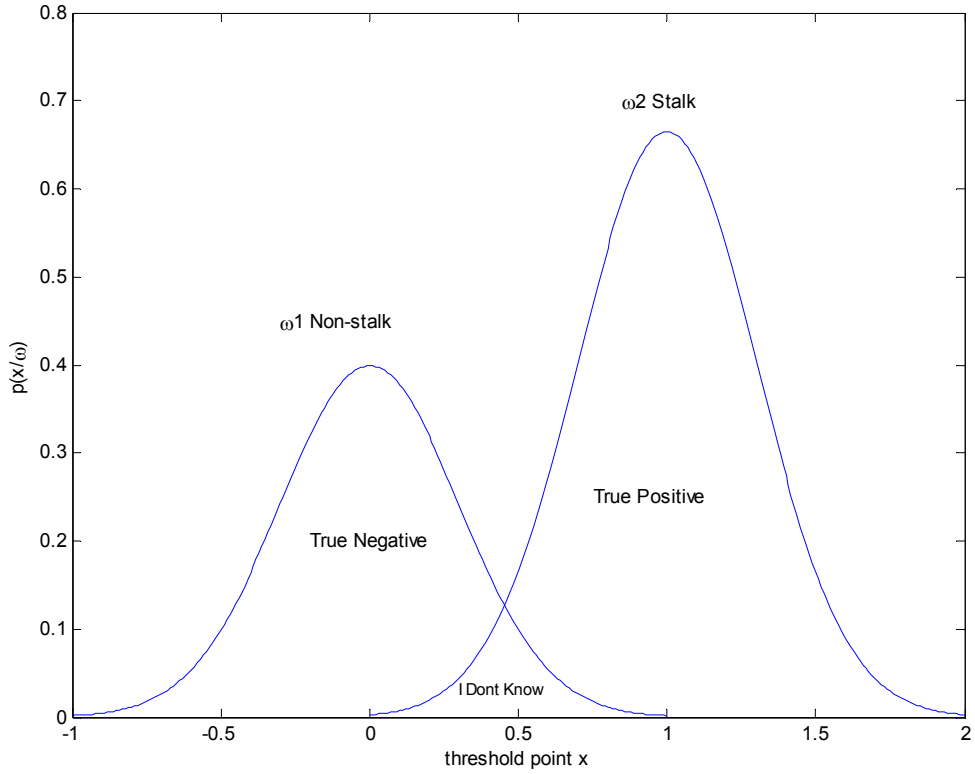

Figure 91. Illustration of classification into three categories.

Accuracy and Resolution Investigation

Mean square error (MSE) in the outputs of successive training iterations was used as the stopping criterion for neural network training. This criterion produced neural network models trained into a state where the number of false positive classifications is close or even equal to the number of false negative classifications, maximizing prediction accuracy over large areas. However, stalk count prediction over small areas of the field is more meaningful for field management and seed germination and stalk survival rates.

Two different methods were used for the small area stalk count predictions: length-based and event-based. The length-based method involved creating data subsets of the final feature set that contained the events in a fixed length (9 m) row. The event-

based method divided the final feature set into segments containing a number of consecutive events (5, 10, 20, 30, 40, and 50 events). For example, 60 subsets of 50 events would be created from 3000 events. The data were organized by harvest time order for both methods. Both hand count and neural network predicted count were obtained for each data subset and the prediction error calculated.

Linear regression with a forced zero intercept was used to describe the relationship between the hand count and the predicted count for the length-based data sets. For the event based data sets, the difference between hand count and the predicted count for each plot was calculated. For example, when the resolution was 50 events, there were 42 stalk events and 8 non-stalk events. If the model predicted 43 stalks, the miscount was 1. The total number of the miscount plots at each miscount level was found and used to investigate the model prediction accuracy.

Neural Network Structure Determination

Both perceptrons and backpropagation neural networks developed in Matlab (MathWorks, 2002) were tested. A single two-layer linear structure was developed and tested. This model correctly predicted only 2% of the stalk events. The low accuracy indicated the data was not linearly separable and the development of a multiple-layer, non-linear neural network was necessary.

The first step in developing the multiple-layer neural network was to determine the structure of the network (i.e., the number of layers and the number of neurons in each layer. As previously discussed, a carefully designed 2-layer network can adequately

model most systems. Both 2- and 3-layer neural network layers with different numbers of neurons in each layer (2, 3, 4, 5, 6, 9, 12, and 15) were considered. Each structure was trained 30 times using the training data set and the test data set input to each trained model to produce predicted stalk counts. There were a total of 2162 confirmed stalk events in the test data set. Table 10 presents the predicted stalk counts for a representative selection of model structures.

Table 10. Representative results from the neural network structure determination

NN structure	Predicted Number		Absolute Mean Prediction Error
	Mean	Standard Deviation	
3-1	2155	48	0.32%
4-1	2150	31	0.55%
5-1	2151	39	0.51%
6-1	2177	40	0.69%
12-1	2187	32	1.15%
6-3-1	2127	43	1.62%

Results

The network structures were evaluated in terms of precision and accuracy. Since a stable model is more repeatable, model stability was used as a measure of precision. Precision and accuracy were inversely related to the standard deviation of the predicted count and the prediction error, respectively. Based on these criterion, the 4-1 (1 hidden layer with four neurons) structure was the best combination for precision (standard deviation =31) and accuracy (prediction error = 0.55%). Both the 3-1 and 5-1 structures are more accurate than the 4-1 structure (prediction errors of 0.32 and 0.51%, respectively) but less stable (standard deviations of 48 and 39, respectively). The stability of the 12-1 structure was similar (standard deviation = 32) to that of the 4-1 structure but the prediction error (1.55%) was nearly twice that of the 4-1 structure and the 12-1 structure was considerably more complex than the 4-1 structure. The 4-1 structure with a *tansig* activation function for the first layer and a *purelin* activation function for the second layer was selected. The 4-1 structure schematic is presented in Figure 92.

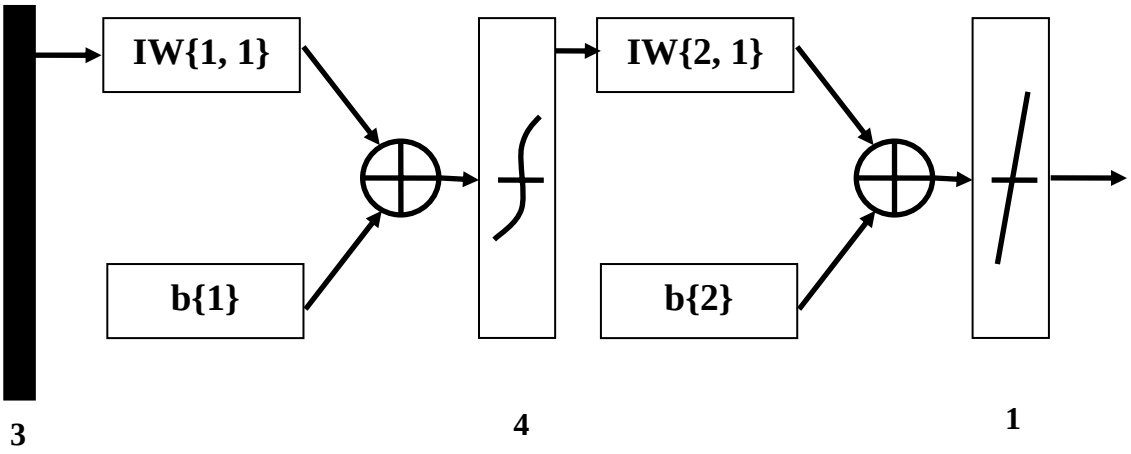

Figure 92. Schematic of the 4-1 neural network structure

The 4-1 structure had two layers and each layer had one corresponding matrix. The first matrix was a 4 × 3 matrix since there were 4 neurons in the first layer and the input feature space was three dimensional. The second matrix was a 1 × 4 matrix. Each layer also had a bias vector. These matrixes and bias vectors were the model for the stalk count prediction. Each feature input (P) was a 3 × 1 matrix. The product of P × IW{1,1} was a 4 × 1 matrix. The first bias vector (b{1}) was added to this product and the first activation function (*tansig*) was applied. The resulting matrix was multiplied by the second layer matrix (IW{2,1})to produce a 1 × 1 scalar result. After adding the second bias vector (b{2}) and applying the second activation function (*purelin*), this product was rounded to its nearest integer. This output is the event classification, either 1 or 0.

$$P_{output} = purelin\{IW\{2,1\} \times [\tan sig(IW\{1,1\} \times P_{input} + b\{1\})] + b\{2\}\} \tag{9.2}$$

The *tansig* function was defined as:

$$\tan sig(n) = \frac{2}{1+e^{-2n}} - 1 \tag{9.3}$$

The following matrixes and bias vectors are based on one backpropagation training iteration of the 4-1 structure neural network:

$$IW\{1,1\} = \begin{bmatrix} 0.13737 & -3.0149 & -2.7643 \\ 0.026909 & 0.45689 & 3.6406 \\ -0.9739 & -2.9087 & 0.031578 \\ -0.30053 & -2.0417 & 0.18778 \end{bmatrix}$$

$$b\{1\} = \begin{bmatrix} -9.4122 \\ 4.2795 \\ -8.7269 \\ -5.6333 \end{bmatrix}$$

$$IW\{2,1\} = \begin{bmatrix} 0.58254 & 0.4679 & 6.7263 & -8.083 \end{bmatrix}$$

$$b\{2\} = -0.2571 \qquad (9.4)$$

"I Don't Know" Determination

Multiple network groups (with at least three networks) were used to better identify the data misclassified by the first pattern classification strategy. The extra networks were used to provide the third dimension necessary to define the third category, "I Don't Know". This method was performed with 20 iterations to evaluate the classification strategy. An average of 185 of the 335 (55%) previously misclassified events (combination of false positives and false negatives) were re-classified as "I Don't Know" (Figure 93). The three-category classification would produce more accurate predicted stalk counts by reducing the number of misclassified events and removing the bias associated with these events from the predicted stalk count. This strategy could also

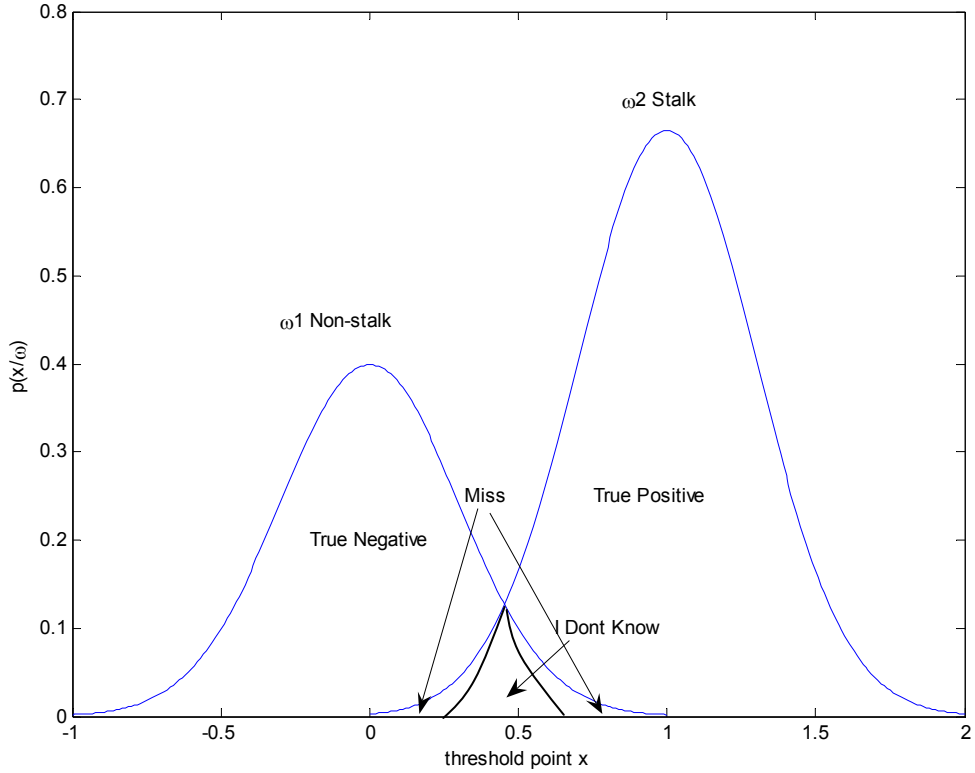

Figure 93. "I Don't Know" reclassification of previously misclassified events

be used to flag areas of a field where prediction confidence is low. This information could be used to help improve the effectiveness of the entire sensing system.

Feature Relationship Investigation

The relationship between the three critical components is shown in Figure 94 and Figure 95. The blue crosses and red circles represent correct and incorrect classifications, respectively. Negative and positive (non-stalk and stalk) classifications are presented separately in Figure 94 and Figure 95, respectively. These plots show how the stalk information can be obscured by noise. Almost all the non-stalk information occurs where

the peak top gap feature magnitude was low or where the average peak magnitude was low. The data also suggested a linear relationship between the peak magnitude and the average peak magnitude. This relationship is logical since an individual stalk would tend to have a moisture content at least somewhat similar to the adjacent stalks. This may appear contrary to earlier conclusions that an individual stalk can not be used to predict the moisture content of adjacent stalks. However, the proposition that the moisture content of a single stalk is closely related to the moisture content of a group of nearby stalks is the converse of the previous conclusion.

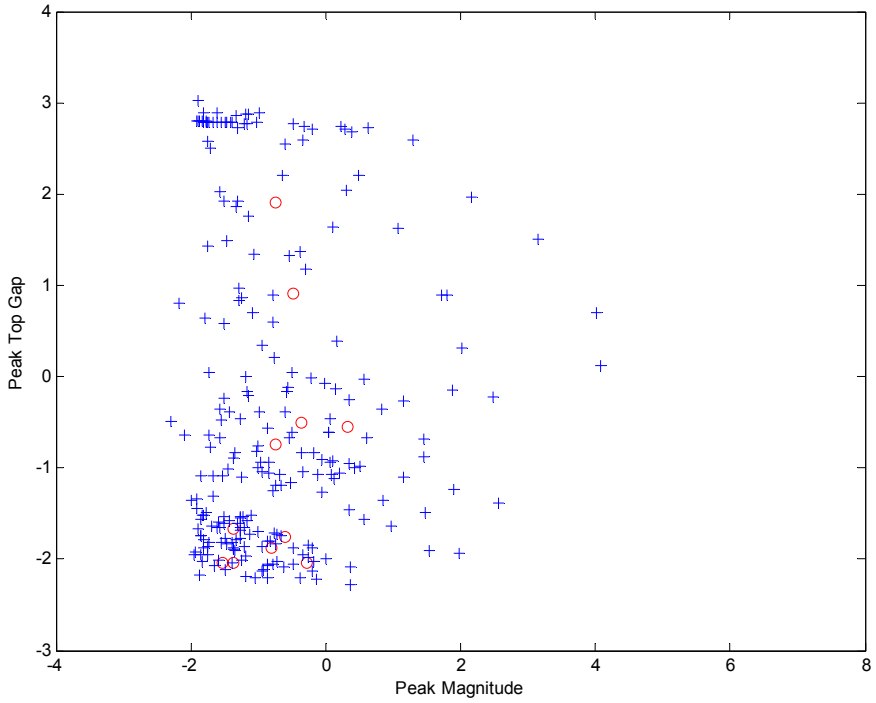

(a)

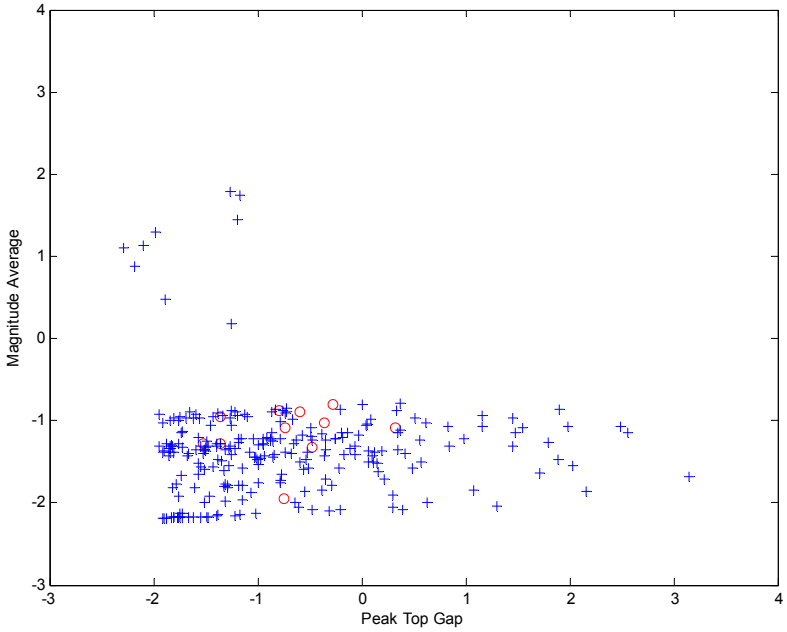

(b)

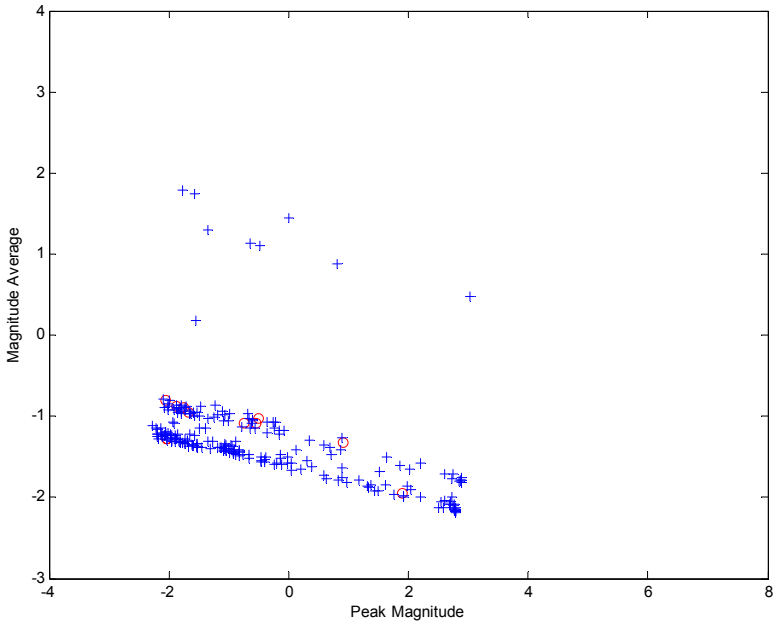

(c)

Figure 94. Relationships among three principal components (true negative & false negative)

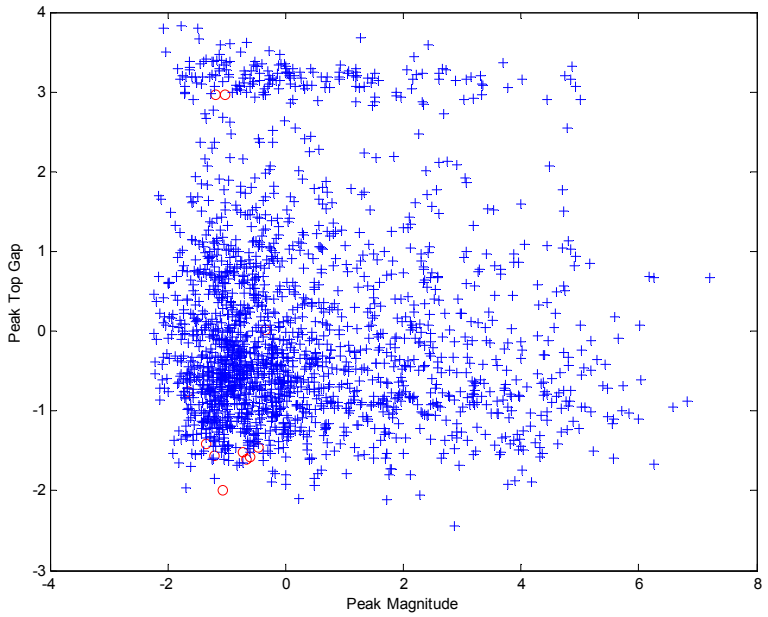
Peak Top Gap
Peak Magnitude
4
3
2
1
0
-1
-2
-3
-4
-2
0
2
4
6
8

(a)

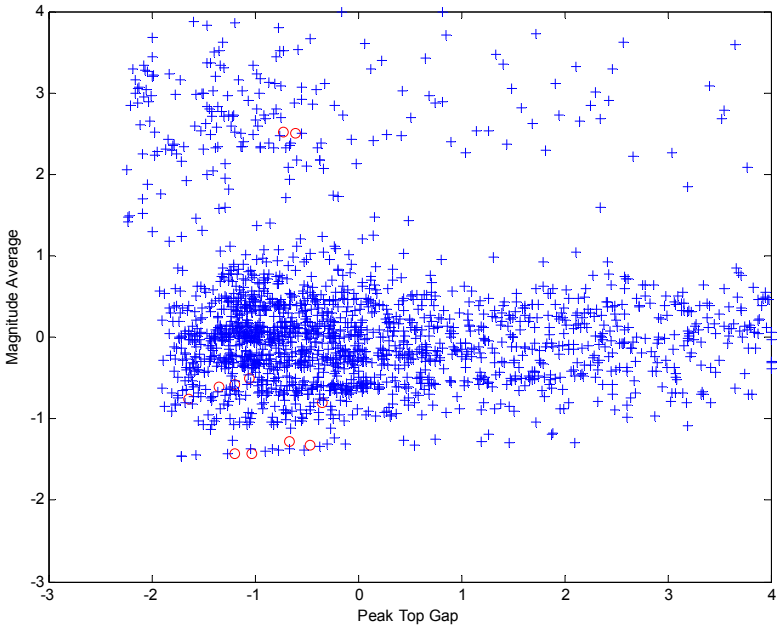
Magnitude Average
Peak Top Gap
4
3
2
1
0
-1
-2
-3
-3
-2
-1
0
1
2
3
4

(b)

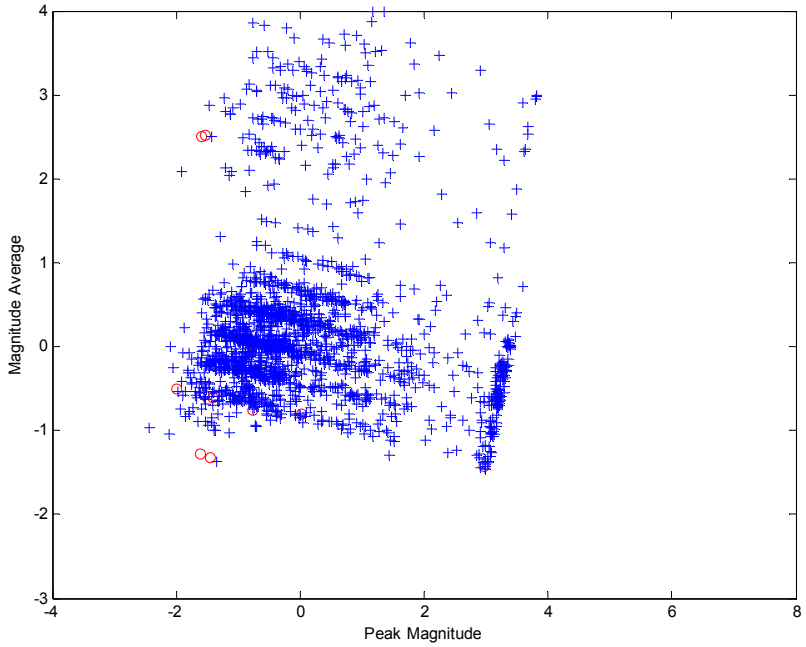

(c)

Figure 95. Relationships among three principal components (true positive & false positive)

Resolution Investigation

Subsets of the final feature set based on fixed row lengths (9 m) and a fixed number of consecutive events were used to examine the accuracy of stalk count predictions at various spatial resolutions. Hand count and predicted counts using the single neural network model were obtained for each subset. Linear regression analysis with a forced zero intercept was used to examine the relationship between hand count and predicted count in (Figure 96) for the fixed row length subsets. The relationship was:

$$y = 1.0216x$$

where y is predicted count and x is the hand count. R square of this regression is 0.8, which mean 80% variation can be explained by this equation. The slope of the regression line indicated good average correlation between the predicted and hand counts with a slight tendency to over estimate. It was found that the largest deviations occurred mostly in the low moisture content range, which confirmed the strong impact of stalk moisture content on prediction accuracy.

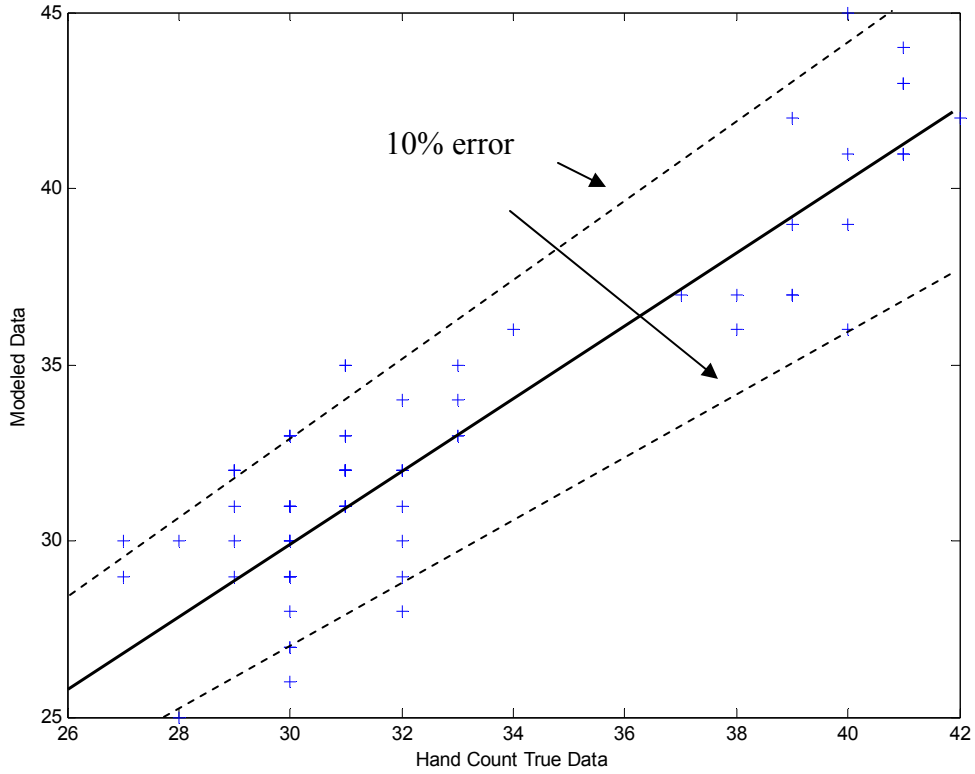

Figure 96. Linear relationship between hand count number and predicted number

For the event-based method, different event resolutions (5, 10, 20, 30, 40, and 50 events) were chosen. These resolutions corresponded approximately to row lengths of 0.75, 1.5, 3, 4.5, 6, and 7.5 m. The cumlative percentage of plots with no more than the indicated prediction count error at different resolutions is presented in Table 11. For example, there were 62 subset plots at resolution of 50. There was no prediction error (error # = 0) for 8 plots (12.9%), 23 plots (37.1%) had a one-stalk error or less per plot, and 44 plots (71%) had a 2-stalk error or less per plot. Higher resolution data is more useful than field-scale data for making precision management practice decisions. From the table, it was found that at a resolution of 1.5 m (10 events resolution), more than half plots can be predicted with no error and almost 90% of plots have a prediction error of one stalk or less.

Table 11. Cumulative percentage of subsets with respect to predicted count error at different resolutions

	Cumulative percentage of plots with predicted error no more than the indicated error							
Error # / Resolution(Events)	0	1	2	3	4	5	6	7
50	12.9%	37.1%	71.0%	85.5%	92.0%	95.2%	96.8%	100%
40	18.2%	48.1%	76.7%	92.3%	96.2%	98.8%	100%	100%
30	27.2%	59.2%	85.4%	92.2%	97.1%	100%	100%	100%
20	34.2%	68.4%	91.0%	98.1%	100%	100%	100%	100%
10	50.5%	88.1%	97.8%	100%	100%	100%	100%	100%
5	72.2%	95.8%	99.5%	100%	100%	100%		

Chapter Summary

A neural network structure was used to develop a stalk pattern classification model. The classification model was used to determine stalk population counts from the final feature set data discussed in Chapter 8. The final feature set was divided into a training data set and a test data set. The training data set was used with backpropagation techniques to train the neural networks and determine neural network model parameters. A number of neural network structures were evaluated and the best model was selected based on model precision, stability, and accuracy. The selected network structure had two layers with 4 and 1 neuron per layer, respectively. This structure could provide 99.5% prediction accuracy for the overall field. Predicted counts for 1.5 row segments were predicted with no error for 50% of the evaluated data subsets and 90% of the data subsets had predicted counts with an error no more than one stalk.

Multiple network groups (with at least three networks) were used to better identify the data misclassified by the first pattern classification strategy. This strategy identified an average of 185 of the 335 (55%) previously misclassified events (combination of false positives and false negatives) as “I Don’t Know”.

CHAPTER 10 – CONCLUSTIONS AND RECOMMENDTIONS

Conclusions

Specific objectives for this study were to develop, prototype, and test a corn population sensor. Based on the results obtained in this study, the following conclusions can be made:

- A single-sided capacitive detection element was successfully optimized to discriminate corn stalks at harvest, especially for low moisture content stalks.
- Finite element analysis proved useful in design of the capacitive sensor pattern, but the very small magnitude of capacitance changes produced by the detection element make accurate quantitative modeling extremely difficult. However, the combination of qualitative modeling and quantitative experimental analysis was effective in producing a functional design that met the design requirements.
- A Wien Bridge oscillator, a phase-locked loop, and an operational amplifier can effectively transform stalk presence (small ΔC) to an electrical potential signal with an acceptable SNR (generally greater than 10).
- Corn stalk dielectric constant, which is coupled to stalk moisture content, and sensor-to-specimen distance are the most important factors influencing sensor sensitivity.

- Principal component analysis showed that three corn stalk features were most important for stalk identification: peak magnitude, average peak magnitude, and peak top gap (Chapter 8). They accounted for 25%, 22%, and 21% of the total variability, respectively. These components are primarily representative of stalk moisture content and stalk spacing.

- A backpropagation neural network with 4-1 structure (two layers with 4 and one neuron per layer, respectively) was found to be the most effective neural network structure. Stalk pattern classification using this structure provided a 99.5% prediction accuracy for the complete data set. This structure was also effective for high-resolution (1.5 m row segment) predictions with no error for 50% of the subplots and an error no more than one stalk for 90% of the subplots.

- Multiple network groups (with at least three networks) were used to better identify the data misclassified by the 4-1 structure. This strategy identified an average of 185 of the 335 (55%) previously misclassified events (combination of false positives and false negatives) as "I Don't Know". Segregating these data points improve the prediction accuracy for the remainder of the field.

Recommendations

The prototype stalk population sensor functioned as designed, accurately counting stalk population. Still, there is considerable room for improvement. This sensor can be separated into three functional components: detection element unit, signal conditioning unit, and field evaluation and analysis unit. Discussion of improvements focuses on each

of these components. System refinements that may improve performance and function are:

Detection element:

- The balance between sensitivity and discrimination may be improved. A high sensitivity provides a higher-magnitude output and a high discrimination capability provides a large gap between two adjacent signal peaks. By design, this sensor is a relatively slow response device. A large magnitude signal peak is prone to overlap with adjacent signal pekas, which decreases the ability to discriminate adjacent stalks.
- The sensor-stalk distance was difficult to precisely control or measure in the laboratory. Therefore, a static test fixture designed to precisely control the sensor-stalk distance could be used to better validate the FEM simulation results, making FEM a more useful tool in detection element design refinement.
- Additional laboratory testing should be conducted using the single detection element configuration. Most laboratory tests were based on a two detection element configuration.

Signal Conditioning:

- The most critical circuit component is the Wien Bridge oscillator. A better understanding of the interaction between the oscillator and detection element would be useful. Specifically, a better understanding of the impact of parasitic capacitance on the circuit board is needed. Some unanticipated behaviors need to

be carefully recorded and analyzed. An improved, more precise static test fixture would provide better data for analyzing these effects.

- A better signal conditioning system may be possible. Some current commercially available capacitance-to-voltage converters may be investigated. The systems used in this research might be incrementally improved or replaced entirely if a more suitable alternative can be identified.
- An 80-Hz first order Butterworth filter should be integrated into the conditioning system. This filter could further improve the SNR and function as an anti-aliasing filter.

Field Evaluation and Analysis:

- The impact of weeds on stalk pattern classification needs to be further investigated so that strategies can be developed to address the impact of weeds. The weed density in this project represented an unrealistic extreme, therefore, a variety of weed densities need to be evaluated. Multiple types of commonly occurring weeds might be considered as well.
- Additional testing needs to be performed with very dry stalks to determine the minimum operation threshold.
- The sensor system needs to be tested on additional fields. Fields in different areas or even different states have different environmental conditions and different stalk properties. Additional varieties of corn should also be considered

- Neural networks are useful and practical classification tool that proved effective in this application. However, models developed by neural network techniques are somewhat complex and requires moderate online computational power to implement. Other classification methods are worth investigating. A simpler model that would be less computationally intensive might be developed using other techniques.
- Testing of multiple sensors on combine corn header should be conducted. The sensor was only mounted on one header row during the field test. The effect between sensors could be investigated by mounting each sensor on each row.
- Integration of the sensor signals with a yield monitor using a CAN bus should be pursued to promote comercialization of this system. The overall objective of this sensor was to improve yield maps. This objective can only be fulfilled by integrating this sensor with yield monitors.

Bibliography

Achmad, Balza, E. M. A. Esam, and M. A. Hussein. 2004. An X-ray Compton scatter method for density measurement at a point within an object. *Applied Radiation and Isotopes* 60 (6):805.

ASTM. 2003. Standard test methods for AC loss characteristics and permittivity (dielectric constant) of solid electrical insulation. *American Society for Testing and Materials Standards.*

Austin, W. M. 2002. CMOS Phase-Locked Loop application using the CD54/74HC/HCT4046A and CD54/74HC/HCT7046A: Texas Instruments.

Baxtor, L. K. 1996. *Capacitive Sensors: Design and Applications*. Wiley-IEEE Press.

Best, Roland E. 1999. *Phase-Locked Loops: Design, Simulation, and Applications.*: McGraw-Hill Professional Publishing.

Birrell, S.J. and K.A. Sudduth. 1995. Corn population sensor for precision farming. Paper No. 951334. ASAE, St. Joseph, MI.

Buehring, N. and Dobbs, R. 2000. UNR cotton plant population effect on growth and yield. Proceedings Beltwide Cotton Conferences. San Antonio, TX, 4-8 January, 2000.

Chen, Z. and R. C. Luo. 1998. Design and implementation of capacitive proximity sensor using microelectromechanical systems technology. *IEEE Transactions on Industrial Electronics.* 45(6): 886-894.

Comsol. 2006. Comsol Multiphysics modeling guide. Comsol.

Gehl, R. J., and C. W. Rice. 2007. Emerging technologies for in situ measurement of soil carbon. *Climatic Change* 80 (1-2):43-54.

Gottlieb, I. 2006. Practical Oscillator Handbook. Elsevier.

Jezek, D., B. Tripalo, M. Brncic, D. Karlovic, D. Vikic-Topic, and Z. Herceg. 2006. Modelling of convective carrot drying. *Croatica Chemica Acta* 79 (3):385-391.

Kandala, C. V. K., S. O. Nelson, and K. C. Lawrence. 1992. Nondestructive moisture determination in single kernels of popcorn by radio-frequency impedance measurement. *Trans A S A E* 35 (5):1559-1562.

Knochel, R., F. Daschner, and W. Taute. 2001. Resonant microwave sensors for instantaneous determination of moisture in foodstuffs. *Food Control* 12 (7):447-458.

Kraszewski, A. W., and S. O. Nelson. 1994. Determination of Moisture Content and Bulk Density of Shelled Corn by Measurement of Microwave Parameters. *Journal of Agricultural Engineering Research* 58 (1):37-46.

Lu, Y. C., J. A. Goldman, and H. N. G. Wadley. 1993. Quantitative Reconstruction of Internal Density Distributions from Laser Ultrasonic Data. *Journal of the Acoustical Society of America* 93 (5):2678-2687.

Mamishev, V.A, K; Dundara-rajan, F; Yang, Y; Du, and M; Zahn. 2004. Interdigital Sensors and Transducers. Proceedings of the IEEE. 92 (5):808-845.

MathWorks. 2002. Matlab neural network toolbox manual. MathWorks.

McQueen, Douglas H., Reginald Wilson, Arvo Kinnunen, and Ejner Paaske Jensen. 1995. Comparison of two infrared spectroscopic methods for cheese analysis. *Talanta* 42 (12):2007-2015.

Mizukami, Y., Y.; Sawai, and Y.; Yamaguchi. 2006. Moisture content measurement of tea leaves by electrical impedance and capacitance. *Biosystems Engineering.* 93 (3):293-299.

Moody, H. 2002. Unpublished laboratory report. University of Tennessee.

Moorehouse, D, and F Bradish. 2006. Recent fiberglass-reinforced plastic applications: Radome and hybrid bridge system. *Materials Performace* 45 (1):48-50.

Nagadi, M. M., and A. A. Naqvi. 2007. Gamma-ray yield dependence on bulk density and moisture content of a sample of a PGNAA setup: A Monte Carlo study. *Journal Of Radioanalytical And Nuclear Chemistry* 271 (3):691-695.

Nichols, S. W. 2000. Method and apparatus for counting crops. USA patent No. 6073427.

Nielsen, R.L. 1995. Planting speed effects on stand establishment and grain yield of corn. *J. Prod. Agric.* 8 (3):391-393.

Ozdemir, D. 2006. Genetic multivariate calibration for near infrared spectroscopic determination of protein, moisture, dry mass, hardness and other residues of wheat. *International Journal Of Food Science And Technology* 41:12-21.

Perez, A. J., F. Lopez, J. V. Benlloch, and S. Christensen. 2000. Colour and shape analysis techniques for weed detection in cereal fields. *Computers and Electronics in Agriculture* 25 (3):197-212.

Pordesimo, L. O., S. Sokhansanj, and W. C. Edens. 2004. Moisture and yield of corn stover fractions before and after grain maturity. *Transactions of the ASAE* 47 (5):1597-1603.

Prather, T. G., and H. P.Denton. 2003. Prcision farming series-Interpreting yield maps. *Biosystems Engineering and Enviromental Sciences Department, University of Tennessee.*

Sacilik, K., C. Tarimci, and A. Colak. 2007. Moisture content and bulk density dependence of dielectric properties of safflower seed in the radio frequency range. *Journal Of Food Engineering* 78 (4):1111-1116.

Sanchez, A. G., N.R.; Martos, and E.; Ballesteros. 2005. Comparative study of various analytical techniques (NIR and NMR spectroscopies, and Soxhlet extraction) for the determination of the fat and moisture content of olives and pomace obtained from Jaen (Spain). *Grasas Y Aceites* 56 (3):220-227.

Schajer, G. S., and F. B. Orhan. 2006. Measurement of wood grain angle, moisture content and density using microwaves. *Holz Als Roh-Und Werkstoff* 64 (6):483-490.

Schmilovitch, Z., A. Hoffman, H. Egozi, and J. Grinshpun. 2006. Determination of single-date water content by a novel RF device. *Applied Engineering In Agriculture* 22 (3):401-405.

Shrestha, D. S., and B. L. Steward. 2003. Automatic corn plant population measurement using machine vision. *Transactions of the ASAE* 46 (2):559-565.

Sorland, G. H., P. M. Larsen, F. Lundby, A. P. Rudi, and T. Guiheneuf. 2004. Determination of total fat and moisture content in meat using low field NMR. *Meat Science* 66 (3):543-550.

Sudduth, K. A., S. J. Birrell, M. J. Krumpelman, P. C. Robert, R. H. Rust, and W. E. Larson. 2000. Field evaluation of a corn population sensor. Paper read at Proceedings of the 5th International Conference on Precision Agriculture, 16-19 July, 2000, at Bloomington, Minnesota, USA.

Takeuchi, Shigeki, Mitsuo Maeda, Yu-ichiro Gomi, Mika Fukuoka, and Hisahiko Watanabe. 1997. The change of moisture distribution in a rice grain during boiling as observed by NMR imaging. *Journal of Food Engineering* 33 (3-4):281-297.

Tien, K. C., and J. Judge. 2006. Sensitivity of passive microwave observations to soil moisture for growing vegetation. *Applied Engineering In Agriculture* 22 (6):843-850.

Thompson, J. F., J. V. Stafford, and B. Ambler. 1990. Weed detection in cereal crops. In *Paper American Society of Agricultural Engineers., No. 90-7516.*

Trabelsi, S. and S. O. Nelson. 2006. Nondestructive sensing of bulk density and moisture content in shelled peanuts from microwave permittivity measurements. *Food Control*. 17 (4): 304-311.

USDA-UASS. *Corn production in 2005.* 2005 [cited. Available from http://www.usda.gov/nass/aggraphs/crops.htm.

Webb, Newman Edward. 2001. Real-time system for determining corn plant population in-situ at harvest time, Biosystems Engineering, University of Tennessee, Knoxville.

Williams Jim. 1991. .Analog circuit design: art, science and personalities. Newnes.

Yonts, C. D., and J. A. Smith. 1997. Effects of plant population and row width on yield of sugarbeet. *J sugar beet res* 34 (1/2):21-30.

Zhao, Jiali, Yong Su, Dejun Wang, and Siwei Luo. 2003. Illumination ratio image: synthesizing and recognition with varying illuminations. *Pattern Recognition Letters* 24 (15):2703-2710.

Appendices

Appendix A. Electrical Drawing

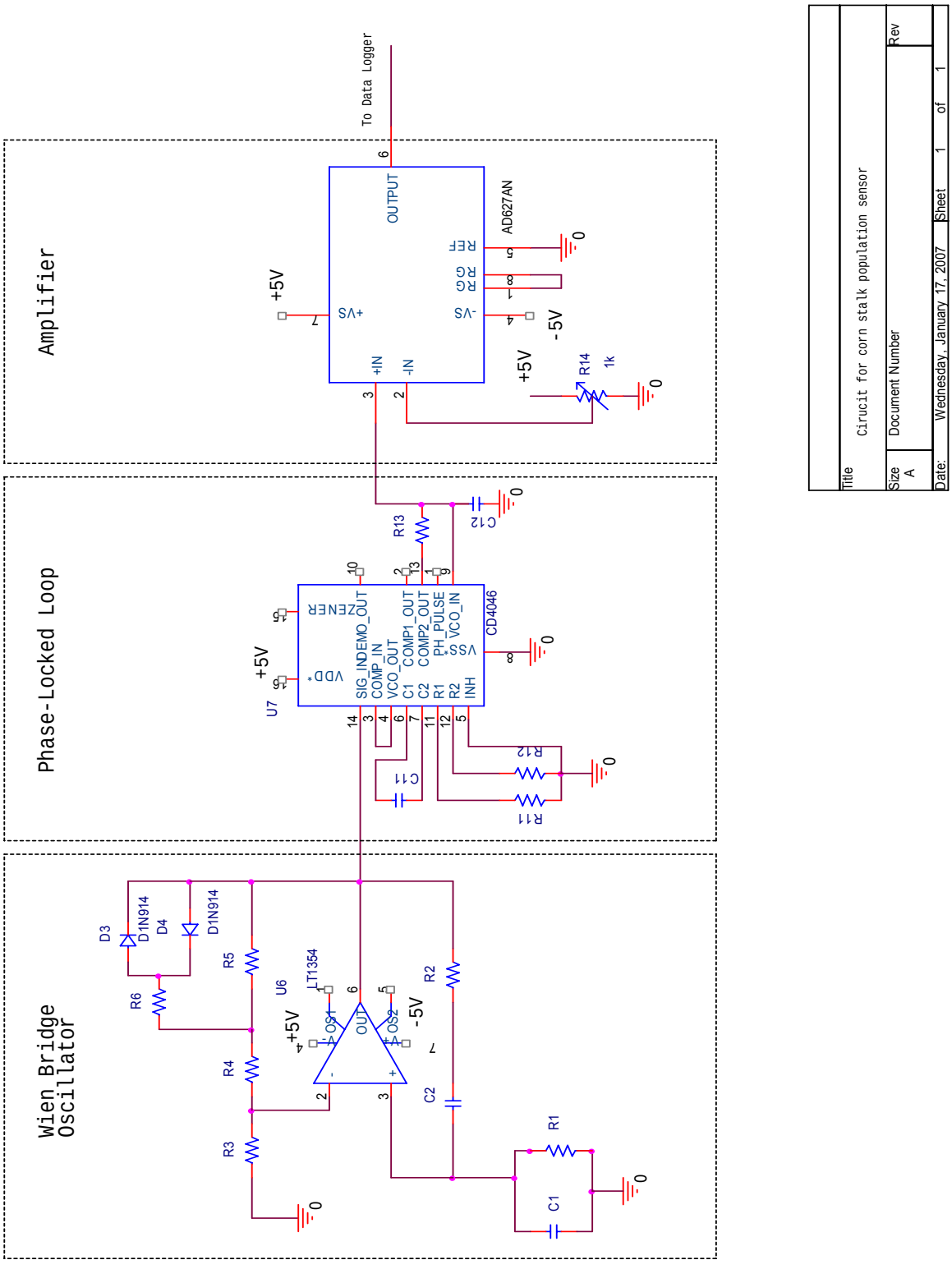
Amplifier
To Data Logger
OUTPUT
AD627AN
+VS
-VS
+IN
-IN
RG
REF
+5V
-5V
R14
1k
Phase-Locked Loop
U7
CD4046
SIG_IN
COMP_IN
VCO_OUT
ZENER
DEMO_OUT
COMP1_OUT
COMP2_OUT
PH_PULSE
VCO_IN
VDD
VSS
C1
C2
R1
R2
INH
R13
C12
R12
R11
C11
Wien Bridge Oscillator
U6
LT1354
OS1
OS2
OUT
R5
R6
R4
R3
R2
C2
R1
C1
D3
D4
D1N914
Title
Cirucit for corn stalk population sensor
Size
A
Document Number
Rev
Date:
Wednesday, January 17, 2007
Sheet
1
of
1

Appendix B. Electronic Device Specifications

Typical Performance Curves (Continued)

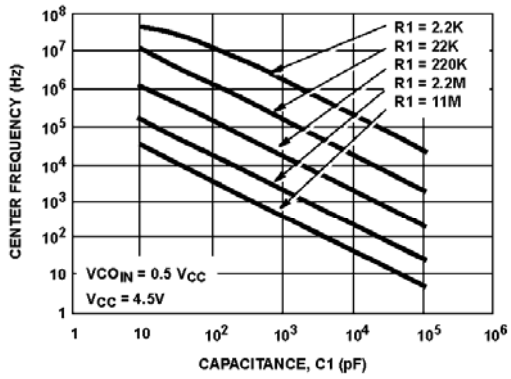

FIGURE 11. HC4046A TYPICAL CENTER FREQUENCY vs R1, C1 (V_{CC} = 4.5V)

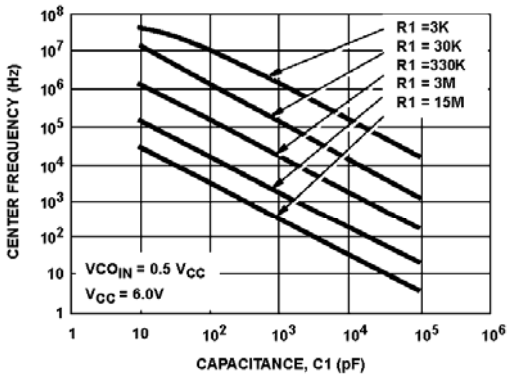

FIGURE 12. HC4046A TYPICAL CENTER FREQUENCY vs R1, C1 (V_{CC} = 6V)

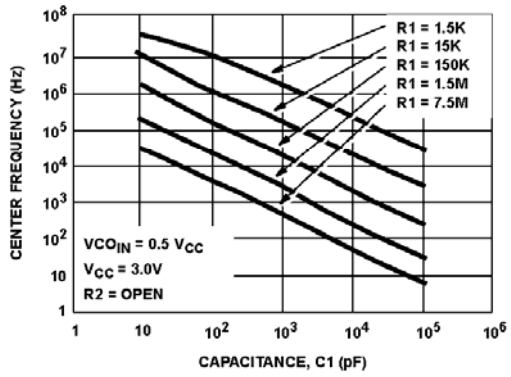

FIGURE 13. HC4046A TYPICAL CENTER FREQUENCY vs R1, C1 (V_{CC} = 3V, R2 = OPEN)

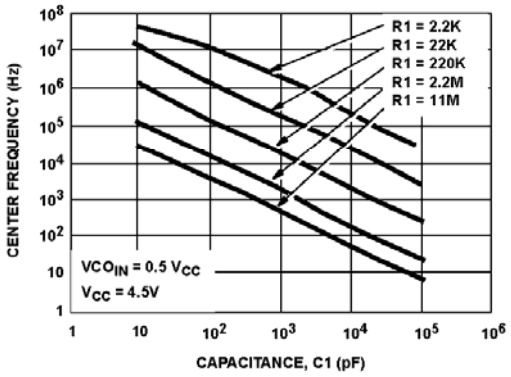

FIGURE 14. HCT4046A TYPICAL CENTER FREQUENCY vs R1, C1 (V_{CC} = 4.5V)

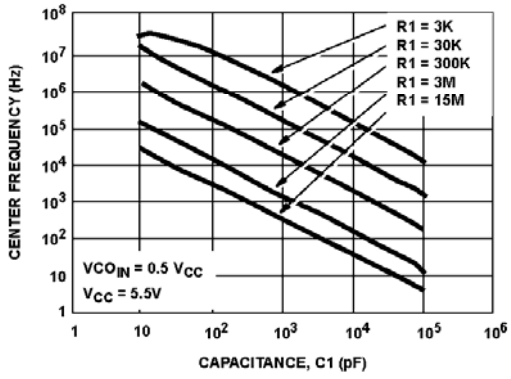

FIGURE 15. HCT4046A TYPICAL CENTER FREQUENCY vs R1, C1 (V_{CC} = 5.5V)

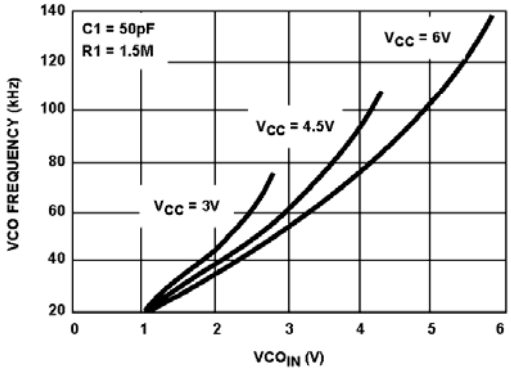

FIGURE 16. HC4046A TYPICAL VCO FREQUENCY vs VCO_{IN} (R1 = 1.5MΩ, C1 = 50pF)

Typical Performance Curves (Continued)

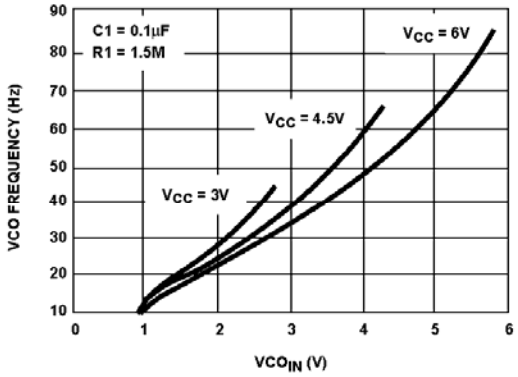

FIGURE 17. HC4046A TYPICAL VCO FREQUENCY vs VCO_{IN} ($R1 = 1.5M\Omega$, $C1 = 0.1\mu F$)

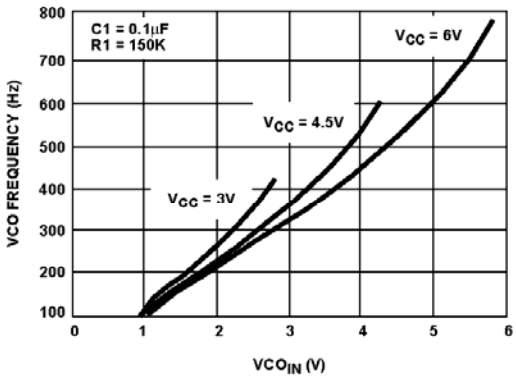

FIGURE 18. HC4046A TYPICAL VCO FREQUENCY vs VCO_{IN} ($R1 = 150k\Omega$, $C1 = 0.1\mu F$)

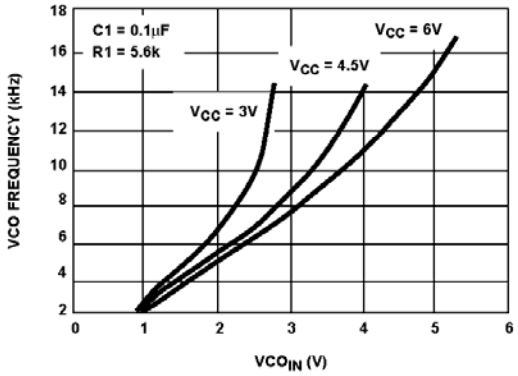

FIGURE 19. HC4046A TYPICAL VCO FREQUENCY vs VCO_{IN} ($R1 = 5.6k\Omega$, $C1 = 0.1\mu F$)

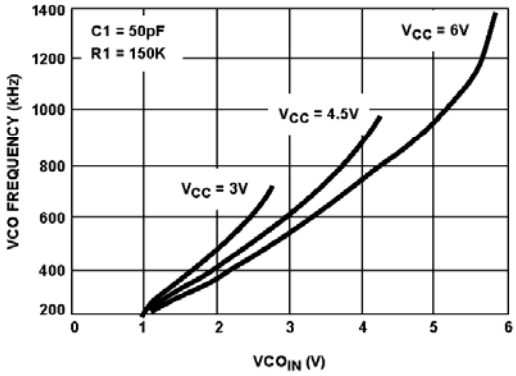

FIGURE 20. HC4046A TYPICAL VCO FREQUENCY vs VCO_{IN} ($R1 = 150k\Omega$, $C1 = 50pF$)

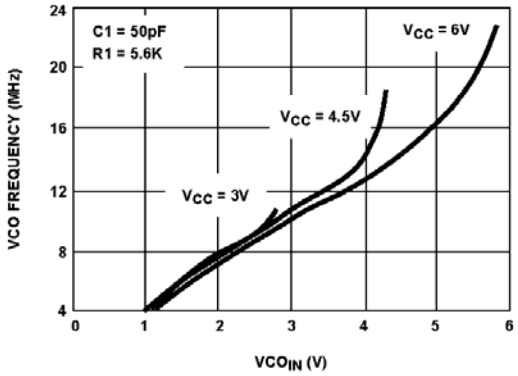

FIGURE 21. HC4046A TYPICAL VCO FREQUENCY vs VCO_{IN} ($R1 = 5.6k\Omega$, $C1 = 50pF$)

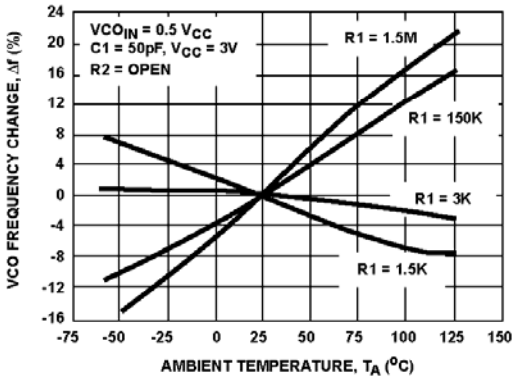

FIGURE 22. HC4046A TYPICAL CHANGE IN VCO FREQUENCY vs AMBIENT TEMPERATURE AS A FUNCTION OF R1 (V_{CC} = 3V)

Typical Performance Curves (Continued)

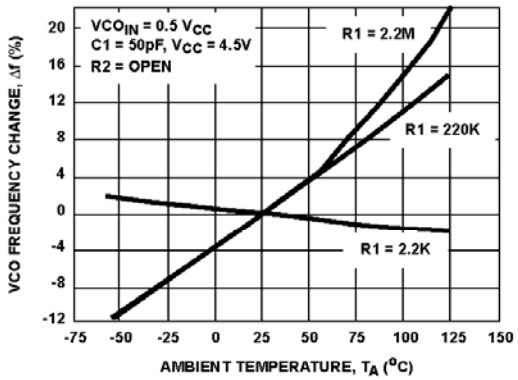

FIGURE 23. HC4046A TYPICAL CHANGE IN VCO FREQUENCY vs AMBIENT TEMPERATURE AS A FUNCTION OF R1 (V_{CC} = 4.5V)

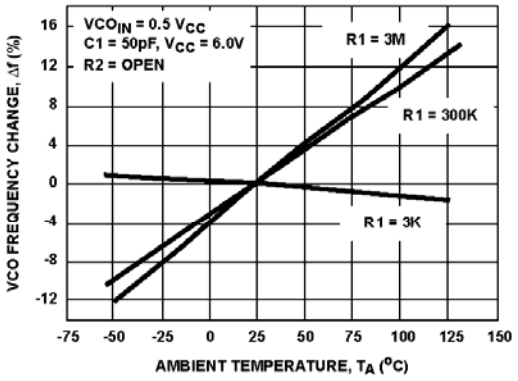

FIGURE 24. HC4046A TYPICAL CHANGE IN VCO FREQUENCY vs AMBIENT TEMPERATURE AS A FUNCTION OF R1 (V_{CC} = 6V)

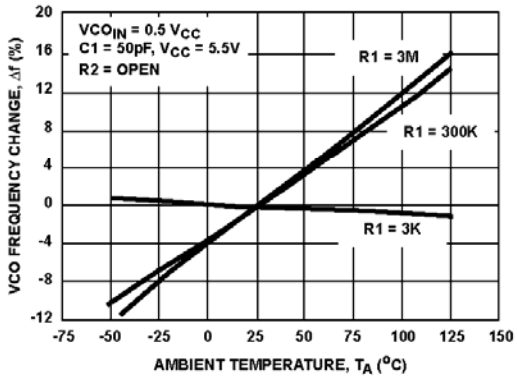

FIGURE 25. HCT4046A TYPICAL CHANGE IN VCO FREQUENCY vs AMBIENT TEMPERATURE AS A FUNCTION OF R1

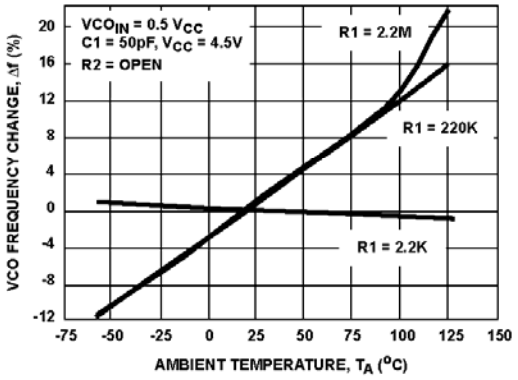

FIGURE 26. HC4046A TYPICAL CHANGE IN VCO FREQUENCY vs AMBIENT TEMPERATURE AS A FUNCTION OF R1 (V_{CC} = 4.5V)

Typical Performance Curves (Continued)

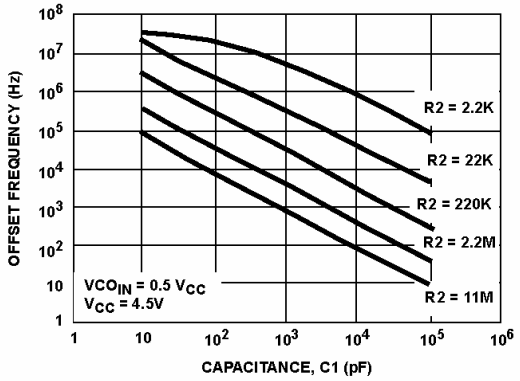

FIGURE 27. HC4046A OFFSET FREQUENCY vs R2, C1 (V_{CC} = 4.5V)

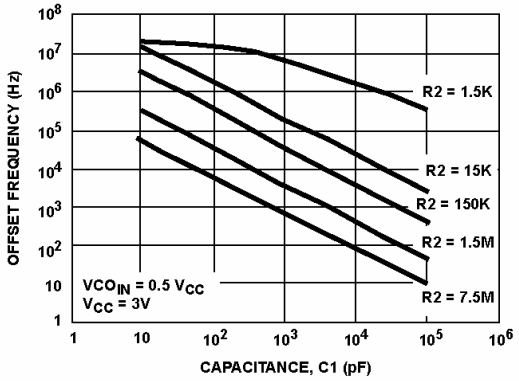

FIGURE 28. HC4046A OFFSET FREQUENCY vs R2, C1 (V_{CC} = 3V)

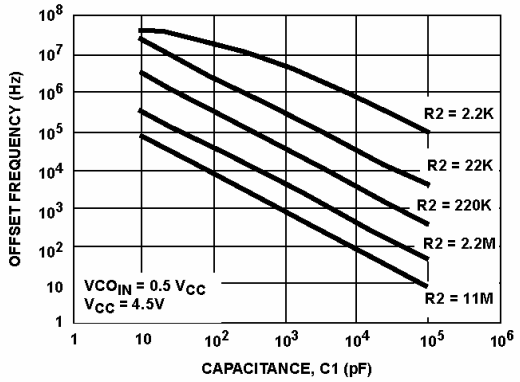

FIGURE 29. HCT4046A OFFSET FREQUENCY vs R2, C1 (V_{CC} = 4.5V)

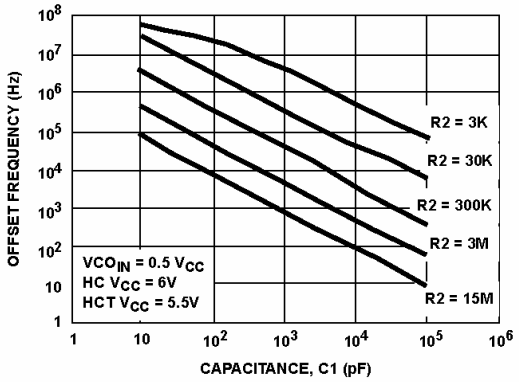

FIGURE 30. HC4046A AND HCT4046A OFFSET FREQUENCY vs R2, C1 (V_{CC} = 6V, V_{CC} = 5.5V)

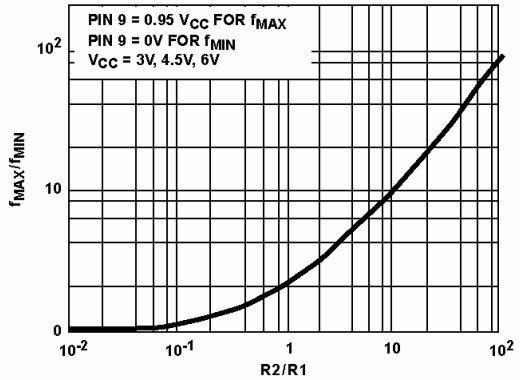

FIGURE 31. HC4046A f_{MIN}/f_{MAX} vs R2/R1 (V_{CC} = 3V, 4.5V, 6V)

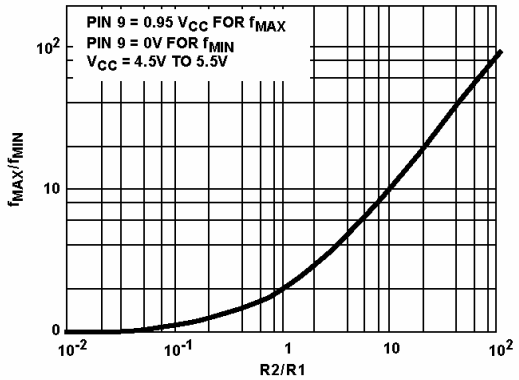

FIGURE 32. HCT4046A f_{MAX}/f_{MIN} vs R2/R1 (V_{CC} = 4.5V TO 5.5V)

Typical Performance Curves (Continued)

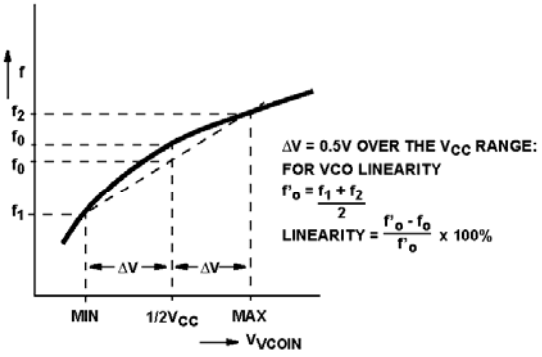

FIGURE 33. DEFINITION OF VCO FREQUENCY LINEARITY

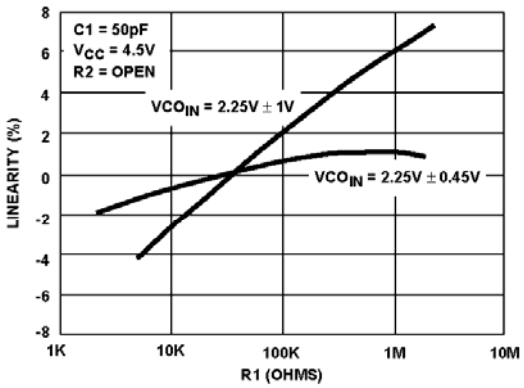

FIGURE 34. HC4046A VCO LINEARITY vs R1 (V_{CC} = 4.5V)

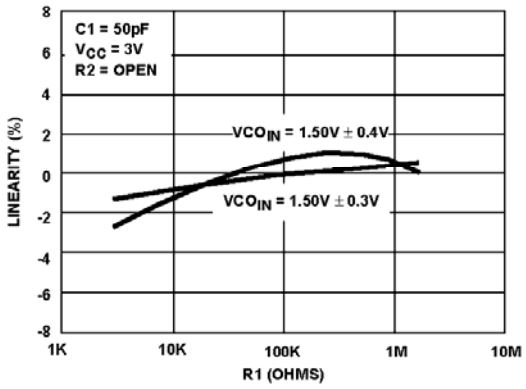

FIGURE 35. HC4046A VCO LINEARITY vs R1 (V_{CC} = 3V)

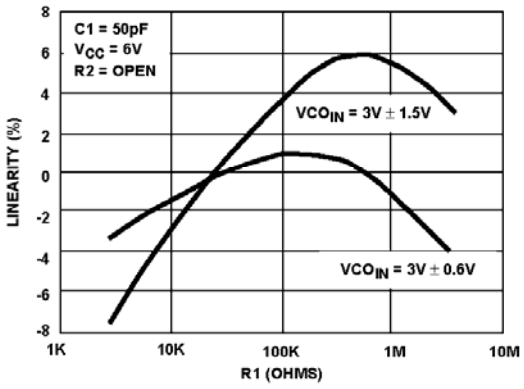

FIGURE 36. HC4046A VCO LINEARITY vs R1 (V_{CC} = 6V)

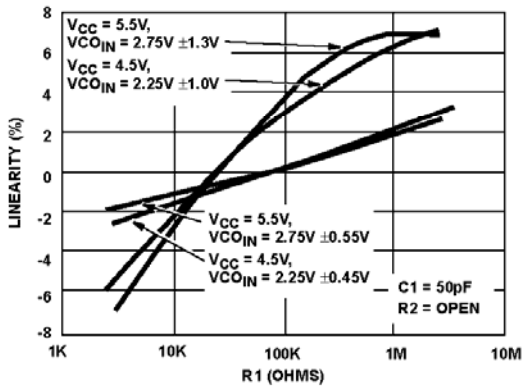

FIGURE 37. HCT4046A VCO LINEARITY vs R1 (V_{CC} = 4.5V, V_{CC} = 5.5V)

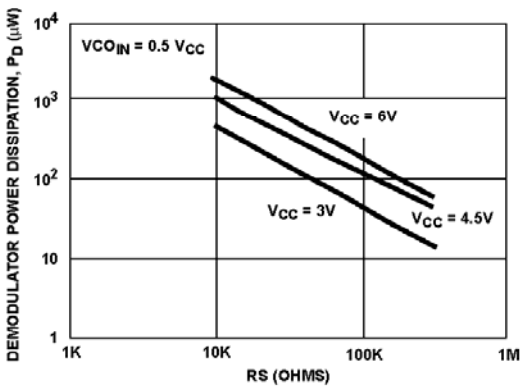

FIGURE 38. HC4046A DEMODULATOR POWER DISSIPATION vs RS (TYP) (V_{CC} = 3V, 4.5V, 6V)

Typical Performance Curves (Continued)

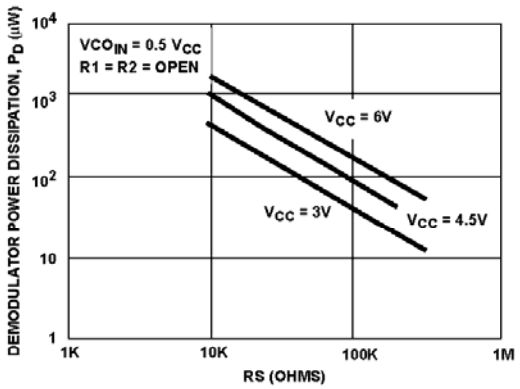

FIGURE 39. HCT4046A DEMODULATOR POWER DISSIPATION vs RS (TYP) (V_{CC} = 3V, 4.5V, 6V)

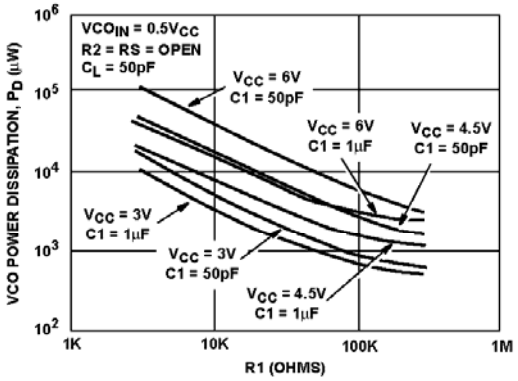

FIGURE 40. HC4046A VCO POWER DISSIPATION vs R1 (C1 = 50pF, 1μF)

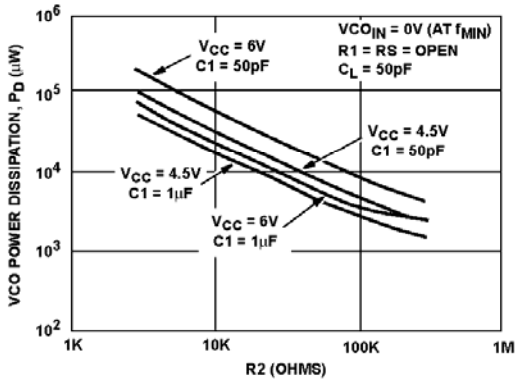

FIGURE 41. HCT4046A VCO POWER DISSIPATION vs R2 (C1 = 50pF, 1μF)

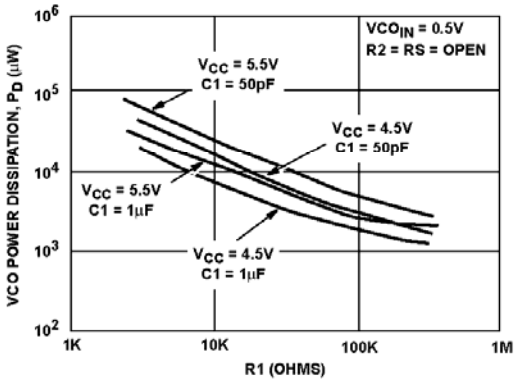

FIGURE 42. HCT4046A VCO POWER DISSIPATION vs R1 (C1 = 50pF, 1μF)

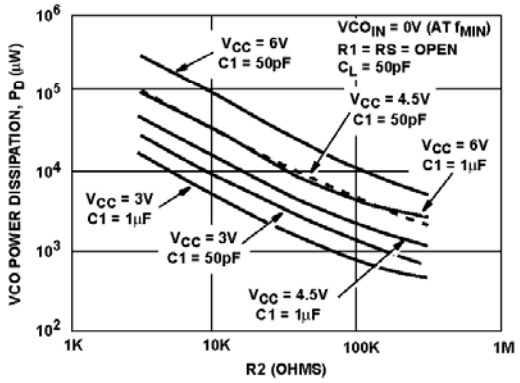

FIGURE 43. HC4046A VCO POWER DISSIPATION vs R2 (C1 = 50pF, 1μF)

Appendix C. Wien Bridge Oscillator Pspice Code

```
.lib "nom.lib"
* CURRENT PULSE TO START OSCILLATIONS
IS       0 1            PWL(0US 0MA   10US 1uA   40US 1uA   50US 0MA   10MS 0MA)
R_R1        0 1  50k    * Positive loop
C_C1        0 1  3p       * Detection Element
C_C2        1 3  3p         * Detection Element
R_R2        3 4  50k
R_R10       0 2  1k       *  Negative  loop
R_R11       2 6  1K
R_R12       6 4  6K
R_R13       6 5  2.4K
D_D1        5 4       D1N914     * Diodes
D_D2        4 5       D1N914
X_OP1       1 2 7 8 4    LT1354/LT   * Amplifier
V_V1        7 0 5Vdc     * Input power (positive)
V_V2        0 8 5Vdc       * Input power (negative)
.TRAN  0.01MS 0.1MS
.PROBE V(4)
.end
```

Appendix D. Matlab Code

AD.1 Import field raw data, Filter data by low pass filter, and downsample the filtered data

```
% Program for field data processing
% Oct. 16th, 2006

%%%%%%%%%%%%%%%%%%%%%%%%%%%%%%%%%%%%%%%%%%%%%%%%%%%%%%%%
%  import raw data
% RT_1,  Raw data collected in field

open ('RT_1.mat')
Rawdata = ans.RT_1(:,2);
%%%%%%%%%%%%%%%%%%%%%%%%%%%%%%%%%%%%%%%%%%%%%%%%%%%%%%%%



%%%%%%%%%%%%%%%%%%%%%%%%%%%%%%%%%%%%%%%%%%%%%%%%%%%%%%%%
%  LowPass Filter built in Matlab Simulink, See Appendix A2.2
%  First order Butterworth low pass filter with cut off frequency at 80 Hz
open ('FilterDesign.mdl')

% reorganize filtered data
SamplingLength = length(Filterdata);
Filtered = ones (1, SamplingLength);

for i = 1:SamplingLength
   Filtered (i) = Filterdata(1,1,i);
end
%%%%%%%%%%%%%%%%%%%%%%%%%%%%%%%%%%%%%%%%%%%%%%%%%%%%%%%%



%%%%%%%%%%%%%%%%%%%%%%%%%%%%%%%%%%%%%%%%%%%%%%%%%%%%%%%%
% Downsample the data by averaging.
SampleAve = 100;
SampleFreq = 10000/SampleAve;
RowSize = floor(SamplingLength/SampleAve);
MatrixSize = SampleAve*RowSize;
```

```
NewFiltered = Filterdata(1:MatrixSize);
Matrix_Reshaped = reshape(NewFiltered, SampleAve, RowSize);
Matrix_ave = (1/SampleAve)*ones(1, SampleAve)*Matrix_Reshaped;

timeline = 0.0001*SampleAve:0.0001*SampleAve:SamplingLength/10000;

figure(1)
plot(timeline, Matrix_ave); hold on;
xlabel('Time (s)');
ylabel('Voltage (V)');
title('Road Side,  Row 1, 2.1mph, 3.08 ft/s, Filtered Data (1 Order, 100 Hertz)');
figure(2)
plot(timeline, Matrix_ave); hold on;
xlabel('Time (s)');
ylabel('Voltage (V)');
title('Cursor Searching');
%%%%%%%%%%%%%%%%%%%%%%%%%%%%%%%%%%%%%%%%%%%%%%%%%%%%%%%%%%%%%%%%%%%%%%%%%%%%%%%%
```

A2.2 Low pass filter module developed in Simulink.

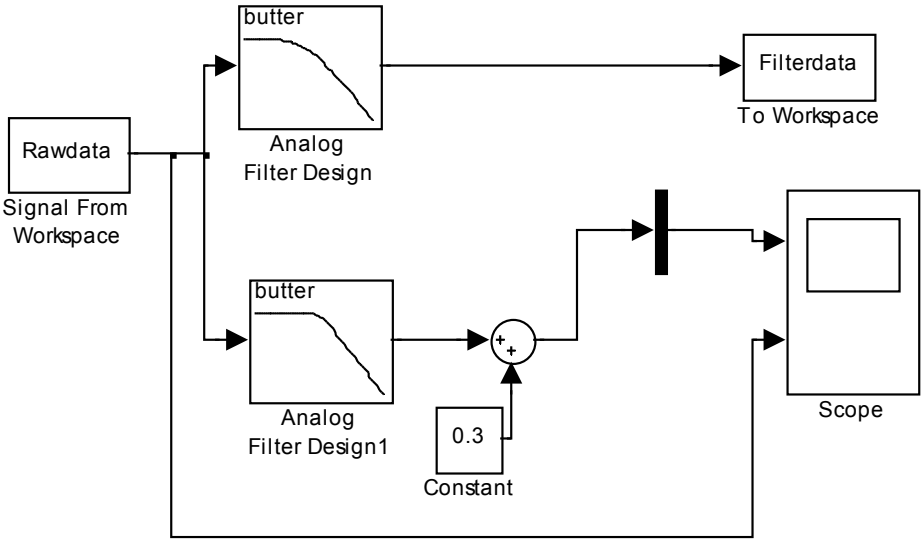

A2.3 Import the hand count position

```
%%%%%%%%%%%%%%%%%%%%%%%%%%%%%%%%%%%%%%%%%%
% load the corn stalk position file and count the column number

load 'RT_Dist'  % Matrix including the hand count position information

Location = RT_1;
[m, n] = size(Location);
%%%%%%%%%%%%%%%%%%%%%%%%%%%%%%%%%%%%%%%%%%



%%%%%%%%%%%%%%%%%%%%%%%%%%%%%%%%%%%%%%%%%%
% Automatically find the stalk peak and the peak maximum.

Cur_Num = n*2;
Cur_Index = zeros(1,Cur_Num);
Sampling_Freq = 10000/SampleAve;
for i = 1:Cur_Num
   indexrange = cursor_info(i).DataIndex-
        0.02*Sampling_Freq:cursor_info(i).DataIndex+0.02*Sampling_Freq;
   datarange = Matrix_ave(indexrange);
   [Maxdata, index] = sort(datarange, 'descend');
   Cur_Index(i) = cursor_info(i).DataIndex-0.02*Sampling_Freq + index(1) -1;
end

% order the cursors' locations
CursorPoint = sort(Cur_Index);
%%%%%%%%%%%%%%%%%%%%%%%%%%%%%%%%%%%%%%%%%%



%%%%%%%%%%%%%%%%%%%%%%%%%%%%%%%%%%%%%%%%%%
% Plot the stalk location

 for k = 1:n;
```

```
    b = isnan(Location(:,k));
    c = find(b);
    d = sort(c);
    if c
       Last_data = d(1)-1;
    else
       Last_data = length(Location(:,k));
    end
    temp1 = Location(2:Last_data, k)';
    temp2 = Location(1,k)*ones(1,(Last_data-1));
    Dist_Gap = temp1 - temp2;
    Dist = Location(Last_data,k) - Location(1,k);
    Point_Dist = CursorPoint(2*k) - CursorPoint(2*k-1);
    ratio = Point_Dist/Dist;
    format long
    ratio;
    Location_Turepoint = Location(1:Last_data, k);
    Location_Plot = CursorPoint(2*k-1)*ones(1, Last_data) + [0, Dist_Gap*ratio];
    format long
    Location_Plot;
    figure(1)
    stem(Location_Plot/SampleFreq,5*ones(1,Last_data),':sr','fill','MarkerSize',2);%hold on;
    stem(Location_Plot/SampleFreq,-5*ones(1,Last_data),':sr','fill','MarkerSize',2);%hold on;%
  end
%%%%%%%%%%%%%%%%%%%%%%%%%%%%%%%%%%%%%%
```

A2.4 Find the moving average, get the difference between downsampled data and moving average, and discard the information below 0.01

```
%%%%%%%%%%%%%%%%%%%%%%%%%%%%%%%%%%%%%%%
% Moving Average to minimize drift effect.

MovingAveRate = 13;

for l = MovingAveRate-floor(MovingAveRate/2):length(Matrix_ave)-floor(MovingAveRate/2);
   MovAved_temp(l)= Matrix_ave((l-ceil(MovingAveRate/2)+1):l+floor(MovingAveRate/2))*ones(MovingAveRate,1)/MovingAveRate;
end

MovAved = [MovAved_temp, zeros(1, floor(MovingAveRate/2))];
%%%%%%%%%%%%%%%%%%%%%%%%%%%%%%%%%%%%%%%


%%%%%%%%%%%%%%%%%%%%%%%%%%%%%%%%%%%%%%%
Diffe = Matrix_ave - MovAved;

figure(3)
plot(timeline, Matrix_ave, timeline, MovAved,'--g', timeline, Diffe, 'r');hold on; %, timeline, Diffe2,'b'); hold on;% timeline_ave, MovingAve_Ave,':.g');
title('Moving Average Data, Blue: Raw; Green, Moving Average; Red, Difference');
xlabel('time (s)');
ylabel('Voltage (V)');
%%%%%%%%%%%%%%%%%%%%%%%%%%%%%%%%%%%%%%%


%%%%%%%%%%%%%%%%%%%%%%%%%%%%%%%%%%%%%%%
%  Get rid of the information below 0.01

datalength1 = length(Diffe);

for i = 1: datalength1
   if (Diffe(i)<0.01)
```

```
   Diffe(i) = 0;
   end
end

Diffe(1:3) = 0; % Clean extreme situation

figure(4)
plot(timeline, Diffe);
title('Moving Average Cleaned by A Single Threshold');
xlabel('time (s)');
ylabel('Voltage (V)');
%%%%%%%%%%%%%%%%%%%%%%%%%%%%%%%%%%%%%%%%%%%%%%%%%%%%%%%%%%%%%%%%%%%%%%%%%%%%%%%%
```

A2.5 Feature Extraction 1. The first 5 features.

```
% Feature Spaces. Feature predefine (Not necessary, To show the Features extracted)
SigWid = zeros(1, datalength1);
SigMax = zeros(1, datalength1);
PlantNumber=  zeros(1,datalength1);
% Distance between two maxs
% Gap between two signals
% Average Moisture Content of last potential 5 stalks.

FeaIndex = 0;

% Feature Extractionn
a1 = 1;
b1 = 0;

for i = 2: datalength1

   % Determine signal Height and width

   if (( Diffe(i) > Diffe(i-1) ) &  (Diffe(i-1) == 0))
      a1 = i;
   end

   if ((Diffe(i) < Diffe(i-1)) &  (Diffe(i) == 0))
      b1 = i-1;
   end

   if (b1 > a1)
   SigWid(1, a1:b1) = b1 - a1 + 3;
   SigMax(1, a1:b1) = max(Diffe(a1 : b1));
   [Temp_Max, Max_Index] = max(Diffe(a1 : b1));

   FeaIndex = FeaIndex + 1;
   Features_Pre(1, FeaIndex) = b1 - a1 + 3;
```

```
Features_Pre(2, FeaIndex) = max(Diffe(a1 : b1));
Features_Pre(4, FeaIndex) = Max_Index + a1 -1;
Features_Pre(5, FeaIndex) = a1 - 1;
Features_Pre(6, FeaIndex) = b1 + 1;
end

% Detemine Signal Mono Properties.

if ((b1 > a1) & ((b1 - a1) < 2))
   PlantNumber(1, a1:b1) = 1;
   Features_Pre(3, FeaIndex) = 1;
end

if ((b1 - a1) >= 2)

LocalLength = length(a1:b1);
[LocalMax, LocalMaxIndex] = max(Diffe(a1:b1));

Increase = 1;
for p1 = (a1-1):(LocalMaxIndex+a1-2)
   if (Diffe(p1+1) >= Diffe(p1))
      Inc = 1;
   else
      Inc = 0;
   end
   Increase = Increase*Inc;

end


Decrease = 1;
for p2 = (LocalMaxIndex+a1-1):b1
   if (Diffe(p2+1) <= Diffe(p2))
      Dec = 1;
   else
```

```
        Dec = 0;
      end
      Decrease = Decrease*Dec;

   end

   MonoDetect = Increase*Decrease;

   if MonoDetect == 1
      PlantNumber(1, a1:b1) = 1;
      Features_Pre(3, FeaIndex) = 1;
   else
      PlantNumber(1, a1:b1) = 2;
      Features_Pre(3, FeaIndex) = 2;
   end

   end
end

figure(5)
plot(timeline, Diffe, timeline, PlantNumber, timeline, SigWid);hold on;

figure(6)
plot(Diffe,'k'); hold on;
%plot(PlantNumber,'y');hold on;
%plot(SigWid,'b');hold on;


% Plot the stalk location

 for k = 1:n;

   b = isnan(Location(:,k));
   c = find(b);
   d = sort(c);
```

```
    if c
        Last_data = d(1)-1;
    else
        Last_data = length(Location(:,k));
    end
    temp1 = Location(2:Last_data, k)';
    temp2 = Location(1,k)*ones(1,(Last_data-1));
    Dist_Gap = temp1 - temp2;
    Dist = Location(Last_data,k) - Location(1,k);
    Point_Dist = CursorPoint(2*k) - CursorPoint(2*k-1);
    ratio = Point_Dist/Dist;
    format long
    ratio;
    Location_Turepoint = Location(1:Last_data, k);
    Location_Plot = CursorPoint(2*k-1)*ones(1, Last_data) + [0, Dist_Gap*ratio];
    format long
    Location_Plot;
    figure(5)
    stem(Location_Plot/SampleFreq,5*ones(1,Last_data),':sr','fill','MarkerSize',2);%hold on;
    stem(Location_Plot/SampleFreq,-5*ones(1,Last_data),':sr','fill','MarkerSize',2);%hold on;%
    figure(6)
    stem(Location_Plot,5*ones(1,Last_data),':sr','fill','MarkerSize',2);%hold on;
    stem(Location_Plot,-5*ones(1,Last_data),':sr','fill','MarkerSize',2);%hold on;%

  end

% Feature Space Simplification

Features = zeros(6,30);
Fealength = length(Features_Pre(2,:));
k = 0;
for i = 1:Fealength-1
    k = k + 1;
    Features(:,k) = Features_Pre(:,i);
```

```
    if ((Features_Pre(1,i) == Features_Pre(1,(i+1))) & (Features_Pre(2,i) == Features_Pre(2,(i+1))) &
        (Features_Pre(3,i) == Features_Pre(3,(i+1))))
      k = k - 1;
    end
end

Features_Temp1 = Features(4,1:(length(Features(4,:))-1));
Features_Temp2 = Features(4,2:length(Features(4,:)));
Features(4,:) = [0, Features_Temp2 - Features_Temp1];

Features_Temp3 = Features(5,2:length(Features(5,:)));
Features_Temp4 = Features(6,1:(length(Features(6,:))-1));
Features(5,:) = [0, Features_Temp3 - Features_Temp4];
```

A2.5 Feature Extraction 2. The last 3 features.

```
% A11_2 Feature Reorganization

load ('Features_RT_1.mat')
load ('Features_RT_2.mat')
load ('Features_RT_3.mat')
load ('Features_RT_4.mat')
load ('Features_RT_5.mat')
load ('Features_RT_6.mat')



load ('Features_A11_2_1.mat')
load ('Features_A11_2_2.mat')
load ('Features_A11_2_3.mat')
load ('Features_A11_2_4.mat')
load ('Features_A11_2_5.mat')
load ('Features_A11_2_6.mat')



load ('Features_A11_9.mat')
load ('Features_A11_10.mat')
load ('Features_A11_11.mat')
load ('Features_A11_12.mat')
load ('Features_A11_15.mat')



Reorg_Temp1 = [Features_RT_1 Features_RT_2 Features_RT_3 Features_RT_4 Features_RT_5
        Features_RT_6 Features_A11_2_1 Features_A11_2_2 Features_A11_2_3 Features_A11_2_4
        Features_A11_2_5 Features_A11_2_6 Features_A11_9 Features_A11_10 Features_A11_11
        Features_A11_12 Features_A11_15];


ReorgLength = length(Reorg_Temp1(1,:));


% eliminate the effect of subsampling
for ii = 1: ReorgLength;
```

```
    if Reorg_Temp1(4,ii) == 0
        Reorg_Temp1(4,ii) = 17;
    end

    if Reorg_Temp1(5,ii) == 0
        Reorg_Temp1(5,ii) = 5;
    end

    if Reorg_Temp1(4,ii) > 40
        Reorg_Temp1(4,ii) = 40;
    end

    if Reorg_Temp1(5,ii) > 36
        Reorg_Temp1(5,ii) = 36;
    end

end

% Maximum Value Pattern
% stem(Reorg_Temp1(2,:),'sr', 'fill', 'markersize', 3);

% the feature of potential moisture content effect

Reorg_Temp2 = [Reorg_Temp1(2,1:5) Reorg_Temp1(2,:) Reorg_Temp1(2,(ReorgLength-
        4):ReorgLength)];

for jj = 6: (ReorgLength+5);
    Sort_temp = sort(Reorg_Temp2((jj-5):(jj+5)));
    NoLittle = Sort_temp(1,3);

    for kk = -5:5
        if Reorg_Temp2(jj+kk) < NoLittle;
            Reorg_temp3(kk+6) = 0;
        else
```

```
            Reorg_temp3(kk+6) = Reorg_Temp2(jj+kk);
        end
    end
    Reorg_temp4 = sort(Reorg_temp3);
    Reorg_temp5 = Reorg_temp4(3:11);
    Reorg_Temp1(6, (jj-5)) = (1/9)*Reorg_temp5*ones(9,1);
end

% Feature 7

Reorg_Temp1(7,:) = [Reorg_Temp1(2, ReorgLength), Reorg_Temp1(2, 1:(ReorgLength-1))];

% Feature 8

Reorg_Temp1(8,:) = [Reorg_Temp1(2, 2:ReorgLength), Reorg_Temp1(2, 1)];
```

A2.5 Principal Component Analysis

```
% Both prepca and princomp are principal component analysis function.  The first one is designed specially
        for neural network.  The second can show more detail information on each component.


[pn,meanp,stdp] = prestd(Reorg_Temp1);
[NN_P, NN_Mat] = prepca(pn, 0.1);
stdr = std(Reorg_Temp1');
sr = Reorg_Temp1'./repmat(stdr,3116,1);
[pcs,newdata,variances,t2] = princomp(sr);
percent_explained = 100*variances/sum(variances);
```

A2.5 Artificial Neural Network

```
%%%%%%%%%%%%%%%%%%%%%%%%%%%%%%%%%%%%%%%%
%  Build input/target dataset
load ('NN_T_RTRaw')

load ('NN_T_Raw')

load ('NN_T_A11Raw')

NN_T = [NN_T_RTRaw(1,:) NN_T_RTRaw(2,:) NN_T_RTRaw(3,:) NN_T_RTRaw(4,:)
        NN_T_RTRaw(5,:) NN_T_RTRaw(6,:) NN_T_Raw(1,:) NN_T_Raw(2,:) NN_T_Raw(3,:)
        NN_T_Raw(4,:) NN_T_Raw(5,:) NN_T_Raw(6,:) NN_T_A11Raw(1,:) NN_T_A11Raw(2,:)
        NN_T_A11Raw(3,:) NN_T_A11Raw(4,:) NN_T_A11Raw(5,:) 10];

NN_T_Leng = length(NN_T);

k = 1;

while NN_T(k) ~= 10

  if isnan(NN_T(k))
    NN_T(k) = [];
    k = k-1;
  end
  k = k + 1;

end

NN_T_Leng = length(NN_T);

NN_T = NN_T(1:(NN_T_Leng - 1));

NN_Data = [NN_P; NN_T];
%%%%%%%%%%%%%%%%%%%%%%%%%%%%%%%%%%%%%%%%
```

```
%%%%%%%%%%%%%%%%%%%%%%%%%%%%%%%%%%%%%
% Determine two stalks in one signal
% NN_T modification

PotentialTwoStalk = 0;

NN_T_Leng = length(NN_T);

for i = 1:NN_T_Leng
   if NN_T(i) == 2
      NN_T(i) = 1;
      PotentialTwoStalk = PotentialTwoStalk + 1;
   end
end
 %%%%%%%%%%%%%%%%%%%%%%%%%%%%%%%%%%%%%


%%%%%%%%%%%%%%%%%%%%%%%%%%%%%%%%%%%%%
% Determine test, valadation, and training data sets.

[R, Q] = size(NN_Data);

NNtst = [1:5:Q 3:5:Q 5:5:Q];
%NNval = 4:4:Q;
NNtr  = [4:5:Q 2:5:Q];


%P_Val = NN_P(:,NNval);  T_Val = NN_T(:,NNval);
P_Tst = NN_P(:,NNtst);  T_Tst = NN_T(:,NNtst);
P_Tr  = NN_P(:,NNtr);   T_Tr  = NN_T(:,NNtr);

%%%%%%%%%%%%%%%%%%%%%%%%%%%%%%%%%%%%%
```

```
%%%%%%%%%%%%%%%%%%%%%%%%%%%%%%%%%%%%%%%%%%%%
% Neural Network

net = newff(minmax(P_Tr),[3 1], {'tansig' 'purelin'},'trainbfg');
net.trainParam.epochs = 300;
[net tr] = train(net, P_Tr, T_Tr);
SimT = sim(net, P_Tst);
figure(10)
plot(T_Tst, SimT, '+');
xlabel('Hand Count Value');
ylabel('Modeled Value');
title('Overfitting Evaluation');
axis([-0.5 3.5 -1 2.5]);



HitZero = 0;
HitOne  = 0;
MisTrg  = 0;
Fail    = 0;



SimTRound = round(SimT);

SimTlength = length(SimT);
for ss = 1:SimTlength
   if ((SimTRound(ss) <= 0) & (T_Tst(ss) == 0))
      HitZero = HitZero + 1;
   elseif ((SimTRound(ss) == 1) & (T_Tst(ss) == 1))
      HitOne = HitOne + 1;
   elseif ((SimTRound(ss) <= 0) & (T_Tst(ss) == 1))
      Fail = Fail + 1;
   elseif ((SimTRound(ss) == 1) & (T_Tst(ss) == 0))
      MisTrg = MisTrg + 1;
   end
end
```

```
% True value of corn stalks by hand count

TureTotalStalksLength = length(NNtst);

TureTotalStalks = 0;
for i = 1:TureTotalStalksLength
   if T_Tst(i) == 1;
      TureTotalStalks = TureTotalStalks + 1;
   end
end

TureTotalStalks = TureTotalStalks + PotentialTwoStalk;

ModelTotalStalks = HitOne + MisTrg;

disp('The true stalk number by hand count is:')
disp(TureTotalStalks)

disp('The stalk number calculated by model is:')
disp(ModelTotalStalks)

disp('Hit Zero = ')
disp(HitZero)

disp('Hit One =')
disp(HitOne)

disp('False Positive =')
disp(MisTrg)

disp('False negative =')
disp(Fail)
%%%%%%%%%%%%%%%%%%%%%%%%%%%%%%%%%%%%%%%%%%%%%%%%%%%%%%%%
```

A2.5 Accuracy Analysis at different Resolution

```
GroupSize = 5;  % Resolution
k = 0;

NN_P_length = length(NN_P(1,:));

GroupNumber = floor(NN_P_length/GroupSize);

NN_P_group = NN_P(:,1:GroupNumber*GroupSize);
NN_T_group = NN_T(1:GroupNumber*GroupSize);

NN_P_groupinput = reshape(NN_P_group, 3, GroupSize, GroupNumber);
NN_T_groupinput = reshape(NN_T_group, 1, GroupSize, GroupNumber);

Features_org = Reorg_Temp1(:,1:GroupNumber*GroupSize);
Features_Raw_Group =  reshape(Features_org, 8, GroupSize, GroupNumber);



for p = 1:GroupNumber

    SimT_ind = sim(net, NN_P_groupinput(:,:,p));

    HitZero = 0;
   HitOne  = 0;
   HitTwo  = 0;
   MisTrg  = 0;
   Fail    = 0;
   MisTrg2_1 = 0;
   MisTrg1_2 = 0;

   SimTRound = round(SimT_ind);

   for ss = 1:GroupSize
      if ((SimTRound(ss) <= 0) & (T_Tst(ss) == 0))
```

```
        HitZero = HitZero + 1;
    elseif ((SimTRound(ss) == 1) & (T_Tst(ss) == 1))
        HitOne = HitOne + 1;
    elseif ((SimTRound(ss) <= 0) & (T_Tst(ss) == 1))
        Fail = Fail + 1;
    elseif ((SimTRound(ss) == 1) & (T_Tst(ss) == 0))
        MisTrg = MisTrg + 1;
    elseif ((SimTRound(ss) >= 2) & (T_Tst(ss) == 2))
        HitTwo = HitTwo + 1;
    elseif ((SimTRound(ss) <= 1) & (T_Tst(ss) == 2))
        MisTrg2_1 = MisTrg2_1 + 1;
    elseif ((SimTRound(ss) >= 2) & (T_Tst(ss) == 1))
        MisTrg1_2 = MisTrg2_1 + 1;
    end
end

NN_T_ind = NN_T_groupinput(:,:,p);
TureTotalStalks_ind = 0;
for i = 1:GroupSize
    if NN_T_ind(i) == 1;
        TureTotalStalks_ind = TureTotalStalks_ind + 1;
    end
    if NN_T_ind(i) == 2;
        TureTotalStalks_ind = TureTotalStalks_ind + 2;
    end
end


ModelTotalStalks_ind = HitOne + HitTwo*2 + MisTrg*1 + MisTrg2_1 + MisTrg1_2*2;


Result_ind(p,:) = [TureTotalStalks_ind ModelTotalStalks_ind HitZero HitOne HitTwo Fail MisTrg
        MisTrg2_1 MisTrg1_2];


Result_Diff = abs(TureTotalStalks_ind - ModelTotalStalks_ind);
```

```
    if Result_Diff == 0
        k = k + 1;
        zerosorder(k) = p;
        ZeroDataSet(:,:, k) = [NN_T_ind' SimTRound' NN_P_groupinput(:,:,p)' Features_Raw_Group(:,:,p)'];
    end
end

Result_diff = abs(Result_ind(:,1) - Result_ind(:,2));

Rightcatch = 0;
MissOne = 0;
MissTwo = 0;
MissThree = 0;
MissFour = 0;
MissFive = 0;
MissSix = 0;
MissSeven = 0;
MissMore = 0;

    for mm = 1:GroupNumber
        if (Result_diff(mm) == 0)
            Rightcatch = Rightcatch + 1;
        elseif (Result_diff(mm) == 1)
            MissOne = MissOne + 1;
            elseif (Result_diff(mm) == 2)
                MissTwo = MissTwo + 1;
                elseif (Result_diff(mm) == 3)
                    MissThree = MissThree + 1;
                    elseif (Result_diff(mm) == 4)
                        MissFour = MissFour + 1;
                        elseif (Result_diff(mm) == 5)
                            MissFive = MissFive + 1;
                                elseif (Result_diff(mm) == 6)
                                MissSix = MissSix + 1;
                                    elseif (Result_diff(mm) == 7)
```

```
                    MissSeven = MissSeven + 1;
                elseif (Result_diff(mm) > 7)
                    MissMore = MissMore + 1;
        end
    end

disp('Sample Signal Size = ')
disp(GroupSize)

Result_miss = [Rightcatch MissOne MissTwo MissThree MissFour MissFive MissSix MissSeven
        MissMore]

percent = 100*Result_miss/sum(Result_miss)

Result_mean = mean(Result_ind(:,1:2))
```

A2.5 “I Don’t Know” Test

```
clear
clc


RotationTime = 20;


% A11_2 Feature Reorganization

load ('Features_RT_1.mat')
load ('Features_RT_2.mat')
load ('Features_RT_3.mat')
load ('Features_RT_4.mat')
load ('Features_RT_5.mat')
load ('Features_RT_6.mat')


load ('Features_A11_2_1.mat')
load ('Features_A11_2_2.mat')
load ('Features_A11_2_3.mat')
load ('Features_A11_2_4.mat')
load ('Features_A11_2_5.mat')
load ('Features_A11_2_6.mat')


load ('Features_A11_9.mat')
load ('Features_A11_10.mat')
load ('Features_A11_11.mat')
load ('Features_A11_12.mat')
load ('Features_A11_15.mat')
```

```
Reorg_Temp1 = [Features_RT_1 Features_RT_2 Features_RT_3 Features_RT_4 Features_RT_5
        Features_RT_6 Features_A11_2_1 Features_A11_2_2 Features_A11_2_3 Features_A11_2_4
        Features_A11_2_5 Features_A11_2_6 Features_A11_9 Features_A11_10 Features_A11_11
        Features_A11_12 Features_A11_15];


ReorgLength = length(Reorg_Temp1(1,:));


% eliminate the effect of subsampling
for ii = 1: ReorgLength;


   if Reorg_Temp1(4,ii) == 0
      Reorg_Temp1(4,ii) = 17;
   end


   if Reorg_Temp1(5,ii) == 0
      Reorg_Temp1(5,ii) = 5;
   end


   if Reorg_Temp1(4,ii) > 40
      Reorg_Temp1(4,ii) = 40;
   end


   if Reorg_Temp1(5,ii) > 36
      Reorg_Temp1(5,ii) = 36;
   end


end


% Maximum Value Pattern
% stem(Reorg_Temp1(2,:),'sr', 'fill', 'markersize', 3);


% the feature of potential moisture content effect


Reorg_Temp2 = [Reorg_Temp1(2,1:5) Reorg_Temp1(2,:) Reorg_Temp1(2,(ReorgLength-
        4):ReorgLength)];
```

```
for jj = 6: (ReorgLength+5);
   Sort_temp = sort(Reorg_Temp2((jj-5):(jj+5)));
   NoLittle = Sort_temp(1,3);

   for kk = -5:5
       if Reorg_Temp2(jj+kk) < NoLittle;
          Reorg_temp3(kk+6) = 0;
       else
          Reorg_temp3(kk+6) = Reorg_Temp2(jj+kk);
       end
   end
   Reorg_temp4 = sort(Reorg_temp3);
   Reorg_temp5 = Reorg_temp4(3:11);
   Reorg_Temp1(6, (jj-5)) = (1/9)*Reorg_temp5*ones(9,1);
end

% Feature 7

Reorg_Temp1(7,:) = [Reorg_Temp1(2, ReorgLength), Reorg_Temp1(2, 1:(ReorgLength-1))];

% Feature 8

Reorg_Temp1(8,:) = [Reorg_Temp1(2, 2:ReorgLength), Reorg_Temp1(2, 1)];


% Neural Network Preprocessing by std and Principal component Analysis
[pn,meanp,stdp] = prestd(Reorg_Temp1);
[NN_P, NN_Mat] = prepca(pn, 0.1);
[pcs,newdata,variances,t2] = princomp(Reorg_Temp1');
percent_explained = 100*variances/sum(variances);

% Neural Network Target Data Set

load ('NN_T_RTRaw')
```

```
load ('NN_T_Raw')


load ('NN_T_A11Raw')


NN_T = [NN_T_RTRaw(1,:) NN_T_RTRaw(2,:) NN_T_RTRaw(3,:) NN_T_RTRaw(4,:)
        NN_T_RTRaw(5,:) NN_T_RTRaw(6,:) NN_T_Raw(1,:) NN_T_Raw(2,:) NN_T_Raw(3,:)
        NN_T_Raw(4,:) NN_T_Raw(5,:) NN_T_Raw(6,:) NN_T_A11Raw(1,:) NN_T_A11Raw(2,:)
        NN_T_A11Raw(3,:) NN_T_A11Raw(4,:) NN_T_A11Raw(5,:) 10];


NN_T_Leng = length(NN_T);


k = 1;


while NN_T(k) ~= 10

   if isnan(NN_T(k))
      NN_T(k) = [];
      k = k-1;
   end
   k = k + 1;

end



NN_T_Leng = length(NN_T);


NN_T = NN_T(1:(NN_T_Leng - 1));


NN_Data = [NN_P; NN_T];



% NN_T modification


PotentialTwoStalk = 0;


NN_T_Leng = length(NN_T);
```

```
for i = 1:NN_T_Leng
   if NN_T(i) == 2
      NN_T(i) = 1;
      PotentialTwoStalk = PotentialTwoStalk + 1;
   end
end

% Determine test, valadation, and training data sets.

[R, Q] = size(NN_Data);

NNtst = [1:5:Q 3:5:Q 5:5:Q];
%NNval = 4:4:Q;
NNtr  = [4:5:Q 2:5:Q];

% First group

%P_Val = NN_P(:,NNval);  T_Val = NN_T(:,NNval);
P_Tst1 = NN_P(:,NNtst);  T_Tst1 = NN_T(:,NNtst);
P_Tr1  = NN_P(:,NNtr);   T_Tr1  = NN_T(:,NNtr);

% Second Group

NNtr2 = NNtst;
NNtst2 = NNtr;

%P_Val = NN_P(:,NNval);  T_Val = NN_T(:,NNval);
P_Tst2 = NN_P(:,NNtst2);  T_Tst2 = NN_T(:,NNtst2);
P_Tr2  = NN_P(:,NNtr2);   T_Tr2  = NN_T(:,NNtr2);

NN_T = [T_Tst1 T_Tst2];
%%%%%%%%%% Rotation Process
```

```
Totallength = length(NN_P);

T_PR = zeros(RotationTime, Totallength);

endpoint = length(NNtst);

beginpoint = endpoint + 1;

for RO = 1:RotationTime


% Neural Network

% First group
net = newff(minmax(P_Tr1),[4 1], {'tansig' 'purelin'},'trainbfg');
net.trainParam.epochs = 300;
net.trainParam.goal = 0.05;
[net tr] = train(net, P_Tr1, T_Tr1);
SimT = sim(net, P_Tst1);
figure(10)
plot(T_Tst1, SimT, '+');
xlabel('Hand Count Value');
ylabel('Modeled Value');
title('Overfitting Evaluation');
axis([-0.5 3.5 -1 2.5]);

2*RO-1

SimTRound = round(SimT);

roundsimt = round(SimT);

T_PR(RO, 1:endpoint) = roundsimt;
```

```
%%%%%%%%%%%%%%%%%%%%%%%%%%%%%%%%%%%%%%%

% second group
net = newff(minmax(P_Tr2),[4 1], {'tansig' 'purelin'},'trainbfg');
net.trainParam.epochs = 300;
net.trainParam.goal = 0.05;
[net tr] = train(net, P_Tr2, T_Tr2);
SimT = sim(net, P_Tst2);
figure(10)
plot(T_Tst2, SimT, '+');
xlabel('Hand Count Value');
ylabel('Modeled Value');
title('Overfitting Evaluation');
axis([-0.5 3.5 -1 2.5]);

2*RO

SimTRound = round(SimT);

roundsimt = round(SimT);

T_PR(RO, beginpoint:Totallength) = roundsimt;

end

%%%%%%%%%%%%%%%%%%%%%%%%%%%%%%%%%

NumDtKnown = 0;
NumStalks = 0;
Miss = 0;

for PR = 1:Totallength
   TestPoint = 1;
   for OR = 1:(RotationTime - 1)
```

```
        if T_PR(OR,PR) ~= T_PR((OR+1),PR)
            TestPoint = TestPoint * 0;
        end
    end

    if TestPoint == 0
        PR;
        NumDtKnown = NumDtKnown + 1;
    end

    if TestPoint == 1
        if T_PR(1, PR) ~= NN_T(1, PR)
            Miss = Miss + 1;
        end
    end
end



for PR = 1:Totallength
    TestPoint = 1;
    for OR = 1: RotationTime
        TestPoint = T_PR(OR,PR) * TestPoint;
    end
    if TestPoint
        NumStalks = NumStalks + 1;
    end
end


NumDtKnown
NumStalks
Miss
```

Vita

Haizhou Li was born in Jiaozuo, Henan Province, China on April 3, 1978. He attended Student Road Elementary School and graduated from Jiaozuo No. 1 High School in July 1996.

In September 1996, he entered Henan University of Technology and graduated in June 2000 with a Bachelor's of Science in Food Engineering. Immediately following his undergraduate studies, he enrolled at the University of Tennessee at Knoxville, August 2000. In December 2002, he completed his Master's of Science in Biosystems Engineering. He initiated requirements for fulfilling a terminal degree in January 2003 and received Doctor of Philosophy Degree in May 2007 from the University of Tennessee, Knoxville, TN.

He is a member of the American Society of Agricultural and Biological Engineer, Institute of Food Technologists, and Gamma Sigma Delta.